Ph.D. Thesis

Université de Limoges

University of Limoges
ED 614 - Chimie , Environnement, Géosciences, Agrosciences (CEGA)
Laboratoire PEIRENE

A thesis submitted to University of Limoges
in partial fulfillment of the requirements of the degree of
Doctor of Philosophy
Chemistry

Presented and defensed by
João Carlos Salgueiro Simões

On November 26, 2021

RADIOLABELLED PORPHYRINIC METALLA-ASSEMBLIES LINKED TO CELLULOSE NANOCRYSTALS AS PDT AND IMAGING AGENTS

Thesis supervisor: Vincent SOL

JURY:

President of jury
M. **Bruno Therrien**, Professeur, Université de Neuchâtel

Reporters
M. **Eric Benoist**, Professeur, Paul Sabatier Université - Toulouse III

Examiners
Mme. **Sophia Sarpaki**, Doctoresse, BioEmTech
M. **Vincent Sol**, Professeur, Laboratoire PEIRENE EA 7500, Université de Limoges
M. **Stephan H. von Reuss**, Professeur, Université de Neuchâtel

Rights

Acknowledgments

I would like to express my gratitude to the following people, without whom this thesis would not have been possible:

PROFESSORS Bruno Therrien, Vincent Sol, and George Loudos for giving me the opportunity to do my Ph.D. thesis in their research groups and for their patience and resilience. DR. Sophia Sarpaki for helping me throughout the PhD in all matters one can imagine, and the rest of the team at BioEmTech for their generosity and for always taking care of me. Prof. Eric Benoist for the co-examination of my thesis and for the useful remarks. Prof. Paul Dyson from the EPFL for having allowed me to conduct the biological analysis of my metalla-assemblies, and his Ph.D. student Mouna Hadiji for the warm welcome and help throughout my stay. Dr. Georges Wagnières, also from EPFL, for allowing me to utilize the diode laser in his group for the PDT treatments.Prof. Stephan von Reuss for accepting to evaluate my thesis and for being my examiner as a chemistry expert. Dr. Fredy Nydegger and Dr. Albert Ruggi from the University of Fribourg for the ESI-MS measurements; the team responsible for the elemental analysis at the ETH Zürich; and Dr. Sylvain Roger Aimé Sutour for the help with the NMR machine.

Also from Limoges Neuchâtel: Salma and Yasmina Mahmoud as well as the rest of my little Italian family in Limoges; Leonardo Palaferri, Chrysanthi Papadimou, Daniel Resa, Santiago Pons Allés, and Sirine Sghaier, the other Ph.D. students in our group, it was nice to meet you and have you around. You were always fun and ready to learn. Hoang-Giau Le, Aurélien Sébastien Pierre Billot, Ahmed Yassine Chadi, Rocìo de kas Nieves Rivera Sánchez, Siva Bandi, Dragan Alexandre Dalaveraj, and Bastian Guerry. Whenever you were around, there were always some reason to laugh, and there was never a dull moment. Hanna Laaroussi, Luana Cuvilier, and Arianna Passaretti, for the short ammount of time I got to know you, you were always kind, I wish we had had more time. With a special thank you to Marie Gaschard-Stefanelli (husband included) for your kindess and friendship when I first arrived at Neuchâtel, it helped me in an indescribable way, and for sharing your knowledge with me so selflessly; Magdalena Albelda Berenguer, Mathilde Monachon, and Sarah James for the good times during lunch and for organizing the Halloween and Christmas parties, the Secret Santa and so much more, thank you for making me company and feel welcomed in a strange place; and lastly Célia Bergame for your weird mind, thank you for being such a crazy and thoughtful friend, and for making me feel less normal in the best way.

To the other ESRs at the Polythea Project: Bhavya Khurana, Claire Donohoe, Dáire Gibbons, Harry Sample, Piotr Gierlich, and Manuel Gallardo Villagran for sharing this ridiculous ride with me, and helping each other find our way without a map. With a special thank you to Nidia Maldonado-Carmona (another husband also included) for being always so generous with me and for their incredible heart, and to Emma Robbins for being my new best friend all the way, for the support, for the time and fun, and for all the plans we have waiting for us. You were the best thing to come out of this hellish journey. Also to Aurore Berthier, our project manager, for going above and beyond in order to care for all ESRs, for her help and attention.

I would like to thank my friends, old and new, Joana Cardoso, Bruna Marques, Cláudia Alves, Cristiana Ramos, Carlota Gamboa, João Ribeiro, Filipe Brito, and Veronica Ambrosini, for believing in me more than I do myself, for always being there for me, incentivizing me to not give up, for the laughs, cries, and everything in between, I carry you all in my heart.

Finally, my family, especially my sister and my parents, everything I do is for you and because of you. I love you more than I can put into words. Thank you.

Abstract

Cancer is one of the biggest set of diseases in our society, and although there are some very interesting treatments and drugs used in pratice, one of the biggest challenges of anticancer treatment is the specific delivery of drugs to the target cells in order to avoid deleterious effects on normal cells. In fact, most of the anticancer drugs have potent effects also on normal cells due to the strong similarity of the mechanisms of growth regulation of normal cells as compared to their transformed counterparts. Photodynamic therapy (PDT) imposes itself as one of the most preponderant voices to tackle cancer and provide solutions for the problems encountered with traditional therapies. With the combination of a photosensitizer, light and oxygen, PDT achieves a unique selectivity by the production of localized reactive oxygen species (ROS) inside cancerous cells, which leads to their destruction with limited side effects. Alongside treatment, early diagnosis undertakes a critical role for the outcome. In particular, imaging is an extremely intriguing tool since it allows not only for diagnosis but to follow treatment as well.

This study aims to use cellulose nanocrystals to transport and deliver photo-responsive molecules to biological targets and create a new generation of theranostic agents. For that, porphyrins and phthalocyanines were synthesized,[1] with the aim of exploring their peculiar set of absorption bands for PDT treatment. These were then used as panels to construct metalla-assemblies through coordination with ruthenium dimers, with the goal of enhancing not only their solubility but also helping with aggregation.[2] The ruthenium metalla-clips also offer stability and inherent cytotoxicity through reduction in the cancer site.[3]

These complexes were subsequently linked to cellulose nanocrystals (CNCs)[4] for better targeting. This is achieved through the increase of their size, making them interesting EPR (enhanced permeation retention) effect enhancers. This delivery strategy is based upon the particular structure of tumor neoangiogenic vessels that allow the passive targeting. Another advantage of grafting these compounds to CNCs is that they ensure biological compatibility and prolonged blood circulation time. From the resulting photo-responsive compounds, the ones that were considered to have the best characteristics were then radiolabeled with either technetium-99m or indium-111 through direct radiolabelling, allowing them to also be used as imaging probes.

After synthesis, *in vitro* assays were performed to determine the IC_{50} and whether the PDT agents were selective towards cancer cells. At the same time, it allowed to determine the optimal concentration for *in vivo* experiments. Their cytotoxicity and potential therapeutic effects were evaluated on two ovarian cancer (A2780 and A2780cis) and one normal hepatic cell lines (HEK293T) through a metabolic activity assay. Their cellular uptake was determined as well. Finally, the radiolabeled compounds that showed the best *in vitro* results were used for scintigraphic imaging in Severe Combined Immunodeficiency (SCID) mice at several timepoints (1, 2, 4 and 24 h) with the intent of studying their biodistribution, which showed preferential accumulation mainly in the liver, but also in the bladder.

The hypothesis is therefore that through consecutive modifications of the initial photosensitizers in order to ameliorate their biophysical characteristics (through coordination with organometallic compounds and cellulose nanocrystals) and later their radiolabelling, we will be able to achieve novel PDT theranostic agents. The present work, therefore, deals with the synthesis, characterization, *in vitro* and *in vivo* evaluation of a small family of novel PDT theranostic agents.

Keywords : photodynamic therapy**,** theranostic agents**,** metalla-assemblies, radiolabeling

Résumé

Le cancer est l'un des plus grands ensembles de maladies dans notre société, ce qui signifie qu'il y a un besoin urgent de nouveaux médicaments pour traiter le cancer. L'un des plus grands défis du traitement anticancéreux est l'administration spécifique de médicaments aux cellules cibles afin d'éviter les effets délétères sur les cellules saines. En fait, la plupart des médicaments anticancéreux ont également des effets puissants sur les cellules normales en raison de la forte similitude des mécanismes de régulation de la croissance des cellules normales par rapport à leurs homologues transformés. La thérapie photodynamique (PDT) s'impose comme l'une des voies innovantes pour lutter contre le cancer et apporter des solutions aux problèmes rencontrés avec les thérapies traditionnelles. Avec la combinaison d'un photosensibilisateur, de la lumière et de l'oxygène, la PDT atteint une sélectivité unique par la production d'espèces réactives de l'oxygène (ROS) localisées à l'intérieur des cellules cancéreuses, ce qui conduit à leurs destructions avec des effets secondaires limités. Parallèlement au traitement, le diagnostic précoce joue un rôle essentiel pour le résultat. En particulier, l'imagerie est un outil extrêmement intrigant puisqu'il permet non seulement le diagnostic mais aussi l'accompagnement du traitement.

Cette étude vise à utiliser des nanocristaux de cellulose pour transporter et livrer des molécules photosensibles à des cibles biologiques et créer une nouvelle génération d'agents théranostiques. Pour cela, des porphyrines et des phtalocyanines ont été synthétisées,[1] dans le but d'explorer leur ensemble particulier de bandes d'absorption pour le traitement en PDT. Celles-ci ont ensuite été utilisées pour construire des métalla-assemblages par coordination avec des dimères de ruthénium, dans le but non seulement d'améliorer leur solubilité, mais aussi d'éviter l'agrégation.[2] Les unités métalla-ruthénium offrent également une stabilité et une cytotoxicité inhérente grâce à la présence de ruthénium sur le site du cancer.[3]Ces complexes ont ensuite été liés à des nanocristaux de cellulose (CNC)[4] pour un meilleur ciblage par l'augmentation de leur taille, ce qui en fait d'intéressants activateurs d'effet EPR (enhanced permeability and retention effect). Cette stratégie de livraison est basée sur la structure particulière des vaisseaux néoangiogéniques tumoraux qui permettent un ciblage passif. Un autre avantage du greffage de ces composés sur les CNC est qu'il assure une compatibilité biologique et un temps de circulation sanguine prolongé. À partir des composés photosensibles ayant les meilleures caractéristiques, un marquage isotopique avec du technétium-99m et de l'indium-111 par radiomarquage direct a été effectué, afin de les utiliser comme sondes d'imagerie.

Après la synthèse, des tests *in vitro* ont été effectués pour déterminer la toxicité (IC_{50}) et si les agents PDT étaient sélectifs vis-à-vis des cellules cancéreuses. Dans le même temps, il a été permis de déterminer la concentration optimale pour les expériences *in vivo*. Leur cytotoxicité et leurs effets thérapeutiques potentiels ont été évalués sur deux lignées de cellules cancéreuses de l'ovaire (A2780 et A2780cis) et une lignée cellulaire hépatique normale (HEK293T) par un test d'activité métabolique. Leur absorption cellulaire a également été déterminée. Enfin, les composés radiomarqués qui ont montré les meilleurs résultats *in vitro* ont été utilisés pour l'imagerie scintigraphique chez des souris à immunodéficience combinée sévère (SCID) à différents intervalles (1, 2, 4 et 24 h) dans le but d'étudier leur biodistribution, qui a montré une accumulation préférentielle dans le foie, mais aussi dans la vessie.

L'hypothèse est donc que par des modifications consécutives des photosensibilisateurs initiaux afin d'améliorer leurs caractéristiques biophysiques (par coordination avec des composés organométalliques et des nanocristaux de cellulose) et plus tard leur radiomarquage, nous avons réalisé de nouveaux agents théranostiques pour la PDT. Le présent travail porte donc sur la synthèse, la caractérisation, l'évaluation *in vitro* et *in vivo* d'une petite famille de nouveaux agents théranostiques.

Mots clés : thérapie photodynamique**,** agents théranostiques**,** metalla-assemblages, radiomarquage

Table Of Contents

Abstract 2

Résumé 3

Table Of Contents 5

Figure Index 7

  List of Schemes 10

  List of Tables 10

Glossary 11

List of Compounds 13

Chapter 1 – Answering a problem 19

  1.1. The Problem of Cancer 19

  1.2. The Answer of Theranostics 20

  1.2.1. Therapy – Photodynamic Therapy 20

  1.2.1.1. PDT mechanism of action 21

  1.2.1.2. Active components on PDT 23

    i) Oxygen 23

    ii) Light 23

    iii) Photosensitizers 24

  1.2.2. Ruthenium metalla-assemblies as promising PDT agents 26

  1.3. Cellulose Nanocrystals as Biocompatibility and Targeting units 30

  1.3.1. Cellulose's Molecular Structure 31

  1.3.2. Production of CNCs 32

  1.3.2.1. Acid hydrolysis 33

  1.3.3. Properties of CNC 33

  1.3.3.1. Reactivity 34

  1.3.4. Chemical Modification of Nanocellulose 35

  1.3.4.1. Sulfonation 36

  1.3.4.2. TEMPO Oxidation 37

  1.4. Diagnostics - Imaging 38

Chapter 2 – Results and Discussion 71

2.1. Chemistry Results 71

  2.1.1. The photosensitizers 71

2.1.2. Constructing Metalla-clips and metalla-assemblies 72
2.1.3. Grafting to Cellulose Nanocrystals 78
2.2. Radiolabelling & Kinetic Studies 80
2.2.1. Radiolabelling with technetium-99m 82
2.2.2. Radiolabelling with indium-111 84
2.3. The *in vitro* Results 87
2.3.1. Metabolic Inhibition Assays 87
2.3.2. Cellular Uptake of Radiolabelled Compounds 93
2.4. The *In vivo* Results 99
Chapter 3 – Conclusions and Future Perspectives 105
Chapter 4 – Experimental Section 107
4.1. Chemistry 107
4.1.1. MATHERIALS AND METHODS 107
4.1.2. SYNTHESIS & CHARACTERIZATION 107
4.1.2.1. Synthesis of porphyrins and phthalocyanines 107
4.1.2.2. Synthesis of dichloro(*p*-cymene)ruthenium(II) dimer 108
4.1.2.3. Synthesis of organic ligands/spacers 109
4.1.2.4. Synthesis of metalla-clips: conjugation of spacer and dimer 110
4.1.2.5. Synthesis of metalla-assemblies 111
4.1.2.6. Grafting of Metalla-AssemblIies to CNC 112
4.2. *In vitro* 115
4.3. In vivo 117
4.3.1. Imaging Protocol 118

References 119
Electronic Supplementary Information (ESI) 129

Figure Index

Figure 1 – Modified Jablonski diagram depicting the process of photodynamic therapy. When PSs in cells are exposed to specific wavelengths of light, they are transformed from the singlet ground state (S0) to an excited singlet state (S1–Sn), which is followed by intersystem crossing to an excited triplet state (T1). Abbreviation: IC: internal conversion; ISC: intersystem crossing; PS: photosensitizer; 1PS*: Singlet excited photosensitizer; T1: Triplet excited state; R: biological substrate; R*: oxidized biological substrate; $1O_2$: Singlet oxygen; H_2O_2: hydrogen peroxide; O_2*: superoxide; HO*: hydroxyl radical……………………………………………………………………………………………**20**

Figure 2 – Illustration showing the differential uptake of NPs and small molecules based on their size across (A) normal and (B) cancerous tissues……………………………………………………………………………………………**23**

Figure 3 – RM175 (left) and RAPTA-C (right) are typical examples of 18-electron ruthenium arene "piano-stool" complexes, in which an η6-arene ring stabilises the 2+ oxidation state of the ruthenium metal centre…………………**25**

Figure 4 – NAMI-A is an octahedral Ru(III) pro-drug, which is hypothesized to undergo an "activation by reduction" mechanism inside cells to form more active Ru(II) species………………………………………………………………**26**

Figure 5 – Arene ruthenium metalla-cubes ……………………………………………………………………………**27**

Figure 6 – Molecular structure of cellulose representing the cellobiose unit as a repeating unit showing reducing (right) and non-reducing (left) end-groups……………………………………………………………………………**29**

Figure 7 – Cellulose structures showing the intramolecular hydrogen bonding (left) between C2-OH and C6-OH (i), and C3-OH with endocyclic oxygen (ii); and the intermolecular hydrogen bonding (right) between C3-OH and C6-OH (supramolecular structure)……………………………………………………………………………………**30**

Figure 8 – Numbering system for carbon atoms in anhydroglucose unit of cellulose…………………………………**33**

Figure 9 – Distinctive surface chemistries provided by the most common extraction methods of cellulose nanoparticles: sulfuric acid hydrolysis provides sulphate ester groups (route 1), hydrochloric acid hydrolysis provides hydroxyl groups (route 2), acetic acid hydrolysis provides acetyl groups (route 3), TEMPO mediated hypochlorite treatment (route 4) and carboxymethylation (route 5) provide carboxylic acid groups…………………**33**

Figure 10 – Schematic representation of the hydrolysis of amorphous and crystalline cellulose with H_2SO_4, and consequent sulfonation. ……………………………………………………………………………………………**34**

Figure 11 – Scheme of TEMPO-mediated oxidation of cellulose………………………………………………………**35**

Figure 12 – Structural representation of all photosensitizers used in this work…………………………………………**69**

Figure 13 – Structural representation of S1-S4……………………………………………………………………………**70**

Figure 14 – Structural representation of metalla-clips **C1-C4** resulted from the reaction of spacers **S1-S4** with dichloro(*p*-cymene)ruthenium(II) dimer…………………………………………………………………………**71**

Figure 15 – ^{1}H NMR spectra of **M1**, **M2**, and **M3** in DMSO-d6……………………………………………………**72**

Figure 16 – ^{1}H NMR spectra of **M5** (top) and **M5** (bottom) in DMSO-d6…………………………………………**75**

Figure 17 – UV-Vis spectra of **M5** (red) and **M5** (black) in DMSO. The peaks show the typical Soret band at 412 and 415 nm, respectively, as well as the Q-bands (500-650 nm)…………………………………………………… **76**

Figure 18 – IR spectra **MC4** (yellow) and **MC5** (blue), and free CNC (red)………………………………………**78**

Figure 19 – Radiochemical data of free, reduced [^{99m}Tc]TcO$_4^-$, and radiolabeled compounds·. The radio-iTLCs were developed on Whatman 1 MM with **saline** as the mobile phase, RCC 99.0%......**80**

Figure 20 – Radiochemical data of free, reduced [^{99m}Tc]TcO$_4^-$, and radiolabeled compounds·. The radio-iTLCs were developed on Whatman 1 MM with **acetone** as the mobile phase, RCC 99.0%......**81**

Figure 21 – Graph presenting the results obtained from kinetic stability tests of [^{99m}Tc]Tc-**MC5**. The radioactive molecule was incubated at 37 ˚C with different media (1:10) for up to 24 hrs. Error bar stands for standard error (±SE), calculated from three repeated measurements......**81**

Figure 22 – Radiochemical data of free [^{111}In]InCl3, and radiolabeled compounds·. The radio-iTLCs were developed on Whatman paper 3 MM with EDTA 1M as the mobile phase showing, RCC 95.0%......**83**

Figure 23 – Graph presenting the results obtained from kinetic stability tests of [^{111}In]In-**MC5**. The radioactive molecule was incubated at 37 ˚C with different media (1:10) for up to 24 hrs. Error bar stands for standard error (±SE), calculated from three repeated measurements......**83**

Figure 24 – Schematic representation of an *in vitro* study from cell culture to PDT treatment and metabolic inhibition assays......**85**

Figure 25 – Comparison of the IC50 values of P**5**, **M5** and **MC5** against the ovarian cancer cell lines A2780 and A2780cis, as well as the normal hepatic cell line HEK293T, in the dark and after irradiation......**89**

Figure 26 – Cell uptake for **[^{99m}Tc]Tc-P5** in the HEK293T, A2780, and A2780cis cell lines up until 4 h. Error bar stands for standard error (±SE), calculated from three repeated measurements......**92**

Figure 27 – Cell uptake for **[^{99m}Tc]Tc-M5** in the HEK293T, A2780, and A2780cis cell lines up until 4 h. Error bar stands for standard error (±SE), calculated from three repeated measurements......**92**

Figure 28 – Cell uptake for **[^{99m}Tc]Tc-MC5** in the HEK293T, A2780, and A2780cis cell lines up until 4 h. Error bar stands for standard error (±SE), calculated from three repeated measurements......**93**

Figure 29 – Cell uptake for **[^{99m}Tc]Tc-P5**, **[^{99m}Tc]Tc-M5**, and **[^{99m}Tc]Tc-MC5** in the A2780 cancer cell line up until 4 h. Error bar stands for standard error (±SE), calculated from three repeated measurements......**93**

Figure 30 – Cell uptake for **[^{111}In]In -P5** in the HEK293T, A2780, and A2780cis cell lines up until 4 h. Error bar stands for standard error (±SE), calculated from three repeated measurements......**94**

Figure 31 – Cell uptake for **[^{111}In]In –M5** in the HEK293T, A2780, and A2780cis cell lines up until 4 h. Error bar stands for standard error (±SE), calculated from three repeated measurements......**95**

Figure 32 – Cell uptake for **[^{111}In]In -MC5** in the HEK293T, A2780, and A2780cis cell lines up until 4 h. Error bar stands for standard error (±SE), calculated from three repeated measurements......**95**

Figure 33 – Cell uptake for **[^{111}In]In -P5**, **[^{111}In]In -M5**, and **[^{111}In]In -MC5** in the A2780 cancer cell line up until 4 h. Error bar stands for standard error (±SE), calculated from three repeated measurements......**96**

Figure 34– Indicative static 20 – 50 min scintigraphy/optical images of a normal Swiss Albino mouse intratracheal administered with [^{99m}Tc]Tc-**M5** (375 nM) at 1, 2, 4 and 24 hours p.i. The gradual alteration in colour indicates a lower to a higher number of recorded counts......**99**

Figure 35 – Indicative static 20 – 50 min scintigraphy/optical images of a normal Swiss Albino mouse intratracheal administered with [^{99m}Tc]Tc-**MC5** (375 nM) at 1, 2, 4 and 24 hours p.i. The gradual alteration in colour indicates a lower to a higher number of recorded counts......**99**

Figure 36 – Indicative static 20 – 50 min scintigraphy/optical images of a normal Swiss Albino mouse intratracheal administered with [^{99m}Tc]Tc-**MC5** (1500 nM) at 1, 2, 4 and 24 hours p.i. The gradual alteration in colour indicates a lower to a higher number of recorded counts…………………………………………„„……………………………………**99**

Figure 37 – Indicative static 20 – 50 min scintigraphy/optical images of a normal Swiss Albino mouse intratracheal administered with [^{99m}Tc]Tc-**MC5** (750 nM) at 1, 2, 4 and 24 hours p.i. The gradual alteration in colour indicates a lower to a higher number of recorded counts……………………………………………………………………………………**100**

Figure 38 – Clearance Yield for [^{99m}Tc]Tc-**MC5** at different concentration: 375, 750 and 1500 nM (right); and for [^{99m}Tc]Tc-**M5** and [^{99m}Tc]Tc-**MC5** at 375 nM (left). Error bar stands for standard error (±SE), calculated from three repeated measurements Error bar stands for standard error (±SE), calculated from three repeated measurements……**100**

Figure 39 – Indicative static 20 – 50 min scintigraphy/optical images of a normal Swiss Albino mouse intratracheal administered with [^{111}In]In-**M5** (375 nM) at 1, 2, 4 .and 24 hours p.i. The gradual alteration in colour indicates a lower to a higher number of recorded counts……………………………………………………………………………………**101**

Figure 40 – Indicative static 20 – 50 min scintigraphy/optical images of a normal Swiss Albino mouse intratracheal administered with [^{111}In]In-**MC5** (375 nM) at 1, 2, 4 and 24 hours p.i. The gradual alteration in colour indicates a lower to a higher number of recorded counts……………………………………………………………………………………**101**

Figure 41 – Clearance Yield for [^{111}In]In-**M5**, [^{111}In]In-**MC5**, [^{99m}Tc]Tc-**M5,** and [^{99m}Tc]Tc-**MC5** at 375 nM. Error bar stands for standard error (±SE), calculated from three repeated measurements…………………………………………**102**

Figure 42 – Structural representation of the different spacers synthesized (**S1-S4**)…………………………………………**106**

Figure 43 – Structural representation of the different metalla-clips synthesized (**C1-C4**)………………………………………**107**

Figure S1 – Mass spectrometry spectra for **M1** – ESI (+)……………………………………………………………………………**123**

Figure S2 – Mass spectrometry spectra for **M2** – ESI (+)……………………………………………………………………………**123**

Figure S3 – Mass spectrometry spectra for **M3** – ESI (+)……………………………………………………………………………**124**

Figure S4 – Mass spectrometry spectra for **M4** – ESI (+)……………………………………………………………………………**124**

Figure S5 – Mass spectrometry spectra for **M5** – ESI (+)……………………………………………………………………………**125**

Figure S6 – Dynamic light scattering (DLS) data of **MC5** collected for the measurement of average hydrodynamic diameters……**125**

Figure S7 – ζ-potential data of MC**5** collected through electrophoretic light scattering……………………………………**126**

Figure S8 – Metabolic activity against ovarian cancer cell line A2780 in both the dark and after irradiation. Error bar stands for standard error (±SE), calculated from 3 repeated measurements………………………………………………**126**

Figure S9 – Metabolic activity against ovarian cancer cell line A2780cis in both the dark and after irradiation. Error bar stands for standard error (±SE), calculated from 3 repeated measurements………………………………………………**126**

Figure S10 – Metabolic activity against normal liver cell line (HEK293T) in both the dark and after irradiation. Error bar stands for standard error (±SE), calculated from 3 repeated measurements………………………………………………**127**

Figure S11: ^{1}H NMR spectra (between 0 and 10 ppm) of **C3** in DMSO-d_6……………………………………………………**127**

Figure S12: ^{1}H NMR spectra (between 0 and 10 ppm) of **C4** in DMSO-d_6……………………………………………………**128**

Figure S13: ^{1}H NMR spectra (between 0 and 10 ppm) of **M1** in DMSO-d_6……………………………………………………**128**

Figure S14: ^{1}H NMR spectra (between 0 and 10 ppm) of **M2** in DMSO-d_6……………………………………………………**129**

Figure S15: ^{1}H NMR spectra (between 0 and 10 ppm) of **M3** in DMSO-d_6……………………………………………………**129**

Figure S16: ^{1}H NMR spectra (between 0 and 10 ppm) of **M4** in DMSO-d_6……………………………………………………**130**

Figure S17: ^{1}H NMR spectra (between 0 and 10 ppm) of **M5** in DMSO-d_6……………………………………………………**130**

List of Schemes

Scheme 1 – Overview of the synthetic route for the metalla-macrocycle assemblies **M1-M3.** ……………………………73

Scheme 2 – Overview of the synthetic route for the metalla-macrocycle assemblies **M4-M5**…………………………………74

Scheme 3 – Synthetic route for the grafting of **M4** and **M5** to CNCs by reaction with N-Hydroxysuccinimide (NHS) and 1-ethyl-3-(-3-dimethylaminopropyl) carbodiimide hydrochloride (EDC)……………………………………………………77

Scheme 4 – Structural comparison between **P5, M5, MC5**………………………………………………………………………………**79**

Scheme 5 – Synthetic route for the synthesis of 5-(4-aminophenyl)-10,15,20-tri(4-pyridyl)porphyrin (**P4**).……**105**

Scheme 6 – Synthetic route for the synthesis of 5-(4-hydroxyphenyl)-10,15,20-tri(4-pyridyl)porphyrin (**P5**)….**105**

Scheme 7 – Synthesis of [(η6-*p*-cymene)2Ru2(μ2-Cl)2Cl2]………………………………………………………………………**106**

Scheme 8 – Overview of the H_2SO_4 hydrolysis of cellulose nanocrystals………………………………………………**109**

Scheme 9 – Overview of the TEMPO oxidation of cellulose nanocrystals………………………………………………………**110**

List of Tables

Table 1 –List of clinically approved photosensitizers with their excitation wavelengths and indications……………**18**

Table 2 – IC_{50} ± standard deviation (in μM) values of all **M1-M5** against the three cell lines studied (A2780, A2780cis, and HEK293T)………**85**

Table 3 – Selectivity (SI) and Photodynamic efficiency (PE) index values of **M1-M5**………………………………………**86**

Table 4 – IC_{50} ± standard deviation (in μM) values of different compounds against the three cell lines studied (A2780, A2780cis, and HEK293T)……………………………………………………………………………………………………**87**

Table 5 – Selectivity (SI) and Photodynamic efficiency (PE) index values of **P4**, **P5**, **M4**, **M5**, **MC4**, and **MC5**……….**89**

Glossary

$^1O_2$ – singlet oxygen

ε_{max} – maximum value of the molar absorptivity

5-ALA – 5-aminolevulinic acid

A2780 – human cell line, ovarian carcinoma

A2780cis – human cell line, ovarian carcinoma, Cisplatin® resistant

aPS –activatable photosensitizer

BODIPY – boron-dipyrromethene

Ce6 – chlorin e6

CNC – cellulose nanocrystals

CT – computer tomography

DLI – Drug-light interval

DMEM – Dulbecco's Modified Eagle's Culture Medium

DMSO – dimethyl sulfoxide

EGFR – epidermal growth factor receptor

EPR – Enhanced Permeability and Retention

FMISO – fluoromisonidazole

HEK293T – human embryonic kidney 293 cells expressing a mutant version of the SV40 large T antigen

HpD – hematoporphyrin derivative

IC_{50} – half maximal inhibitory concentration

ISC – intersystem crossing

LDL – low-density lipoprotein

MDR – multidrug resistance

MOF – metal-organic frameworks

MRI – magnetic resonance imaging

MTT – 3-(4,5-dimethylthiazol-2-yl)- 2,5-diphenyltetrazolium bromide

NI – nitrimidazole

NCI – national cancer institute

NIR – near infrared n–p - n-methylpyrrolidone

NMI – nuclear medical imaging

NMR – nuclear magnetic resonance

NP – nanoparticle

NSE – lung cancer tumor marker

OFI – optical fluorescence imaging

PBS – Phosphate-Buffered Saline

Pc – phthalocyanine

PDD – photodynamic diagnosis

PDT – photodynamic therapy

PEG – polyethylene glycol

PET – positron emission

pH – negative logarithm of hydrogen ion concentration

p.i. – post injection

PPIX – protoporphyrin IX

PS – photosensitizer

PPM – parts per million

Q – quencher particle

QD – quantum dots

QY – quantum yield

ROS –reactive oxygen species

SiNP – silica nanoparticles

SPECT – single-photon emission computed tomography

ROS – reactive oxygen species

RPMI – Roswell Park Memorial Institute 1640 Medium

THPP – tris(3-hydroxypropyl)phosphine

TPP – tetraphenylporphyrin

UV-Vis – ultraviolet–visible

Tt – lifetime of the excited triplet state

ΦT – quantum yield of the excited triplet state

List of Compounds

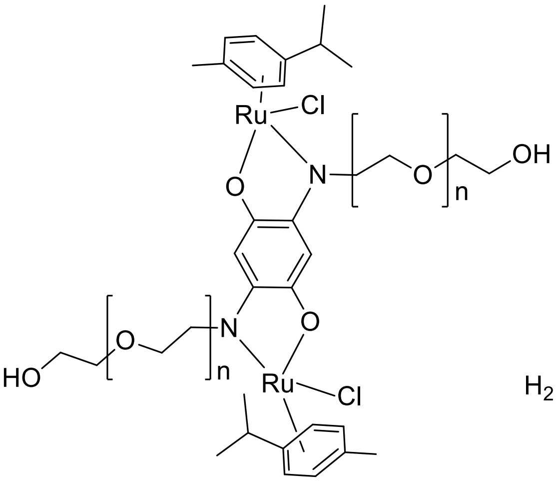

C1

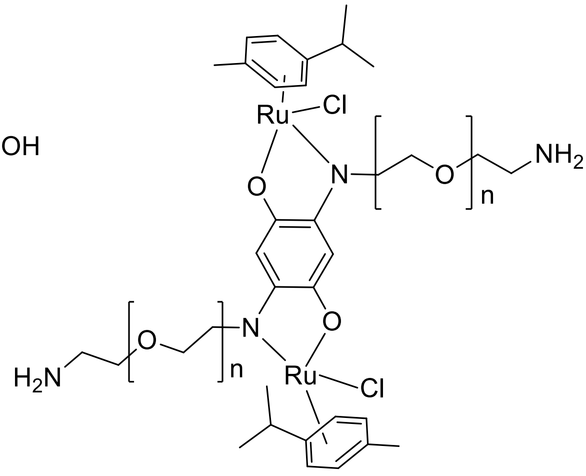

C2

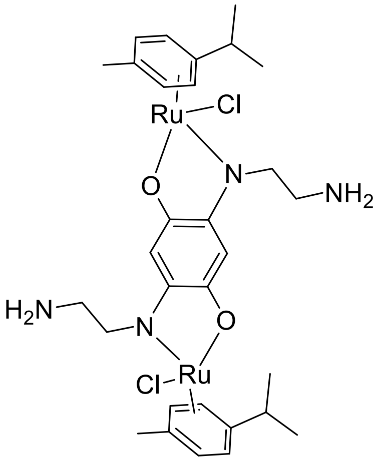

C3

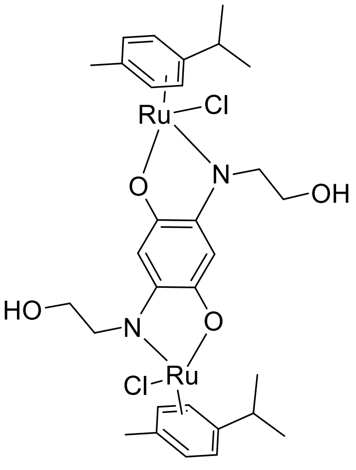

C4

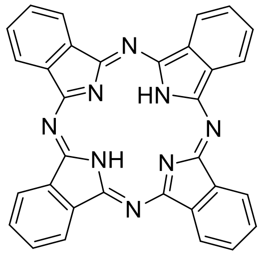

P1

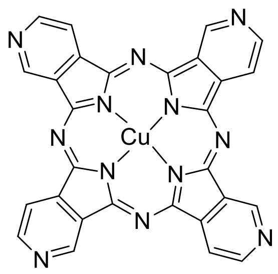

P2

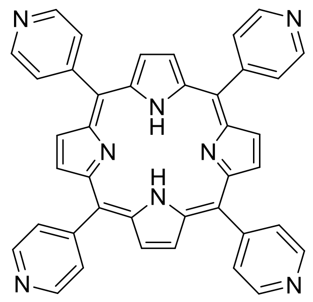

P3

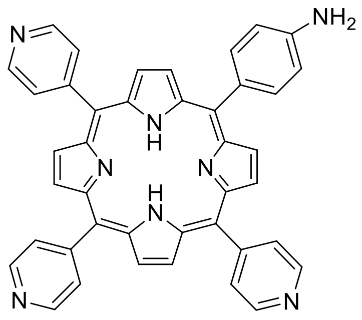

P4

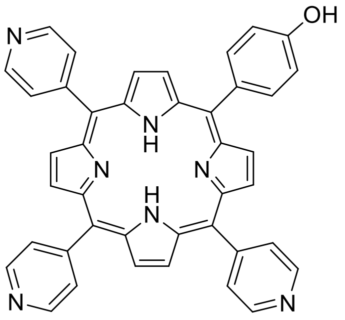

P5

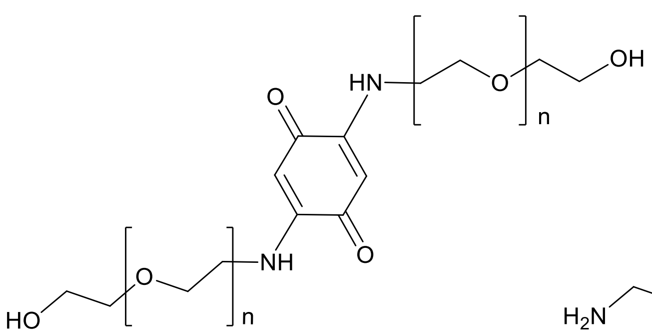

S1

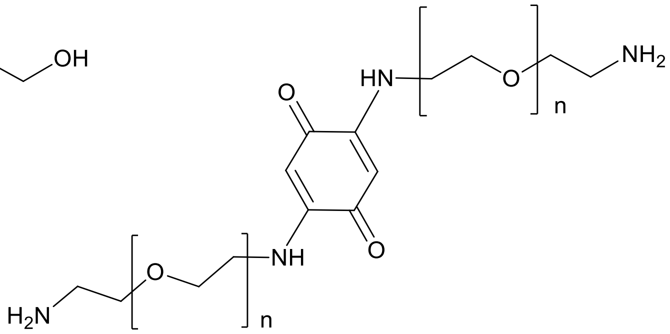

S2

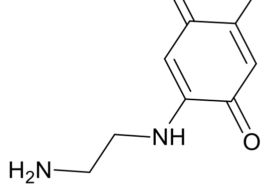

S3

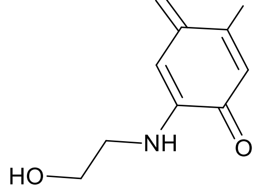

S4

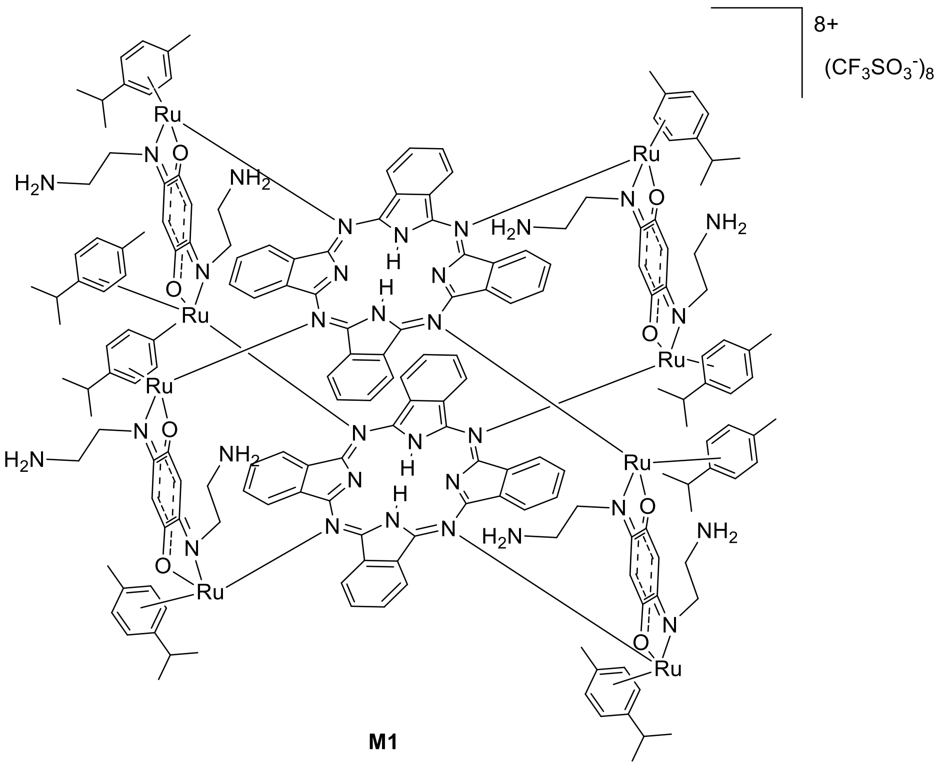

M1

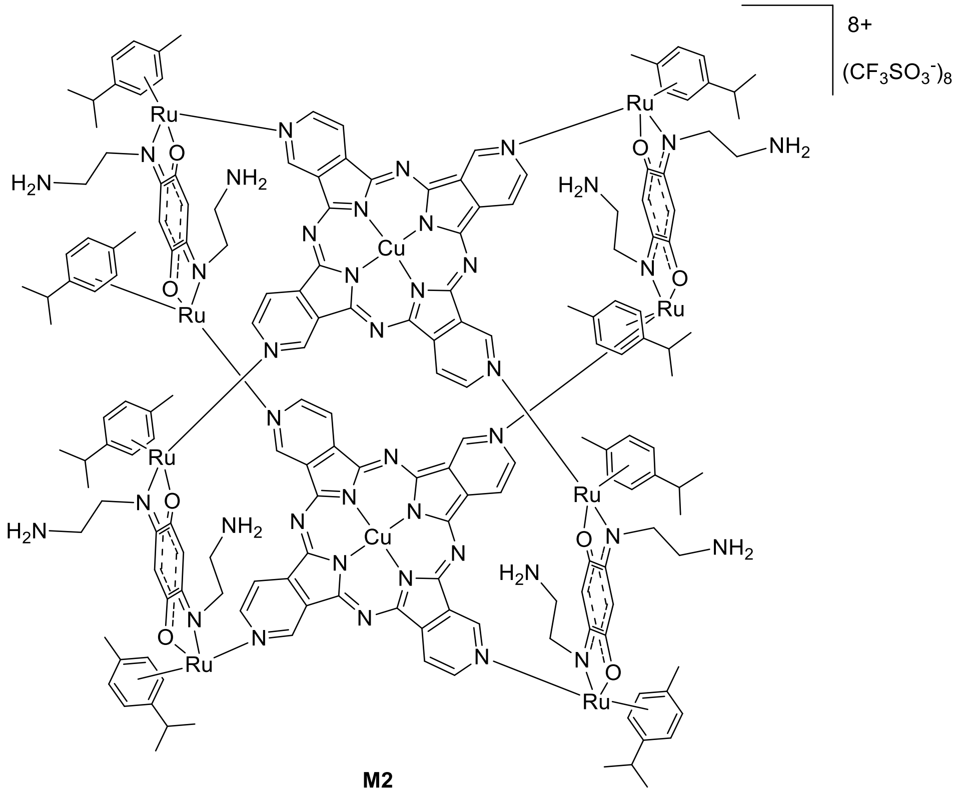

M2

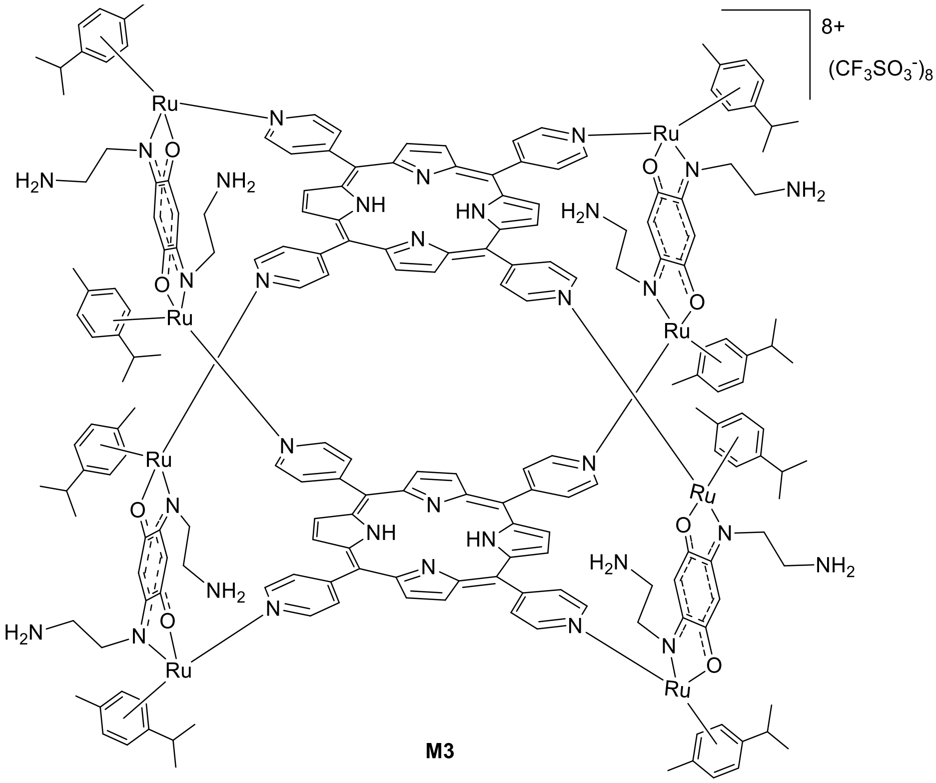

M3

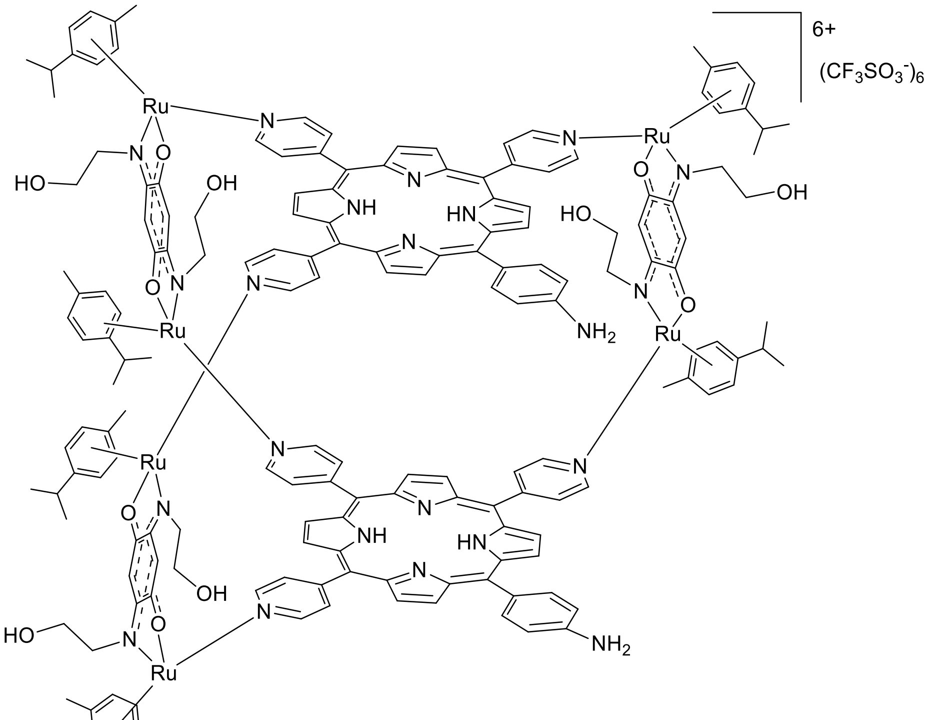

M4

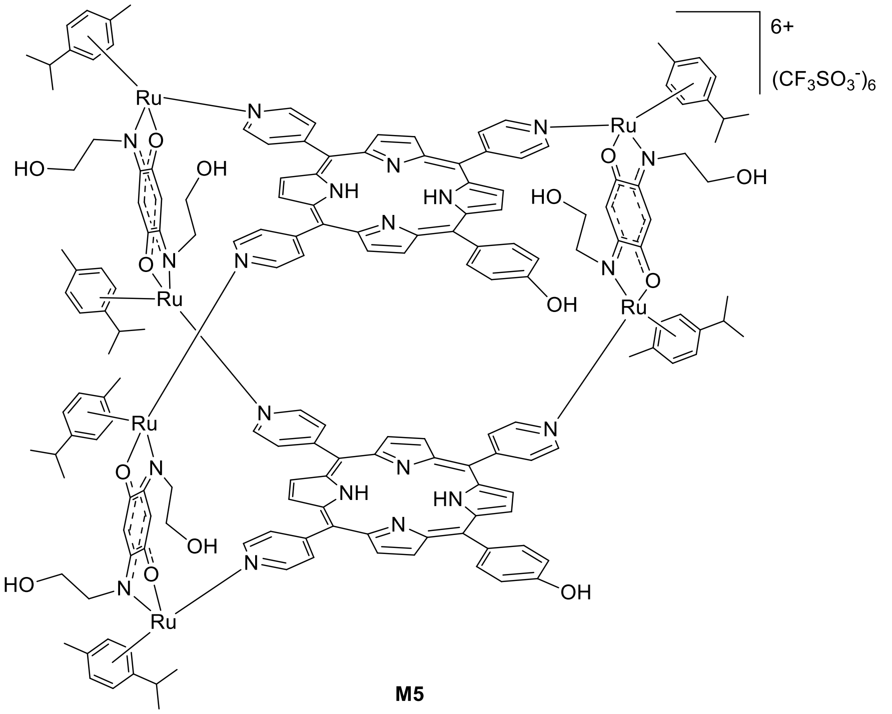
6+
$(CF_3SO_3^-)_6$
Ru
N
O
HO
OH
NH
HN
OH

M5

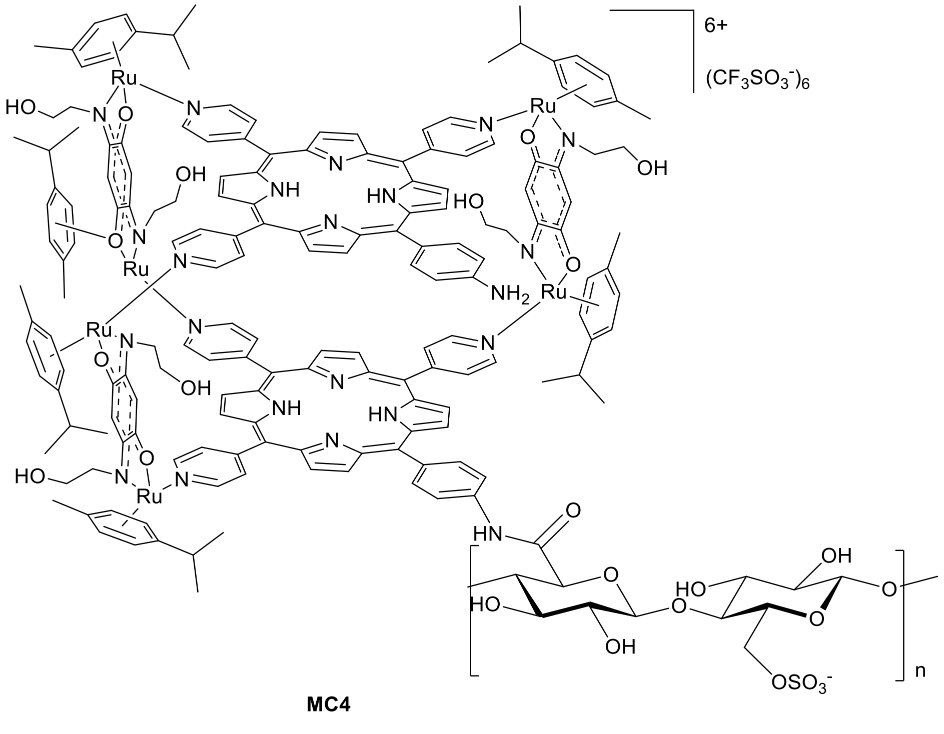
6+
$(CF_3SO_3^-)_6$
Ru
N
O
HO
OH
NH
HN
NH_2
HN
O
n
OSO_3^-

MC4

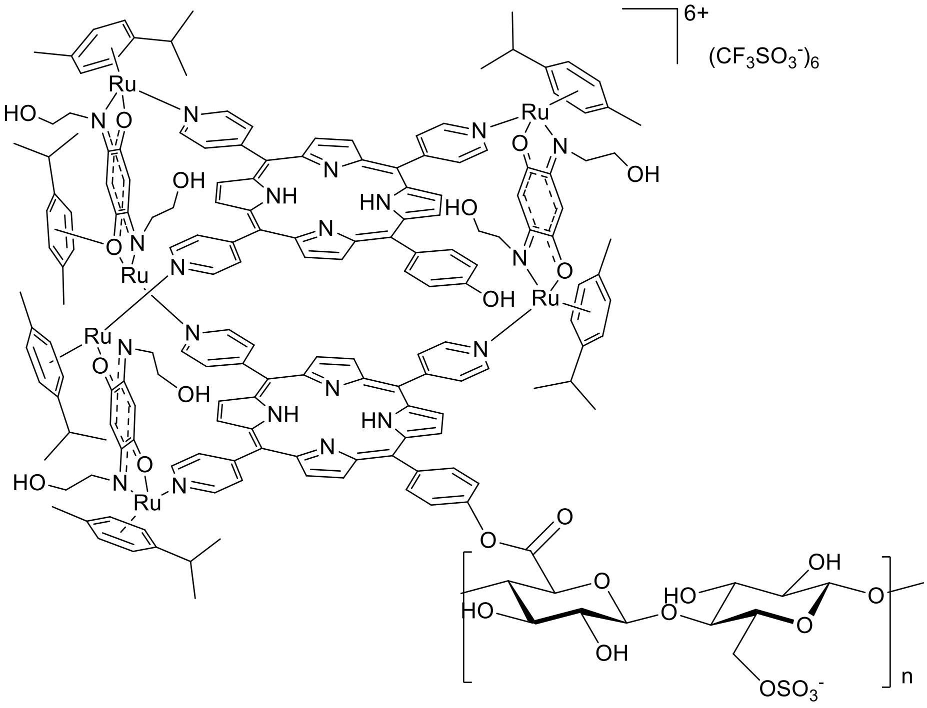

MC5

Chapter 1 – Answering a problem

"Divide et imperais", in English "Divide and Conquer", is a Latin phrase as old as politics and war. The famous quote attributed to Julius Cesar can also be applied to our study – Cancer. It is by dividing and spreading in the human body that cancer ends up conquering it, leaving us defenceless. Cancer is a cruel enemy, unmerciful, unjust, difficult to tackle and defeat. That is not, however, a reason to surrender instead of gathering all the weapons that are at our service to try our best and slay the beast. One of those weapons is science, not any science, but science allied by our reason, our capability to think and to strategize. Medicinal chemistry is, therefore, an important discipline. It gives us the tools to be on the right side of this historic fight and end up being the heroes, not the casualties. In the next chapters, the characteristics of cancer are investigated, and how to take advantage of these characteristics are highlighted, suggested, and put to the test. One of the main goal of this study is to add knowledge to the state of the art. This is important because it was only using the knowledge that was given to us by others that it was possible to come up with our own promising ideas. So, we hope that from this work, others will be inspired. The second goal is to highlight the importance of chemistry to the world, and how rational design works if we are methodical, intelligent, and persistent. Lastly, we aim to try to give answers to an ever-growing problem, to be able to say, this worked and this did not… we tried… we gave our best, and therefore, we are one step closer to win this battle, maybe it won't be us, but we helped.

1.1. The Problem of Cancer

Cancer is a serious disease that affects people all over the world. Every year, tens of millions of people are diagnosed, with more than half of those diagnosed dying from it. It is the second leading cause of death in many nations, after heart disease and stroke, and thanks to considerable advances in cardiovascular disease treatment and prevention, it has or will soon become the leading cause of death in many regions of the world.[5] Furthermore, cancer has become a rising global socioeconomic problem due to an increase in overall incidence rates and non-response to current medicines. After all, despite massive global research efforts, cancer remains among the world's leading cause of death, with 8 million deaths each year, and the problem isn't going away anytime soon. It's expected that this number will double in the next 20 to 40 years, with a higher incidence in developing countries.[6]

Due to the prevalence of this problem, the discovery of new antitumor medicines has become a worldwide topic of interest. While traditional therapeutic procedures have made great advancements, with high cure rates for some types of cancer, they are also responsible for major side effects. The variability and genetic complexity of tumors within the population explains why areas from medicine and medicinal chemistry to pharmaceutics have worked so hard to find novel, safer, more effective, and specialized cancer medicines. The development of drug resistance, which is typically related to the establishment of tumor cell populations that are insensitive to cytotoxic drugs, is one of the biggest obstacles to standard cancer therapy. One of the most well-known reasons for this is cancer cells' rapid mutation rate. Other possibilities include decreased drug absorption or greater drug efflux, drug target, or the activation of alternative cell survival mechanisms.[7] The active transport of a wide range of hydrophobic anticancer drugs from the cytoplasm to the extracellular medium, mediated by a membrane carrier family known as the ATP binding cassette, is another mechanism commonly related with multiple drug resistance in chemotherapy.[8] Angiogenesis inhibitors, active cytotoxic drug focus, gene therapy, and immunotherapy have all been developed as a result of a growing understanding of the genesis, progression, and dissemination pathways of cancer across time. When compared to traditional oncology therapies, photodynamic therapy has shown to be a promising cancer therapy because it has several advantages in terms of tolerability profiles, the absence of specific resistance mechanisms, and the ability to stimulate the immune system, which is seen as a significant differentiation factor.[7,9]

1.2. The Answer of Theranostics

1.2.1. Therapy – Photodynamic Therapy

The concept of utilizing light to treat diseases is not new. In fact, different forms of phototherapy have been used to treat psoriasis and vitiligo for over 5000 years in India and ancient Greece, using a combination of psoralens and sunlight. However, the current concept and clinical application of PDT were only described in the early twentieth century, when Oscar Raab, a medical student working on his Ph.D., made an unintentional discovery that microorganisms incubated with certain dyes, such as acridine, could be killed when exposed to light but not when kept in the dark.[10]

When it was revealed in 1903 that oxygen in the air was also required for this light-mediated killing impact to occur, Oscar Raab's advisor Herman von Tappeiner coined the term "photodynamic effect".[11] The earliest attempts to use this phenomena as a cancer therapy were made not long after these discoveries, by putting dyes on superficial skin lesions and then exposing them to light. Actually, it was von Tappeiner and Jesionek that carried out the first PDT clinical experiments.[12]

Dougherty and co-workers reported between 1975 and 1978 complete cures of malignant tumors by combining HpD (Hematoporphyrin Derivative) and red light, initially in a breast cancer model, and afterwards in patients with skin, prostate, breast, and colon malignancies. Clinical experiments including enhanced forms of HpD in individuals with skin and bladder cancer eventually validated these encouraging outcomes. Weishaupt and colleagues proposed in 1976 that the cytotoxic agent responsible for the death of tumor cells was singlet oxygen ($^1O_2$).[13]

The last two decades have been marked by advancements in better, safer, and more effective photosensitizers (PS). Simultaneously, improved, less expensive, and easier-to-use light sources have transformed the PDT from a curiosity to a highly promising therapeutic strategy with several applications.[10] In this regard, clinical applications of PDT have demonstrated high cure rates for some types of early-stage tumors,[14,15] such as melanoma,[16] oesophageal cancer,[17] and multidrug-resistant breast cancer.[18] PDT has been proven to also possess antibacterial properties[19] and can be widely used in minor skin disease,[20] actinic keratosis, or Condyloma acuminatum.[21] A summary of the clinically approved photosensitizers with their excitation wavelengths and indications is presented in **Table 1**.

PHOTOSENSITIZER	wavelength	INDICATION
Porfimer sodium (Photofrin®)	630 nm	High grade dysplasia in Barret's Esophagus. Obstructive esophageal or lung cancer
5-ALA (Ameluz®/Levulan®)	635 nm	Mild to moderate actinic keratosis
Metvix®/Metvixia®	570-670 nm	Non-hyperkeratocic actinic keratosis and basal cell carcinoma
Temoporfin/mTHPC/Foscan®	652 nm	Advanced head and neck cancer
Talaporfin/NPe6/Laserphyrin®	664 nm	Early centrally located lung cancer
Verteporfin/Visudyne®	690 nm	Age-related macular degeneration
Synthetic hypericin/SGX301	570-650 nm	Cutaneous T-cell lymphoma
Redaporfin®/LUZ11	749 nm	Biliray tract cancer

Table 1 - List of clinically approved photosensitizers with their excitation wavelengths and indications

1.2.1.1. PDT mechanism of action

PDT consists of multiple steps, the first of which is administering the photosensitizer (PS) to the patient. The so-called drug-light interval (DLI), which varies depending on the route of administration and the kind of PS, more especially its pharmacokinetics and biodistribution features, is required for the PS to arrive and preferably accumulate in the target tissue after delivery. The PS is triggered with a proper beam of light after the right concentration of photosensitizer in the target cells is attained, passing into a triplet state of energy, which causes a sequence of photochemical processes that result in the creation of ROS and, as a result, cell death (**Figure 1**).[22]

The electrically excited oxygen molecule is usually in its lower energy singlet state ($^1O_2$) which can cause substantial oxidative damage to biomolecules and cell structures, eventually leading to cell death. The superoxide ion, hydrogen peroxide, and hydroxyl radical are some of the other ROS that can be produced in PDT.[7,23,24] PS can decay back to the ground state with fluorescence emission or pass through intersystem intersection to a more stable excited state after it absorbs light and enters an electronically excited state (a triplet state). Because the triplet state has a longer lifetime (tens of microseconds versus nanoseconds or fewer), it has enough time to interact with molecular oxygen via two separate mechanisms, both resulting in ROS generation:

i) A type I reaction in which electrons are transferred to O_2 and superoxide anions are formed, called photooxidation; or photoreduction, in which electrons or protons are transferred from an organic substrate and a radical cation is formed.

ii) A type II reaction in which energy is transferred directly from the ground state O_2 (a triplet state) to produce singlet oxygen. This approach is only permitted when the triplet energy PS exceeds the excitation energy of 94.5 kJ/mol.

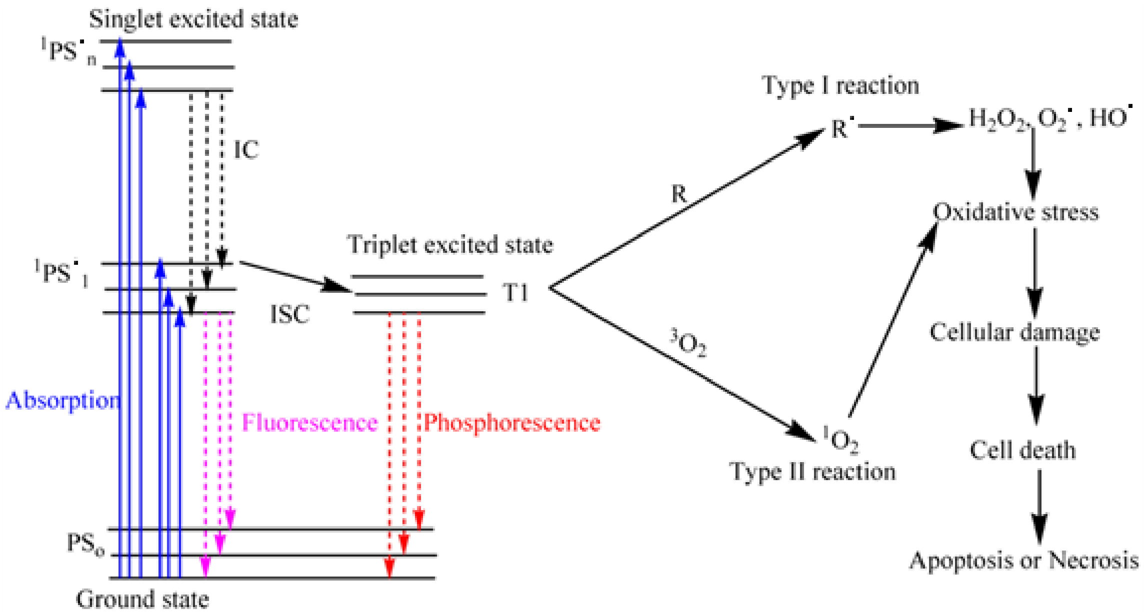

Figure 1 - Modified Jablonski diagram depicting the process of photodynamic therapy. When PSs in cells are exposed to specific wavelengths of light, they are activated, passing from a singlet ground state (S0) to an excited singlet state (S1–Sn), which is followed by intersystem crossing to an excited triplet state (T1). Abbreviations: IC: internal conversion; ISC: intersystem crossing; PS: photosensitizer; $^1PS^{\cdot}$: Singlet excited photosensitizer; T1: Triplet excited state; R: biological substrate; $R^{\cdot}$: oxidized biological substrate; $^1O_2$: Singlet oxygen; H_2O_2: hydrogen peroxide; $O_2^{\cdot}$: superoxide; $HO^{\cdot}$: hydroxyl radical.

Because type II reaction has a simpler mechanism and is generally more thermodynamically favourable than the red absorbing PS, it is more likely to occur. This helps to explain why $^1O_2$ is thought to be the primary cause of PDT phototoxicity.[7,24–26]

When both processes are active at the same time, as is the case with some photosensitizers, the PDT response is magnified. The relative extent of type I and type II mechanisms is determined by ’he PS's properties, the PDT methodology, and potentially the local oxygen content. For example, the tumour’s microenvironment is frequently described as hypoxic, particularly in the centre, due to limited blood flow; this, together with PDT's oxygen consumption, can substantially lower local oxygen concentrations, favouring the occurrence of type I reaction.[10] While less aggressive PDT protocols appear to favour apoptotic cell death, some findings imply that more aggressive PDT protocols (high doses of PS and light and short DLI) have a tendency to cause significant necrosis-induced cell death. Because oxygen concentration is not constant across tumor tissues and light distribution is not homogeneous due to strong attenuation of light by tissues, heterogeneous intra-tumor ROS production will result, with different areas of the tumor undergoing different levels of oxidative damage. This will almost probably have a negative influence on the overall outcome and treatment efficacy.[13,27,28]

1.2.1.2. Active components on PDT

The perfect conjugation of the three PDT components (light, oxygen, and photosensitizer) is critical for PDT's efficacy in selectively destroying target tissue. This poses a significant challenge in clinical practice when it comes to optimizing therapeutic protocols because a large number of factors must be taken into account, including the type of PS and dose administered, intracellular location, DLI, total light dose applied, wavelength and fluence rate, tumor characteristics, and local toxicity. Because it is the combination of these seemingly harmless substances that causes the generation of ROS, which is responsible for the inactivation and killing of tumor cells, it is critical to thoroughly comprehend which role each of them plays in PDT efficacy for drug and protocol development.

i) Oxygen

PDT relies heavily on oxygen, and its intracellular concentration has an evident impact on the treatment's success. It is perhaps the component whose value is most neglected, especially when we consider that O_2 concentration might change between tumors and even between different tumor sections, depending on the density of the vasculature, especially in deeper solid tumors with a hypoxic microenvironment. Surprisingly, photodynamic treatment can cause acute tumor hypoxia, which is caused by the high oxygen consumption during the photochemical reaction, which stops the generation of ROS and reduces the therapeutic efficacy. Furthermore, PDT can induce additional hypoxia by destroying the vascular system and occluding the peritumoral vasculature, resulting in a decrease in blood flow to the tumor tissue and inhibiting the oxygen supply.[29]

Porphyrins and phthalocyanines, which are the subject of this dissertation, are type II photosensitizers that cause cytotoxicity by producing singlet oxygen. This brings up another point to consider: despite its great reactivity, singlet oxygen has a very limited lifetime,[24,27] and because the oxidative response occurs largely in the area of the photosensitizer, pinpointing its specific position is critical for assessing the cytotoxic effect.[12,30,31]

ii) Light

Over time, light sources with clinical applications have evolved rapidly, and the most often utilized light sources today are lasers (e.g., argon, diode) and LEDs, which create a very homogeneous monochromatic light. The combination of various light sources with optical fibre technology transformed the PDT idea and broadened its application to previously inaccessible areas.[7,11,12,32,33] Furthermore, light penetration into human tissue is important because its intensity determines not only whether the PS inside a tumor is photoactivated efficiently or not, but also the type of antitumor response. As a result, it is critical to understand how reflection, absorption, and dispersion processes alter the mode of light propagation in tissues, to the point where the occurrence of these processes is dependent on the wavelength employed.

The wavelength determines the depth of light penetration into the tissue, together with tissue characteristics and heterogeneities (e.g., macromolecules, organelles). On the one hand, the efficient optical window is limited, ranging from 600 to 1200 nm, to protect endogenous chromophores such as haemoglobin (Hb), myoglobin, melanin, and cytochromes.[13,28,34]Longer wavelengths beyond 850 nm, on the other hand, do not have enough energy to produce singlet oxygen, limiting the "phototherapeutic window" to 600-850 nm. As a result, having an intense absorption band within this wavelength range, the red and near-infrared (NIR) spectral area, is a crucial property for a chemical to be regarded as potent PS.[35] As a result, the best wavelength for PDT should be a compromise between PS activation and deep penetration with the least amount of dispersion. The choice should be based on the photosensitizer's absorption spectrum as well as the qualities of the affected tissue (location, lesion size, and accessibility).

iii) Photosensitizers

Finally, the photosensitizer, which is responsible for the absorption of energy of a given wavelength and converting it into useable energy, is undoubtedly the most significant component of PDT. The chemical structure of the photosensitizer, which is commonly based on a tetrapyrrole structure, similar to that of protoporphyrin found in haemoglobin, is thought to play a substantial impact in the therapeutic outcome.

According to the literature, the photosensitizers of the tetracyclic macrocycles can be classified into three generations. In 1995, Photofrin® was the first tetrapyrrole macrocycle to be used in PDT,[33,36,37] and together with HpD (hematoporphyrin derivatives) are known as first generation photosensitizers mainly because they exist as complex mixtures of monomeric, dimeric, and oligomeric structures. Despite its success, photofrin has a number of flaws, including a low intensity of light absorption at the maximum wavelength of photofrin, which means it absorbs light weakly at 630 nm; a low molar extinction coefficient, which necessitates the administration of large amounts of compound to achieve an effective phototherapeutic response; and a slow rate of elimination.[24,27,31,37]

The need to overcome these limitations led to the development of second-generation photosensitizers, which include numerous derivatives of porphyrins, phthalocyanines, naphthalocyanines, chlorins, and bacteriochlorins.[38] Chlorins, in particular, have a large absorption band in the 650 nm range, making these tetracyclic macrocycles attractive candidates for second-generation photosensitizers for PDT since they absorb in a region where light penetration is deep and tissue damage low.[39] As a result, the chlorin family's temoporfin (Foscan®) was licensed in Europe in 2001, with the benefit of being able to reduce skin post-treatment photosensitivity to roughly 2 to 4 weeks, a significant improvement over the 4 to 12 weeks with Photofrin®. Furthermore, compared to porphyrins, it requires ten times lower light doses due to its higher light absorption at a longer wavelength (652 nm) to be effective. Despite being a significant improvement over Photofrin® in terms of pharmacokinetic profiles and higher phototherapeutic indices, which can be defined as the relationship between phototoxicity and toxicity in the dark, there was still a lot of work to be done in terms of pharmacokinetic profiles and higher phototherapeutic indices. In addition, there were certain limits in terms of lipophilicity for these molecules.

As a result, a third generation of photosensitizers with amphiphilic characteristics for diffusion through the lipid barrier and endocellular localisation has been developed. They must also be triggered by long wavelength light, show more selectivity for tumor tissue, and limit or eliminate the occurrence of skin photosensitivity reactions. With their generally high selectivity for neoplastic tissue, absorption radiation in the 650-750 nm region, suitable solubility in physiological media, and no toxicity in the absence of light, second- and third-generation photosensitizers have come to shine a light on the negative aspects of first-generation photosensitizers and bring back hope to the field.

In addition to the presence of a π electron system which ensures a strong absorptive potential, making them appealing for medical applications, these structures have an inherent tendency to accumulate selectively in tumors, as shown in multiple investigations.[27] The mechanisms underlying this selectivity are yet unknown, however various authors have proposed several theories, such as their predilection to bind to low-density lipoprotein (LDL) receptors, which are frequently overexpressed in tumor cells.[40] Another possibility is that tumors have surrounding vessels with morphological changes, which are typical of the neovascularization process that occurs during tumor angiogenesis, making them leaky and convoluted“ The "enhanced permeability and retention (EPR) effect" (**Figure 2**) refers to this occurrence, as well as the absence of lymphatic outflow in tumors.[40]

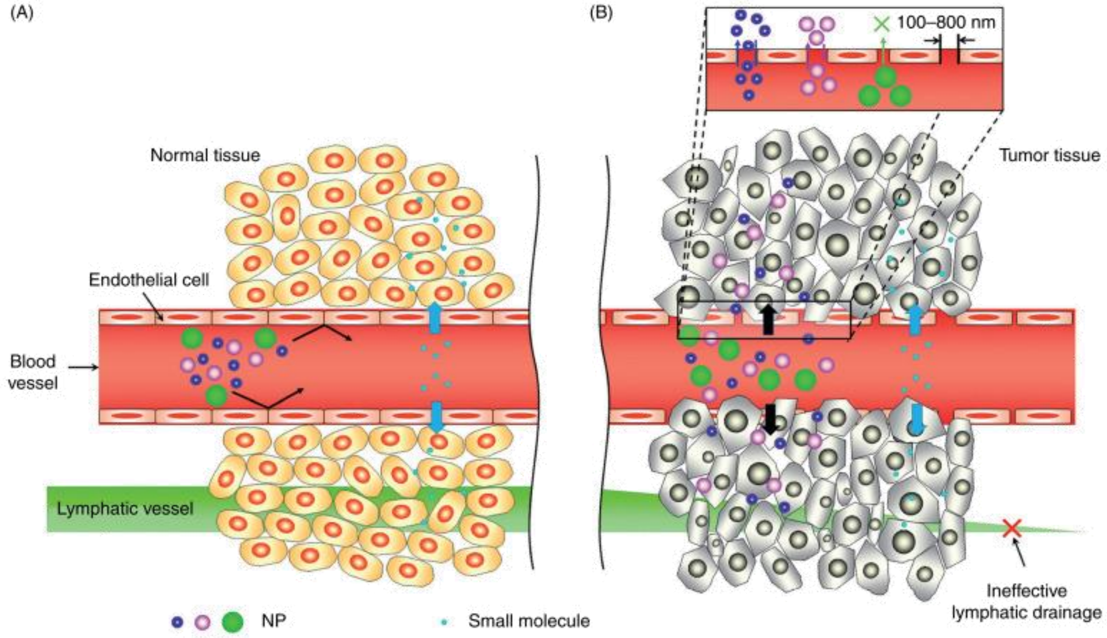

Figure 2 – Illustration showing the differential uptake of NPs and small molecules based on their size across (A) normal and (B) cancerous tissues.[40]

First investigated in 1995 by Jain *et al.*, the molecular weight dependency of compounds in a mouse transplanted human colon adenocarcinoma was confirmed[41] as well as the fact that tumor vessels are less permselective than healthy vessels, largely due to pores in the vessel wall caused by large gaps between single endothelial cells. It was discovered that the concentration of such high-molecular-weight compounds in tumors is 10 to 200 times higher than in normal tissues after administration.[42] The cut-off size of the pores, according to the same group's experiments on tumors with liposomes, is between 400 and 600 nm in diameter.[41] However, tumor microvascular permeability varies depending on tumor size and rate of development, but it is often greater than in normal tissues. It could, therefore, be concluded that systematic clearance decreases as molecular size increases.

1.2.2. Ruthenium metalla-assemblies as promising PDT agents

The aim of this project is to investigate the use of large ruthenium-containing organometallic assemblies as PDT agents. While platinum organometallic assemblies have already been proven to have anti-cancer activity ,[43,44] anti-cancer treatments based on ruthenium have over the last years been shown to have less side effects than those based on platinum,[45] and have over the years shown their importance in different fields, including PDT. Therefore, this route seems to be more conscious and appealing. However, in order to first understand the role of ruthenium metalla-assemblies as promising PDT agents, we first need to start by understanding the role that ruthenium complexes have had over the years, especially in the case of their use as anticancer agents.

Platinum resistance in the clinic, both intrinsic and acquired,[46–48] is becoming a growing clinical problem, especially as platinum medications are now utilized in more than half of all chemotherapy regimens.[46] This has prompted the development of a new class of medications based on various metals and their coordination complexes, which excel in cellular selectivity and can be used to treat a wide spectrum of cancers while demonstrating distinct mechanisms of action. Because of the chemical similarities of the platinum group of metals (Pt, Pd, Rh, Ir, Ru, and Os) and the effectiveness of platinum therapies, interest in ruthenium(II/III) complexes has grown significantly.

Ruthenium compounds have been shown to be a good place to start looking for alternatives to platinum medications in the clinic, as they have similar ligand exchange kinetics and a larger variety of available coordination geometries. Ruthenium anticancer compounds have a wider spectrum of intracellular targets, and several instances have showed promise in chemical systems, [49] *in vitro*, and *in vivo*.[50–52]

RM175 and RAPTA-C

By using different ligands or functionalizing the building blocks, the assembly's properties can be tuned according to the desired effect. The ruthenium(II) complex RM175 (**Figure 3**) was one of the first to be investigated for anticancer action. Developed by the Sadler group in 2001, this pseudo-octahedral organometallic compound is made up of monodentate (chloride), bidentate (diamine), and arene (biphenyl) ligands, and has a 3-legged "piano-stool" shape. Originally designed to target DNA, it is designed to take advantage of the lower +2 oxidation state, which does not require cellular reduction for activation.[53] The halogen atom was designed to behave as a leaving group, similar to how cisplatin is activated, allowing for covalent attachment to the N7 of guanine in the DNA double helix.[53] Although Ru(II) complexes have been shown to bind to guanine residues in DNA,[54] the extended arene in this complex is anticipated to allow hydrophobic interactions between RM175 and DNA via arene-intercalation between base pairs.[55] The structure is relatively flexible as a result of biphenyl's free rotation around the Ru(II) centre, which is expected to reduce steric hindrance and boost the complex's DNA-binding affinity.[56] The complex's conformational flexibility may allow it to intercalate into base pairs while also binding to guanine, as has been seen with previous ruthenium complexes.[56] This could explain why the RM175-DNA adduct is more resistant to DNA repair than platinated DNA; as a result, the lack of cross-resistance with platinum could be explained.[57] RM175 inhibits cancer growth via delaying cell cycle progression that leads to death, as well as the "traditional" disruption of DNA replication caused by strand intercalation and nucleobase binding.

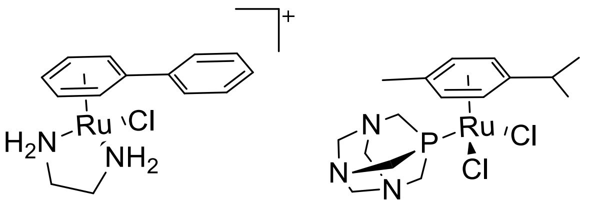

RM175 **RAPTA-C**

Figure 3 - RM175 (left) and RAPTA-C (right) are typical examples of 18-electron ruthenium arene "piano-stool" complexes, in which an η6-arene ring stabilises the 2+ oxidation state of the ruthenium metal centre

The most successful Ru-based anticancer drugs in recent decades have been half-sandwich Ru-arene complexes with 1,3,5-triaza-7-phosphaadamantane (PTA) ligands termed RAPTAs.[58] These ligands have demonstrated moderate anti-cancer activity in a variety of cell lines, as well as excellent activity in reducing the number of solid metastases.[59] Since then, the RAPTA family has been the subject of research, and a number of analogues with anticancer activity *in vitro* and *in vivo* have been developed and tested.

RAPTA-C, created by the Dyson group, is a ruthenium(II) arene complex that includes an amphiphilic 1,3,5-triaza-7-phosphaadamantane (PTA) ligand and two labile chloride ligands (**Figure 3**).[59] PTA is thought to contribute to RAPTA-C's higher water solubility when compared to other Ru(II) arene complexes.[60-61] RAPTA-C, like cisplatin, hydrolyses Ru–Cl rapidly at low (intracellular) chloride concentrations, primarily generating the mono-hydrated complex $[\mathrm{Ru}(p\text{-cymene})\mathrm{Cl}(\mathrm{H_2O})(\mathrm{PTA})]^+$. At higher chloride concentrations (in the blood), the Ru–Cl bond stays intact, and RAPTA-C, like cisplatin, can be considered a pro-drug in its di-chloride form.[60] RAPTA-C and RAPTA-B (in which the arene unit has been replaced with a benzene ring) both showed promise in reducing the size of solid lung metastases *in vivo*.[62] Even at the greatest dose supplied to mice, no negative effects were found in the case of RAPTA complexes. Ruthenium was shown to be swiftly eliminated by the kidneys and did not accumulate appreciably in important organs. A comparative study of RAPTA-C and cisplatin metabolism was recently published.[63]

Despite their variations in oxidation state, ligands, charge, and shape, RAPTA complexes showed a similar spectrum of action to NAMI-A.[64] With a "piano stool" geometry", the chelating characteristics of the bidentate ligand appear to be beneficial for anticancer activity. Furthermore, when paired with other carefully chosen ligands, the robust Ru-arene unit can give a wide range of new anticancer drug discovery paths with both hydrophilic and hydrophobic properties.[65]

NAMI-A

First synthesized by the Alessio and Sava groups, NAMI-A is a complex composed of chloride, imidazole, and dimethylsulfoxide (DMSO) in an octahedral arrangement around a Ru(III) centre (**Figure 4**). Because Ruthenium(III) complexes are often less reactive than Ru(II) congeners and require activation by reduction, they are frequently referred to as pro-drugs.[66,67] The hypoxic cellular environment allows for this reduction, resulting in antiproliferative selectivity for malignant cells relative to healthy cells, which improves tumor targeting.[67,68]

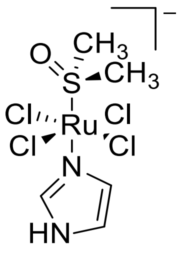

NAMI-A

Figure 4 - NAMI-A is an octahedral Ru(III) pro-drug, which is hypothesized to undergo an “activation by reduction” mechanism inside cells to form more active Ru(II) species.

NAMI-A has a wider range of biological targets than cisplatin, the majority of which are extracellular rather than DNA-based.[66] The most well-known is its synergistic ability to inhibit cell invasion and neo-angiogenesis,[69] making it more effective at preventing metastasis than fully formed tumors.[68] The scavenging of nitric oxide is regarded to be one of the key mechanisms by which NAMI-A exerts its anti-angiogenic actions.[70] The nitric oxide synthase (NOS) pathway promotes angiogenesis and endothelial cell migration by catalysing the production of NO, a signalling molecule involved in these activities. [70,71] Through displacement of the DMSO ligand, the ruthenium core of NAMI-A, as well as its albumin adducts, have been shown to bind strongly to NO.[72] Because NO release is unfavourable even in the presence of glutathione or other reducing agents, this response is assumed to be irreversible *in vivo*. Endothelial cell migration is mediated by nitric oxide, which is a downstream mediator of VEGF.[71] NO scavengers, such as NAMI-A, have been shown to effectively prevent VEGF-mediated endothelial cell activities associated with angiogenesis, such as cell migration.[70] Because malignant growth requires oxygen and nutrients, angiogenesis is critical for tumor proliferation. Angiogenic inhibition is another method for preventing metastatic spread. NAMI-A also inhibits malignant cell migration induced by VEGF.[73] As a result, inhibiting VEGF activity provides a specific method for NAMI-A to limit neo-angiogenesis and metastasis formation.

Metalla-assemblies

These three examples have opened the path for future study on new ruthenium anticancer complexes that push the envelope with a greater variety of coordination spheres and a wider spectrum of ligands.[3] Of all the investigated compounds since, metalla-assemblies have gotten a lot of attention lately.[74] Zelonka and Baird, who researched the behaviour of the benzene ruthenium dichloride dimer in water, discovered the water solubility of arene ruthenium complexes 40 years ago.[75] They noticed the generation of hydrated species in water without the breaking of the arene ruthenium bond. [76] Since then, the chemistry of arene ruthenium complexes in aqueous solution is presently flourishing, thanks to the stability of the arene ruthenium bond in water,[77,78] and several groups have looked at the assembly of transition-metal complexes with polydentate ligands to produce distinct supramolecular structures.

Most importantly, this opened the investigation into metalla-assemblies, in particular metalla-assemblies incorporating porphyrin-based panels, which aim to solve two of the main issues with the use of these photosensitizers in PDT: solubility and aggregation. Solubility is mainly solved by the fact that these metalla-assemblies give positively charged compounds in the form of salts, which consequently increase solubility. In the case of aggregation, the creation of discrete supramolecular coordination complexes, especially three-dimensional (3D) metalla-assemblies, made possible via coordination-driven self-assembly, work by ensuring a rigid structure with exceptional structural stability effectively increasing the distance between two porphyrin units and inhibiting aggregation induced by molecular contact.[79] An example of these kind of structures can be found on **Figure 5**, adapted from Barry *et al.*'s work on the interactions of ruthenium coordination cubes with DNA.

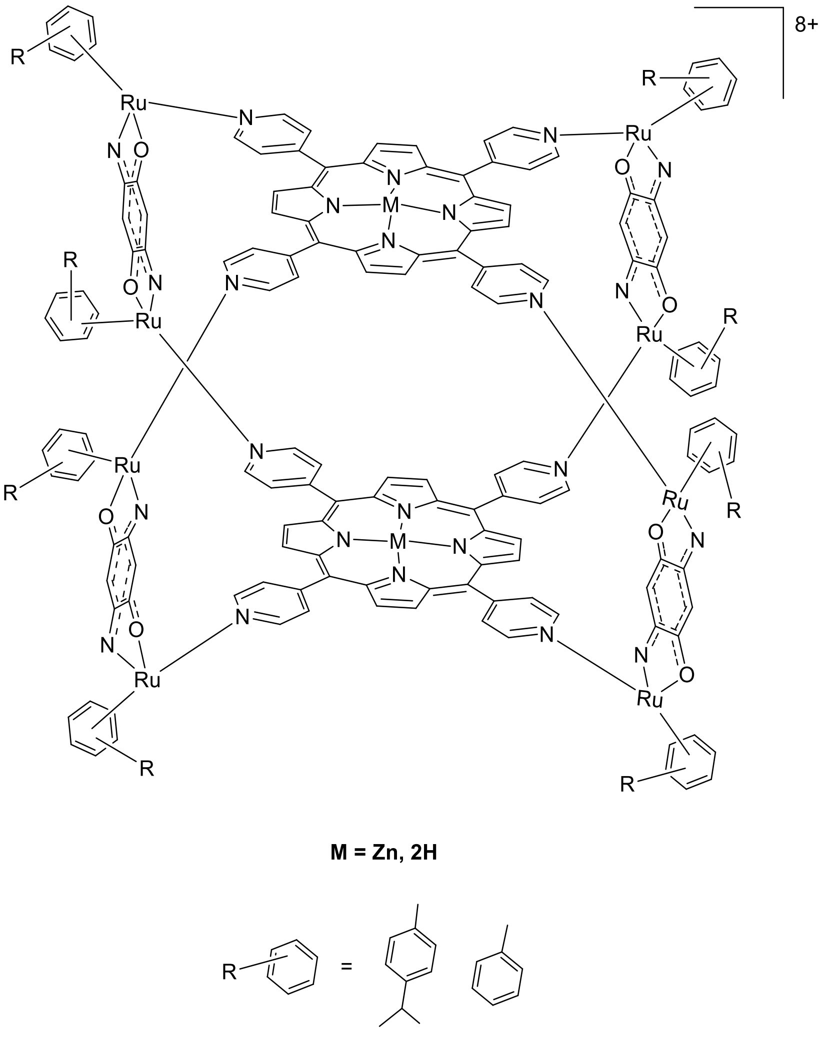

Figure 5 - Arene ruthenium metalla-cubes.

As previously explained, the extended delocalized aromatic π-conjugated system of planar porphyrin always suffers severe π–π stacking that leads to significant quench of the excited state, which favour aggregation and hence impair ROS generating efficiency thus limiting their applications in PDT and raising challenges for the development of suitable pharmaceutical formulations.[80,81] Porphyrin derivatives and many other PSs have been limited in their therapeutic applications because to this property. Despite the fact that many novel carrier systems have been developed to improve the solubility of porphyrin-based PSs, reduce aggregation, and provide efficient direct transport to cancer cells, it remains difficult to achieve molecular level separation of PSs in these systems due to strong molecular interactions.

As shown by nuclear magnetic resonance (NMR) studies and electrospray ionization mass spectrometry (ESI-MS),[82] this coordination-driven self-assembly strategy provides structural simplicity and enhances stability compared to multicomponent systems previously investigated, therefore assisting in the production of more ROS.[79] This PDT efficacy has been investigated both *in vitro* and *in vivo*, and showed significant anticancer action with low doses and little side effects.

In summary, combining the advantages of both ruthenium and *p*-cymene, ruthenium metalla-assemblies present themselves as possible building blocks in the construction of novel PDT agents. Apart from helping with aggregation, the amphiphilic property of the ruthenium unit is one of the key reasons for the blooming design of ruthenium-based anticancer medicines, along with the low general toxicity and hypothetical high selectivity of ruthenium compounds for cancer cells. This is especially significant for porphyrin and phthalocyanine (characterized by their low solubility) based arene ruthenium compounds, which can use the arene ligand to balance hydrophilicity and lipophilicity. Several researchers have coordinated pyridyl-porphyrin with ruthenium moieties in the recent few decades, each with a different type of physiologically relevant activity, including some with good photocytotoxicities toward human cancer cells.[83–88] Furthermore, the arene 'ligand's synthetic variety allows for the coupling of organic segments for targeted chemotherapy.[78] As a result, based on the advantages of the construction of supramolecular structures, this thesis focuses on a promising methodology for effective cancer treatment.

1.3. Cellulose Nanocrystals as Biocompatibility and Targeting units

In general, a promising drug must meet certain criteria: it must be water soluble, long-lasting, biologically stable, biocompatible, inert, and non-toxic, with no associations with blood components or blood vessels. It must also be cytotoxic to specific cells, have no antigenicity, have selective clearance by the reticuloendothelial system, and no cell lysis. It also has to circulate for a long time in the bloodstream.[42,89,90] This is, however, very difficult to achieve with a small molecule, usually being necessary to undergo consecutive modifications that tend to ameliorate one or more of the weaker aspects of the main active reagent. When considering that we are dealing with photosensitizers for PDT in an organometallic structure that helps with solubility and aggregation, according to the list of criteria presented before one of the main issues that needs to be solved in these systems is targeting.

As previously mentioned, the EPR effect is an interesting consequence of the tumor angiogenesis that we can take advantage of.[41,91] Although there is no standard treatment for solid cancers that ensures adequate drug distribution to all tumor regions,[92] the preservation of high-molecular-weight substances in the tumor setting, while low-molecular-weight substances are returned to the blood circulatory system through diffusion,[93] appears to be an excellent way of attributing selectivity to anticancer compounds through passive targeting. Therefore, the ideal drug for exploiting the EPR effect has a specific size that allows it to pass through the membrane and avoid being excreted by the renal clearance threshold. Knowing this, the addition of nanomaterials to these systems presents itself as a viable option to not only aid with this but also with biocompatibility.[94]

Many different types of nanomaterials have been developed and designed as a result of current nanotechnology interest. However, the majority of chemicals used in the synthesis of these nanomaterials are actually obtained from petroleum. Because of ongoing concerns about global warming caused by greenhouse gases released during the processing of such feedstocks, a growing trend has emerged to focus on the creation of polymeric nanostructures derived from renewable resources.[95] Over the last decade, increased research activity on plentiful, natural, biodegradable, and biocompatible polymers has resulted from a desire to design novel products for different applications using renewable resources.

Among all those, cellulose nanocrystals (CNC) have sparked interest in the last decade due to their accessibility, low cost, and high surface area per volume. CNC has several beneficial properties, including non-toxicity, biodegradability, and biocompatibility, making it a good choice for pharmaceutical applications.[96] The surface of CNC can be modified with different functional groups due to the existence of many hydroxyl groups, which extends its applicability in several formulations.[97] Aldehyde, carboxylic acid, and amine functionalities can be formed from the primary hydroxyl groups. Amine functionalization of CNC, for example, can be used to conjugate biomolecules to CNC for biomedical applications. CNC's possible applications in pharmaceuticals have been investigated, and attempts to improve nanocrystal-based drug delivery systems have been made.[96–100] CNC has a range of potential applications in controlled release systems and drug delivery due to its ability to shape stable aqueous suspensions.[101]

It is important to further understand the role of CNC in this project, since it is aimed at using cellulose nanocrystal (CNC) as multi-purpose platform for the construction of porphyrinic ruthenium metalla-assemblies as PDT theranostic agents. Therefore, some essential information needs to be given about this nanomaterial.

1.3.1. Cellulose's Molecular Structure

Cellulose is a linear homopolysaccharide of β(1→4) linked D-glucose units with a high molecular weight. The cellulose polymer has two chemically distinct side chain ends (**Figure 6**):

- A reducing end group comprised of a D-glucopyranose unit with a cyclic hemiacetal as the anomeric carbon atom. A small proportion of this terminal hemiacetal group is an aldehyde acting as a reducing group, which is in equilibrium.

- A non-reducing end group comprised of a D-glucopyranose unit with a closed ring structure around the anomeric carbon atom.

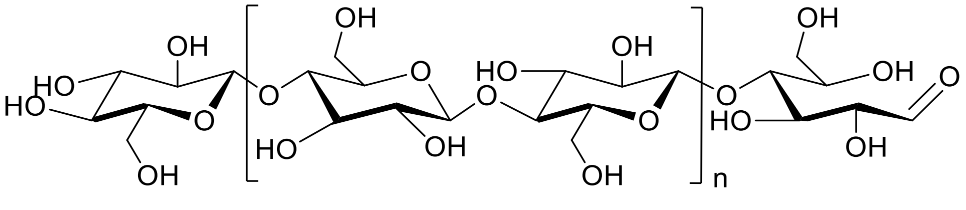

Figure 6 – Molecular structure of cellulose representing the cellobiose unit as a repeating unit showing reducing (right) and non-reducing (left) end-groups.

The chemical and physical properties of cellulose and the effects of different substituents on these can only be properly understood by acquiring knowledge of the chemical nature of the cellulose molecule in addition to its structure and morphology in the solid state.[102] On the molecular level, cellulose is treated as a single macromolecule. In the late 1920s, Haworth suggested a chain-like macromolecular structure, while Staudinger provided conclusive evidence of the cellulose molecule’s highly polymer existence.[103] At this level, the following concepts are also considered: chemical constitution, molecular mass, molecular mass distribution, the presence of reactive sites and potential intramolecular interactions.

The chemical character and reactivity of cellulose are determined by the presence of three equatorially positioned OH groups in the AGU, one primary and two secondary groups.[104] Furthermore, the glycosidic connections in cellulose are sensitive to hydrolysis.[104] The 14 hydroxyl groups play an important role in cellulose solubility as well as in the typical interactions of primary and secondary alcohols.[104] Cellulose is insoluble in water and most organic solvents.[104] This is due to the vast hydrogen bonding network formed by the hydroxyl groups, which produces both intramolecular and intermolecular hydrogen bonds, as illustrated in **Figure 7**.[102] To disintegrate cellulose, the hydrogen bonding network must be disturbed. Two mechanisms exist for the OH groups in the cellulose molecule to generate hydrogen bonds. One mechanism is by interactions between the OH groups rightly placed in the same molecule (intramolecular). These occur between the C2-OH and C6-OH groups, as well as between the C3-OH and endocyclic oxygen. The other process happens when adjacent cellulose ’hains' C3-OH and C6-OH groups interact (intermolecular).

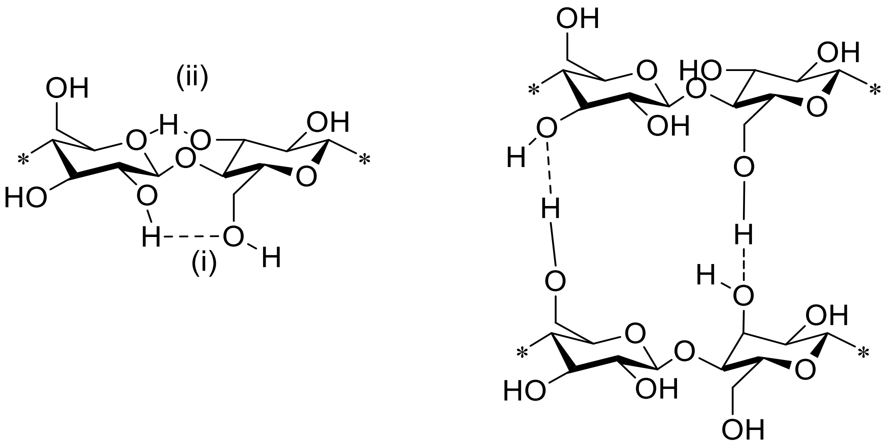

Figure 7 – Cellulose structures showing the intramolecular hydrogen bonding (left) between C2-OH and C6-OH (i), and C3-OH with endocyclic oxygen (ii); and the intermolecular hydrogen bonding (right) between C3-OH and C6-OH (supramolecular structure)

1.3.2. Production of CNCs

Because cellulose is mostly found in plants, it opens up a lot of possibilities for source materials. Wood is a common industrial material, and waste materials such as saw dust and wood pulp are abundant during the processing of wood. CNC is generally made from wood pulp, which has already been partially processed to remove non-cellulose material.[105] Due to the constraints of recycling paper materials back into paper, previous study has also looked at the use of wastepaper for the manufacturing of CNC, resulting in a considerable volume of waste paper materials that can be exploited for the production of CNC.[106,107] Another example of repurposed waste materials for CNC manufacturing is waste cotton cloth. Wang et al.[108] recently investigated the usage of bed sheets to manufacture CNC. The sheets were effectively refined into cellulose-based nanomaterials, with the CNC generated ranging in length from 28 to 470 nm.

Several methods for extracting CNC from cellulose have been devised. The most common way is to break down amorphous areas of cellulose fibres using a hydrolysis process. There are a variety of hydrolysis procedures available, with acid hydrolysis being the most popular due to its quick reaction time. Enzymatic hydrolysis is advantageous since it does not necessitate harsh conditions such as extremely concentrated acids. On the other hand, it is frequently undesirable due to the lengthy time necessary for the process to complete effectively. Furthermore, mechanical energy (such as pressurized homogenisation) is frequently used during or after the hydrolysis to aid in the further breakdown of the extracted crystalline areas into individual whiskers.[109]

1.3.2.1. Acid hydrolysis

A more in depth look into acid hydrolysis might be necessary, since it was the method used in this work. The size and aspect ratio of the CNC varies based on the source material and the manufacturing method. The size of the nanocrystals is proportional to the size of the crystalline sections of the cellulose fibres; however the size of the nanocrystals can be reduced due to deterioration during the hydrolysis process.[105]

In comparison to other acids, sulphuric acid is the ideal acid for the acid hydrolysis process since it requires comparatively mild conditions, with the key parameter for the hydrolysis process being the concentration of the acid. However, it is not the only acid that has been employed; formic acid and hydrochloric acid have also been used to successfully break down cellulose into nanocrystals.[110] The hydrolysis method is generally agreed to use a reasonably high acid concentration (between 50 and 70 wt%), a temperature of roughly 40-50 °C, and a hydrolysis time of between 30 and 90 minutes.[111] The length of the crystals and the efficiency of eliminating the amorphous portions of the base cellulose have been proven to be affected by changing these parameters, which has an impact on the quality of the CNC produced. While hydrolysis process conditions such as acid concentration, temperature, and time can affect the properties of the produced crystalline regions, the type of acid used can also affect the properties of the CNC because the acid residue adsorbs on the nanocrystals' surface.[105] Mechanical processing is used to break down microcrystalline into nanocrystalline. This technique is performed several times to separate the fibres and lower their overall size. Typically, pressure homogenization or ultrasonication are used as part of the process.[112] The use of sonication after hydrolysis was investigated and shown to be beneficial in further refining the CNC by breaking down large crystalline areas into individual nanowhiskers and resulting in smaller crystals with better aspect ratios.[113]

1.3.3. Properties of CNC

The chain length or degree of polymerization of cellulose affects several of its features. Another key aspect that impacts the characteristics of cellulose is the strong hydrogen bond network within the cellulose chains.[114] The average amount of glucose residues per cellulose molecule is referred to as the degree of polymerization (DP), and it determines a range of cellulose properties. DPs in cellulose vary depending on the source, because obtaining pure cellulose involves multiple stages, including pulping, partial hydrolysis, dissolution, re-precipitation, and organic solvent extraction. These techniques generally split cellulose chains, resulting in underestimated DP values, depending on the process used.[115]

The free hydroxyl groups at the equatorial regions of cellulose can form hydrogen bonds, resulting in a variety of crystalline structures. These hydrogen bonds hold the chains together in highly organized crystalline formations. As a result, preventing the pyranose rings from rotating freely boosts the polymer's strength while decreasing its flexibility. Hydrogen bonding is responsible for features including swelling, absorption, and optical activity in cellulose chains. The hydrogen bond network also improves the thermal stability of cellulose. As previously stated, hydrogen bonding can occur both intramolecularly and intermolecularly.[116]

Despite the fact that CNC is generated from cellulose, a widely ingested material, it is a nanomaterial that poses new health risks. CNC has been tested for cytotoxicity to confirm that it is safe to ingest. According to the findings, there are no substantial health hazards associated with the eating, inhalation, or general handling of the product.[117] While there have been no reported health risks associated with CNC materials, the toxicity of nanocellulose materials may be influenced by the manufacturing process and how the surface is treated (such as the presence of sulphate groups or modifying agents on the surface). CNC has been investigated for usage in biomedical applications due of its biocompatibility. The use of fluorescent CNC in bioimaging and medication delivery systems has shown to be promising.[118]. The cellular intake was found to be dependent on the surface charge used, with the positively charged sample causing cells to rupture while the negatively charged sample caused no damage to the cell membrane or cytotoxicity.

1.3.3.1. Reactivity

The cellulose structure has several hydroxyl groups principally responsible for its reactivity. The chemistry of cellulose as a carbohydrate is mostly that of alcohols, and it generates many of the common alcohol derivatives, such as esters and ethers. Despite its molecular similarity to sugars with three hydroxyl groups, cellulose's reactivity should not be confused with that of a trihydric alcohol.

According to the numbering scheme presented in **Figure 8** for carbon atoms in anhydroglucose units of cellulose, the hydroxyl group at position 6 functions as a primary alcohol, while the hydroxyl groups at positions 2 and 3 operate as secondary alcohols, since the carbon atom with the hydroxyl group in position 6 is only linked to one alkyl group, whereas the carbons with the hydroxyl groups in positions 2 and 3 are linked to two alkyl groups directly. The inherent chemical reactivity of these three hydroxyl groups, as well as steric effects generated by the reacting agent and steric effects resulting from cellulose's supramolecular structure, can all impact their reactivity under heterogeneous conditions.[119] The relative reactivity was evaluated by esterification assays, and it was concluded that the hydroxyl group at position 6 reacts ten times faster than the other OH groups.[120] Its strong reactivity is generally attributed to its isomerization. Meanwhile, it has been discovered the hydroxyl groups in the 2 position has twice the reactivity of one of the hydroxyl groups in the 3 position. To make useful derivatives, the hydroxyl groups of cellulose can be partially or completely reacted with a variety of chemicals. Most of today's cellulose industrial technology is built on these derivatives. The degree of substitution is a critical criterion for determining the scope and efficiency of the cellulose reaction (DS) and describes the average number of hydroxyl groups substituted in the unit after the reaction, usually ranging from 0 to 3, with 3 suggesting complete substitution of all hydroxyl groups.

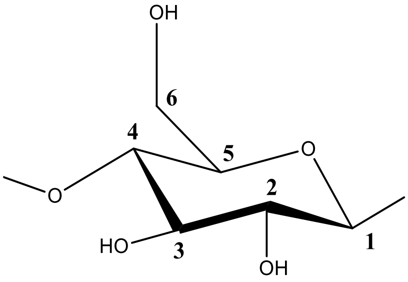

Figure 8 - Numbering system for carbon atoms in anhydroglucose unit of cellulose

1.3.4. Chemical Modification of Nanocellulose

Using zeta potential testing, it was discovered that CNC possesses a negative surface charge. This can be owed to the presence of hydroxyl or sulfonic groups, for example, depending on the hydrolysis method used to obtain the CNCs. Its hydroxyl groups can also explain its hydrophilic qualities and cause hydrogen bonding between individual strands, which might be an issue, because larger agglomerates of CNC can be formed as a result of these hydrogen bonding. Cellulose nanoparticles have a huge surface area because to their nanoscale dimensions, allowing for focused surface modification to accomplish practically any desired surface functionality.[121] The surface chemistry of these nanoparticles is mostly determined by the extraction procedure utilized to prepare cellulose nanoparticles from the natural cellulosic substrate.[122] **Figure 9** depicts the surface chemistries produced by the most common extraction procedures.

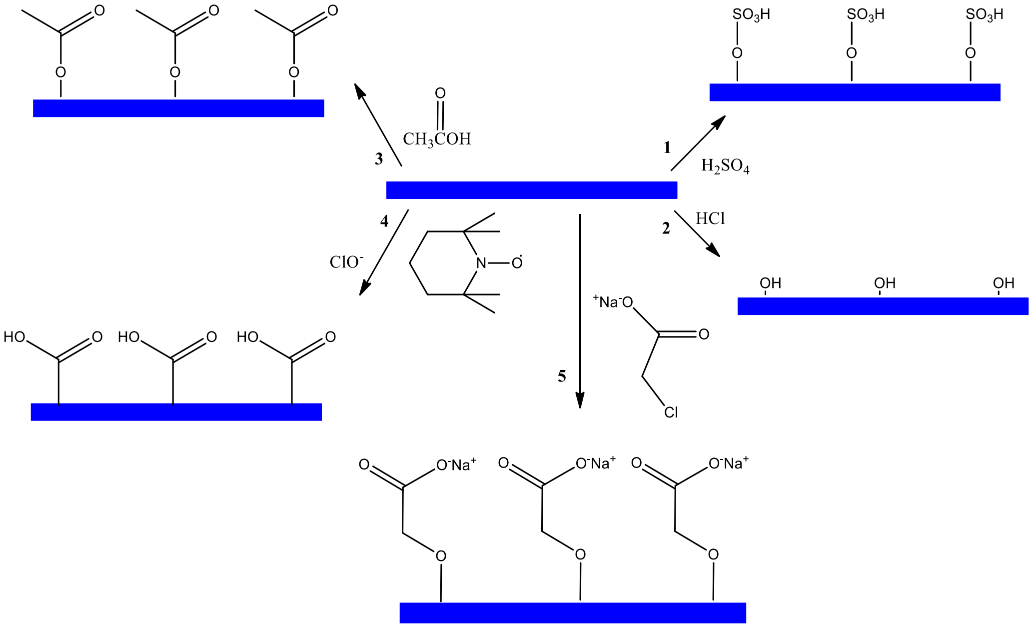

Figure 9 - Distinctive surface chemistries provided by the most common extraction methods of cellulose nanoparticles: sulfuric acid hydrolysis provides sulphate ester groups (route 1), hydrochloric acid hydrolysis provides hydroxyl groups (route 2), acetic acid hydrolysis provides acetyl groups (route 3), TEMPO mediated hypochlorite treatment (route 4) and carboxymethylation (route 5) provide carboxylic acid groups'

CNC's applications are limited due to its hydrophilic properties. To increase compatibility with organic networks, surface modification is required to minimize this. When deciding the material/functional group to modify on the surface of CNC, some thought must be given to the type of material with which CNC will interact. In certain situations, other adjustments may be more effective. Modifying the CNC with an isocyanate, for example, aids dispersion of the CNC inside a polyurethane network.[123] Many of the existing modification strategies, like those for other nanomaterials, take advantage of the hydroxyl groups on the cellulose surface. Despite of what modification is desired, either it being silylation, acetylation, carbamation, cationization, or TEMPO oxidation, most of them usually start with sulfonation.

1.3.4.1. Sulfonation

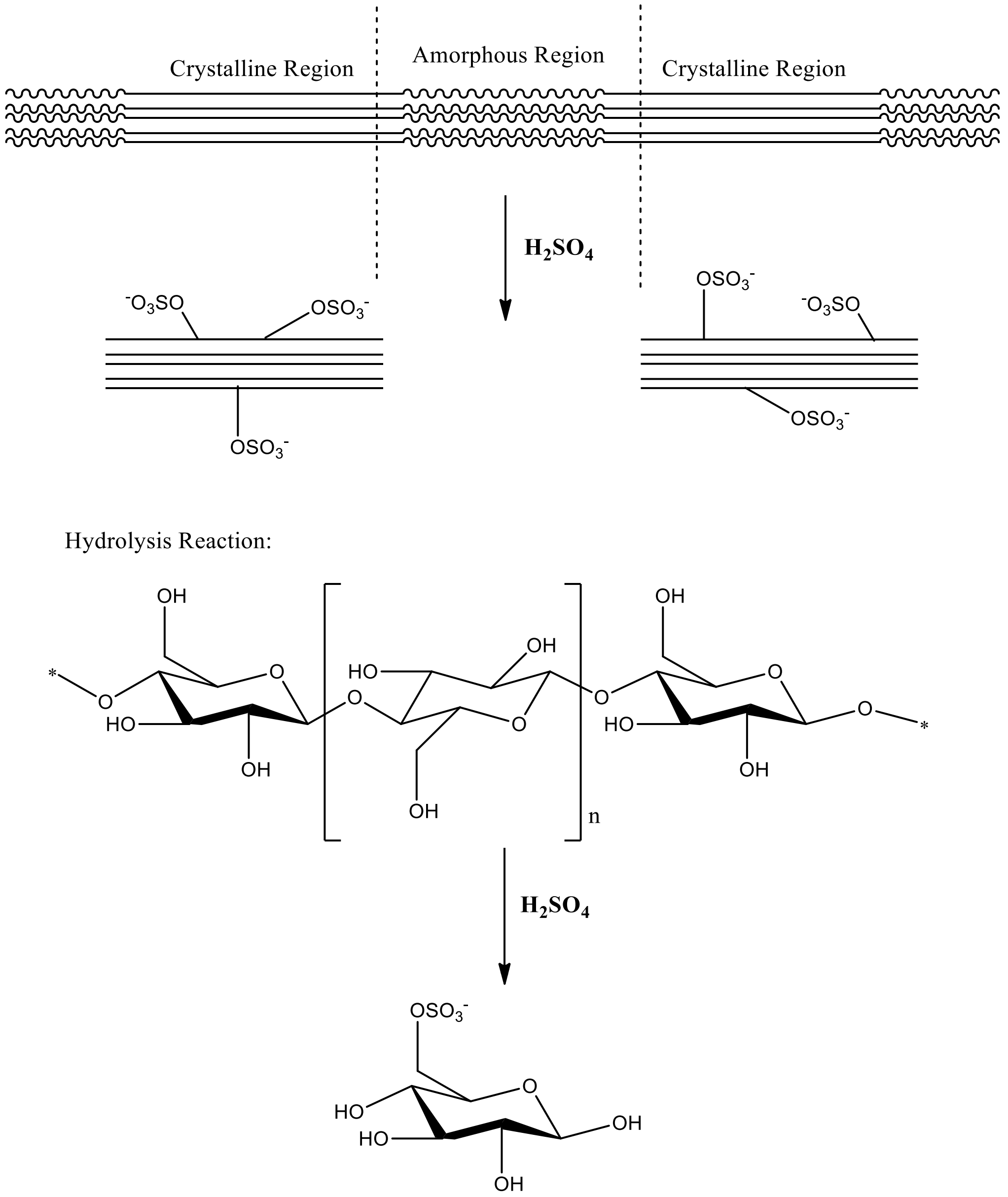

Figure 10 - Schematic representation of the hydrolysis of amorphous and crystalline cellulose with H_2SO_4, and consequent sulfonation.

Although hydrobromic acid and phosphoric acid treatments could also give nanoscaled cellulosic particles,[124,125] sulfuric acid and hydrochloric acid have mainly been used.[126] The most commonly used being sulfuric acid, which renders negatively charged CNC surfaces due to the sulphate incorporation onto nanocrystals (**Figure 10**), electrostatically stabilizing CNCs because of the insertion of negatively charged groups onto CNC surfaces.[127]

The degree of sulfonation is determined by the period of hydrolysis and the concentration of sulfuric acid. Typical reactions are carried out at 45 °C for 30 minutes in 64 percent (w/w) aqueous solutions.[128]
From this several other modifications can be made to the CNC. In the next section, special attention to TEMPO oxidation will be given due to the fact of this was the main modification used in the experimental part of this thesis.

1.3.4.2. TEMPO Oxidation

The great efforts made with TEMPO-mediated oxidation since its inception by De Nooy et *al.*[129] have made this CNC modification one of the most used and studied. TEMPO is a typical oxidation agent for converting alcohols to aldehydes, although it can also create carboxylates and ketones. Under mild aqueous circumstances, this oxidation method selectively alters the surface of cellulosic materials.[130,131] Although the oxidizing reaction can be done under a variety of conditions, the most common method is to use NaBr and NaClO in the presence of the stable nitroxyl radical 2,2,6,6-tetramethyl-1-piperidinyloxy (TEMPO), as illustrated in **Figure 11.**

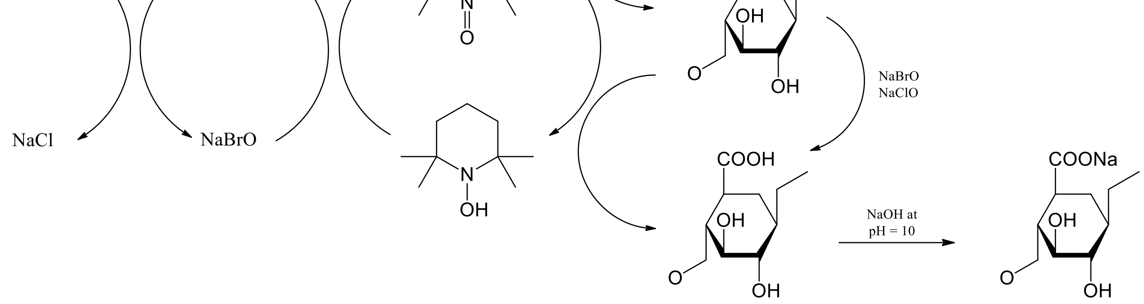

Figure 11 – Scheme of TEMPO-mediated oxidation of cellulose.[131]

This reaction should be carried out at pH values between 9 and 11 in order to achieve higher selectivity towards primary alcohols, as it occurs slowly and without selectivity at pH 8. The CNC surface's' more reactive C6 -OH groups are changed to carboxylate groups via the C6 aldehyde groups when NaClO is used as the oxidant. Only half of the exposed hydroxymethyl groups respond since the other half is hidden within the nanocrystal during this highly discriminative method (secondary hydroxyls remain unaffected).[132] TEMPO oxidation is widely used to selectively activate cellulose nanoparticles by changing the principal hydroxyl groups to carboxylic acids. Although TEMPO-oxidation normally does not damage the structural integrity of CNCs, long reaction periods cause partial delamination of surface chains, which reduces crystal size.[133] Furthermore, Sadeghifar *et al.* discovered that acetamido-TEMPO treatments result in CNCs that are more uniformly oxidized. Finally, it’s worthy to be noted that TEMPO-oxidized CNCs could be further changed in a variety of ways to add new moieties.. [125]

Even though there are several other chemical and surface modifications possible to be done, this thesis will only focus particularly on these, given that these were the ones used in the course of this work. The grafting of porphyrinic ruthenium metalla-assemblies is, indeed, the last step for the construction of the desired therapeutic PDT agents. However, this project intended not only for the construction of therapeutic agents, but also to take advantage of the fact that the porphyrin cores are suitable hosts for metal ions, such as indium-111 and technetium-99m, allowing the implementation of highly effective imaging techniques, like magnetic resonance imaging (MRI) and positron emission tomography (PET) imaging, therefore making them appropriate building blocks for diagnostic agents through imaging.

1.4. Diagnostics - Imaging

Early identification of cancer and a thorough understanding of the disease are critical for effective treatment, therefore diagnostic agents play a crucial part. Imaging is an intriguing tool since it allows not only to perform an initial diagnosis, but also it can be used to follow treatment and follow-up to the patient. A more in-depth report about the construction of photosensitizers for both PDT and imaging that could be used for cancer research can be found in the following review.

Journal of
Medicinal
Chemistry

pubs.acs.org/jmc

Perspective

Conjugated Photosensitizers for Imaging and PDT in Cancer Research

João C. S. Simões, Sophia Sarpaki, Panagiotis Papadimitroulas, Bruno Therrien,* and George Loudos*

Cite This: *J. Med. Chem.* 2020, 63, 14119−14150

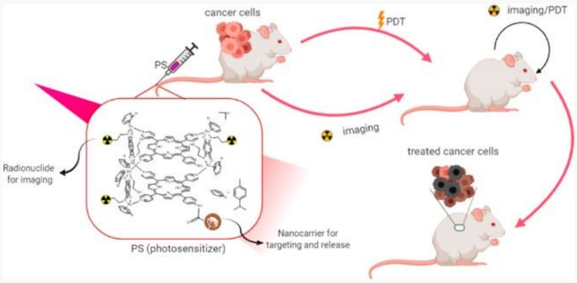

ABSTRACT: Early cancer detection and perfect understanding of the disease are imperative toward efficient treatments. It is straightforward that, for choosing a specific cancer treatment methodology, diagnostic agents undertake a critical role. Imaging is an extremely intriguing tool since it assumes a follow up to treatments to survey the accomplishment of the treatment and to recognize any conceivable repeating injuries. It also permits analysis of the disease, as well as to pursue treatment and monitor the possible changes that happen on the tumor. Likewise, it allows screening the adequacy of treatment and visualizing the state of the tumor. Additionally, when the treatment is finished, observing the patient is imperative to evaluate the treatment methodology and adjust the treatment if necessary. The goal of this review is to present an overview of conjugated photosensitizers for imaging and therapy.

1. INTRODUCTION

Photodynamic therapy (PDT) is an attractive cancer theranostic platform, mainly due to its precise controllability, minimal invasiveness, and high spatiotemporal accuracy.[1] It works by combining photosensitizers (PS) with negligible cytotoxicity and excitation light in compatible doses to produce cytotoxic reactive oxygen species (ROS), which eradicate cancer cells.[2] PDT presents, therefore, several unique and distinct characteristics, which make it a very advantageous therapy not only as a stand-alone treatment but also in combination with other established modalities.

Although conventional imaging remains critical to the management of patients with cancer, molecular imaging can provide additional information. Imaging, in such manner, is an extremely intriguing tool since it is not only assuming an essential role after treatment to access its success and recognize any conceivable repeating injuries, but also because it allows an examination of the disease and to investigate whether the behavior of the tumor has changed. Additionally, when the treatment is finished, observing the patient is vital in order to evaluate the outcome and, if necessary, to revise the protocol.[3] Imaging, in combination with PDT, may therefore be used not only for research but also as a tool for studying basic PDT mechanisms, developing models of diseases, understanding PDT tissue interactions,[4,5] and even as a therapy response.[6] Moreover, it can provide a basis to establish the prospect of success of new therapeutic approaches.[7−11]

PDT imaging can be divided into different modalities: optical, ultrasound, magnetic resonance, and nuclear imaging, according to the mechanism of action.[12] This can either be through radioactive compounds that produce a flag on a screen (PET or SPECT), by utilization of nonradioactive materials that may enhance the contrast of tumors (computer tomography (CT) and magnetic resonance imaging (MRI)) or through acoustic (ultrasound and photoacoustic) and fluorescence signals upon activation (Figure 1).

While both, optical and nonoptical imaging, have been used to monitor PDT, the outcomes are often assessed too late, usually when the disease has progressed more than expected. This creates a new challenge for developing online or early monitoring strategies to envision as soon as possible a new approach to treat a disease.[13] Imaging techniques combined with PDT offer new opportunities for the treatment of different cancers. This concept introduces the so-called theranostic agent, a single compound that inherently possesses both imaging and treatment properties, allowing for the visualization of the problem while being able to treat the condition.[3,14] These modalities have correlative properties that make them appropriate for various kinds of *in vivo* imaging applications. They are overall conceivable to be conjugated

Received: January 10, 2020
Published: September 29, 2020

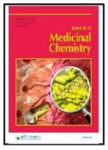

https://dx.doi.org/10.1021/acs.jmedchem.0c00047

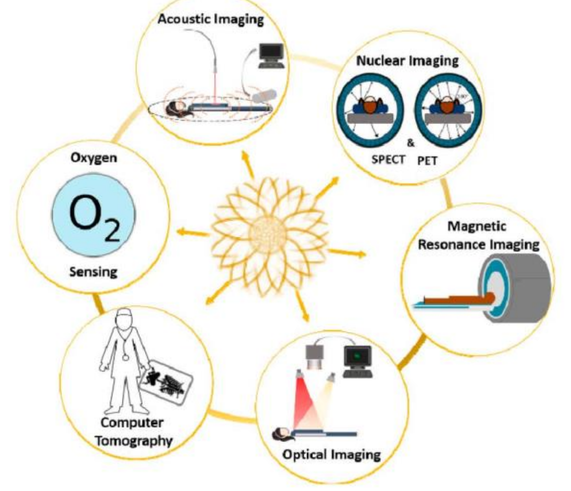

Figure 1. Imaging applications in photodynamic therapy.

with PDT agents so as to accomplish a definitive objective of having a single agent that does "all".[3,15]

Theranostic agents are commonly divided into two groups according to their design: (1) an agent with both properties, imaging and therapeutic, and (2) double-functionalized nanoparticles (theranostic particles) that are modified with an assortment of imaging and therapeutic moieties.[3] Exploiting the same biodistribution such theranostic agents can pave the way to personalized medicine (Figure 2).[16−19] Due to the development of instruments for imaging and PDT treatment, several imaging and therapeutic modalities have been combined, using different assembly strategies, to develop novel theranostic agents.[20]

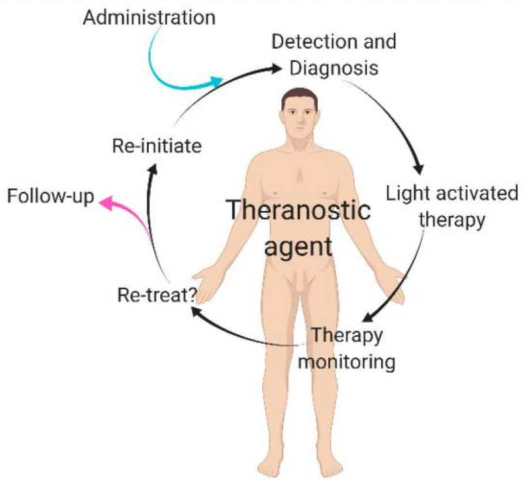

Figure 2. Cartoon depicting personalized medicine with theranostic agents.

2. BASIC PRINCIPLES OF PHOTODYNAMIC THERAPY (PDT) AND PHOTOSENSITIZERS

2.1. Photodynamic Therapy (PDT). The true potential of PDT was only realized after the extensive work of Dougherty and co-workers who, between 1975 and 1980, reported a complete cure of malignant tumors by combining an HpD (hematoporphyrin derivative) and red light.[21] Initially, it was applied in a breast cancer model and later in patients with skin, prostate, breast, or colon tumors. These promising results were later confirmed in clinical trials with improved versions of HpDs in patients with skin or bladder cancer. At the same time, Weishaupt and his colleagues postulated that singlet oxygen ($^1O_2$) generated in PDT was the cytotoxic agent responsible for the destruction of tumor cells.[22,23] Finally, in 1993, a landmark for PDT was achieved with the regulatory approval in Canada of porfimer sodium, a semipurified version of HpD, for the treatment of bladder cancer.

Light, oxygen, and PS precise cooperation are key for the efficacy of PDT to trigger the production of ROS, responsible for the inactivation and destruction of tumor cells. Furthermore, PDT provides spatiotemporal control through the photosensitizer and the light source.[13] The PS can reach the tumor compartment utilizing various targeted methodologies,[24] such as immunoconjugates or nanotechnologies.[25] A localized light activation ensures an optimal treatment, thus sparing surrounding tissues. While a specific location of light illumination provides spatial control, a time delay between PS administration and light irradiation provides a temporal control of the therapy.

Nevertheless, the combination of light, oxygen, and PS represents a great challenge in the optimization of therapeutic protocols. To obtain the desired therapeutic effect, a great number of factors should be considered, namely, the type of PS, the dose administered, the intracellular location, the drug to light interval (DLI), the total light dose applied, its wavelength and fluence rate, tumor characteristics, and local availability of oxygen. Since the PS is only activated in the presence of light, PDT presents several advantages over other conventional cancer treatments such as low systemic toxicity and the capability to destroy tumor cells selectively. Furthermore, it can also be applied in combination with other therapeutic modalities and is often cheaper than other cancer treatments.[26,27] On the other hand, PDT presents some disadvantages including the fact that most of the PS used in PDT are hydrophobic molecules, they show a poor cell specificity, and light penetration through tissues is minimal, thus limiting PDT treatments to superficial tumors such as skin cancer, nasopharyngeal cancer, and oral cancer.[28−32]

2.2. Photosensitizers in PDT. When developing new photosensitizers, there are a series of advantages and limitations that we can find. The limitations include photosensitivity after treatment, the fact that the treatment efficacy depends on optimal light activation to the tumor, and the presence of oxygen remains crucial to PDT. Another big disadvantage is that no current photosensitizer can treat metastatic cancers.[33] The advantages, on the other side, make for a compelling case for the continuation of the development of such compounds. These include fewer adverse effects and little invasiveness, short treatment time and selectivity, and lower costs than other treatments. Other advantages include the following: it can be used in outpatient settings, can be applied multiple times, and leaves little or no scarring after healing.[33]

A PS should, ideally, be a single and pure compound that accumulates preferentially in tumors. At the same time, it should have low toxicity in the dark to minimize phototoxic side effects, and it should be rapidly eliminated from the body.[27,34] To reach target cells, the PS needs a good balance between hydrophilicity and lipophilicity. Indeed, it must possess amphiphilicity. An ideal photosensitizing agent ought to have a high absorption peak between 600 and 800 nm (red to deep-red region). Absorption of photons at higher wavelengths (>800 nm) does not provide enough energy to excite oxygen to its singlet state and accordingly to generate sufficient ROS. These characteristics as well as others are summarized in Figure 3.

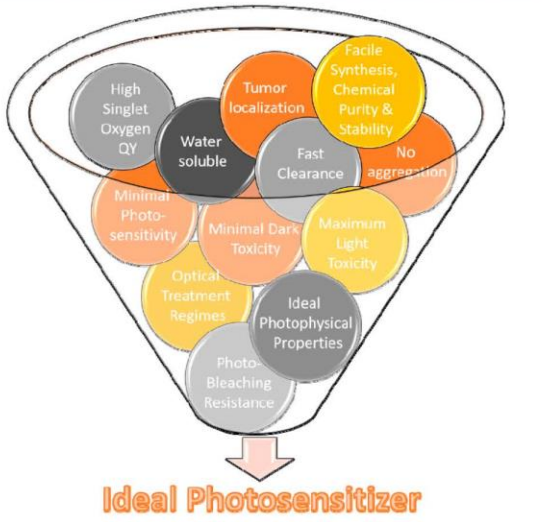

Figure 3. Ideal characteristics of photosensitizers.

In addition, a PS must have good photophysical properties, such as high quantum yields of triplet state formation, high singlet oxygen production, and an appropriate triplet lifetime. The triplet lifetime is crucial to allow the PS to interact with oxygen and other substrates in view to generate ROS.[27,34] Moreover, PSs should have good absorption between 600 and 800 nm to ensure strong light penetration into tissues. Therefore, agents absorbing strongly in the red, such as chlorins, bacteriochlorins, and phthalocyanins, are more suitable for PDT treatments. However, most known PSs do not possess all requirements. In the past few years, efforts have been focused on the development of PSs that can be activated with the light of a longer wavelength, with mild photosensitivity and high tumor specificity. Tetrapyrrole-based structures seem to gather most of these characteristics, making them the best option for PS when compared with other classes of molecules.

Many different molecular structures have been studied for PDT (Figure 4), including some natural products such as hyperacin,[35−37] curcumin,[38−41] hypocrellin[42,43] and riboflavin,[44−47] as well as synthetic dyes. When it comes to synthetic dyes, the most commonly studied are phenothiazinium salts such as Methylene Blue[48] and Toluidine Blue,[49] which have been widely studied both for antimicrobial applications[50] and, less often, anticancer activity.[51] Rose Bengal, which has a long history as a photoactive dye and has been explored for antimicrobial applications,[52] tissue bonding applications,[53] and anticancer applications is another example.[54] Squaraine and BODIPY dyes, with delocalized systems of molecular orbitals, provide good absorption in the visible range.[55]

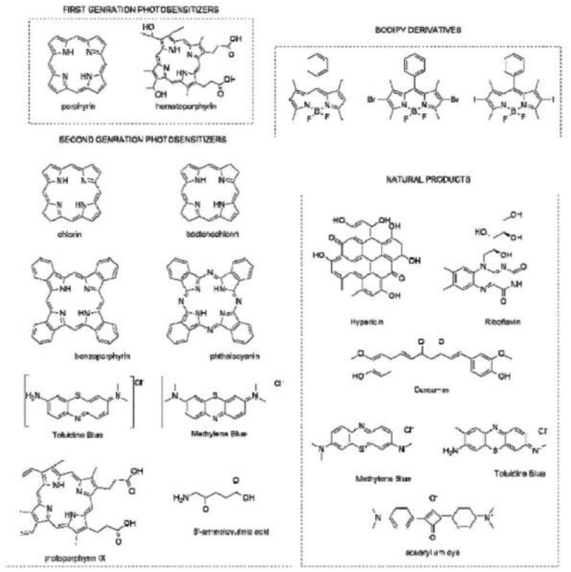

Figure 4. Structures of photosensitizers currently used in PDT.

Most BODIPY dyes have the right characteristics, such as a low dark toxicity, a good cellular uptake, a high extinction coefficient, and a low quantum yield for photobleaching, which make them good PDT agents. However, some modifications can be made to their structure in order to enhance intersystem crossing (ISC) and prevent photodamage in PDT, which is thought to occur predominantly via triplet excited states. Spin-coupling to heavy atoms ("heavy atom effect") is a common modification. Generally, the addition of heavy atoms occurs at positions that will not disrupt the planarity of the dye. An appropriate placing of heavy atoms on a BODIPY core promotes spin−orbit coupling, without any energy loss from excited states.[56] In the case of Rose Bengal, the introduction of halogens into the rings, such as bromine or iodine, seems to increase the triplet yield of the molecule by facilitating intersystem crossing. In a similar manner, the introduction of iodine into the delocalized system of squarines also increases the triplet yield.

Other synthetic dyes include phenalenones,[57] often used as a standard for the generation of $^1O_2$ and recently developed into an antimicrobial PS,[58,59] and coordinated to transition metals. These are a relatively new class of PSs. Ruthenium(II) polypyridyl complexes are perhaps the most studied,[60] although other ruthenium,[61] rhodium,[62] and cyclometalated iridium[63] complexes have also been studied. There is also evidence that luminescent platinum(II) and gold(III) complexes can act as PSs.[64] In addition to these structures, nowadays, most PSs utilized in PDT (Figure 5 and Table 1) show a tetrapyrrole structure.

It is possible to categorize the photosensitizers into three generations, especially with regards to porphyrin-based PSs. Porfimer sodium and the hematoporphyrin derivative (HpD) are known as the first generation of photosensitizers.[22,65] Porfimer sodium shows many drawbacks, such as a poor light absorption at the maximum wavelength (ε_{max} at 630 nm), a low molar extinction coefficient (~3000 M^{-1} cm^{-1}), and a slow clearance, which causes prolonged photosensitivity of the skin after treatment.[65−68]

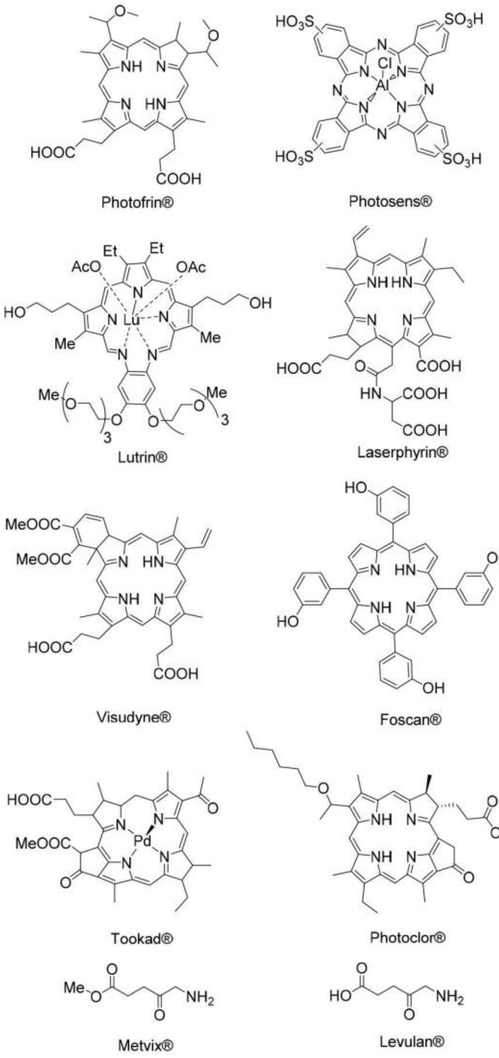

Figure 5. Most commonly used PSs in the clinic.

While a photodynamic impact can be achieved with porfimer sodium, efficiency can be improved by red-shifting the absorbance band and by increasing the absorbance at longer wavelengths. There has been a noteworthy exertion among therapeutic physicists to find second-generation PSs, and numerous compounds have been proposed as potent anticancer agents for PDT.[34] The so-called second generation of photosensitizers, which include various derivatives of porphyrins, phthalocyanines, naphthalocyanines, chlorins, and bacteriochlorins, was created from not only just the need to overcome drawbacks but also to increase the formation of singlet oxygen ($^1O_2$), through a type II process.[69,70]

When the wavelength is higher, the light penetrates through tissues deeper; therefore, PSs with strong absorbance in the deep-red region, such as chlorins, bacteriochlorins, and phthalocyanins, can have a better impact on tumors. Chlorin derivatives show an intense absorption band around 650 nm, which make them good candidates for PDT applications. These PSs with increased light penetration were classified as second-generation photosensitizers.[71]

An early example is temoporfin, which was approved in Europe in 2001. This chlorin derivative reduces the skin post-treatment photosensitivity by at least a factor of two, from 4 to 12 weeks with porfimer sodium to only 2 to 4 weeks. Moreover, because it possesses an increased light absorption at a longer wavelength (652 nm), the light dose required for treatment is reduced by a factor of 10. Although showing significant progress when compared to sodium porfimer, some other aspects needed to improve such as pharmacokinetic profiles and higher phototherapeutic indices, as well as solubility.[72] The side effects of the second generation of PSs caused by nonspecific localization, and the need for better pharmacokinetic profiles gave rise to the development of a third generation of photosensitizers: PSs with amphiphilic properties appropriate for diffusion through the lipid barrier and for endocellular localization.[73]

Therefore, to improve the efficacy of PSs in PDT, the so-called third generation of PSs must show a longer wavelength activation and a better selectivity for tumor tissues. To achieve these goals, conjugation of targeting molecules (such as antibodies) to the PS, encapsulation of a PS into carriers (such as liposomes, micelles, or nanoparticles), or functionalization with prodrugs that get activated only at the tumor site, is among the new strategies employed.[65−68] The main goals being the improvement of specificity and efficacy, reduction of off-target accumulations, and optimization of the pharmacokinetic.

In order to reduce the impact on adjacent tissues, the concept of prodrug has been evaluated. The strategy consists of the administration of a PS in an inactive form, which will become active only after reaching the target. The activation will be triggered by proteases, the pH, or another biological response. A PS producing singlet oxygen in a specific environment, acidic conditions, for example, will have a stronger impact on tumors where the pH is lower.[73] Such activatable photosensitizers combine the concept of local treatment and personalized therapy, the main objective being to display minimal phototoxicity when off-target, and high activity in the targeted tissue to increase PDT selectivity.[74] Although the strategy of activatable agents seems to be of great interest for the future of photodynamic therapy, the main strategy applied nowadays still seems to be the functionalization of these molecules through conjugation with biomolecules and carriers such as porphysomes, quantum dots, nanoparticles, and targeting moieties.

2.3. Functionalization of PSs. Incorporation of hydrophilic groups on the PS, such as HSO_3^-, COO^-, and NR_4^+, increases the water solubility, but the delivery of lipophilic PSs to target cells remains an important PDT goal.[75,76] To achieve that goal, different types of functionalization of PS can be performed, usually through the conjugation with other molecules. The choice of the conjugates is driven by the tumor microenvironment, such as hypoxia,[77] enzymes,[78] leaky vasculature,[79,80] and receptors overexpressed by cancer cells.[81,82]

Lately, certain limitations of potent PSs, such as (i) poor solubility in aqueous media, (ii) high potency for aggregations, and/or (iii) undesired interactions with proteins or biomolecules in aqueous media, in combination to the rapid advances in nanotechnology, led to the development of another round of the third generation of PSs, which are encapsulated to the nanostructure,[83−87] with the most commonly used nanoparticles being listed in Table 2.

Table 1. PSs Currently Used in Clinics or Under Clinical Trials[73]

		generic name	chemical name	excitation wavelength (nm)	application	manufacturer
clinically approved	first generation	photofrin	porfimer sodium	630	esophageal cancer, lung adenocarcinoma, endobronchial cancer	Axcan Pharma, Canada
	second generation	ameluz/ levulan	aminolevulinic acid hydrochloride	635	mild to moderate actinic keratosis	DUSA, USA
		foscan	temoporfin	652	advanced head and neck cancer	Biolitec, Germany
		laserphyrin	aspartyl chlorin	664	Early centrally located lung cancer	Meiji Seika, Japan
		metvix/ metvixia	methyl aminolevulinate	570−670	nonhyperkeratotic actinic keratosis, basal cell carcinoma	Galderma, UK
		redaporphine		749	biliary tract cancer	Luzitin, Portugal
		visudyne	verteporfin	690	age-related macular degeneration	Novartis, Switzerland
under clinical trials		antrin	motexafin lutetium	732	coronary artery disease	Pharmacyclics
		fotolon		665	nasopharyngeal sarcoma	Apocare Pharam, Germany
		photoclor		664	head and neck cancer	Rosewell Park
		photosens	sulfontaed alumunium phthalocyanines	675	age-related macular degeneration	Russia
		photrex		664	age-related macular degeneration	Miravant, USA
		radachlorin		662	skin cancer	Rada-pharma, Russia
		talaporfin	L-aspartyk chlorin e6	664	colorectal neoplasms, liver metastasis	Novartis, Switzerland
		TOOKAD	padeliporfin	762	prostate cancer	Negma-Lerads

Table 2. Clinically Approved Nanoparticles[130]

	type	agent	modality	indication	trade name
clinically approved	sulfur colloid	^{99m}Tc	SPECT	lymphoscintigraphy, bone marrow, gastrointestinal, liver, and spleen	Technecoll (US)
	albumin colloid	^{99m}Tc	SPECT	lymphoscintigraphy, inflammation imaging, melanoma, prostate	Nanocoll (EU)
	SnF_2 colloid	^{99m}Tc	SPECT	lymphoscintigraphy, gastrointestinal, liver, and spleen	Hepatate (France)
	Re_2S_7 colloid	^{99m}Tc	SPECT	lymphoscintigraphy, gastrointestinal, melanoma, prostate	Nanocis (EU)
	albumin colloid	^{99m}Tc	SPECT	lymphoscintigraphy of breast	Senti-Scint
	dextran-coated iron oxide (ferumoxide)	$Fe^{2+}\ Fe^{3+}{}_2O_4$ $(Fe^{3+}\ Fe^{2+}{}_2)O_4$	MRI	mononuclear phagocyte system imaging, cellular labeling	Feridex (US), Endorem (Britain)
	carboxydextran-coated iron oxide (ferucarbotran)	$Fe^{2+}\ Fe^{3+}{}_2O_4$ $(Fe^{3+}\ Fe^{2+}{}_2)O_4$	MRI	lymph node imaging, perfusion imaging	Sinerem (EU), Combidex (US)
	carboxydextran-coated iron oxide (ferucarbotran)	γ-Fe_2O_3	MRI	hepatocellular carcinoma, cell labeling	Resovist (US, EU), Cliavist (France)
	polyglucose sorbitol carboxymethyl ether-coated iron oxide (ferumoxytol)	γ-Fe_2O_3	MRI	iron-deficiency anemia, off-label uses in imaging	Faraheme (US)
under clinical trials	sulfur colloid	^{99m}Tc	SPECT	colon cancer	
	sulfur colloid	^{99m}Tc	SPECT	cancer	
	sulfur colloid	^{99m}Tc	SPECT	head and throat cancer	
	gold	nanoshell	photothermal	head and neck cancer	
	silica	^{124}I and Cy5	PET and optical	melanoma	
	iron oxide	ferumoxytol	MRI	glioma	
	iron oxide	ferumoxytol	MRI	pancreatic cancer	
	iron oxide	ferumoxide	MRI	inflammation	
	iron oxide	ferumoxytol	MRI	myocardial infarction	

Medicinal nanoparticles (NPs) are drug-loaded, and their overall size does not exceed the 100 nm in order to cross effectively physiological barriers *in vivo*.[91,92] Appropriate modification of NPs enables improved solubility, excess in drug loading, and to control drug release and enhancing their imaging modalities.[92−94] These interesting and sometimes unexpected properties of nanoparticles are largely due to their high surface-area-to-volume ratio. Introduction of different functional groups at the surface of NPs provide a variety of chemical properties.[91] In other words, the surface or core of the nanoparticle might be loaded with various agents, allowing the use in multiple applications simultaneously (such as imaging and therapy).[95−97] A common example of indirect PS functionalization is the usage of peptide linkages that can be cut by metalloproteinases (MMP's), which are ordinarily abundant in an assortment of tumors. Nanoparticles can likewise help in the delivery of hard-to-formulate drugs within water-based solutions, by either protective biopolymer coating or encapsulation.[3]

Nanoparticles can also be surface-covered with polymers such as poly(lactic-*co*-glycolic corrosive) (PLGA) or polyethylene glycol (PEG) for increased tumor selectivity.[98] The surface can be decorated with drugs, pro-drugs, contrast agents, or a mixture of different elements.[99] Optimally, the monitoring of treatments (before, during, after) is conducted by the contrast agent. Nanoparticles can also be loaded with drugs or prodrugs (peripherally or internally).[99] Such theranostic nanoparticles can be tweaked to release the drug based on tumor microenvironment conditions.[99−102] Indeed, many tumors possess a poor blood vessel system, of leaky, dilated, and irregular shapes, which allow large molecules to reach the tumor.[103] Then, when inside, the lack of efficient lymphatic drainage traps the NPs in the tumor. These two phenomena are known as the enhanced permeability and retention effect (EPR).[103,104] The surface of the NPs can be functionalized with targeting agents to interact with overexpressed tumor-related receptors.[105] Targeting biomolecules can be combined so that one functional group may allow the nanoparticle internalization by endocytosis, while another functional group targets a specific receptor before drug release.[106]

Recent studies have demonstrated the possibility of using metal-based nanoparticles as photosensitizers, up-conversion tools delivery, and vehicles.[107] Moreover, metal-based NPs show good sizes and shapes to ensure prolonged activity and biodistribution. Studies dealing with nanoparticles based on molybdenum oxide, TiO_2, ZnO, and tungsten oxide as photosensitizers in PDT have been conducted in recent years.[108,109]

The first investigation of nanoscaled metal−organic frameworks (MOF) in PDT was reported by Lu et al. in 2014.[110] Their study suggests that the Hf−porphyrin nanoscale metal−organic framework (DBP−UiO) is an excellent photosensitizer in PDT treatments of resistant head and neck cancers. The DBP−UiO framework shows enhanced *in vitro* and *in vivo* PDT efficacy. Following this initial study, other applications of nanoscaled MOFs in PDT were reported.[111] MOFs have indeed become popular metal-based nanoparticles for PDT applications.

A very common conjugation of photosensitizers is with porphysomes. Porphysomes are derived from porphyrin−lipid bilayers, and they show a high static quenching effect. In addition, they have a structure and a loading capacity similar to those observed for liposomes. Most importantly, they have a high porphyrin payload that is advantageous for PDT treatment, while being biocompatible, nontoxic, and biodegradable.[112]

Jin et al. have constructed folate-porphysomes by incorporating a small percentage of folate conjugate lipids in porphysome formulation. This allowed FR-mediated cell uptake of nanoparticles, which, subsequently, resulted in a rapid disruption in cells upon activation of porphyrin fluorescence and production of ROS. The irradiation of the folate porphysomes increases folate receptor-selectivity and ultimately PDT efficacy. Once systematically administrated to FR-positive tumor-bearing mice, the folate-porphysomes were reducing the tumor size and increasing the survival rate. Furthermore, such targeting-porphysome formulation facilitates the introduction of additional targeting moieties to realize disease-specific and personalized PDT treatments.

Similarly, Lovell et al. developed porphysomes with a higher quenching capacity than the PS alone.[113] Located inside a simple bilayer, the porphyrin−lipid orientation promotes porphyrin interaction and quenching. However, after loading porphyrins into the nanocarrier, the fluorescence response was regained, thus confirming the benefit of these combinations.

Another example of a successful porphysome design was published by Philp et al., in which porphysomes were used to monitor in real time the resection of primary tumors, lymph nodes, and abdominal metastases in rabbits.[114] Another proof of the diagnostic ability of nanoparticles was reported by Ng et al., who employed bacteriopheophorbide as a fluorescent energy acceptor in a self-sensing porphysome (FRETysome).[115] Following subcutaneous injection in mice, the presence of FRETysome has permitted to image the tumor. Moreover, they observed after 24 and 48 h postinjection the persistence of nanovesicles at the tumor site.[116]

Several research groups have recently focused their interest in the functionalization of "quantum dots" QDs with PDT agents. Nanostructured semiconductor materials were first applied in heterogeneous photocatalysis in the 1980s, and their unique properties have raised attention.[88,117−120] Scientists used these nanocrystals as PSs, due to their ability to selectively transfer energy and to produce light over a broad range of wavelengths, which can be optimized to the appropriate wavelength for PS excitation.[121−125] Unlike most organic photosensitizers, QDs do not have metastable excited states, which can promote effective energy transfer, and therefore, distinct processes are expected to occur, thus yielding reactive oxygen species in a different way.[126]

Wang et al. developed a water-soluble and pH/H_2O_2 responsive silicon QDs-based nanocomplex and explored their applications in PDT.[127] Silicon is not only an outstanding semiconductor but also a promising fluorescent probe for targeting and imaging cancer cells. The developed QDs could not only deliver more photosensitizers but also image the tumor by fluorescence. *In vivo* experiments have confirmed that, under light exposure, the growth of tumor was effectively repressed.[127]

When administered individually, both PSs and QDs have advantages and limitations. Some properties such as NIR absorption, broad absorption bands, and photostability are required for PDT. Surprisingly, the actual PSs present disadvantages when compared to the unique optical properties of QDs, such as narrow absorption band, poor photostability, and visible light absorption.[128] QDs' properties such as efficient light outputs and the capacity of tuning their absorption and emission bands gave them an exceptional photoresistance. This allows light excitation for continuous ROS production either via type I or type II processes and accordingly ensures prolonged phototherapies.[129]

Nanotechnology in PDT has created new opportunities and new modalities in the field by providing efficient nanoscale PSs delivery systems. While allowing a controlled release of drug and efficient uptake by cells, their surface area can be modified with functional groups for additional chemical/biochemical properties, which together improve the treatment efficacy and minimize side effects associated with classic PDT. Moreover, it has been demonstrated that it is conceivable to have a single nanoparticle formulation conveying a lower dose of the imaging probe and a high payload of the therapeutic drug, meaning that nanocarriers can positively modulate biodistribution and pharmacokinetic profiles of the drug formulations overcoming the current drawback of most molecular theranostic agents.[130−132] To date, there has been a high number of different synthetic strategies,[133] which only consolidates the potential interest in NPs, both as drug carriers and as imaging agents. Hence, many tactics have been used to incorporate PSs into polymers, gold nanoparticles, magnetic and silica nanoparticles, as well as other various delivery carriers such as liposomes, quantum dots, and so on.[134−137] These NPs show high selectivity, high efficacy, and limited side effects.[138] Currently, there are only a few nanoparticle-based theranostic platforms tested in clinical trials, but this might change in the near future.[139,140]

2.4. Active and Passive Targeting of PSs. One of the main challenges in PDT is linked to drug delivery and targeting.[84,85] An ideal PS is delivered in therapeutic concentrations to only the target cells, while healthy cells remain untouched. This basic concept ensures minimal side effects, when keeping and efficient PDT treatment.[85,133] For more than 20 years, intensive efforts have been put in the development of targeted photodynamic therapy. The subcellular localization of the PS in mitochondria, lysosomes, endoplasmic reticulum, and plasma membrane (different organelles) plays a crucial role in the cell death mechanism involved (apoptotic, necrotic, and autophagy-associated cell death). For example, the majority of the clinically approved photosensitizers, temoporfin,[138] porfimer sodium,[141] and verteporfin,[142] already partially localize to the mitochondria,[143] which is considered as one of the most pivotal subcellular organelles in eukaryotic cells.[144] Moreover, defects or dysfunctions of mitochondria are connected to cancer progression and programmed cell death. Therefore, intensive research has been done toward the development of mitochondria-targeting therapeutics and diagnosis, which can effectively overcome tumor hypoxia, evade MDR, improve photothermal cancer treatment efficiency, and so on.[145,146] A study by Sibrian-Vazquez et al. demonstrated an increased localization of guanidinium and bisguanidinium porphyrin derivatives to the mitochondria, due to the positive charge of the compounds.[147]

One of the two main approaches to accomplish tumor-targeted PDT is by covalent conjugation of the photosensitizer with targeting biomolecules (Figure 6). These include proteins (essentially antibodies and their fragments), peptides, nucleic acids, and small molecules (biotin, folic acid, gefitinib, etc.). This is called active tumor targeting and refers to specific interactions at the molecular level between the drug/nanocarrier and target cells, usually through specific recognition and ligand−receptor interactions.[148,149]

Active targeting can be further separated in vascular targeting and tumor targeting. Both can work simultaneously to achieve better therapeutic efficacy. The first aims to eradicate tumorous blood vessels, which supply nutrients and oxygen to the tumors, by facilitating the accumulation of nanoparticles in vascular tissues.[150] Tumor targeting, on the other hand, increases the accumulation and cellular uptake of nanoparticles by selecting an appropriate receptor−ligand or antigen−antibody pairing. This is one of the most important issues in active targeting. Tumor cell markers must have two defining characteristics: (1) overexpression on the surface of tumor cells while being mostly quiescent on the surface of a normal, noncancerous cell and, (2) at the same time, should be selectively identified and bound by corresponding ligands.[150] Only in this way, they can be used as sites (i.e., the receptor) for the targeted delivery of specific drugs (such as anticancer drugs or photosensitizers). Targeting moieties can be separated into different categories: nonprotein small molecules, receptor-specific peptides, aptamers, and a variety of proteins, such as transferrins, lectins, and antibodies.[151,152]

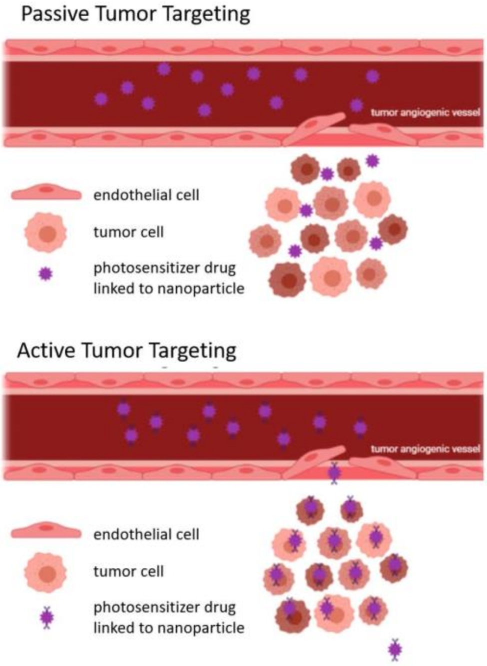

Figure 6. Two main strategies to accomplish tumor-targeted PDT.

Several tumor cell markers have been explored for active photodynamic targeting, including transferrin receptors (TR), folic acid receptors (FR), glucose transporters, growth factor receptors, LDL receptors, integrin receptors, and insulin receptors. Other potential tumor cell markers often include glycoproteins, such as lung cancer tumor markers (i.e., CEA, Cyfra21−1, and NSE), gastrointestinal tumor markers (i.e., CEA, CA199, the CA242 group, and CA724), breast cancer markers (CA153), ovarian cancer markers (CA125), hepatocellular carcinoma markers (AFP), prostate cancer markers (PSA), and choriocarcinoma markers (HCG).[150]

Recently, for example, Kim et al. synthesized a tumor penetrating trastuzumab (Tra) derivative by chemical conjugation to chlorin e6 (Ce6).[153] Tra is a monoclonal antibody used for treating human epidermal growth factor receptor 2 (HER2) overexpressing cancers.[154] The ability of Ce6 to generate ROS and the targeting of HER2 receptors increased the internalization of the conjugated PS. In this derivative, Tra and Ce6 were linked by a maleimide-poly(ethylene glycol) spacer. A confocal microscopy study showed that the fluorescence associated with Ce6 was only detected for the HER2-positive cell lines (SK-BR-3, BT-474), thus confirming selectivity. In comparison, the Ce6-Tra conjugate compound penetrated more deeply, which can contribute to better destruction of dense tumor tissue. In this system, visualization and PDT treatment were combined.[155]

When it comes to conjugated biomolecules, several types have been investigated, including receptor-specific peptides, transferrins, antibodies, oligonucleotide aptamers, and nonprotein small molecules, which include vitamins (e.g., folic acid, vitamin D, vitamin E, and vitamin B), retinoic acid, steroids, and other hormones. Some very effective binders include those interacting preferentially to low-density lipoprotein (LDL), suggesting that upregulated LDL receptors found on tumor cells are important.[156] Consequently, studies dealing with PSs covalently linked to molecules with affinity for neoplasia or to receptors expressed on specific tumors have been published.[157] In particular, those involving small molecular-based targeting drugs have received a great deal of attention in the design of targeted photosensitizers for cancer therapeutics.[158]

Conjugation of PSs to tumor-specific biomolecules such as monoclonal antibodies, epidermal growth factor, and small molecules (e.g., short peptides or peptidomimetics) provides another promising strategy to increase selectivity. Incorporation of functional groups to target specific receptors associated with cancer is, indeed, a common strategy to increase the efficiency of PSs (Figure 7). As mentioned before, an overexpressed receptor that has already been explored for the targeting of cancer cells is the folate receptor α.[159]

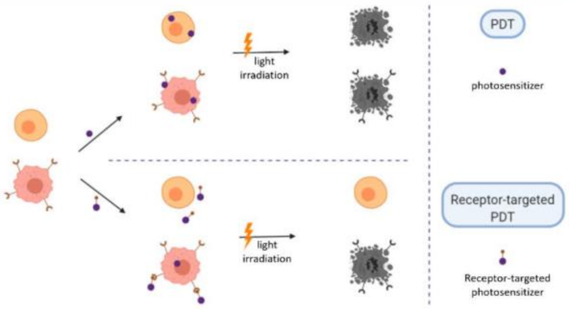

Figure 7. Receptor-targeted approach in PDT.

Another example of this kind of functionalization for targeting can be found in the work of Soukos et al., where a monoclonal antibody was conjugated to Ce6 as a tumor-specific targeting agent for imaging and therapy in a hamster cheek pouch carcinogenesis model.[9] This "photoimmunoconjugate" derivative (PIC), as it was defined, increases the specific delivery of the PS. In this study, EGFR, which is overexpressed in several human tumors, was the target. The anti-EGFR monoclonal antibody (C225) was selected and attached to Ce6. Then, the PIC was used as a diagnostic platform and monitoring tool to determine the therapeutic response. The same antibody (C225) was also conjugated to the benzoporphyrin derivative (BPD, verteporfin), thus providing another PIC derivative.[160]

Besides antibody-based PICs, small molecules and peptides can also be introduced to PSs. For example, Choi et al. introduced a membrane-penetrating arginine oligopeptide (R7) on 5-[4-carboxyphenyl]-10,15,20-triphenyl-2,3-dihydroxychlorin (TPC), in view to enhance cellular uptakes.[161] For similar reasons, new kinds of PSs with high water solubility, as well as with one or more functional groups for conjugation with biological agents, have been prepared by Li et al.[122] They have reported on the synthesis and characterization of asymmetrically substituted highly water-soluble phthalocyanines (Pc), with two different types of peripheral substituents: one reactive group for conjugation and the others for water solubility (Figure 8).

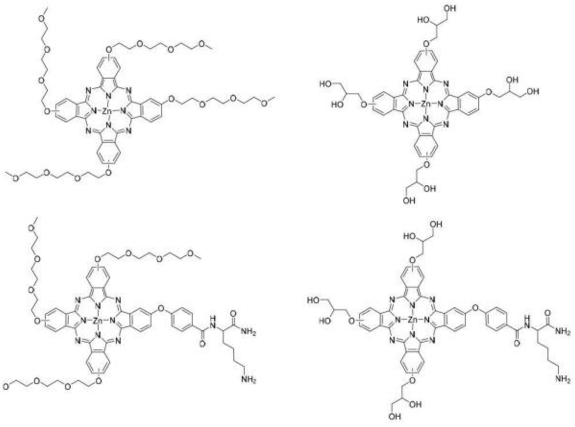

Figure 8. Structures of conjugated PSs.

Passive targeting is occasionally interpreted as physical targeting, which exploits the physiological and morphological differences between healthy and tumor tissues to achieve tumor selectivity and preferential accumulation of PSs. As mentioned previously, nanocarriers provide the potential for improvement of PS delivery to the target area to maximize PDT efficacy. Due to the uncontrolled proliferation of tumor cells, solid tumors have an abnormal tissue composition and architecture, which limit the uptake and distribution of drugs.[162] While rapid vascularization promotes fast-growing tumor sites, inflamed tissues embrace a leaky and defective architecture, thus leading to the enhanced permeability and retention (EPR) effect.[163,164] In addition, there is an accumulation of drugs due to inefficient lymphatic drainage, which make it harder for tumor sites to clear nanoparticles.[164]

Hyperproliferative tumor cells have a high metabolic rate and keep growing despite limited oxygen and nutrients. Therefore, in order to maintain its activity, tumor cells employ an enhanced level of anaerobic glycolysis, which produces a large quantity of lactic acid, resulting in intratumoral hypoxia and a lower pH environment.[165] The accumulation of PSs in tumors is known to be enhanced as its hydrophobicity increases. This is due to the fact that hydrophilic molecules are retained in the blood circulation system, while hydrophobic molecules tend to extravasate and accumulate in tumor tissues. PSs, however, generally have large π-conjugation domains for high quantum yields and effective energy absorption, which enable most classical PSs to easily aggregate in an aqueous environment. For this reason, these PSs are not suitable for intravenous administration, and further functionalization is needed, usually through the conjugation with a nanocarrier.

Since accumulation at the tumor involves a passive process requiring a long circulation half-life, the targeted delivery of PS-loaded nanocarriers is largely dependent on the biophysical and morphological properties of the nanocarrier. These properties include the material composition, morphology, hydrodynamic size, and surface charge.[166] The hydrodynamic size affects NP concentrations in the vessel, NP permeability, and clearance from the body.[167,168]

Another important factor concerning passive targeting is the surface properties. *In vivo* experiments have shown that hydrophobicity and surface charge affect the fate of nanoparticles and determines their behavior with plasma proteins, cells of the immune system, and nontargeted cells.[169]

Table 3. Commonly Used Imaging Agents

modality	agent	application
MRI	gadolinium	highlights areas of tumor or inflammation
PET/SPECT	$[^{64}Cu]$Cu-ATSM	identify hypoxic tissue
	$[^{18}F]$FDG	radioactive sugar molecule (-$[^{18}F]$-fluorodeoxyglucose) that shows the metabolic activity of tissues
	$[^{18}F]$-fluoride	imaging of new bone formation
	$[^{18}F]$FLT	3′-deoxy-3′-$[^{18}F]$-fluorothymidine allows to detect growth in the primary tumor; detect tumor response to treatment
	$[^{18}F]$FMISO	$[^{18}F]$-fluoromisonidazole is used to identify hypoxia
	$[^{68}Ga]$Ga(III)	attaches to areas of inflammation, such as infection; attaches to areas of rapid cell division, such as cancer.
	technetium-99m	used to radiolabel many different common radiopharmaceuticals; most used in bone and heart scans
	thallium-201	examine heart blood flow
X-ray and CT imaging	barium	contrast agent used to enhance images of the abdomen and pelvis
	gastrografin	same as barium but contains iodine instead
	iodine contrast agents	highlight blood vessels as well as the tissues of various organs; can be ionic or nonionic (less side effects)

3. IMAGING AND THERAPY TECHNIQUES IN PDT

In the medical field, approval to run clinical trials is often a limiting step, and this is also true for the implementation of molecular imaging biomarkers.[170] However, it is undeniable that molecular imaging, if the modality is chosen correctly, is more efficient in a timely and resource manner when compared to other practices such as tissue dissection and histological analysis.[171] From all of the different imaging techniques used for PDT, optical imaging is more broadly studied due to the fluorescence properties of the PSs. For this reason, we cannot exclude from this review where we will also focus on nuclear medical imaging (PET/SPECT) due to the great potentials the authors believe it holds, even though other techniques like MRI[172−175] and ultrasound[176] have also been developed and extensively studied on PDT over the past decade. A summary of the most used imaging agents currently in medicine can be found in Table 3.

In addition, PSs are fundamentally theranostic agents when used for PDT treatments, since such compounds absorb and emit light upon activation. Hence, the fluorescence property is used for imaging to monitor tumor uptake. Moreover, the PS fluorescence holds promise for fluorescence-guided resection (FGR) treatment, which is approved in Europe for both brain[177] and bladder cancers,[178] Another advantage of using PSs for FGR is that it allows a posteriori follow-up of treatments.[179] The specificity of PDT presents itself as the same molecule that may do both, the therapeutic and imaging roles.

3.1. Optical Imaging. A pivotal role has already been played by optical imaging in PDT dosimetry.[13] The presence of PSs at the targeted location before PDT treatment was used to quantitatively monitor the fluctuation of fluorescence before and after treatment, thus showing a correlation between clinical response and fluorescence.[180] This different outcome was associated with photobleaching during the production of reactive oxygen species. Zhou et al. have also observed that the response to treatment is less influenced when the light dose is adjusted to PS uptake.[181] Such studies confirm the significance of fluorescence imaging in PDT dosimetry.[179]

The fluorescence property of PSs can also serve for imaging as most PSs upon activation emit light in the visible region. Moreover, as PSs have a tendency to accumulate better in neoplastic tissues, this approach, frequently named photodynamic diagnosis (PDD), is very much appropriated for selective visualization of tumors and to outline the frontiers between cancerous and healthy tissues. The ability to precisely define tumor boundaries is a crucial step during an optimization process of a surgical intervention. At the moment, this fluorescence imaging technique constitutes the majority of the imaging applications. Ensuring a cancer-free margin around cancerous tissues is a crucial factor in avoiding recurrence. Resection of excess healthy tissue, on the other hand, can have serious and severe implications for the patient. This is one of the reasons why combining imaging and therapy is so important, and why over the past years, there has been an increasing interest in the development of innovative theranostic agents.

Therefore, the preparation of PSs with high fluorescence intensity and excellent singlet oxygen ($^1O_2$) quantum yields (QYs) is particularly needed for cancer diagnosis and PDT. In this regard, diketopyrrolopyrrole (DPP) and boron dipyrromethene (BODIPY) are two kinds of a building block with great potential for PDT. Recently, Zou et al. have linked DPP and BODIPY through a series of donor−acceptor−donor (D−A−D) linkers, thus forming a DPPBDPI structured organic photosensitizer (Figure 9).[182] The results indicate that the synergistic effect, resulting from the combination of the two photosensitizers, can simultaneously increase the fluorescence intensity by 5.0% and the $^1O_2$ QY by up to 80%.

Upon nanoprecipitation, the DPPBDPI can form uniform nanoparticles (NPs), which display not only high phototoxicity but also insignificant dark toxicity toward HeLa cells. *In vivo* fluorescence imaging shows that the DPPBDPI-NPs target tumors rapidly and inhibit tumor growth upon PDT treatment, even at reduced doses (0.5 mg kg^{-1}). The imaging and photodynamic behavior of DPPBDPI suggest a synergistic effect that can provide a novel theranostic platform for cancer diagnosis and PDT.

The high sensitivity of the method, the harmless nature of the agent, and the low cost of the procedure, makes optical imaging and detection an ideal imaging modality.[5] Among several characteristics, a potent PDD needs to have an intense absorption band in the red or the near-infrared (NIR) spectral region.[183] The optimal wavelength for PDT treatment must be a good compromise between activation and tissue penetration with low dispersion. Moreover, it should take into consideration the characteristics of the damaged tissue (location, lesion size, and accessibility). Because of these, and by utilizing near-infrared wavelengths (650−900 nm), which combine deep tissue with enough energy to excite the photosensitizer, fluorescence has ended up being an excellent asset for disease diagnostics and treatment.[184] It is easy to understand now how

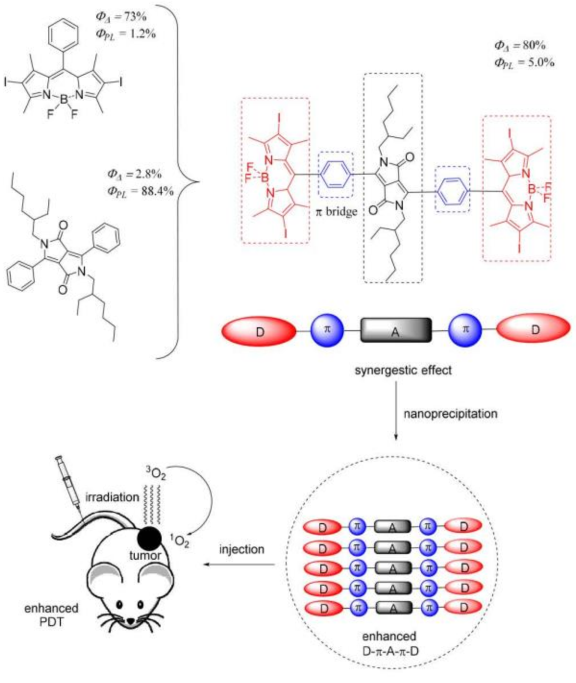

Figure 9. Illustration of a theranostic agent for PDT with a D−A−D structure with enhanced $^1O_2$, QYs, and fluorescence.

PSs are not limited exclusively to the therapeutic generation of singlet oxygen species, since numerous photosensitizers are additionally excellent fluorophores valuable for imaging, thus helping to characterize and to modify parameters amid PDT treatments. The tetrapyrrolic skeleton remains the most prominent structure for the development of photosensitizers. Tetrapyrrolic units show strong absorption in the visible region, and they possess an excellent photosensitizing ability to produce reactive oxygen species (ROS). In addition, the photophysical parameters of tetrapyrrolic units can be tuned by the insertion of metal ions or halogen atoms, like chlorine and fluorine, which induce macrocycle changes that modify the balance between fluorescence and intersystem crossing.[185−187]

The most fascinating and valuable imaging probes are photosensitizers that are nonphototoxic outside their destination and are only dynamic within the presence of a targeting molecule whereupon fluorescence and singlet oxygen production happen. Activatable photosensitizers (aPS) are perfect imaging probes since they share comparative activation mechanisms to fluorophores, and they can distinguish cancer cells from ordinary cells.[74] A few authors have researched into what they call "killer beacons" comprised of up to four modules: a fluorescent probe, a quencher, a linker, and a delivery vehicle, whose properties can be adjusted, modified, or joined to fill diverse needs (Figure 10). These beacons are based on a unique fluorescent photosensitizer linked to other functional groups. The dye should theoretically be hushed in the absence of the target, and its fluorescence re-established simply after the target is reached. To accomplish that, the PS must be linked to a quenching unit (Q) through a reasonable linker, which should keep the PS and quencher close enough to ensure fluorescence resonance energy transfer (FRET).

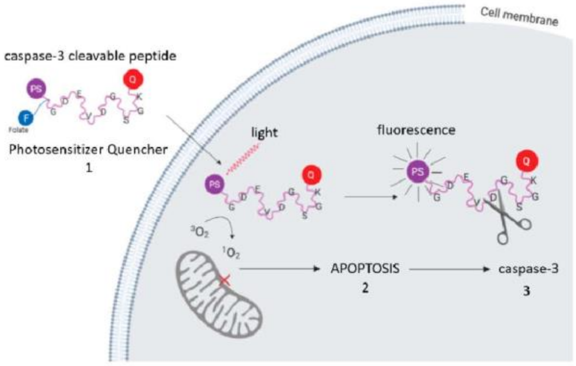

Figure 10. Principles behind a beacon system for post-PDT imaging of apoptosis.[184] The system is composed of four parts: a PS (violet dot), a folate delivery entity (blue dot), a caspase-3 cleavable linker (KGDEVDGSGK), and a quencher (red dot).

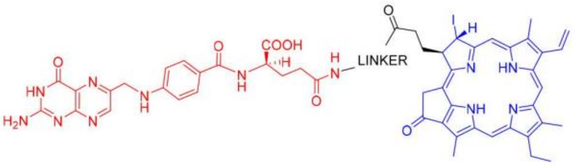

Figure 11. Pyro-GDEVDGSGK-Folate comprising three components: pyropheophorbide-a (imaging and therapeutic agent), a peptide sequence (linker), and folate (delivery vehicle).

In another example of activatable photosensitizers, Stefflova et al. have designed and synthesized a folate receptor-targeted, hydrophilic, and pharmaco-modulated PDT agent (Figure 11).[184] This molecule, obtained after three synthetic steps from Spirulina algae, selectively detects and destroys cancer cells, while avoiding healthy tissues.[188] Pyropheophorbide-a (Pyro) is a fluorescent photosensitizer that can also be used for NIR imaging and PDT (over 50% quantum yield). The Photochlor derivative is in phase I/II of clinical trials. In this compound, the folate moiety serves as a guiding molecule to bring the photosensitizer to folate receptor (FR)-overexpressing cancer cells. The PS and guiding folate are linked by a short GDEVDGSGK peptide. This peptidic sequence is stable and water-soluble, thus preventing cleavage prior to reaching the target. Moreover, the length of the sequence ensures that no steric hindrance takes place. Lastly, it serves as a pharmacomodulator for efficient delivery and reduced toxicity, and the system is easily modified to introduce other peptide sequences for different targeting.

At last, photosensitizers' efficiency can be upgraded by linking them with different particles that can deliver the entire cargo in malignant cells either nonspecifically or specifically, by focusing on "disease fingerprints". For instance, PSs linked to oil dispersions, liposomes, or hydrophilic polymers (PEG) can be internalized to disease cells through passive diffusion or phagocytosis. Such carriers help to solubilize the PS in biological media (for intravenous infusion) and, furthermore, to increase uptake and retention by tumors.[184] The bifunctional chelator approach presents itself as one of the most interesting and viable solutions for a theranostic goal, using porphyrins as the perfect building blocks since they offer both a metal isotope chelator and a targeting vector.

3.2. PET/SPECT Imaging. Two main directions can be pursued for the radiolabeling of dyes, including photosensitizers: the first one focuses on hydrogen-3 and carbon-14 marking for biodistribution studies and tissue autoradiography, while the second focuses on labeling these molecules with a short half-life (the time is needed for a radioisotope to decay to its half) γ- or positron-emitting radionuclides for tumor imaging and nonintrusive quantitation of photosensitizers.[189] Nuclear medical imaging (NMI) strategies like positron emission tomography (PET) and single-photon emission computed tomography (SPECT) are interesting complementary techniques, as they provide a further tissue penetration and decreased scattering of the produced signal.

In 1951, the first radiolabeled porphyrin system was prepared, introducing copper-64 in the core of protoporphyrin IX (Scheme 1). Soon after, hydrogen-3, carbon-14, palladium-109, sulfur-35, zinc-65, cobalt-57, and iodine-125 were likewise investigated. However, they are unacceptable for *in vivo* imaging as a result of their long half-lives or powerless gamma photon energy.[190] Currently, iodine-124, copper-64, and zinc-62 are the most promising radionuclides for PET imaging in PDT.[114,190−192]

Scheme 1. Synthesis of [^{64}Cu]CuPPIX (Protoporphyrin IX)[141]

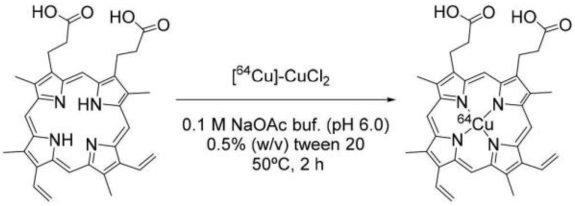

In the 1980s, it was demonstrated that the *in vivo* biodistribution and pharmacokinetics of porphyrins are not affected by chelation with copper-64 in light of the fact that the copper molecule fits into the focal point of the tetrapyrrole ring without modifying the side chains that dictate the *in vivo* conduct. This made it conceivable to exploit porphyrins' inborn capacity to chelate metals to fuse the radionuclide, taking into account the direct radiolabeling of photosensitizers with copper-64 without adjusting their conduct *in vivo*, which ultimately yields to exceptionally stable radiolabeled photonic nanoparticles.[193] Subsequently, the radiolabeling of metal complexes of porphyrins is the most encouraging strategy, the only issue being whether the metal has a radioactive species suitable for quantitative *in vivo* scanning and whether this can be exchanged with the nonradioactive species.

For nonmetallo-photosensitizers, the inclusion of the radioactive metal may change the biodistribution so that, for each metal-photosensitizer, combination biodistribution tests must be performed, normally with hydrogen-3 or carbon-14 labeling or quantitative fluorometry of excited tissues as a standard. In general, just as standard porphyrins, radiolabeled porphyrins accumulate in the tumor without changing the principle attributes of the host porphyrin molecules. Gallium-68[191] and copper-64[192,194,195] are promptly accessible and inexpensive metal isotopes, both appropriate for human PET imaging that may very well turn into the prime isotopes for radiolabeling porphyrins since complexation chemistry with the porphyrin core is quite straightforward, especially when it comes to copper-64.

While copper-64 marking has shown that, at least in animal tumor models, the fuse of this metal particle into the porphyrin ring does not significantly alter the uptake kinetics in tumors and healthy tissues. Marked differences between gallium-67 and technetium-99-labeled sulfonated phthalocyanines have shown that the metal ion modifies the dye conformation and thus may influence the molecular aggregation.[189,196] This leads to the conclusion that it is necessary to proceed with biodistribution investigations of radiolabeled analogues of photosensitizers at the beginning of *in vivo* studies.

On the other hand, the bifunctional chelator approach enables guided delivery of radioisotopes to selected cells by a kinetically and thermodynamically stable chelator conjugated to cancer-specific biomolecules such as antibodies, antibody fragments, peptides, or proteins. These systems exploit the overexpression of receptors and proteins on tumor cells. Some investigators accomplish this functionalization through the introduction of glucose and galactose moieties on the photosensitizer, thus culminating in an increased activity in tumor uptake.[190]

Since fluorine-18 is the most common radioisotope used in clinics, further research has been done regarding its potentials linkage to PSs. A dual-modality agent named [^{18}F]-PET/fluorescence, in which both the positron-emitting and fluorescence properties are combined, has been developed by Li et al.[197] They used a BF$_2$ unit, typically present in BODIPY dies, which can provide a [^{18}F]-radiofluorination site. Through PET imaging, they observed 2 h post-injection, an accumulation of the radiolabeled PS in the liver and kidneys, as well as in the gall bladder. Considering the lipophilicity and electronic property of the radiolabeled system, an accumulation in these organs is not surprising, as the BF$_2$ group possesses no targeting value.

The utilization of the fluorine-18 isotope in studies including antibodies and in photodynamic treatment (PDT) is, however, limited by its short half-life (110 min). In this regard, iodine-124 is considered a better choice for longitudinal imaging studies utilizing preclinical PET due to its half-life of 4.2 days. The labeling strategy for the iodine-124 isotope is well recognized, and it has been used in the labeling of an assortment of biologically active molecules.[198]

Developed by Roswell Park's group, the [^{124}I]-1′-3-(*m*-iodobenzylox)ethylpyropheophorbide-*a* derived from chlorophyll-*a* has demonstrated *in vivo* PET-imaging capacity.[199] As a nonradioactive analogue of chlorophyll-*a*, it shows PDT efficiency, and therefore, it is an interesting candidate for PET imaging. With great pharmacokinetic and pharmacodynamics profiles, it can be utilized for imaging (PET/fluorescence) and PDT. Curiously, when comparing to nonradioactive compounds, the postloading of the iodinated analogues in polyacrylamide-based (PAA) nanoparticles (NPs) had a striking effect in the biodistribution. In mice, the imaging and treatment agents are better taken up by tumors, with decreased uptake in different organs, particularly in the spleen (Figure 12).

Focusing on another approach, some authors have detailed the labeling of phthalocyanines (Pc) with PET isotopes for both tumor imaging and drug development studies. Phthalocyanines, which are structurally like porphyrins, are powerful PSs in their own right because of their high singlet oxygen quantum yield and high activation wavelength (600−850 nm). Van Lier et al. have demonstrated that the level of Pc sulfonation strongly affects the level of complex aggregation

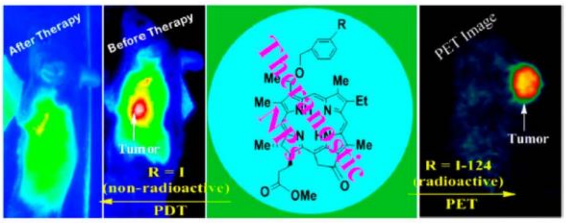

Figure 12. Multifunctional nanoplatform for cancer imaging and therapy with radiolabeled (^{124}I) chlorophyll-*a* (right) and the nonradioactive analogue (left), showing the accumulation in the tumor.[3]

and biodistribution, still conserving photosensitivity.[200] Consequently, they prepared a series of phthalocyanines with increasing sulfonate groups and radiolabeled each of them with copper-64 (Scheme 2). The tri- and tetra-sulfonated water-soluble phthalocyanines have shown rapid renal clearance on the EMT-6 tumor model, being both under the detection limits. Despite having a comparable excretion pathway, the disulfonated analogue showed an increased uptake in tumors, thus providing sufficient contrast for PET imaging.[199]

Scheme 2. Synthesis of ^{64}Cu-Labeled Phthalocyanines[200]

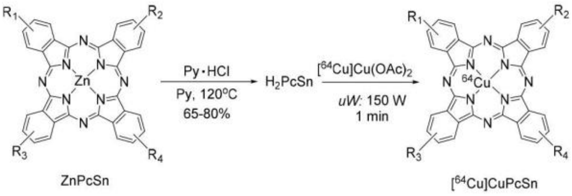

With imaging and treatment in mind, Liu and MacDonald have looked into the synthesis and evaluation of radiolabeled porphysomes. These nanoparticle platforms have been used as drug delivery vehicles.[98] As opposed to standard NPs, porphysomes do not require functionalization of the nanoparticle surface with metal radioisotope chelators.[98] Benzoporphyrin derivative monoacid (BPD-MA) was demonstrated to be a potent photosensitizer both *in vitro* and *in vivo*, as well as in clinical trials.[201] However, as many porphyrins exhibit a high level of lipophilicity, including BPD-MA, they have a tendency to aggregate in aqueous solution, therefore, limiting its bioavailability.[37] To circumvent this problem, porphyrins have been incorporated into liposomes for improved delivery, solubility, and efficacy.

Verteporfin, for example, has been utilized in clinical preliminaries and endorsed for clinical use, showing how liposomes have been considered as good delivery frameworks and as a feasible choice for the improvement of hydrophobic PSs.[202] A few authors extended the capacity of porphysomes by investigating the inherent capacity of the porphyrin−lipid conjugates to form steady, high-affinity complexes with copper-64, which has good attributes for nanoparticle tracking through positron emission tomography (PET).

Shi et al. prepared [^{64}Cu]-Cu(II)-labeled pyropheophorbide-α (a near-infrared fluorescent porphyrin) derivatives coupled to folic acid for improved folate receptor interceded take-up in the tumor, opting to utilize the porphyrin element in a chelating role.[192] The porphysomes, composed of lipid functionalized porphyrin units, have been labeled specifically with copper-64 with a radiochemical load of 98%. The [^{64}Cu]Cu(II)-labeled porphyrin units contribute to <5% of the porphysome molecular weight, unaffecting the nanoparticle size and photonic properties. The tumor uptake of the [^{64}Cu]Cu(II)-porphysomes was evaluated at 24 h post-injection by PET/CT (Figure 13A) and fluorescence imaging (Figure 13B,C).

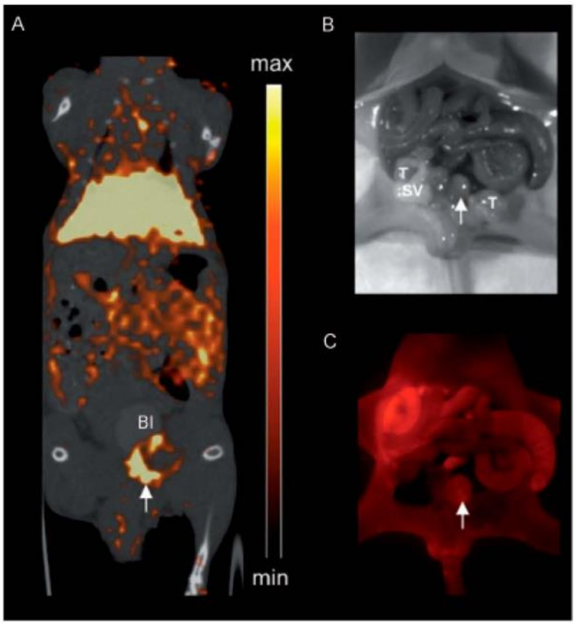

Figure 13. *In vivo* multimodal imaging of [^{64}Cu]-Cu(II)-porphysomes in an orthotropic prostate cancer model.[192]

3.3. Combination of PET/SPECT and Optical Imaging toward Multimodal Theranostic Agents.

The different techniques used for imaging cancers are stand-alone techniques, and it becomes imperative to have multimodal probes, in order to progress in cancer treatments.[203−205] At the moment, our current imaging modalities are limited in what they can perform individually,[206] but by combining different techniques, new achievements are expected. In principle, multimodal imaging agents can combine magnetic resonance imaging (MRI),[175,207] fluorescence imaging,[207−209] computed tomography (CT),[175,210] positron emission tomography (PET),[208,210] and single-photon emission computed tomography (SPECT).[175,203]

Recently, the feasibility of using multimodal agents has been verified in multiple *in vitro* and *in vivo* models.[211,212] A series of multimodal probes, with magnetic elements, such as iron oxide,[213,214] or Gd(III)-based chelates,[215,216] were coupled to PS. These studies demonstrate a remarkable potential for image-guided cancer therapy. However, such hybrid materials have limited applications since they are difficult to synthesize and produce in large quantities.[210] Therefore, the extended clinical use of theranostic agents will require affordable and easy-to-make derivatives. Not all multimodality combinations are useful, but certain imaging combinations are more attractive because some possess synergistic properties, like the combination of optical fluorescence imaging and PET (OFI/PET).

As previously discussed, fluorescence is an inexpensive modality. It is easy to operate; it possesses multiplexing capacity and high spatial resolution at histologic or superficial levels. On the other hand, PET shows quantitative, noninvasive, and extremely sensitive *in vivo* imaging without depth restraint.[217,218] The molar sensitivity of OFI and PET are relatively equal and both excellent; therefore, they can be used at nontoxic tracer quantities.[217] Fluorescence contrast imaging shows a better spatial resolution than PET at the histologic and superficial levels.[219] Moreover, fluorescence probes are stable, unlike PET probes, which rapidly decay. PET, on the other hand, has a superior resolution to fluorescence imaging through deep tissues. Therefore, the OFI/PET dual modality is a promising combination in clinical preoperative PET imaging and intraoperative optical imaging-guided surgery or PDT. Among dual-modality OFI/PET probes, those containing NIR dye and especially those based on cyanine-based NIR organic dyes (Figure 14), are of particular interest due to optimal tissue penetration.[220]

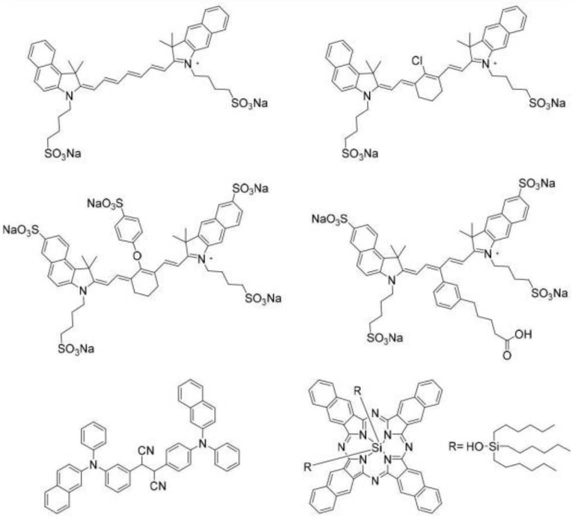

Figure 14. Structures of Cyanine-Based NIR dyes.

Not only NIR dyes should be considered, those emitting in the visible region are also suitable, as fluorescence imaging can be partially compensated by PET. Similarly, dual-modality OFI/SPECT combines SPECT's depth penetration, high sensitivity, and quantitative signals with the already mentioned advantages of OFI. The design remains very similar; however, γ-emitting radioisotopes such as technetium-99m and indium-111 are used. Indium-111 is the most common SPECT radionucleus, and it is often coupled to cyanine-based NIR fluorescent groups. Moreover, to increase the response for cancerous tissues, targeting groups are generally employed.

In view of generating a "trifunctional agent" for double-imaging (PET and fluorescence) and PDT treatment, Pandey et al. have modified the tumor-avid porphyrin (pyropheophorbide a), and reported the synthesis of a ^{124}I-labeled PS with high (>95%) radioactive specificity.[199] The half-lifetime of the nuclide allows us to perform the synthesis of the labeled PS and to accumulate in the target tissues after injection. They were the first to demonstrate that selective accumulation of porphyrin-based trifunctional agents to tumors can be achieved, thus confirming that using a single agent for imaging (PET and optical) and therapy is a promising avenue. In contrast to other studies, the different techniques are noninvasive, and the use of a single agent limits inconsistencies in the pharmacokinetic and pharmacodynamic patterns of the compound at all stages.

Another example of multiple-modality imaging with a known photosensitizer as the fluorescence probe was published by Cheng and co-workers.[221] A PEG-Ce6 nanomicelle was successfully prepared and used for OFI/PET dual-modal image-guided photodynamic cancer therapy. The presence of chlorin e6 molecules allows the PEG-Ce6 nanomicelles to work as a chelating agent for [^{64}Cu]Cu^{2+}. After internalization, PDT was carried out *in vivo* at a low irradiation rate, showing an excellent therapeutic effect on tumors. They were able to elaborate a simple approach to synthesize biocompatible multifunctional PEG-Ce6-based theranostic agents with the right properties for multimodality imaging-guided tumor therapy. The size and shape of nanoparticles and nanomicelles ensure high tumor uptake *in vivo* and partial renal clearance. These results might improve future applications and end up in clinical trials for these theranostic agents. In addition, these

Table 4. Representative Nanoparticles and their Biomedical Applications[90,291]

type of nanoparticle	possible surface modifications	imaging modality applicable	possible therapeutic strategies	synthetic protocol
quantum dots	lipids, polymer, targeting ligands or biomolecules	optical	PDT	colloidal synthesis, self-assembly, viral assembly
dendrimer	charge, polymer, targeting ligands, or biomolecules	MRI, optical	drug and gene delivery	organic chemistry techniques
liposome	charge, polymer, targeting ligands or biomolecules, viral protein coating	MRI, optical, radionuclide imaging	drug, gene and protein delivery, PDT	emulsion, polymerization
gold nanoparticle	lipids, polymeric shell, targeting ligands, or biomolecules	CT, optical	drug delivery, PTT	biological reduction, colloidal synthesis, vapor precipitation
carbon nanotube	polymeric shell, targeting ligands or biomolecules	MRI, optical, radionuclide imaging	drug delivery, PTT	arc discharge, laser ablation, vapor precipitation
mircrobubble	polymeric shell, targeting ligands or biomolecules	ultrasound	drug, gene and protein delivery	emulsion, layer-by-layer fabrication, polymerization
iron oxide	charge, dextran, lipids, polymer, targeting ligands or biomolecules	MRI	siRNA delivery, PT	coprecipitation, decomposition, microemulsion, sol−gel, thermal
micelle	charge, polymer, targeting ligands or biomolecules	MRI, optical, radionuclide imaging	drug and gene delivery	microemulsion
silica nanoparticle	charge, polymer, targeting ligands or biomolecules	MRI, optical	drug and gene delivery	chemical polymerization, microemulsion

PEG-Ce6 nanomicelles can chelate other metals (Mn^{2+} or Gd^{3+}) for additional imaging modalities, thus providing high-resolution imaging for anatomical information. Combining PET/OFI/MRI can be a winning combination since it can gather crucial information. The high sensitivity of the imaging techniques and excellent resolution of the images should help physicians to design better therapeutic approaches for cancer treatments.[221] In this regard, Li et al. acknowledged that nanotechnology is an ideal platform to combine different imaging agents into hybrid materials. Moreover, they can have a tremendous impact on tumor diagnoses.[222] Representative nanoparticles for their use as multimodal agents and their biomedical applications can be found in Table 4.

Nanoparticles are behaving differently from single molecules or bulk particles. They have properties of their own, and this can be nicely exploited in medicine. For example, nanoparticles tend to accumulate and internalize selectively to cells, being transported across membranes via transcytosis.[223] Furthermore, structural modifications of nanoparticles can be performed chemically, thus modifying not only their properties but also their biocompatibility.[224] However, to develop nanoparticles with multimodal imaging or therapeutic capacity, multiple factors need to be considered, such as toxicity, interaction with metabolites, biocompatibility, and biodegradability.[224]

Among multimodal techniques associated with nanoparticles, those involving SPECT/CT are the most common. For example, a liposomal nanocarrier incorporating technetium-99 has been developed for SPECT/CT imaging.[225] The imaging probe was used to visualize the amount of drug delivered to tumors. In addition, the therapeutic effects of this probe were determined using different tools. These probes can gather multiple information from different imaging modalities without having to inject other substances.

Overall, multimodal imaging agents should have a low toxicity and/or high biodegradability. They should have a high selectivity to target the disease. These characteristics would allow us to evaluate the efficacy of specific targeting and to determine the toxicity caused by the off-target accumulation of the multimodal imaging agent. On the other hand, there is a need to develop more efficient nanocarriers for controlling the external release of nanoparticles. Only then can this approach start to be considered for effective clinical translation and accurate diagnosis.

4. IMAGING HYPOXIA IN PDT

One of the major drawbacks in PDT is the increased oxygen needs. As mentioned earlier, oxygen consumption is predominant through the active mechanism of PDT, resulting in aggravate further the hypoxic conditions in tumors. It is well-known nowadays that tumor hypoxia can be linked to tumor aggressiveness, metastatic spread, poor tumor control, increased level of recurrence, and unfortunate therapeutic outcomes, mainly due to radiation and chemotherapy resistance.[10,226−230] Taking into account the variability of O_2 concentrations within tumors and even tumor regions, it is quite undeniable that O_2 concentrations will have an impact on PDT treatments.[231] Regrettably, solid tumors are known to show acute hypoxia due to a series of abnormal physiological variations in the tumor microenvironment including uncontrollable tumor cell proliferation, an irregular vascular system, and a deteriorating microenvironment.[232,233] The degree of hypoxia is, therefore, directly linked to cancer treatment effectiveness.[234,235]

An increasing interest in developing methods to measure tumor hypoxia has, therefore, been raised. These techniques can either be invasive (e.g., polarographic O_2 sensor) or noninvasive (e.g., molecular imaging), and they both aim at measuring the oxygen level within the tumors. Medicinal imaging (optical, MRI, PET, and SPECT) has become a useful tool to characterize the variability and magnitude of hypoxia within tumors and to help the physicians' decisions.[236] Optical imaging techniques assess the optical absorption, scattering, and fluorescence in tissues.[237] MRI techniques, based on contrast agents (endogenous or exogenous), embrace techniques such as electron paramagnetic resonance (EPR),[238] dynamic contrast MRI (DCE-MRI), magnetic resonance spectroscopy (MRS),[239] and blood oxygen-dependent level (BOLD) imaging.[240,241] However, undoubtedly, one of the most extensively investigated imaging modality toward hypoxia imaging is PET due to the various advantages discussed in the previous section and to the development of hypoxia-specific radiolabeled agents.[242−244] Since the very early stages of hypoxia research, it has been revealed that several nitroimidazoles and thiosemicarbasides can directly and reproducibly identify the absence of oxygen.[245]

In 1981, Chapman et al. pioneered the use of nitroimidazole derivatives and molecular imaging techniques to evaluate the degree of hypoxia in tumors.[237] These compounds are particularly interesting because the oxygen-binding affinity to nitroimidazoles is directly linked to cell retention and O_2 concentration (Scheme 3).[246] Following this study, hypoxia-specific agents targeting intracellular macromolecules have made possible the widespread use of PET for imaging hypoxia.

Nowadays, copper-based complexes incorporating bis(thiosemicarbazone) ligands have become the most effective class of compounds for imaging diagnostics of hypoxic tumors. The pharmacological activity and theranostic properties of these complexes have allowed the determination of the origin of hypoxia and how it is involved in tumors and heart diseases. The mechanisms by which these copper complexes (CuATSM) are hypoxia selective seem to be associated with metal coordination. The hypoxia selectivity involves intricate intracellular reduction−oxidation processes, leading to Cu(I) species, which are free from the chelated complex via redox reactions (Figure 15). In hypoxic environments, Cu(II) species are easily reduced to Cu(I) derivatives, and upon decomplexation, the Cu(I) can interact with biomolecules.[247] This phenomenon is essential for delivering free copper to cells. However, it does not guarantee a selective uptake.[248] Therefore, to increase selectivity, bis(thiosemicarbazonato) complexes as well as thiosemicarbazide analogues have been modified to better target tumors, and their responses *in vitro* have been explored worldwide.[247,249−251]

To date, only a few PET agents have been evaluated in clinical trials: [^{18}F]-fluoromisonidazole ([^{18}F]FMISO),[253,254] [^{18}F]-fluoroazomycin arabinoside ([^{18}F]FAZA),[255] and [^{64}Cu]copper-diacetyl-bis(*N*(4)-methylthiosemicarbazonato),[248,249] being the most promising ones. Although [^{18}F]FMISO is consensually known as the gold standard in clinical research for hypoxia measurement, it is considered to have low-specific tissue accumulation resulting in limited imaging contrast of hypoxic tissues compared to normoxic areas, slow nonhypoxic cellular wash out, and no specific time for image acquisition.[256,257] [^{18}F]FAZA was developed along

Scheme 3. Mechanism of Nitroimidazole Derivatives in Hypoxic Cells

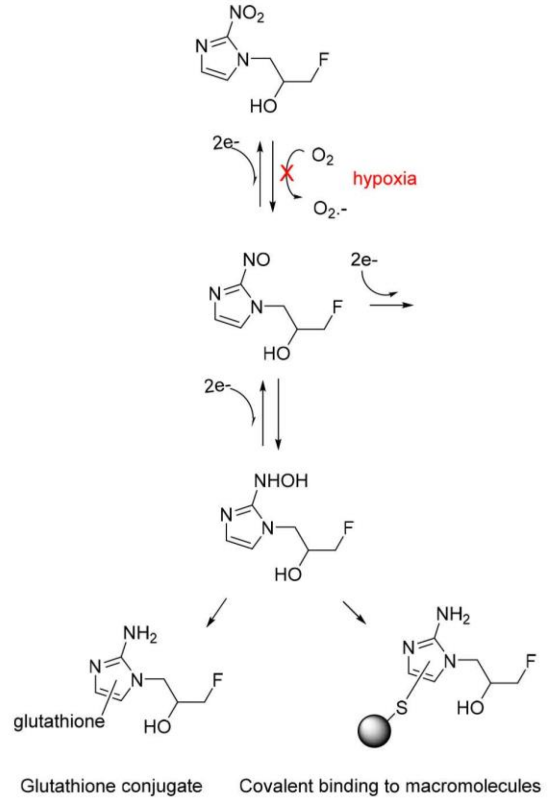

with the second-generation 2-nitroimidazoles, and while it has been denoted that it overcomes most of [^{18}F]FMISO's limitations, its intertumoral activity is lower.[254,258]

On the other side, studies suggest that [^{64}Cu]Cu(ATSM) occasionally possesses better properties,[259,260] due to its capacity to enter hypoxic cells and localize in tissues with low O_2 concentrations.[261] However, its selectivity seems to be related to the intracellular redox potential (Figure 16).[262,263] Subsequently, regardless of the collection of different tracers that are currently used for hypoxia tracing, none of them provide reproducibility across variant hypoxia subtypes, and new ones need to be developed in order to raise the sensitivity, the selectivity, and the resolution of the imaging studies.

Lately, gallium-68 (∼68 min) is one of the radionuclides that has been commonly applied as a probe. These systems usually contain a nitroimidazole or a macrocyclic ligand, which is able to complex gallium-68 (for example, 1,4,7,10-tetraazacyclododecane-1,4,7,10-tetraacetic acid or 1,4,7-triazacyclononane-1,4-diacetic acid, generally alluded to as DOTA and NOTA). A variety of studies have shown improved clearance and successful hypoxia imaging compared to [^{18}F]FMISO. Recent studies have also demonstrated an affinity for the (HIF)-1 regulated carbonic anhydrase-IX receptor (CA-IX), a renowned endogenous marker of hypoxia.[264]

Hypoxia-responsive domains have been reported, and functional groups, such as nitro, quinone, transition metals, aliphatic, and aromatic N-oxides, have been identified for chemo-drug release. Such derivatives have been studied by different groups and recently added to the design of carriers for PSs and for anticancer drugs. These systems have led to the development of hypoxia-responsive nanoplatfom domains.[265,266] For instance, light-activatable nanoparticles (NPs) with nitroimidazole groups was developed by Lin et al. to selectively release drugs in hypoxic cells.[267] Furthermore, Gu's team has reported a 2-nitroimidazole (NI) conjugate linked to the dithiophene-benzotriazole polymer (NI-CP), which can encapsulate doxorubicin (DOX) via a double emulsion method, thus forming a DOX decorated polymer (DOX/NI-CP).[268] Near-infrared (NIR) light irradiation was performed after accumulation in the tumor region, showing a good production of ROS despite the hypoxic conditions. Moreover, the tumor hypoxia aggravated by the photodynamic reaction facilitated the cargo release, which turns this procedure into a self-feedback process, leading to selective drug release and an excellent therapeutic effect. This study suggests that the introduction of PSs in hypoxia-sensitive delivery carriers offers spatiotemporal control over the drug released, thus providing another type of theranostic agent.[269]

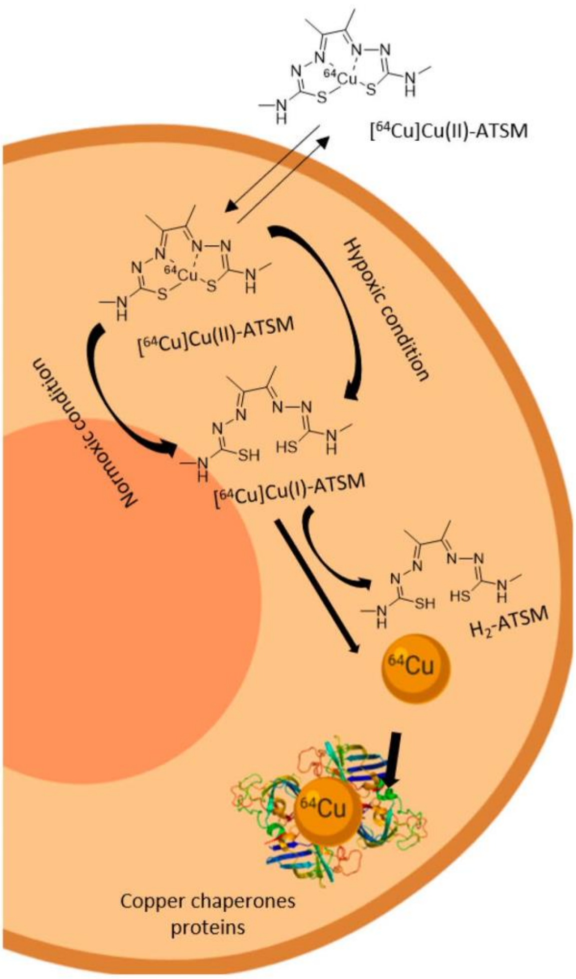

Figure 15. Proposed mechanism of hypoxic selectivity for [^{64}Cu]-CuATSM.[247,251,252]

Moreover, it has been established that PDT planning might be facilitated by molecular imaging through the estimation of

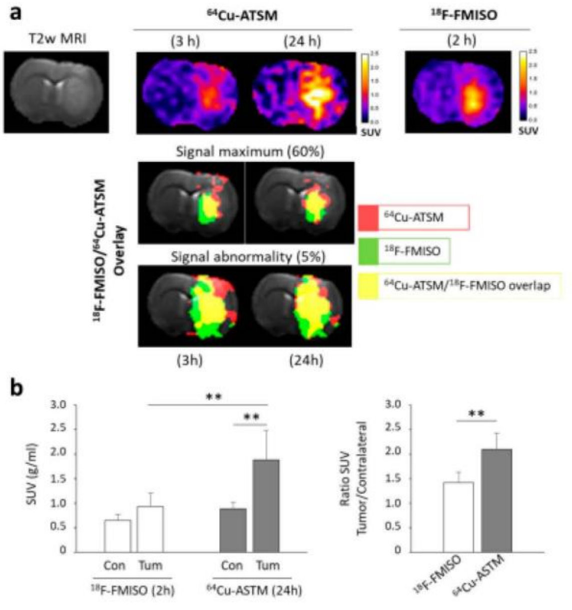

Figure 16. Studies showing the relationships between the retention of [^{18}F]FMISO and [^{64}Cu]Cu(ATSM) and hypoxia. (a) Coregistration of the [^{18}F]FMISO PET signal (2 h postinjection) with the [^{64}Cu]Cu(ATSM) PET signal (3 or 24 h postinjection. (b) [^{18}F]FMISO and [^{64}Cu]Cu(ATSM) uptake was evaluated at 2 and 24 h after radiotracer injection, respectively.[260]

the biodistribution of the PS in tumors. However, the concentration of oxygen remains crucial for PDT efficacy, and the role of imaging in this regard is often overlooked. Increasing intratumoral blood flow, using oxygen carriers, generating oxygen *in situ*, and targeting hypoxia-induced factors are some of the strategies that have, up to now, been developed to overcome tumor hypoxia. From all techniques, one, in particular, has stood out. This technique takes into consideration the existence of endogenous hydrogen peroxide (H_2O_2), which is naturally produced in cancerous cells. This approach utilizes H_2O_2 catalysts, such as catalase (CAT), to decompose H_2O_2 into O_2. Though, as an exogenous enzyme, the protease induced degradation as well as the immunogenicity of CAT, two non-negligible factors that need to be considered.[270−273]

Some authors have looked into the possibility of taking advantages of the porphyrin structure of THPP to coordinate metal ions and have come up with catalase-entrapped nanocapsules (CAT-THPP-PEG). To increase solubility, the nanocapsules are functionalized with short polyethylene glycol (PEG) chains. The enzymatic activity and stability of catalase are ensured by the CAT-THPP-PEG nanoparticles, which, after labeling with technetium-99m, can be traced by *in vivo* SPECT imaging. These nanoparticles have prolonged blood circulation and show efficient tumor retention after intravenous (iv) injection, and once located in the tumor, the catalytic activity is regained, transforming H_2O_2 to O_2. These very interesting therapeutic responses were associated with the nature of the PS (THPP) and tumor hypoxia. Moreover, in mouse tumor models, reduced immunogenicity was observed as compared to free catalase. The authors, therefore, presented an easy approach for the preparation of a unique type of enzyme entrapped theranostic nanocapsules, using PS as linkers. This, ultimately, allows for enhanced cancer therapy by modulation of tumor hypoxia via nanoparticle functionalization. The enzyme stability and reduced immunogenicity, which also enhance PDT, enable *in vivo* SPECT imaging to become an attractive cancer theranostic nanoscale platform.

5. DISCUSSION AND PERSPECTIVES

In general, standard medical protocols analyze a disease or disorder, determine its characteristics, and then apply treatments. A similar strategy is employed by the researcher when developing new drugs or new modalities of treatment.[274] Despite the predominance of this old-fashioned strategy, studies suggest that, for some diseases, another approach should be taken. Most of the modern diseases are heterogeneous in their behavior and appearance.[274] For instance, with a cancer patient, the first step is to identify the phenotype, then the heterogeneity is assessed, and finally, the stage in which the cancer has evolved is determined.[89,275] According to the stage and the characteristic of the cancer, the patient will receive a specific modality of treatment, so two patients with a similar disease may end up with different treatments.[17] The "one size fits all" approach that has been preconized for many years is not viable with cancers; the more we learn about the disease, the better we understand that a different approach is needed for developing successful treatment against cancer.[276]

The preferential localization of porphyrins in tumors, their ability to produce reactive oxygen species upon light activation, and their low toxicity have made them perfect molecules for photodynamic therapy. Moreover, the photophysical properties of porphyrins and the possibility to bind metal ions provide a unique platform for developing imaging agents. An ideal imaging agent is harmless to the body, and it possesses a fluorescence intensity above the cellular autofluorescence. These characteristics have been incorporated in recently synthesized porphyrins or porphyrin conjugates.[277] It is also important to note that porphyrin analogues, such as phthalocyanines, chlorins, and bacteriochlorins, are also good candidates for imaging, and several reviews have been written on the subject.[278,279] Although porphyrin analogues show similar behaviors and similar applications, they are often studied separately. Metalloporphyrin is another type of porphyrin derivatives that can be used as imaging agents. The introduction of metal ions in the porphyrin core modifies the photophysical property of porphyrins, and accordingly, it can improve the phototherapeutic efficacy, provide MRI contrast, and enhance Raman imaging.[280] In conclusion, metalloporphyrins own all of the essential characteristics of becoming theranostic agents.

There are, however, two main limitations of porphyrin-based imaging agents in therapy, and they come down to the synthesis and the aggregation of porphyrins. The principal strategy for the synthesis of these compounds is based on the condensation of mixed aldehydes resulting in a complex mixture of porphyrin derivatives, which are often difficult to purify and to isolate. Then, despite having pure molecules, the planar aromatic structure of porphyrins increases the probability of aggregation, a problem encountered by most researchers in the field.[281] Aggregation is not only a problem when it comes to therapy because it is usually related to low solubility, which, in the case of PDT, means worse pharmacokinetic profiles but also in imaging because aggregation usually translates into changes in the absorption spectra.[282] In this way, having lower Soret bands would damage the pharmacodynamics of PDT as well as the imaging due to their decreased fluorescence. Therefore, many researchers have turned, as previously explained, to the solution of these problems by conjugation with nanostructures, which promise to help overcome these challenges.

On the other hand, more specific and individualized modalities of treatment are needed.[283] Diagnostic tools are vital for determining the progress of a disease in a patient, and combining diagnostic and therapeutic applications in a single molecule can, in principle, provide personalized treatments.[226] Having a single platform[99] will help doctors to apply the best treatment to individuals and, by doing so, will reduce side effects and other undesirable outcomes.[284]

The advent of novel drug delivery technologies is essentially driven by the observation that many therapeutic agents are not able to localize preferentially in target tissues and/or because of their lack of selectivity against diseased cells. Commonly, a preclinical biodistribution study leads to the quantification of the drug over time in tissues/organs. Generally, these studies are carried out *ex vivo* through time-consuming methods that required the sacrifice of many animals. These days, this can be done *in vivo* and in real time using imaging methodologies and tailored imaging probes. In a typical nanomedicine approach, the nanocarrier is loaded with both the drug and the imaging agent, an agent that can be detected by the corresponding imaging technique. Due to the good quantification properties and outstanding detection sensitivity, radioisotopes that have been broadly utilized for *ex vivo* biodistribution studies may have an interesting potential for *in vivo* applications. Kopelman et al. gave an example of such systems, in which an intricate mixture of porphyrin oligomers (porfimer sodium) and MRI contrasting agents were trapped together in a nanoparticle (Figure 17).[172] In these systems, the nanoparticles were functionalized at the surface with RGD targeting sequences and PEG for immune cloaking. Then, after delivery to tumors in rats, the photosensitizers were activated by light. The results show a complete necrosis of 9 L gliosarcoma tumors in rats within 5 min.[172]

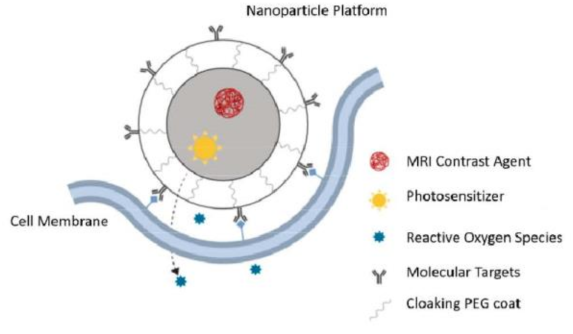

Figure 17. Schematic PAA core matrix nanoplatform with photodynamic dye, MRI contrast agent, polyethylene glycol (PEG) loading, and molecular targeting groups.[172]

As it was mentioned earlier, the effectiveness of photoinactivation can be affected due to PS aggregation.[285] Taking this into consideration, several studies have looked at different carriers to avoid aggregation, to stop degradation, and to increase uptake. For example, silica-based NPs (SiNPs) have been loaded with PSs.[286−288] In the clinical field, SiNPs are used as cell markers,[289−291] drug and gene delivery platforms,[291,292] enzyme adsorption, and immobilization agents,[293] and they are able to internalize cells.[289−291] Therefore, it made sense for them to be investigated for PDT applications. Synthetically modified SiNPs, such as ORMOSIL, mesoporous silica NPs (MSiNP), and hollow SiNPs (HSiNP), are frequently used in the clinic. These SiNPs are particularly appropriate for PDT as they show chemical inertness, and they are structurally stable. At the same time, they are resistant to pH variations and do not absorb light. However, perhaps most importantly, the functionalization of SiNPs ensures a monomeric environment to all PSs, thus avoiding aggregation phenomena. Moreover, singlet oxygen can travel through the SiNP shell.[294] Finally, the functionalization of SiNPs remains relatively easy, and the surface of SiNPs can accommodate all kinds of functional groups, including PEGs, antibodies, peptides, glycosides, and several other biomolecules.[286,295,296]

ORMOSIL functionalized NPs have shown great promises for PDT applications.[286] They have been widely studied because of their hydrophobic/hydrophilic tunability, which can ease the solubility of PSs. Accordingly, Ohulchanskyy et al. have prepared ORMOSIL NP derivatives with covalently bound PSs. The covalent attachment of the PS increases the stability and avoids leaching of the PS before reaching its target.[297] Among different systems, the iodobenzylpyropheophorbide derivative (Figure 18) was synthesized to initiate a coprecipitation reaction, thus facilitating purification and isolation of the compound. These ORMOSIL and ORMOSIL-PS conjugates were evaluated on two tumor cell lines, Colon-26 and RIF-1. The study shows an excellent uptake by cells and that the photophysical properties of the PSs are preserved. Indeed, upon light activation, the phototoxicity of the PSs was comparable to that of the PS alone. Moreover, the authors highlighted the possibility of replacing the natural iodine of iodobenzylpyropheophorbide with a different isotope (e.g., I-124, I-125, etc.). This modification implies that the same systems can be used as contrast agents (PET/SPECT), while still having PDT effect, thus becoming theranostic agents.[297] A similar observation was made by other groups, on systems involving other PSs covalently linked or encapsulated in ORMOSIL NPs.[298]

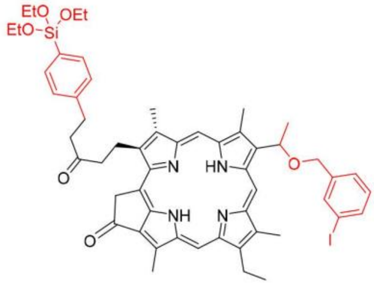

Figure 18. Iodobenzylpyropheophorbide precursor for functionalization to ORMOSIL NPs.

Metal NPs are another category of NPs commonly used in PDT. Among metal-based NPs, gold NPs (AuNPs) are particularly attractive, due to their distinctive properties, which make them perfect candidates for labeling, delivery, heating, imaging, and sensing applications.[299−301] Mostly linked to their biocompatibility, precise structure, limited surface, and optical properties, gold NPs have received a great deal of attention in PDT.[302−304] While the introduction of specific groups (thiol, amino, cyano) confer the colloidal stability,[221] the functionalization of gold NPs with lipids, proteins, oligonucleotides, or PSs can improve their biological properties (targeting, stability, selectivity).[300] In fact, the conjugation of PSs on the surface of AuNPs may produce an enhanced electromagnetic field as a result of localized surface plasmon resonance of AuNPs upon light activation and, consequently, an increase the PDT efficacy (Figure 19). This phenomenon will enhance the PS excitation rate, increase ROS production, and, ultimately, will generate an improved PDT agent.[301,302]

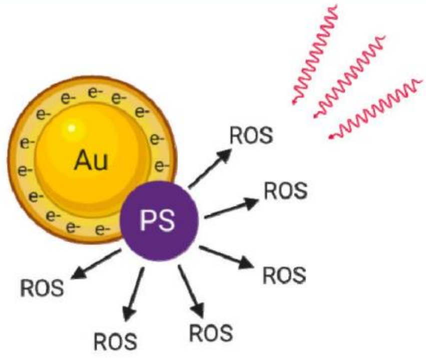

Figure 19. Cartoon illustrating the surface plasmon resonance phenomena on gold NPs.

The use of hydrophilic AuNPs as a platform to prepare multimodal systems was recently published by Penon et al.[305] The multifunctional AuNPs (PS-AuNPs-PEG-Ab) show porphyrins and PEG chains connected to an anti-erbB2 antibody. The antibody aims to target overexpressed erbB2 receptors, which are commonly found on the membrane of SK-BR-3 breast cancer cells. The different components are attached to the AuNPs via thiol groups, which have a high chemical affinity for AuNPs. These functionalized NPs are photoactive, producing $^1O_2$ and killing cells under PDT conditions. It was also demonstrated that the PS-AuNP-PEG-Ab conjugate accumulates in cells, and upon photoactivation, damage to membranes and modification to cellular morphology were detected.[305]

Like metal-based nanoparticles, nanotheranostic particles involving PDT can destroy their targets. However, to be effective, nanotheranostic particles need to reach their target, to avoid off-target phototoxicity. Therefore, it is important to monitor the localization of these particles in real time, in order to minimize side effects linked to the generation of reactive oxygen species outside the tumors.

Luckily, most photosensitizers used for PDT are also fluorescent molecules, a useful property that can be employed to localize the photosensitizer. Fluorescence spectroscopy is cheap to operate, it shows outstanding resolution in the appropriate spectral region, and it can be used in parallel to radioisotopes (PET and SPECT), thus being perfectly compatible with other techniques.[306,307] Photons released by naturally fluorescent biomolecules or from externally administered fluorescent probes can be used for imaging. However, some limitations are associated with fluorescence, including poor tissue penetration, high noise, and background from tissue scattering of photons in the visible region, autofluorescence, light absorption by proteins, and interference from water molecules.[99] Nevertheless, NIR activation can overcome these limitations in that region: tissue penetration of light is up to several centimeters, a low autofluorescence is observed, and tissue scattering is reduced to a minimum.[308,309]

Selectivity and targeting strategies are keys for fluorescence imaging and PDT. This can be achieved by passive transport, which implies the use of large molecules, such as nanoparticles. The particular size of nanoparticles increases their accumulation in tumors, and after internalization, the particles are retained (EPR effect). Peng et al. have developed multifunctional polymeric nanoparticles loaded with IR-780, which provide both NIR fluorescent dyes and photosensitizers in a large particle.[310] These micellar nanoparticles confirm that passive targeting can be accomplished with nanoparticles.

Using similar concepts, Tsai and co-workers studied the accumulation in cells of nanoparticles decorated with the photosensitizer PPIX.[311,312] They found that the pH-sensitive particles were delivering PPIX in the nucleus, while non-pH-sensitive nanoparticles were delivering PPIX in lysosomes.[313] In mice bearing A549 xenografts, the different accumulation was nicely linked to the biological activity. Indeed, the pH-sensitive nanoparticles have a stronger inhibition on tumor growth, suggesting that the localization of the photosensitizer in cells can strongly affect PDT.

Like PPIX, chlorin e6 (Ce6) is another popular photosensitizer used as a theranostic agent.[314−316] Lee et al. have developed glycol chitosan nanoparticles to transport Ce6 to cells.[317] Two transport systems were evaluated: one involving physical encapsulation and the other involving covalently linked Ce6 nanoparticles. The conjugated system showed a longer circulation time, a better-controlled release of Ce6, and a higher accumulation of the PS to tumors. The increased accumulation in tumors of mice bearing HT-29 human colon adenocarcinoma was established by NIR imaging. Then, PDT treatments on the same tumors showed severe necrosis and mass reduction of tumors.

Phthalocyanines (Pc) are also a class of molecules with significant potential as theranostic agents, given the strong absorption within the NIR window. For example, a fluorescent Pc-loaded graphene nanoplatform was used as an imaging and PDT agent on ovarian cancer cells.[318] Similarly, a biocompatible carbon nanodot loaded with zinc Pc was used for the same modalities (imaging and PDT) on HeLa cells, as well as on animal models.[319] Both examples confirm the usefulness of passive transport in view to target tumors for PDT and fluorescence imaging.

A second strategy to target tumors and add selectivity to PDT/imaging agents implies the development of activatable multifunctional agents, which can become active after responding to a biological or physical stimulus.[28] The activation can be triggered artificially (exogenous stimuli) by applying, for example, a magnetic/electrical field, ultrasound, or light. On the other hand, the activation can be triggered biologically, by physiological conditions associated with cancer (endogenous stimuli), such as the temperature, pH, or enzymatic activity.[152,320−322] Among these endogenous stimuli, pH is probably one of the most attractive targets, as tumors tend to have a mildly acidic pH.[173] Accordingly, charge-switching nanoparticles have been designed to react under acidic conditions (Figure 20). In such system, the positively charged region of the compound interacts strongly with

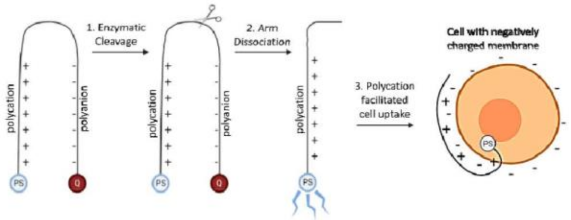

Figure 20. Mechanism of an activatable peptidic zipper-based PS.

negatively charged particles, especially those located in membranes, thus overall increasing cellular uptake.[315]

Enzymes such as matrix metalloprotease-2 that are overexpressed in tumor cells can be targeted by activatable nanoparticles.[323] Likewise, a theranostic agent with double targeting possibilities can, for example, be fluorescent and phototoxic only after being released by tumor-associated lysosomal enzyme cathepsin B. This is particularly attractive for targeting folate receptor-positive cancer cells.[324] This strategy focuses on selectivity and specificity for malignant cells, using targeted moieties that can aim specific receptors found on the surface of biomolecules and inside cells. One frequently mentioned group is the RGD peptide (tripeptide Arg-Gly-Asp), which can target the integrin avb3 receptors that are overexpressed in several tumor types. RGD conjugates loaded in ICG nanoparticles showed promises for FGS in liver resection.[221] Conjugation of (i) RGD peptides for improved tumor targeting, (ii) temoporfin as a photosensitizer, and (iii) with fluorescent dye molecules for improved contrast has been performed.[325] An *in vivo* study has confirmed the dual modalities of these systems, fluorescence imaging and PDT.

Folic acid (FA) is another functional group that can be used to target specific receptors. Folate receptors are upregulated in ovarian, lung, brain, and breast cancers, thus making folate conjugates good candidates for increasing selectivity.[326] Wang et al. reported a nanoparticle that incorporates fluorescence imaging, PDT, and FA targeting ability.[327] Later on, a highly biocompatible carbon nanodot was synthesized, which incorporates the same modalities. Biological studies showed that the functionalized carbon nanodot increases fluorescence and has PDT effects *in vitro* and in mice.[319] More recently, FA-coupled nanoprobes loaded with Ce6 were synthesized, and after a series of *in vitro* and *in vivo* experiments to access specificity, efficacy, and safety, the multifunctional theranostic agent ability was demonstrated.

Radionuclide imaging is another strategy that combines high sensitivity and unlimited tissue penetration. It can be associated with imaging to monitor disease development. Usually, the half-life of the selected PET isotope matches the time necessary for imaging,[328,329] with the necessity of producing a high signal-to-background ratio at a target localization. For tumor imaging, copper-64 or zirconium-89 are normally used with systemic injection of an intact antibody to maximize the tumor-to-background ratio. Fluorine-18 is also a good radioisotope, which is already used in the clinic ([^{18}F]FDG). However, ^{18}F radiochemistry can be hard to manipulate at the radiochemical level, and ^{18}F radiochemistry involved a covalent bond.[330−333] DOTA, on the other hand, involves coordination chemistry, and it is quite easy to use the same platform for different radionuclides and different imaging techniques, for example, copper-64 and gallium-68 for PET, indium-111 for SPECT, and yttrium-90 for radiotherapy. The versatility of DOTA provides an ideal system, where different imaging techniques can be applied to a single platform.

Another significant consideration when selecting a PET radionuclide is the time frame associated with the targeted biological event. In other words, the half-life of the positron-emitting radionuclide must fit with the biological event; otherwise, the results may be misleading and the imaging may not provide answers. For example, copper-64 possesses a half-life of 12.7 h, ideal for tracking monoclonal antibodies over a period of 48 h, while fluoride-18 with a half-life of 110 min can be used to trace fast clearance molecules.[334] Therefore, radioisotopes such as carbon-11, fluoride-18, copper-64, bromide-76, technetium-99m, indium-111, and yttrium-90 have been utilized along with various copolymers, in view to develop robust nanodelivery systems.[335−337]

If we take into consideration the already mentioned impact of hypoxia on tumor progression, metastatic spread, absence of tumor control, amplified recurrence phenomena, and poor therapeutic outcome, then imaging hypoxia is a step forward. As opposed to other noninvasive techniques, PET imaging offers specificity for the detection of hypoxic tissues. In this regard, the first compounds to address the imaging of hypoxia tissues were developed in the early 1980s.[338] They consist of 2-nitroimidazole derivatives linked to multiple PET tracers (Figure 21).

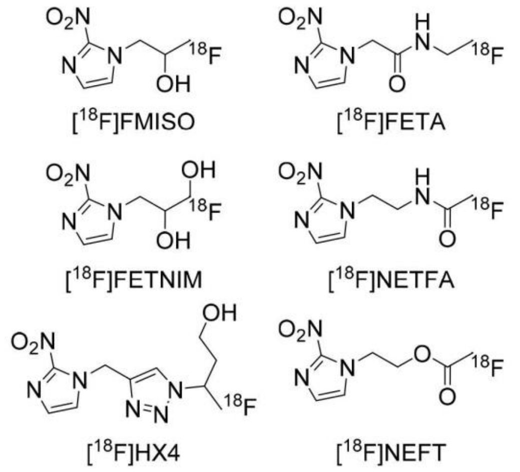

Figure 21. Structures of known [^{18}F]-based 2-nitroimidazole derivatives.

The main idea behind these [^{18}F]-based 2-nitroimidazole derivatives is to have a stable compound showing high specificity for imaging hypoxia without the inconsistent correlation that is often associated with other imaging techniques like PET with [^{18}F]-fluorodeoxyglucose ([^{18}F]FDG). The most common PET tracer for hypoxia imaging is the fluorinated nitroimidazole derivative [^{18}F]-fluoromisonidazole ([^{18}F]FMISO).[338,339] Like other compounds in the nitroimidazole family, [^{18}F]FMISO can diffuse passively through cell membranes due to its lipophilicity. Then, after internalization, the compound is reduced into R-NO_2 radicals by the nitroreductase enzyme (NTR). This process remains reversible, meaning the tracer will only stay in the cell under hypoxic conditions; otherwise, in the presence of oxygen, the tracer is released. As mentioned, in the absence of oxygen (pO_2 < 10 mmHg), the reduction process is much slower. Consequently, the increasing production of R-NHOH derivatives that bind directly to intracellular molecules ensures that the level of tracers inside cells is high.[340−343] However, the main drawbacks of [^{18}F]FMISO include the fact that passive transport requires 2−4 h after intravenous injection for [^{18}F]FMISO to accumulate to hypoxic tissues[344,345] and that, despite this uptake period, tracer accumulation remains low.[344,346]

Alternatively, among the non-nitroimidazole compounds, radioactive copper (copper-60, -61, -62, -64) labeled with diacetyl-bis(*N*4-methylthiosemicarbazone) [^{64}Cu]CuATSM) is another promising PET radiopharmaceutical for hypoxia imaging. First studied in 1997, the compound has shown suitability for the detection of hypoxia in living tissues.[250] However, the mechanism of uptake remains unclear. Nevertheless, it is known that [^{64}Cu]CuATSM is a neutral lipophilic molecule, which is easily crossing membranes by passive diffusion.[340] Fujibayashi et al. suggested that, after internalization, the accumulation in tumor cells mainly depends on the cytosolic/microsomal bioreduction process.[347] The bivalent [^{64}Cu]Cu(II)-ATSM, once inside cells, undergoes a thiol reduction and is converted to the less stable Cu(I) complex [^{64}Cu]Cu(I)-ATSM.[348] In hypoxic conditions, this complex is progressively dissociated into H_2-ATSM and free Cu(I), which can rapidly coordinate to proteins.[250,347−349]

It is, therefore, plausible that copper itself plays a major role in the [^{64}Cu]CuATSM entrapment. In order to verify this hypothesis, Hueting et al. analyzed the *in vitro* and *in vivo* distribution of [^{64}Cu]CuATSM and [^{64}Cu]CuOAc in animal models (EMT6 and CaNT).[248] The study shows that both copper tracers accumulate in similar fashion in tissues, confirming that copper metabolism takes part in the activity of [^{64}Cu]CuATSM.

Hypoxia for cancer patients is very important, and the development of prognostic biomarkers for hypoxia can make a huge difference in the success or failure of a treatment. Additionally, identifying hypoxia *in vivo* without any intrusive intervention may facilitate its use in the clinic. Nonetheless, determining the best tracer for this purpose remains difficult. While some data suggest that [^{18}F]FMISO is an excellent candidate, a suboptimal imaging limitation remains. On the other hand, high PET image quality favored the use of [^{64}Cu]CuATSM. Besides, when directly compared to the principal 2-nitroimidazole family representative ([^{18}F]-FMISO), [^{64}Cu]CuATSM uptake is significantly better in hypoxic tissues than in other areas, and it reaches its target more rapidly (10−15 min versus 2−4 h).[259] It is clear that these achievements are important and can potentially generate better theranostic-PDT agents.

Even though the outlook for imaging seems encouraging, obstacles remain high for commercial applications. In fact, both imaging agent development and standard drug discovery and development share much in common, especially those binding to a specific target *in vivo*. Both must overcome several challenges when it comes to factors such as target authentication, identification of the best possible candidate, showing high affinity and selectivity, as well as good clearance, and low toxicity.[350]

The impact of a therapeutic intervention is difficult to evaluate in cancer treatment, which makes the validation of molecular imaging biomarkers difficult when compared to existing surrogate markers. A quantitative assessment through imaging can help to determine the real impact of a new treatment (complete or partial response), and it can provide information on the progression of the disease.[351] PET/CT and other hybrid imaging modalities, by overlaying different images, allow the determination of the therapeutic effect with PET and the size of the tumor with CT.[352]

Another challenge is the need to understand the drug's mechanism of action when integrating PET or SPECT into clinical research. For example, [^{18}F]FDG PET may help to identify downstream effects at an early stage of cancer development, even before tumor shrinkage. Routine clinical use of [^{18}F]FDG PET involves static imaging 2 h post-injection, which can be useful if we only want the localization of tumors and metastases. On the other hand, if we are intent to perform dynamic imaging, the recollection of PET data from the initial injection of [^{18}F]FDG will give direct access to pharmacokinetics and pharmacodynamics information on the tracer, which can be very important for better understanding how drugs and therapies work in real time.[353] This example illustrates the careful planning and deep understanding that is required of all of the processes involved when trying to perform the imaging of cancer and how they can limit or help each other.

We can, by this, conclude that the similarities between the processes of developing therapeutic drugs and diagnostic agents make their simultaneous development into theranostic agents even more challenging. At the same time, technologies and development from one domain can accelerate the development processes of the other (PET microdosing, for example). Finally, the development of new drugs incorporating tracers and imaging biomarkers can also contribute to the emergence of theranostic agents.[350]

6. OUR CONTRIBUTIONS

As it can be understood from this review, there is an urgent need for new drugs and practices to treat cancer. Photodynamic therapy (PDT) imposes itself as one of the most preponderant voices to answer this demand. With the combination of a photosensitizer, light, and oxygen, PDT achieves a unique selectivity by the production of localized reactive oxygen species inside tumor cells, which leads to their destruction with limited side effects.[354] Our approach aims to use cellulose nanocrystals to transport and deliver radiolabeled photoresponsive molecules to biological targets and create new theranostic agents.

In order to achieve our goal of using these cellulose-metal-porphyrin assemblies and to trace them using SPECT imaging, several steps have been taken so far. First, we have prepared and characterized CNCs[355] as well as photoresponsive molecules through stoichiometric quantities of aldehydes and pyrrole in propionic acid (Scheme 4).[356] Then metalla-assemblies were obtained using inorganic metalla-clips under a well-developed methodology.[357] The last step was to load these metalla-assemblies to nanocrystals by dissolution in methanol, adding them dropwise to the CNC solution and leaving it to react for 24 h.[355] Derivatives of the 5,10,15,20-tetra(4-pyridyl)-21*H*,23*H*-porphine were chosen as photoresponsive molecules, due to their ability to simultaneously be linked to the cellulose nanocrystals (CNC) and coordinated to ruthenium. Even though different grafting methods were explored, the best results were achieved through the covalent amide binding of the photosensitizer and the CNC.

Scheme 4. Synthesis of Cellulose-Metallo-Porphyrin Theranostic Agents

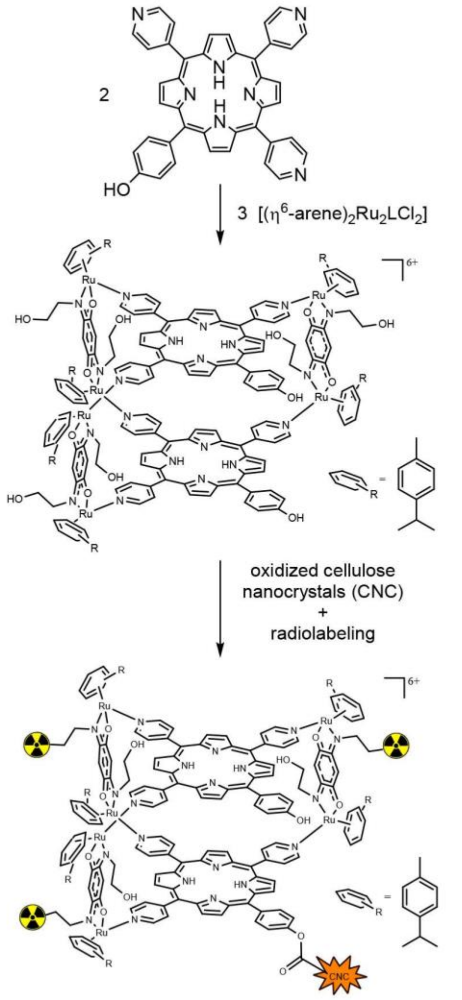

Labeling of CNC with the nonradioactive metallic isotope has also been explored, and the radiolabeling experiments will follow shortly. A full set of *in vitro* assays with the nonradioactive derivatives will be performed to determine the IC_{50} and the influence of the cage and CNC to cells. Following the *in vitro* study, *in vivo* imaging will be conducted, and the data will be processed and statistically analyzed.

Our preliminary results are very promising regarding the synthesis of a multimodal agent that combines a photosensitizer for PDT treatment and a radioactive agent for imaging (before, during, and after the process), thus aiming to develop an innovative theranostic agent. The conjugation with cellulose nanocrystals and coordination to inorganic entities intend to ameliorate their delivery, solubility, and metabolism.

7. CONCLUSIONS

The importance of PDT in the treatment of cancers as well as nononcological diseases is growing rapidly. However, despite increasing reports showing the benefits of PDT over traditional treatments, extensive use in the clinics remains to be seen. This limited utilization of PDT in the clinics is due to different factors, some linked to the pharmaceutical formulations of PDT agents (solubility, administration, aggregation, selectivity) and some to the technology involved (instrument, light source, etc.).

For more than 20 years, researchers have focused on developing safer and more effective PDT agents not only to cure cancers but also to be used in many other domains.[358] During that period, the clinical success of PDT for the treatment of head and neck cancers is undeniable, showing an increased survival rate of patients with such cancers, as well as an improved quality of life. Similarly, the cure of some early stage tumors, precancerous lesions, and nonmelanoma skin cancers has been enormously effective.[7] In addition, the association of PDT to NPs technology has offered new solutions and new perspectives to further develop the field of photodynamic therapy.

Photodynamic treatment (PDT) is and should be considered a therapy with promising outcomes for the treatment of different diseases, the most studied one being cancer. This treatment depends on the impacts of light conveyed to photosensitized cells. Therefore, adding molecular imaging to PDT treatment is crucial and keeps on expanding, from disease detection, treatment planning, to real-time monitoring and its outcome evaluation. While there has been impressive progress over the past decade, to be successful in the clinic, numerous technical difficulties must be investigated and ameliorated, for example, the requirement of imaging probes to precisely recognize the spatial and temporal occurrence of specific cell death processes. As cancer is proliferating fast, innovative diagnostic and therapeutic strategies are imperative for early detection and precision treatment. In addition, to optimize the therapeutic outcome of PDT, an evaluation of the local microenvironment before treatment is essential. For example, as photosensitizers (PSs) need oxygen to operate, the presence or absence of O_2 is crucial for the production of toxic reactive oxygen species (ROS), according to PDT treatment. Therefore, without specific information on local O_2 concentrations during PDT treatments, the effectiveness of treatments can fluctuate greatly. Moreover, due to O_2 consumption during PDT treatments, the oxygen level needs to be continuously maintained to ensure efficacy. Thus, measuring O_2 levels in real time during PDT treatments has become one of the main challenges for the future of PDT.

So far, multiple sensors have been used to monitor O_2 concentrations in biological media, thus providing convenient imaging tools for refining cancer diagnosis and improving therapeutic efficiency. However, the combination of an imaging agent with a photosensitizer to generate a theranostic O_2 sensory platform for image-guided PDT has been rarely reported.[359] In the clinic, PET imaging has become one of the most effective tools to visualize tumor hypoxia in patients. It has been used clinically on various cancer types with different radiotracers. It is now well-documented; PET imaging can increase treatment response and optimize radiotherapy plans. OFI and PET as double-modality contrasting agents have proven to be an excellent combination. The OFI/PET systems show low toxicity, and they possess high spatial and long temporal resolutions.[206]

In summary, multimodal imaging presents itself as a powerful tool to make an accurate picture of diseased sites. The accumulation and retention of nanoparticles in real time can be quantified by PET imaging, while OFI imaging can provide other information at a cellular/molecular level. Together, they can validate and optimize treatments without being too expensive. Therefore, the emergence of integrated diagnostic and therapeutic agents in a single system is a valuable strategy to develop new therapeutic combinations in PDT.

■ AUTHOR INFORMATION

Corresponding Authors

Bruno Therrien – *Institute of Chemistry, University of Neuchatel, CH-2000 Neuchatel, Switzerland;* orcid.org/0000-0002-0388-2745; Email: bruno.therrien@unine.ch

George Loudos – *BioEmission Technology Solutions, 11472 Athens, Greece;* Email: george@bioemtech.com

Authors

João C. S. Simões – *Institute of Chemistry, University of Neuchatel, CH-2000 Neuchatel, Switzerland; BioEmission Technology Solutions, 11472 Athens, Greece*

Sophia Sarpaki – *BioEmission Technology Solutions, 11472 Athens, Greece*

Panagiotis Papadimitroulas – *BioEmission Technology Solutions, 11472 Athens, Greece*

Complete contact information is available at: https://pubs.acs.org/10.1021/acs.jmedchem.0c00047

Author Contributions

The manuscript was written through contributions of all authors. All authors have given approval to the final version of the manuscript.

Funding

This project has received financial support from the European Union's Horizon 2020 research and innovation program under the Marie Sklodowska-Curie grant agreement no. 764837.

Notes

The authors declare no competing financial interest.

Biographies

João C. S. Simões was born in Coimbra, Portugal. He concluded his Bachelor's in 2016 and Master's in 2018, both at the University of Coimbra in Medicinal Chemistry. His Master's thesis consisted of "Novel Ring-Fused Chlorins as Promising PDT Agents against Cancer". Currently, he is an Early Stage Researcher within the POLYTHEA project, in a Marie Curie Innovative Training Network, which aims for the design, photo-optimization, and biological evaluation of photosensitizers for human health and food security applications.

Sophia Sarpaki is a radiopharmaceutical chemist and obtained her Ph.D. diploma from the Chemistry Department of Bath University, on "Investigations into the Radiochemistry of Gallium- and Fluorine-Containing Compounds for Molecular Imaging Applications". She holds the FELASSA certification for small animal handling. She works as a researcher and project manager on research preclinical imaging projects at BIOEMETCH. Her expertise lies in developing radiolabeling protocols for small molecules, biomolecules, and nanostructures, executing their necessary chemical analysis and performing their *in vivo* evaluation. Her scientific interest has a strong focus on cancer research, but she is also involved with projects related to cardiovascular diseases and stem cell therapy. She has participated in a variety of international research projects under the framework of EuroNanoMed, H2020, and ERC.

Panagiotis Papadimitroulas is cofounder and Project Director of BIOEMTECH (www.bioemtech.com) since 2013. He holds a Ph.D. in Medical Physics (2015) awarded by the University of Patras. He has extensive expertise in the evaluation and optimization of clinical and preclinical dosimetry protocols, in Monte Carlo simulations, image processing tools, and advanced computational models. Since 2019, he gained a Post-Doc Research Grant from the State Scholarships Foundation (IKY). He authored 2 chapter books related to internal dosimetry and computational tools, 18 publications in peer-review journals, and more than 60 announcements in international/national conferences. He has participated in more than 15 international and national research projects under the framework of FP7, COST, H2020, ERANET, NSRF. Since 2017, he is an official member of the OpenGATE collaboration.

Bruno Therrien is an Associate professor at the University of Neuchatel, Switzerland. He studied chemistry at the University of Montreal and obtained his Ph.D. in 1998 from the University of Bern, Switzerland. After his Ph.D., he undertook several postdoctoral positions (Weizmann Institute, Massey University, Tokyo University), before returning to Switzerland. His main research interests are supramolecular chemistry and the biological applications of metalla-assemblies.

George Loudos is an Assistant Professor at the University of West Attica Athens and CEO and cofounder of BIOEMTECH. He has participated as a coordinator or partner in more than 15 EU projects, as well as two National Excellence grants and several smaller national and other projects. He has published over 120 articles in international journals and has >250 publications in conference proceedings and ~1350 citations. He has given 60 invited lectures and holds one patent. He has been the organizer of many international conferences, workshops, and training schools. His research interests are focused on molecular imaging of nanoparticles and other biomolecules using nuclear medicine techniques, medical instrumentation, and he strongly supports interdisciplinary cooperation and education in the field of nanomedicine and molecular imaging.

■ ABBREVIATIONS USED

AFP, hepatocellular carcinoma markers; aPS, activatable photosensitizer; Arg, arginine; Asp, aspartate; AuNPs, gold nanoapricles; BODIPY, boron-dipyrromethene; BOLD, blood oxygen-dependent level; BP, benzoporphyrin derivative; BPD-MA, benzoporphyrin derivative monoacid; C225, EGFR antibody; CA125, ovarian cancer marker; CA153, breast tumor marker; CA199, gastrointestinal tumor marker; CA242, gastrointestinal tumor marker; CA724, gastrointestinal tumor marker; CA-IX, (HIF)-1 regulated carbonic anhydrase-IX receptor; CAT, catalase; Ce6, chlorin e6; CEA, lung cancer tumor marker; CNC, cellulose nanocrystals; CT, computer tomography; Cu-ATSM, Diacetylbis(*N*(4)-methylthiosemicarbazonato) copper(II); Cyfra21–1, lung cancer tumor marker; DBP-UiO, Hf–porphyrin nanoscale metal–organic framework; DLI, drug to light interval; DOTA, 1,4,7,10-tetraazacyclododecane-1,4,7,10-tetraacetic acid; DOX, doxorubicin; DPP, diketopyrrolopyrrole; EGFR, epidermal growth factor receptor; EPR, enhanced permeability and a retention effect; FA, folic acid; FGR, fluorescence-guided resection; FMISO, fluoromisonidazole; FR, folate receptors; FRET, fluorescence resonance energy transfer; GLUT, glucose transporters; Gly, glycine; HCG, choriocarcinoma marker; HeLa, immortal cell line derived from cervical cancer cells; HIF, hypoxia-inducible factors; HpD, hematoporphyrin derivative; HSiNP, hollow SiNPs; ICG, indocyanine green;

ISC, intersystem crossing; LDL, low density lipoprotein; MDR, multidrug resistance; MOF, metal−organic frameworks; MRI, magnetic resonance imaging; MSiNP, metal SiNPs; NI, nitrimidazole; NI-CP, (NI)-conjugated dithiophene-benzotriazole-containing polymer; NIR, near-infrared; NMI, nuclear medical imaging; NOTA, 1,4,7-triazacyclononane-1,4-diacetic acid; NP, nanoparticle; NSE, lung cancer tumor marker; OFI, optical fluorescence imaging; PAA, polyacrylamide; Pc, phthalocyanine; PDD, photodynamic diagnosis; PDT, photodynamic therapy; PEG, polyethylene glycol; PET, positron emission tomography; PIC, photimmunoconjugate; PLGA, poly(lactic-*co*-glycolic acid; PPIX, protoporphyrin IX; PS, photosensitizer; PSA, prostate cancer marker; Q, quencher particle; QD, quantum dots; QY, quantum yield; RGD, arginylglycylaspartic acid; ROS, reactive oxygen species; SiNP, silica nanoparticles; SK-BR-3, human breast cancer cell line; SPECT, single-photon emission computed tomography; THPP, tris(3-hydroxypropyl)phosphine; TPC, 5-[4carboxyphenyl]-10,15,20-triphenyl-2,3-dihydroxychlorin; TR, transferrin receptor.

■ REFERENCES

(1) McGuire, S. World Cancer Report 2014. *Adv. Nutr.* **2016**, *7*, 418−419.

(2) Jin, G.; He, R.; Liu, Q.; Dong, Y.; Lin, M.; Li, W.; Xu, F. Theranostics of Triple-Negative Breast Cancer Based on Conjugated Polymer Nanoparticles. *ACS Appl. Mater. Interfaces* **2018**, *10*, 10634−10646.

(3) Srivatsan, A.; Missert, J. R.; Upadhyay, S. K.; Pandey, R. K. Porphyrin-Based Photosensitizers and the Corresponding Multifunctional Nanoplatforms for Cancer-Imaging and Phototherapy. *J. Porphyrins Phthalocyanines* **2015**, *19*, 109−134.

(4) Evans, C. L.; Rizvi, I.; Hasan, T.; Boer, J. F. de. Vitro Ovarian Tumor Growth and Treatment Response Dynamics Visualized With Time-Lapse OCT Imaging. *Opt. Express* **2009**, *17*, 8892.

(5) Georgakoudi, I.; Solban, N.; Novak, J.; Rice, W. L.; Wei, X.; Hasan, T.; Lin, C. P. In Vivo Flow Cytometry: A New Method for Enumerating Circulating Cancer Cells. *Cancer Res.* **2004**, *64*, 5044−5047.

(6) Solban, N.; Pal, S. K.; Alok, S. K.; Sung, C. K.; Hasan, T. Mechanistic Investigation and Implications of Photodynamic Therapy Induction of Vascular Endothelial Growth Factor in Prostate Cancer. *Cancer Res.* **2006**, *66*, 5633−5640.

(7) Abrahamse, H.; Hamblin, M. R. New Photosensitizers for Photodynamic Therapy. *Biochem. J.* **2016**, *473*, 347−364.

(8) Gibbs-Strauss, S. L. Noninvasive Measurement of Aminolevulinic Acid-Induced Protoporphyrin IX Fluorescence Allowing Detection of Murine Glioma in Vivo. *J. Biomed. Opt.* **2009**, *14*, 014007.

(9) Soukos, N. S.; Hamblin, M. R.; Keel, S.; Fabian, R. L.; Deutsch, T. F.; Hasan, T. Epidermal Growth Factor Receptor-Targeted Immunophotodiagnosis and Photoimmunotherapy of Oral Precancer in Vivo. *Cancer Res.* **2001**, *61*, 4490−4496.

(10) Zheng, X.; Sallum, U. W.; Verma, S.; Athar, H.; Evans, C. L.; Hasan, T. Exploiting a Bacterial Drug-Resistance Mechanism: A Light-Activated Construct for the Destruction of MRSA. *Angew. Chem., Int. Ed.* **2009**, *48*, 2148−2151.

(11) Zhong, W.; Celli, J. P.; Rizvi, I.; Mai, Z.; Spring, B. Q.; Yun, S. H.; Hasan, T. In Vivo High-Resolution Fluorescence Microendoscopy for Ovarian Cancer Detection and Treatment Monitoring. *Br. J. Cancer* **2009**, *101*, 2015−2022.

(12) Li, Y.; Wang, J.; Zhang, X.; Guo, W.; Li, F.; Yu, M.; Kong, X.; Wu, W.; Hong, Z. Highly Water-Soluble and Tumor-Targeted Photosensitizers for Photodynamic Therapy. *Org. Biomol. Chem.* **2015**, *13*, 7681−7694.

(13) Celli, J. P.; Spring, B. Q.; Rizvi, I.; Evans, C. L.; Samkoe, K. S.; Verma, S.; Pogue, B. W.; Hasan, T. Imaging and Photodynamic Therapy: Mechanisms, Monitoring, and Optimization. *Chem. Rev.* **2010**, *110*, 2795−2838.

(14) Kharroubi Lakouas, D.; Huglo, D.; Mordon, S.; Vermandel, M. Nuclear Medicine for Photodynamic Therapy in Cancer: Planning, Monitoring and Nuclear PDT. *Photodiagn. Photodyn. Ther.* **2017**, *18*, 236−243.

(15) Jokerst, J. V.; Lobovkina, T.; Zare, R. N.; Gambhir, S. S. Nanoparticle PEGylation for Imaging and Therapy. *Nanomedicine* **2011**, *6*, 715−728.

(16) Crawley, N.; Thompson, M.; Romaschin, A. Theranostics in the Growing Field of Personalized Medicine: An Analytical Chemistry Perspective. *Anal. Chem.* **2014**, *86*, 130−160.

(17) Kelkar, S. S.; Reineke, T. M. Theranostics: Combining Imaging and Therapy. *Bioconjugate Chem.* **2011**, *22*, 1879−1903.

(18) Terreno, E.; Uggeri, F.; Aime, S. Image Guided Therapy: The Advent of Theranostic Agents. *J. Controlled Release* **2012**, *161*, 328−337.

(19) Yoon, H. Y.; Jeon, S.; You, D. G.; Park, J. H.; Kwon, I. C.; Koo, H.; Kim, K. Inorganic Nanoparticles for Image-Guided Therapy. *Bioconjugate Chem.* **2017**, *28*, 124−134.

(20) Jenni, S.; Sour, A. Molecular Theranostic Agents for Photodynamic Therapy (PDT) and Magnetic Resonance Imaging (MRI). *Inorganics* **2019**, *7*, 10.

(21) Dougherty, T. J. Hematoporphyrin Derivative for Detection and Treatment of Cancer. *J. Surg. Oncol.* **1980**, *15*, 209−210.

(22) Allison, R. R. Photodynamic Therapy: Oncologic Horizons. *Future Oncol.* **2014**, *10*, 123−142.

(23) Calin, M. A.; Parasca, S. V. Photodynamic Therapy in Oncology. *J. Optoelectron. Adv. Mater.* **2006**, *8*, 1173−1179.

(24) Verma, S.; Watt, G. M.; Mai, Z.; Hasan, T. Strategies for Enhanced Photodynamic Therapy Effects. *Photochem. Photobiol.* **2007**, *83*, 996−1005.

(25) Spring, B. Q.; Abu-Yousif, A. O.; Palanisami, A.; Rizvi, I.; Zheng, X.; Mai, Z.; Anbil, S.; Sears, R. B.; Mensah, L. B.; Goldschmidt, R.; Erdem, S. S.; Oliva, E.; Hasan, T. Selective Treatment and Monitoring of Disseminated Cancer Micrometastases in Vivo Using Dual-Function, Activatable Immunoconjugates. *Proc. Natl. Acad. Sci. U. S. A.* **2014**, *111*, E933−E942.

(26) Chilakamarthi, U.; Giribabu, L. Photodynamic Therapy: Past, Present and Future. *Chem. Rec.* **2017**, *17*, 775−802.

(27) Juarranz, Á.; Jaén, P.; Sanz-Rodríguez, F.; Cuevas, J.; González, S. Photodynamic Therapy of Cancer. Basic Principles and Applications. *Clin. Transl. Oncol.* **2008**, *10*, 148−154.

(28) Huang, P.; Lin, J.; Wang, S.; Zhou, Z.; Li, Z.; Wang, Z.; Zhang, C.; Yue, X.; Niu, G.; Yang, M.; Cui, D.; Chen, X. Photosensitizer-Conjugated Silica-Coated Gold Nanoclusters for Fluorescence Imaging-Guided Photodynamic Therapy. *Biomaterials* **2013**, *34*, 4643−4654.

(29) Chen, R.; Zhang, L.; Gao, J.; Wu, W.; Hu, Y.; Jiang, X. Chemiluminescent Nanomicelles for Imaging Hydrogen Peroxide and Self-Therapy in Photodynamic Therapy. *J. Biomed. Biotechnol.* **2011**, *2011*, 1.

(30) Iranifam, M. Analytical Applications of Chemiluminescence Methods for Cancer Detection and Therapy. *TrAC, Trends Anal. Chem.* **2014**, *59*, 156−183.

(31) Laptev, R.; Nisnevitch, M.; Siboni, G.; Malik, Z.; Firer, M. A. Intracellular Chemiluminescence Activates Targeted Photodynamic Destruction of Leukaemic Cells. *Br. J. Cancer* **2006**, *95*, 189−196.

(32) Theodossiou, T.; Hothersall, J. S.; Woods, E. A.; Okkenhaug, K.; Jacobson, J.; MacRobert, A. J. Firefly Luciferin-Activated Rose Bengal: In Vitro Photodynamic Therapy by Intracellular Chemiluminescence in Transgenic NIH 3T3 Cells. *Cancer Res.* **2003**, *63*, 1818−1821.

(33) Calixto, G.; Bernegossi, J.; de Freitas, L.; Fontana, C.; Chorilli, M. Nanotechnology-Based Drug Delivery Systems for Photodynamic Therapy of Cancer: A Review. *Molecules* **2016**, *21*, 342.

(34) Agostinis, P.; Berg, K.; Cengel, K. A.; Foster, T. H.; Girotti, A. W.; Gollnick, S. O.; Hahn, S. M.; Hamblin, M. R.; Juzeniene, A.; Kessel, D.; Korbelik, M.; Moan, J.; Mroz, P.; Nowis, D.; Piette, J.;

Wilson, B. C.; Golab, J. Photodynamic Therapy of Cancer: An Update. *Ca-Cancer J. Clin.* **2011**, *61*, 250−281.

(35) Zheng, Y.; Yin, G.; Le, V.; Zhang, A.; Lu, Y.; Yang, M.; Fei, Z.; Liu, J. Hypericin-Based Photodynamic Therapy Induces a Tumor-Specific Immune Response and an Effective DC-Based Cancer Immunotherapy. *Biochem. Pharmacol.* **2014**, 1.

(36) Theodossiou, T. A.; Hothersall, J. S.; De Witte, P. A.; Pantos, A.; Agostinis, P. The Multifaceted Photocytotoxic Profile of Hypericin. *Mol. Pharmaceutics* **2009**, *6*, 1775−1789.

(37) Liu, X.; Jiang, C.; Li, Y.; Liu, W.; Yao, N.; Gao, M.; Ji, Y.; Huang, D.; Yin, Z.; Sun, Z.; Ni, Y.; Zhang, J. Evaluation of Hypericin: Effect of Aggregation on Targeting Biodistribution. *J. Pharm. Sci.* **2015**, *104*, 215−222.

(38) Ghosh, S.; Banerjee, S.; Sil, P. C. The Beneficial Role of Curcumin on Inflammation, Diabetes and Neurodegenerative Disease: A Recent Update. *Food Chem. Toxicol.* **2015**, *83*, 111−124.

(39) Wikene, K. O.; Hegge, A. B.; Bruzell, E.; Tonnesen, H. H. Formulation and Characterization of Lyophilized Curcumin Solid Dispersions for Antimicrobial Photodynamic Therapy (Apdt): Studies on Curcumin and Curcuminoids LII. *Drug Dev. Ind. Pharm.* **2015**, *41*, 969−977.

(40) Bernd, A. Visible Light And/Or UVA Offer a Strong Amplification of the Anti-Tumor Effect of Curcumin. *Phytochem. Rev.* **2014**, *13*, 183−189.

(41) Leite, D. P. V.; Paolillo, F. R.; Parmesano, T. N.; Fontana, C. R.; Bagnato, V. S. Effects of Photodynamic Therapy With Blue Light and Curcumin as Mouth Rinse for Oral Disinfection: A Randomized Controlled Trial. *Photomed. Laser Surg.* **2014**, *32*, 627−632.

(42) Li, T.; Hou, X.; Deng, H.; Zhao, J.; Huang, N.; Zeng, J.; Chen, H.; Gu, Y. Liposomal Hypocrellin B as a Potential Photosensitizer for Age-Related Macular Degeneration: Pharmacokinetics, Photodynamic Efficacy, and Skin Phototoxicity in Vivo. *Photochem. Photobiol. Sci.* **2015**, *14*, 972−981.

(43) Zhenjun, D.; Lown, J. W. Hypocrellins and Their Use in Photosensitization. *Photochem. Photobiol.* **1990**, *52*, 609−616.

(44) Makdoumi, K.; Bäckman, A.; Mortensen, J.; Crafoord, S. Evaluation of Antibacterial Efficacy of Photo-Activated Riboflavin Using Ultraviolet Light (UVA). *Graefe's Arch. Clin. Exp. Ophthalmol.* **2010**, *248*, 207−212.

(45) Ettinger, A.; Miklauz, M. M.; Bihm, D. J.; Maldonado-Codina, G.; Goodrich, R. P. Preparation of Cryoprecipitate from Riboflavin and UV Light-Treated Plasma. *Transfus. Apher. Sci.* **2012**, *46*, 153−158.

(46) Papaioannou, L.; Miligkos, M.; Papathanassiou, M. Corneal Collagen Cross-Linking for Infectious Keratitis: A Systematic Review and Meta-Analysis. *Cornea* **2016**, *35*, 62−71.

(47) Maisch, T.; Eichner, A.; Späth, A.; Gollmer, A.; König, B.; Regensburger, J.; Bäumler, W. Fast and Effective Photodynamic Inactivation of Multiresistant Bacteria by Cationic Riboflavin Derivatives. *PLoS One* **2014**, *9*, e111792.

(48) Wainwright, M.; Crossley, K. B. Methylene Blue - a Therapeutic Dye for All Seasons? *J. Chemother.* **2002**, *14*, 431−443.

(49) Tseng, S. P.; Hung, W. C.; Chen, H. J.; Lin, Y. T.; Jiang, H. S.; Chiu, H. C.; Hsueh, P. R.; Teng, L. J.; Tsai, J. C. Effects of Toluidine Blue O (Tbo)-Photodynamic Inactivation on Community-Associated Methicillin-Resistant Staphylococcus Aureus Isolates. *J. Microbiol. Immunol. Infect.* **2017**, *50*, 46−54.

(50) Tardivo, J. P.; Adami, F.; Correa, J. A.; Pinhal, M. A. S.; Baptista, M. S. A Clinical Trial Testing the Efficacy of PDT in Preventing Amputation in Diabetic Patients. *Photodiagn. Photodyn. Ther.* **2014**, *11*, 342−350.

(51) Graciano, T. B.; Coutinho, T. S.; Cressoni, C. B.; Freitas, C. de P.; Pierre, M. B. R.; de Lima Pereira, S. A.; Shimano, M. M.; Cristina da Cunha Frange, R.; Garcia, M. T. J. Using Chitosan Gels as a Toluidine Blue O Delivery System for Photodynamic Therapy of Buccal Cancer: In Vitro and in Vivo Studies. *Photodiagn. Photodyn. Ther.* **2015**, *12*, 98−107.

(52) Costa, A. C. B. P.; Rasteiro, V. M. C.; Pereira, C. A.; Rossoni, R. D.; Junqueira, J. C.; Jorge, A. O. C. The Effects of Rose Bengal- and Erythrosine-Mediated Photodynamic Therapy on Candida Albicans. *Mycoses* **2012**, *55*, 56−63.

(53) Xu, N.; Yao, M.; Farinelli, W.; Hajjarian, Z.; Wang, Y.; Redmond, R. W.; Kochevar, I. E. Light-Activated Sealing of Skin Wounds. *Lasers Surg. Med.* **2015**, *47*, 17−29.

(54) Panzarini, E.; Inguscio, V.; Fimia, G. M.; Dini, L. Rose Bengal Acetate PhotoDynamic Therapy (RBAc-PDT) Induces Exposure and Release of Damage-Associated Molecular Patterns (DAMPs) in Human HeLa Cells. *PLoS One* **2014**, *9*, e105778.

(55) Boens, N.; Leen, V.; Dehaen, W. Fluorescent Indicators Based on Bodipy. *Chem. Soc. Rev.* **2012**, *41*, 1130−1172.

(56) Kamkaew, A.; Lim, S. H.; Lee, H. B.; Kiew, L. V.; Chung, L. Y.; Burgess, K. BODIPY Dyes in Photodynamic Therapy. *Chem. Soc. Rev.* **2013**, *42*, 77−88.

(57) Segado, M.; Reguero, M. Mechanism of the Photochemical Process of Singlet Oxygen Production by Phenalenone. *Phys. Chem. Chem. Phys.* **2011**, *13*, 4138.

(58) Cieplik, F.; Späth, A.; Regensburger, J.; Gollmer, A.; Tabenski, L.; Hiller, K. A.; Bäumler, W.; Maisch, T.; Schmalz, G. Photodynamic Biofilm Inactivation by SAPYR - an Exclusive Singlet Oxygen Photosensitizer. *Free Radical Biol. Med.* **2013**, *65*, 477−487.

(59) Späth, A.; Leibl, C.; Cieplik, F.; Lehner, K.; Regensburger, J.; Hiller, K. A.; Bäumler, W.; Schmalz, G.; Maisch, T. Improving Photodynamic Inactivation of Bacteria in Dentistry: Highly Effective and Fast Killing of Oral Key Pathogens With Novel Tooth-Colored Type-II Photosensitizers. *J. Med. Chem.* **2014**, *57*, 5157−5168.

(60) Gill, M. R.; Thomas, J. A. Ruthenium(II) Polypyridyl Complexes and DNA - From Structural Probes to Cellular Imaging and Therapeutics. *Chem. Soc. Rev.* **2012**, *41*, 3179−3192.

(61) Fong, J.; Kasimova, K.; Arenas, Y.; Kaspler, P.; Lazic, S.; Mandel, A.; Lilge, L. A Novel Class of Ruthenium-Based Photosensitizers Effectively Kills In Vitro Cancer Cells and In Vivo Tumors. *Photochem. Photobiol. Sci.* **2015**, *14*, 2014−2023.

(62) Angeles-Boza, A. M.; Bradley, P. M.; Fu, P. K. L.; Wicke, S. E.; Bacsa, J.; Dunbar, K. R.; Turro, C. Dna Binding and Photocleavage in Vitro by New Dirhodium(II) Dppz Complexes: Correlation to Cytotoxicity and Photocytotoxicity. *Inorg. Chem.* **2004**, *43*, 8510−8519.

(63) Li, Y.; Tan, C.-P.; Zhang, W.; He, L.; Ji, L.-N.; Mao, Z.-W. Phosphorescent Iridium(III)-Bis-N-Heterocyclic Carbene Complexes as Mitochondria-Targeted Theranostic and Photodynamic Anticancer Agents. *Biomaterials* **2015**, *39*, 95−104.

(64) To, W. P.; Zou, T.; Sun, R. W. Y.; Che, C. M. Light-Induced Catalytic and Cytotoxic Properties of Phosphorescent Transition Metal Compounds with a D8 Electronic Configuration. *Philos. Trans. R. Soc., A* **2013**, *371*, 20120126.

(65) Senge, M. O. MTHPC - A Drug on Its Way from Second to Third Generation Photosensitizer? *Photodiagnosis Photodyn. Photodiagn. Photodyn. Ther.* **2012**, *9*, 170−179.

(66) Anand, S.; Ortel, B. J.; Pereira, S. P.; Hasan, T.; Maytin, E. V. Biomodulatory Approaches to Photodynamic Therapy for Solid Tumors. *Cancer Lett.* **2012**, *326*, 8−16.

(67) Byrne, A. T.; O'Connor, A. E.; Hall, M.; Murtagh, J.; O'Neill, K.; Curran, K. M.; Mongrain, K.; Rousseau, J. A.; Lecomte, R.; McGee, S.; Callanan, J. J.; O'Shea, D. F.; Gallagher, W. M. Vascular-Targeted Photodynamic Therapy With BF2-Chelated Tetraaryl-Azadipyrromethene Agents: A Multi-Modality Molecular Imaging Approach to Therapeutic Assessment. *Br. J. Cancer* **2009**, *101*, 1565−1573.

(68) Huang, Z.; Xu, H.; Meyers, A. D.; Musani, A. I.; Wang, L.; Tagg, R.; Barqawi, A. B.; Chen, Y. K. Photodynamic Therapy for Treatment of Solid Tumors - Potential and Technical Challenges. *Technol. Cancer Res. Treat.* **2008**, *7* (4), 309−320.

(69) Foote, C. S. Mechanisms of Photosensitized Oxidation. *Science* **1968**, *162*, 963−970.

(70) Ormond, A. B.; Freeman, H. S. Dye Sensitizers for Photodynamic Therapy. *Materials* **2013**, *6*, 817−840.

(71) Pereira, N. A. M.; Serra, A. C.; Pinho e Melo, T. M. V. D. Novel Approach to Chlorins and Bacteriochlorins: [$8\pi+2\pi$] Cycloaddition

of Diazafulvenium Methides with Porphyrins. *Eur. J. Org. Chem.* **2010**, *2010*, 6539−6543.

(72) Forouzanfar, M. H.; et al. Global, Regional, and National Comparative Risk Assessment of 79 Behavioural, Environmental and Occupational, and Metabolic Risks or Clusters of Risks in 188 Countries, 1990−2013: A Systematic Analysis for the Global Burden of Disease Study 2013. *Lancet* **2015**, *386*, 2287−2323.

(73) Baskaran, R.; Lee, J.; Yang, S.-G. Clinical Development of Photodynamic Agents and Therapeutic Applications. *Biomater. Res.* **2018**, *22*, 1.

(74) Lovell, J. F.; Liu, T. W. B.; Chen, J.; Zheng, G. Activatable Photosensitizers for Imaging and Therapy. *Chem. Rev.* **2010**, *110*, 2839−2857.

(75) Derycke, A. S. L.; De Witte, P. A. M. Liposomes for Photodynamic Therapy. *Adv. Drug Delivery Rev.* **2004**, *56*, 17−30.

(76) Postigo, F.; Mora, M.; De Madariaga, M. A.; Nonell, S.; Sagristá, M. L. Incorporation of Hydrophobic Porphyrins Into Liposomes: Characterization and Structural Requirements. *Int. J. Pharm.* **2004**, *278*, 239−254.

(77) Park, W.; Park, S.-J.; Cho, S.; Shin, H.; Jung, Y.-S.; Lee, B.; Na, K.; Kim, D.-H. Intermolecular Structural Change for Thermoswitchable Polymeric Photosensitizer. *J. Am. Chem. Soc.* **2016**, *138*, 10734−10737.

(78) Lee, C. S.; Na, K. Photochemically Triggered Cytosolic Drug Delivery Using PH-Responsive Hyaluronic Acid Nanoparticles for Light-Induced Cancer Therapy. *Biomacromolecules* **2014**, *15*, 4228−4238.

(79) Kim, K.; Lee, C. S.; Na, K. Light-Controlled Reactive Oxygen Species (ROS)-Producible Polymeric Micelles with Simultaneous Drug-Release Triggering and Endo/Lysosomal Escape. *Chem. Commun.* **2016**, *52*, 2839−2842.

(80) Park, S.; Park, W.; Na, K. Tumor Intracellular-Environment Responsive Materials Shielded Nano-Complexes for Highly Efficient Light-Triggered Gene Delivery without Cargo Gene Damage. *Adv. Funct. Mater.* **2015**, *25*, 3472−3482.

(81) Jo, Y.-u.; Lee, C. B.; Bae, S. K.; Na, K. Acetylated Hyaluronic Acid-Poly(L-Lactic Acid) Conjugate Nanoparticles for Inhibition of Doxorubicinol Production from Doxorubicin. *Macromol. Res.* **2020**, *28*, 67−73.

(82) Kim, J.; Kim, K. S.; Park, S. J.; Na, K. Vitamin Bc-Bearing Hydrophilic Photosensitizer Conjugate for Photodynamic Cancer Theranostics. *Macromol. Biosci.* **2015**, *15*, 1081−1090.

(83) Temizel, E.; Sagir, T.; Ayan, E.; Isik, S.; Ozturk, R. Delivery of Lipophilic Porphyrin by Liposome Vehicles: Preparation and Photodynamic Therapy Activity Against Cancer Cell Lines. *Photodiagn. Photodyn. Ther.* **2014**, *11*, 537−545.

(84) Master, A.; Livingston, M.; Sen Gupta, A. Photodynamic Nanomedicine in the Treatment of Solid Tumors: Perspectives and Challenges. *J. Controlled Release* **2013**, *168*, 88−102.

(85) Ogawara, K. I.; Higaki, K. Nanoparticle-Based Photodynamic Therapy: Current Status and Future Application to Improve Outcomes of Cancer Treatment. *Chem. Pharm. Bull.* **2017**, *65*, 637−641.

(86) Tada, D. B.; Baptista, M. S. Photosensitizing Nanoparticles and the Modulation of ROS Generation. *Front. Chem.* **2015**, *3*, 33.

(87) Konan, Y. N.; Gurny, R.; Allémann, E. State of the Art in the Delivery of Photosensitizers for Photodynamic Therapy. *J. Photochem. Photobiol., B* **2002**, *66*, 89−106.

(88) Paszko, E.; Ehrhardt, C.; Senge, M. O.; Kelleher, D. P.; Reynolds, J. V. Nanodrug Applications in Photodynamic Therapy. *Photodiagn. Photodyn. Ther.* **2011**, *8*, 14−29.

(89) Sumer, B.; Gao, J. Theranostic Nanomedicine for Cancer. *Nanomedicine* **2008**, *3*, 137−140.

(90) Koning, Gerben A.; Krijger, Gerard C. Targeted Multifunctional Lipid-Based Nanocarriers for Image-Guided Drug Delivery. *Anti-Cancer Agents Med. Chem.* **2007**, *7*, 425−440.

(91) Batista, C. A. S.; Larson, R. G.; Kotov, N. A. Nonadditivity of Nanoparticle Interactions. *Science* **2015**, *350*, 1242477.

(92) Gmeiner, W. H.; Ghosh, S. Nanotechnology for Cancer Treatment. *Nanotechnol. Rev.* **2014**, *3*, 111−122.

(93) Elias, D. R.; Poloukhtine, A.; Popik, V.; Tsourkas, A. Effect of Ligand Density, Receptor Density, and Nanoparticle Size on Cell Targeting. *Nanomedicine* **2013**, *9*, 194−201.

(94) Sarpaki, S. *Investigations into the Radiochemistry of Gallium- and Fluorine-Containing Compounds for Molecular Imaging Applications*, Ph.D. Thesis, University of Bath: England, 2018.

(95) Liu, T. W.; MacDonald, T. D.; Jin, C. S.; Gold, J. M.; Bristow, R. G.; Wilson, B. C.; Zheng, G. Inherently Multimodal Nanoparticle-Driven Tracking and Real-Time Delineation of Orthotopic Prostate Tumors and Micrometastases. *ACS Nano* **2013**, *7*, 4221−4232.

(96) Mitchell, N.; Kalber, T. L.; Cooper, M. S.; Sunassee, K.; Chalker, S. L.; Shaw, K. P.; Ordidge, K. L.; Badar, A.; Janes, S. M.; Blower, P. J.; Lythgoe, M. F.; Hailes, H. C.; Tabor, A. B. Incorporation of Paramagnetic, Fluorescent and PET/SPECT Contrast Agents Into Liposomes for Multimodal Imaging. *Biomaterials* **2013**, *34*, 1179−1192.

(97) Zhang, R.; Huang, M.; Zhou, M.; Wen, X.; Huang, Q.; Li, C. Annexin A5-Functionalized Nanoparticle for Multimodal Imaging of Cell Death. *Mol. Imaging* **2013**, *12*, 7290.2012.00032.

(98) Liu, T. W.; MacDonald, T. D.; Shi, J.; Wilson, B. C.; Zheng, G. Intrinsically Copper-64-Labeled Organic Nanoparticles as Radiotracers. *Angew. Chem., Int. Ed.* **2012**, *51*, 13128−13131.

(99) Janib, S. M.; Moses, A. S.; MacKay, J. A. Imaging and Drug Delivery Using Theranostic Nanoparticles. *Adv. Drug Delivery Rev.* **2010**, *62*, 1052−1063.

(100) McCarthy, J. R.; Weissleder, R. Multifunctional Magnetic Nanoparticles for Targeted Imaging and Therapy. *Adv. Drug Delivery Rev.* **2008**, *60*, 1241−1251.

(101) McCarthy, J. R. The Future of Theranostic Nanoagents. *Nanomedicine* **2009**, *4*, 693−695.

(102) Summer, D.; Grossrubatscher, L.; Petrik, M.; Michalcikova, T.; Novy, Z.; Rangger, C.; Klingler, M.; Haas, H.; Kaeopookum, P.; Von Guggenberg, E.; Haubner, R.; Decristoforo, C. Developing Targeted Hybrid Imaging Probes by Chelator Scaffolding. *Bioconjugate Chem.* **2017**, *28*, 1722−1733.

(103) Iyer, A. K.; Greish, K.; Seki, T.; Okazaki, S.; Fang, J.; Takeshita, K.; Maeda, H. Polymeric Micelles of Zinc Protoporphyrin for Tumor Targeted Delivery Based on EPR Effect and Singlet Oxygen Generation. *J. Drug Target.* **2007**, *15*, 496−506.

(104) Maeda, H.; Greish, K.; Fang, J. The EPR Effect and Polymeric Drugs: A Paradigm Shift for Cancer Chemotherapy in the 21st Century. *Adv. Polym. Sci.* **2005**, *193*, 103−121.

(105) Cai, W.; Chen, X. Multimodality Molecular Imaging of Tumor Angiogenesis. *J. Nucl. Med.* **2008**, *49*, 113−128.

(106) Haglund, E.; Seale-Goldsmith, M. M.; Leary, J. F. Design of Multifunctional Nanomedical Systems. *Ann. Biomed. Eng.* **2009**, *37*, 2048−2063.

(107) Svenskaya, Y.; Parakhonskiy, B.; Haase, A.; Atkin, V.; Lukyanets, E.; Gorin, D.; Antolini, R. Anticancer Drug Delivery System Based on Calcium Carbonate Particles Loaded with a Photosensitizer. *Biophys. Chem.* **2013**, *182*, 11−15.

(108) Cheng, L.; Wang, C.; Feng, L.; Yang, K.; Liu, Z. Functional Nanomaterials for Phototherapies of Cancer. *Chem. Rev.* **2014**, *114*, 10869−10939.

(109) Ding, D.; Guo, W.; Guo, C.; Sun, J.; Zheng, N.; Wang, F.; Yan, M.; Liu, S. MoO3-X Quantum Dots for Photoacoustic Imaging Guided Photothermal/Photodynamic Cancer Treatment. *Nanoscale* **2017**, *9*, 2020−2029.

(110) Lu, K.; He, C.; Lin, W. Nanoscale Metal-Organic Framework for Highly Effective Photodynamic Therapy of Resistant Head and Neck Cancer. *J. Am. Chem. Soc.* **2014**, *136*, 16712−16715.

(111) Liu, J.; Yang, Y.; Zhu, W.; Yi, X.; Dong, Z.; Xu, X.; Chen, M.; Yang, K.; Lu, G.; Jiang, L.; Liu, Z. Nanoscale Metal-Organic Frameworks for Combined Photodynamic & Radiation Therapy in Cancer Treatment. *Biomaterials* **2016**, *97*, 1−9.

(112) Sansaloni-Pastor, S.; Bouilloux, J.; Lange, N. The Dark Side: Photosensitizer Prodrugs. *Pharmaceuticals* **2019**, *12* (4), 148.

(113) Lovell, J. F.; Jin, C. S.; Huynh, E.; Jin, H.; Kim, C.; Rubinstein, J. L.; Chan, W. C. W.; Cao, W.; Wang, L. V.; Zheng, G. Porphysome Nanovesicles Generated by Porphyrin Bilayers for Use as Multimodal Biophotonic Contrast Agents. *Nat. Mater.* **2011**, *10*, 324−332.

(114) Waghorn, P. A. Radiolabelled Porphyrins in Nuclear Medicine. *J. Labelled Compd. Radiopharm.* **2014**, *57*, 304−309.

(115) Ng, K. K.; Takada, M.; Jin, C. C. S.; Zheng, G. Self-Sensing Porphysomes for Fluorescence-Guided Photothermal Therapy. *Bioconjugate Chem.* **2015**, *26*, 345−351.

(116) Allison, R. R.; Bagnato, V. S.; Sibata, C. H. Future of Oncologic Photodynamic Therapy. *Future Oncol.* **2010**, *6*, 929−940.

(117) Wieder, M. E.; Hone, D. C.; Cook, M. J.; Handsley, M. M.; Gavrilovic, J.; Russell, D. A. Intracellular Photodynamic Therapy With Photosensitizer-Nanoparticle Conjugates: Cancer Therapy Using a 'Trojan Horse.'. *Photochem. Photobiol. Sci.* **2006**, *5*, 727−734.

(118) Samia, A. C. S.; Chen, X.; Burda, C. Semiconductor Quantum Dots for Photodynamic Therapy. *J. Am. Chem. Soc.* **2003**, *125*, 15736−15737.

(119) Jaiswal, J. K.; Mattoussi, H.; Mauro, J. M.; Simon, S. M. Long-Term Multiple Color Imaging of Live Cells Using Quantum Dot Bioconjugates. *Nat. Biotechnol.* **2003**, *21*, 47−51.

(120) Lira, R. B.; Seabra, M. A. B. L.; Matos, A. L. L.; Vasconcelos, J. V.; Bezerra, D. P.; De Paula, E.; Santos, B. S.; Fontes, A. Studies on Intracellular Delivery of Carboxyl-Coated CdTe Quantum Dots Mediated by Fusogenic Liposomes. *J. Mater. Chem. B* **2013**, *1*, 4297−4305.

(121) Jhonsi, M. A.; Renganathan, R. Investigations on the Photoinduced Interaction of Water Soluble Thioglycolic Acid (TGA) Capped CdTe Quantum Dots with Certain Porphyrins. *J. Colloid Interface Sci.* **2010**, *344*, 596−602.

(122) Li, L.; Zhao, J. F.; Won, N.; Jin, H.; Kim, S.; Chen, J. Y. Quantum Dot - Aluminum Phthalocyanine Conjugates Perform Photodynamic Reactions to Kill Cancer Cells via Fluorescence Resonance Energy Transfer (FRET). *Nanoscale Res. Lett.* **2012**, *7*, 386.

(123) Rakovich, A.; Savateeva, D.; Rakovich, T.; Donegan, J. F.; Rakovich, Y. P.; Kelly, V.; Lesnyak, V.; Eychmüller, A. CdTe Quantum Dot/Dye Hybrid System as Photosensitizer for Photodynamic Therapy. *Nanoscale Res. Lett.* **2010**, *5*, 753−760.

(124) Tsay, J. M.; Trzoss, M.; Shi, L.; Kong, X.; Selke, M.; Jung, M. E.; Weiss, S. Singlet Oxygen Production by Peptide-Coated Quantum Dot-Photosensitizer Conjugates. *J. Am. Chem. Soc.* **2007**, *129*, 6865−6871.

(125) Wen, Y. N.; Song, W. S.; An, L. M.; Liu, Y. Q.; Wang, Y. H.; Yang, Y. Q. Activation of Porphyrin Photosensitizers by Semiconductor Quantum Dots via Two-Photon Excitation. *Appl. Phys. Lett.* **2009**, *95*, 143702.

(126) Chen, J. Y.; Lee, Y. M.; Zhao, D.; Mak, N. K.; Wong, R. N. S.; Chan, W. H.; Cheung, N. H. Quantum Dot-Mediated Photoproduction of Reactive Oxygen Species for Cancer Cell Annihilation. *Photochem. Photobiol.* **2010**, *86*, 431−437.

(127) Wang, R. gui; Zhao, M. yao; Deng, D.; Ye, X.; Zhang, F.; Chen, H.; Kong, J. lie An Intelligent and Biocompatible Photosensitizer Conjugated Silicon Quantum Dots-MnO2 Nanosystem for Fluorescence Imaging-Guided Efficient Photodynamic Therapy. *J. Mater. Chem. B* **2018**, *6*, 4592−4601.

(128) Biju, V.; Itoh, T.; Ishikawa, M. Delivering Quantum Dots to Cells: Bioconjugated Quantum Dots for Targeted and Nonspecific Extracellular and Intracellular Imaging. *Chem. Soc. Rev.* **2010**, *39*, 3031−3056.

(129) Viana, O. S.; Ribeiro, M. S.; Fontes, A.; Santos, B. S. Quantum Dots in Photodynamic Therapy. In *Oxidative Stress in Applied Basic Research and Clinical Practice*; Springer International Publishing: Switzerland, 2016; pp 525−539.

(130) Din, F. U.; Aman, W.; Ullah, I.; Qureshi, O. S.; Mustapha, O.; Shafique, S.; Zeb, A. Effective Use of Nanocarriers as Drug Delivery Systems for the Treatment of Selected Tumors. *Int. J. Nanomed.* **2017**, *12*, 7291−7309.

(131) Lombardo, D.; Kiselev, M. A.; Caccamo, M. T. Smart Nanoparticles for Drug Delivery Application: Development of Versatile Nanocarrier Platforms in Biotechnology and Nanomedicine. *J. Nanomater.* **2019**, *2019*, 1.

(132) Singh, R.; Lillard, J. W. Nanoparticle-Based Targeted Drug Delivery. *Exp. Mol. Pathol.* **2009**, *86*, 215−223.

(133) Gupta, A.; Avci, P.; Sadasivam, M.; Chandran, R.; Parizotto, N.; Vecchio, D.; de Melo, W. C. M. A.; Dai, T.; Chiang, L. Y.; Hamblin, M. R. Shining Light on Nanotechnology to Help Repair and Regeneration. *Biotechnol. Adv.* **2013**, *31*, 607−631.

(134) Bechet, D.; Couleaud, P.; Frochot, C.; Viriot, M. L.; Guillemin, F.; Barberi-Heyob, M. Nanoparticles as Vehicles for Delivery of Photodynamic Therapy Agents. *Trends Biotechnol.* **2008**, *26*, 612−621.

(135) Huang, P.; Li, Z.; Lin, J.; Yang, D.; Gao, G.; Xu, C.; Bao, L.; Zhang, C.; Wang, K.; Song, H. Photosensitizer-Conjugated Magnetic Nanoparticles for in Vivo Simultaneous Magnetofluorescent Imaging and Targeting Therapy. *Biomaterials* **2011**, *32*, 3447−3458.

(136) Sun, Y.; Chen, Z. L.; Yang, X. X.; Huang, P.; Zhou, X. P.; Du, X. X. Magnetic Chitosan Nanoparticles as a Drug Delivery System for Targeting Photodynamic Therapy. *Nanotechnology* **2009**, *20*, 135102.

(137) Wang, S.; Gao, R.; Zhou, F.; Selke, M. Nanomaterials and Singlet Oxygen Photosensitizers: Potential Applications in Photodynamic Therapy. *J. Mater. Chem.* **2004**, *14*, 487−493.

(138) Huang, P.; Xu, C.; Lin, J.; Wang, C.; Wang, X.; Zhang, C.; Zhou, X.; Guo, S.; Cui, D. Folic Acid-Conjugated Graphene Oxide Loaded With Photosensitizers for Targeting Photodynamic Therapy. *Theranostics* **2011**, *1*, 2240−250.

(139) Tomao, S. Albumin-Bound Formulation of Paclitaxel (Abraxane Abi-007) in the Treatment of Breast Cancer. *Int. J. Nanomed.* **2009**, *4*, 99−105.

(140) Malam, Y.; Loizidou, M.; Seifalian, A. M. Liposomes and Nanoparticles: Nanosized Vehicles for Drug Delivery in Cancer. *Trends Pharmacol. Sci.* **2009**, *30*, 592−599.

(141) Wilson, B. C.; Olivo, M.; Singh, G. Subcellular Localization of Photofrin and Aminolevulinic Acid and Photodynamic Cross-Resistance in Vitro in Radiation-Induced Fibrosarcoma Cells Sensitive or Resistant to Photofrin-Mediated Photodynamic Therapy. *Photochem. Photobiol.* **1997**, *65*, 166−176.

(142) Celli, J. P.; Solban, N.; Liang, A.; Pereira, S. P.; Hasan, T. Verteporfin-Based Photodynamic Therapy Overcomes Gemcitabine Insensitivity in a Panel of Pancreatic Cancer Cell Lines. *Lasers Surg. Med.* **2011**, *43*, 565−574.

(143) Mahalingam, S. M.; Ordaz, J. D.; Low, P. S. Targeting of a Photosensitizer to the Mitochondrion Enhances the Potency of Photodynamic Therapy. *ACS Omega* **2018**, *3*, 6066−6074.

(144) Zielonka, J.; Joseph, J.; Sikora, A.; Hardy, M.; Ouari, O.; Vasquez-Vivar, J.; Cheng, G.; Lopez, M.; Kalyanaraman, B. Mitochondria-Targeted Triphenylphosphonium-Based Compounds: Syntheses, Mechanisms of Action, and Therapeutic and Diagnostic Applications. *Chem. Rev.* **2017**, *117*, 10043−10120.

(145) Wang, H.; Gao, Z.; Liu, X.; Agarwal, P.; Zhao, S.; Conroy, D. W.; Ji, G.; Yu, J.; Jaroniec, C. P.; Liu, Z.; Lu, X.; Li, X.; He, X. Targeted Production of Reactive Oxygen Species in Mitochondria to Overcome Cancer Drug Resistance. *Nat. Commun.* **2018**, *9*, 1−16.

(146) Zhao, X.; Huang, Y.; Yuan, G.; Zuo, K.; Huang, Y.; Chen, J.; Li, J.; Xue, J. A Novel Tumor and Mitochondria Dual-Targeted Photosensitizer Showing Ultra-Efficient Photodynamic Anticancer Activities. *Chem. Commun.* **2019**, *55*, 866−869.

(147) Sibrian-Vazquez, M.; Nesterova, I. V.; Jensen, T. J.; Vicente, M. G. H. Mitochondria Targeting by Guanidine- and Biguanidine-Porphyrin Photosensitizers. *Bioconjugate Chem.* **2008**, *19*, 705−713.

(148) Canal, F.; Vicent, M. J.; Pasut, G.; Schiavon, O. Relevance of Folic Acid/Polymer Ratio in Targeted PEG-Epirubicin Conjugates. *J. Controlled Release* **2010**, *146*, 388−399.

(149) Farokhzad, O. C.; Langer, R. Impact of Nanotechnology on Drug Delivery. *ACS Nano* **2009**, *3*, 16−20.

(150) Lin, L.; Xiong, L.; Wen, Y.; Lei, S.; Deng, X.; Liu, Z.; Chen, W.; Miao, X. Active Targeting of Nano-Photosensitizer Delivery

Systems for Photodynamic Therapy of Cancer Stem Cells. *J. Biomed. Nanotechnol.* **2015**, *11*, 531−554.

(151) Chen, L.; Miao, W.; Tang, X.; Zhang, H.; Wang, S.; Luo, F.; Yan, J. Inhibitory Effect of Neuropilin-1 Monoclonal Antibody (NRP-1 MAB) on Glioma Tumor in Mice. *J. Biomed. Nanotechnol.* **2013**, *9*, 551−558.

(152) Zhang, Z.; Sun, Q.; Zhong, J.; Yang, Q.; Li, H.; Cheng, D.; Liang, B.; Shuai, X. Magnetic Resonance Imaging-Visible and PH-Sensitive Polymeric Micelles for Tumor Targeted Drug Delivery. *J. Biomed. Nanotechnol.* **2014**, *10*, 216−226.

(153) Kim, K. S.; Kim, J.; Kim, D. H.; Hwang, H. S.; Na, K. Multifunctional Trastuzumab-Chlorin E6 Conjugate for the Treatment of HER2-Positive Human Breast Cancer. *Biomater. Sci.* **2018**, *6*, 1217−1226.

(154) Mitri, Z.; Constantine, T.; O'Regan, R. The HER2 Receptor in Breast Cancer: Pathophysiology, Clinical Use, and New Advances in Therapy. *Chemother. Res. Pract.* **2012**, *2012*, 1−7.

(155) Kim, J.; Jo, Y. um; Na, K. Photodynamic Therapy with Smart Nanomedicine. *Arch. Pharmacal Res.* **2020**, *43*, 22−31.

(156) Kessel, D. The Role of Low-Density Lipoprotein in the Biodistribution of Photosensitizing Agents. *J. Photochem. Photobiol., B* **1992**, *14*, 261−262.

(157) Sibani, S. A.; McCarron, P. A.; Woolfson, A. D.; Donnelly, R. F. Photosensitiser Delivery for Photodynamic Therapy. Part 2: Systemic Carrier Platforms. *Expert Opin. Drug Delivery* **2008**, *5*, 1241−1254.

(158) Ke, M.-R.; Yeung, S.-L.; Ng, D. K. P.; Fong, W.-P.; Lo, P.-C. Preparation and In Vitro Photodynamic Activities of Folate-Conjugated Distyryl Boron Dipyrromethene Based Photosensitizers. *J. Med. Chem.* **2013**, *56*, 8475−8483.

(159) Cheung, A.; Bax, H. J.; Josephs, D. H.; Ilieva, K. M.; Pellizzari, G.; Opzoomer, J.; Bloomfield, J.; Fittall, M.; Grigoriadis, A.; Figini, M.; Canevari, S.; Spicer, J. F.; Tutt, A. N.; Karagiannis, S. N. Targeting Folate Receptor Alpha for Cancer Treatment. *Oncotarget* **2016**, *7*, 52553−52574.

(160) Savellano, M. D.; Hasan, T. Photochemical Targeting of Epidermal Growth Factor Receptor: A Mechanistic Study. *Clin. Cancer Res.* **2005**, *11*, 1658−1668.

(161) Choi, Y.; McCarthy, J. R.; Weissleder, R.; Tung, C. H. Conjugation of a Photosensitizer to an Oligoarginine-Based Cell-Penetrating Peptide Increases the Efficacy of Photodynamic Therapy. *ChemMedChem* **2006**, *1*, 458−463.

(162) Minchinton, A. I.; Tannock, I. F. Drug Penetration in Solid Tumours. *Nat. Rev. Cancer* **2006**, *6*, 583−592.

(163) Greish, K. Enhanced Permeability and Retention (Epr) Effect for Anticancer Nanomedicine Drug Targeting. *Methods Mol. Biol.* **2010**, *624*, 25−37.

(164) McNeil, S. E. Nanotechnology for the Biologist. *J. Leukocyte Biol.* **2005**, *78*, 585−594.

(165) Tanaka, M.; Kataoka, H.; Yano, S.; Ohi, H.; Moriwaki, K.; Akashi, H.; Taguchi, T.; Hayashi, N.; Hamano, S.; Mori, Y.; Kubota, E.; Tanida, S.; Joh, T. Antitumor Effects in Gastrointestinal Stromal Tumors Using Photodynamic Therapy With a Novel Glucose-Conjugated Chlorin. *Mol. Cancer Ther.* **2014**, *13*, 767−775.

(166) Jain, R. K. Delivery of Molecular and Cellular Medicine to Solid Tumors. *Adv. Drug Delivery Rev.* **2001**, *46*, 149−168.

(167) Decuzzi, P.; Causa, F.; Ferrari, M.; Netti, P. A. The Effective Dispersion of Nanovectors Within the Tumor Microvasculature. *Ann. Biomed. Eng.* **2006**, *34*, 633−641.

(168) Decuzzi, P.; Lee, S.; Bhushan, B.; Ferrari, M. A Theoretical Model for the Margination of Particles Within Blood Vessels. *Ann. Biomed. Eng.* **2005**, *33*, 179−190.

(169) Brigger, I.; Dubernet, C.; Couvreur, P. Nanoparticles in Cancer Therapy and Diagnosis. *Adv. Drug Delivery Rev.* **2002**, *54*, 631−651.

(170) Higgins, L. J.; Pomper, M. G. The Evolution of Imaging in Cancer: Current State and Future Challenges. *Semin. Oncol.* **2011**, *38*, 3−15.

(171) Rudin, M.; Rausch, M.; Stoeckli, M. Molecular Imaging in Drug Discovery and Development: Potential and Limitations of Nonnuclear Methods. *Mol. Imaging Biol.* **2005**, *7*, 5−13.

(172) Kopelman, R.; Lee Koo, Y. E.; Philbert, M.; Moffat, B. A.; Ramachandra Reddy, G.; McConville, P.; Hall, D. E.; Chenevert, T. L.; Bhojani, M. S.; Buck, S. M.; Rehemtulla, A.; Ross, B. D. Multifunctional Nanoparticle Platforms for in Vivo MRI Enhancement and Photodynamic Therapy of a Rat Brain Cancer. *J. Magn. Magn. Mater.* **2005**, *293*, 404−410.

(173) Abouelmagd, S. A.; Hyun, H.; Yeo, Y. Extracellularly Activatable Nanocarriers for Drug Delivery to Tumors. *Expert Opin. Drug Delivery* **2014**, *11*, 1601−1618.

(174) Misri, R.; Meier, D.; Yung, A. C.; Kozlowski, P.; Häfeli, U. O. Development and Evaluation of a Dual-Modality (MRI/SPECT) Molecular Imaging Bioprobe. *Nanomedicine* **2012**, *8*, 1007−1016.

(175) Yim, H.; Seo, S.; Na, K. MRI Contrast Agent-Based Multifunctional Materials: Diagnosis and Therapy. *J. Nanomater.* **2011**, *2011*, 1.

(176) Jerjes, W.; Upile, T.; Hamdoon, Z.; Nhembe, F.; Bhandari, R.; Mackay, S.; Shah, P.; Mosse, C. A.; AS Brookes, J.; Morley, S.; Hopper, C. Ultrasound-Guided Photodynamic Therapy for Deep Seated Pathologies: Prospective Study. *Lasers Surg. Med.* **2009**, *41*, 612−621.

(177) Eljamel, M. S.; Goodman, C.; Moseley, H. ALA and Photofrin Fluorescence-Guided Resection and Repetitive PDT in Glioblastoma Multiforme: A Single Centre Phase III Randomised Controlled Trial. *Lasers Med. Sci.* **2008**, *23*, 361−367.

(178) Mark, J. R.; Gelpi-Hammerschmidt, F.; Trabulsi, E. J.; Gomella, L. G. Blue Light Cystoscopy for Detection and Treatment of Non-Muscle Invasive Bladder Cancer. *Can. J. Urol.* **2012**, *19*, 6227−6231.

(179) Mallidi, S.; Spring, B. Q.; Chang, S.; Vakoc, B.; Hasan, T. Optical Imaging, Photodynamic Therapy and Optically Triggered Combination Treatments. *Cancer J. (Philadelphia, PA, U. S.)* **2015**, *21*, 194−205.

(180) Mallidi, S.; Anbil, S.; Lee, S.; Manstein, D.; Elrington, S.; Kositratna, G.; Schoenfeld, D.; Pogue, B.; Davis, S. J.; Hasan, T. Photosensitizer Fluorescence and Singlet Oxygen Luminescence as Dosimetric Predictors of Topical 5-Aminolevulinic Acid Photodynamic Therapy Nduced Clinical Erythema. *J. Biomed. Opt.* **2014**, *19*, 028001.

(181) Zhou, X.; Pogue, B. W.; Chen, B.; Demidenko, E.; Joshi, R.; Hoopes, J.; Hasan, T. Pretreatment Photosensitizer Dosimetry Reduces Variation in Tumor Response. *Int. J. Radiat. Oncol., Biol., Phys.* **2006**, *64*, 1211−1220.

(182) Zou, J.; Yin, Z.; Wang, P.; Chen, D.; Shao, J.; Zhang, Q.; Sun, L.; Huang, W.; Dong, X. Photosensitizer Synergistic Effects: D-A-D Structured Organic Molecule With Enhanced Fluorescence and Singlet Oxygen Quantum Yield for Photodynamic Therapy. *Chem. Sci.* **2018**, *9*, 2188−2194.

(183) Pereira, N. A. M.; Laranjo, M.; Casalta-Lopes, J.; Serra, A. C.; Piñeiro, M.; Pina, J.; Seixas de Melo, J. S.; Senge, M. O.; Botelho, M. F.; Martelo, L.; Burrows, H. D.; Pinho E Melo, T. M. V. D. Platinum(II) Ring-Fused Chlorins as Near-Infrared Emitting Oxygen Sensors and Photodynamic Agents. *ACS Med. Chem. Lett.* **2017**, *8*, 310−315.

(184) Stefflova, K.; Chen, J.; Zheng, G. Using Molecular Beacons for Cancer Imaging and Treatment. *Front. Biosci., Landmark Ed.* **2007**, *12*, 4709−4721.

(185) Pineiro, M.; Pereira, M. M.; Rocha Gonsalves, A. M. D. A.; Arnaut, L. G.; Formosinho, S. J. Singlet Oxygen Quantum Yields From Halogenated Chlorins: Potential New Photodynamic Therapy Agents. *J. Photochem. Photobiol., A* **2001**, *138*, 147−157.

(186) Serra, A.; Pineiro, M.; Santos, C. I.; Rocha Gonsalves, A. M. D. A.; Abrantes, M.; Laranjo, M.; Botelho, M. F. In Vitro Photodynamic Activity of 5,15-Bis(3-Hydroxyphenyl)Porphyrin and Its Halogenated Derivatives Against Cancer Cells. *Photochem. Photobiol.* **2010**, *86*, 206−212.

(187) Serra, A. C.; Pineiro, M.; Rocha Gonsalves, A. M. d. A.; Abrantes, M.; Laranjo, M.; Santos, A. C.; Botelho, M. F. Halogen Atom Effect on Photophysical and Photodynamic Characteristics of Derivatives of 5,10,15,20-Tetrakis(3-Hydroxyphenyl)Porphyrin. *J. Photochem. Photobiol., B* **2008**, *92*, 59−65.

(188) Stefflova, K.; Li, H.; Chen, J.; Zheng, G. Peptide-Based Pharmacomodulation of a Cancer-Targeted Optical Imaging and Photodynamic Therapy Agent. *Bioconjugate Chem.* **2007**, *18*, 379−388.

(189) Wilson, B. C.; Van Lier, J. E. Radiolabelled Photosensitizers for Tumour Imaging and Photodynamic Therapy. *J. Photochem. Photobiol., B* **1989**, 3, 459.

(190) Pandey, S. K.; Sajjad, M.; Chen, Y.; Zheng, X.; Yao, R.; Missert, J. R.; Batt, C.; Nabi, H. A.; Oseroff, A. R.; Pandey, R. K. Comparative Positron-Emission Tomography (PET) Imaging and Phototherapeutic Potential of 1 24i- Labeled Methyl- 3-(1’-Iodobenzyloxyethyl) Pyropheophorbide-A vs the Corresponding Glucose and Galactose Conjugates. *J. Med. Chem.* **2009**, 52, 445−455.

(191) Fazaeli, Y.; Jalilian, A. R.; Amini, M. M.; Ardaneh, K.; Rahiminejad, A.; Bolourinovin, F.; Moradkhani, S.; Majdabadi, A. Development of a ^{68}Ga-Fluorinated Porphyrin Complex as a Possible PET Imaging Agent. *Nucl. Med. Mol. Imaging* **2012**, *46*, 20−26.

(192) Shi, J.; Liu, T. W. B.; Chen, J.; Green, D.; Jaffray, D.; Wilson, B. C.; Wang, F.; Zheng, G. Transforming a Targeted Porphyrin Theranostic Agent into a PET Imaging Probe for Cancer. *Theranostics* **2011**, *1*, 363−370.

(193) Tamura, K.; Kurihara, H.; Yonemori, K.; Tsuda, H.; Suzuki, J.; Kono, Y.; Honda, N.; Kodaira, M.; Yamamoto, H.; Yunokawa, M.; Shimizu, C.; Hasegawa, K.; Kanayama, Y.; Nozaki, S.; Kinoshita, T.; Wada, Y.; Tazawa, S.; Takahashi, K.; Watanabe, Y.; Fujiwara, Y. ^{64}Cu-DOTA-Trastuzumab PET Imaging in Patients with HER2-Positive Breast Cancer. *J. Nucl. Med.* **2013**, *54*, 1869−1875.

(194) Aguilar-Ortíz, E.; Jalilian, A. R.; Ávila-Rodríguez, M. A. Porphyrins as Ligands for 64Copper: Background and Trends. *MedChemComm* **2018**, *9*, 1577−1588.

(195) Moran, M.; MacDonald, T.; Liu, T.; Forbes, J.; Zhen, G.; Valliant, J. Copper-64-Labeled Porphysomes for PET Imaging. *J. Nucl. Med.* **2014**, *55*, 1016.

(196) Rousseau, J.; Ali, H.; Lamoureux, G.; Lebel, E.; Van Lier, J. E. Synthesis, Tissue Distribution and Tumor Uptake of 99mTc- and 67Ga- Tetrasulfophthalocyanine. *Int. J. Appl. Radiat. Isot.* **1985**, *36*, 709−716.

(197) Li, Z.; Lin, T. P.; Liu, S.; Huang, C. W.; Hudnall, T. W.; Gabbaï, F. P.; Conti, P. S. Rapid Aqueous [18F]-Labeling of a BODIPY Dye for Positron Emission Tomography/Fluorescence Dual Modality Imaging. *Chem. Commun.* **2011**, *47*, 9324−9326.

(198) Pandey, R. K.; Goswami, L. N.; Chen, Y.; Gryshuk, A.; Missert, J. R.; Oseroff, A.; Dougherty, T. J. Nature: A Rich Source for Developing Multifunctional Agents. Tumor-Imaging and Photodynamic Therapy. *Lasers Surg. Med.* **2006**, *38*, 445−467.

(199) Pandey, S. K.; Gryshuk, A. L.; Sajjad, M.; Zheng, X.; Chen, Y.; Abouzeid, M. M.; Morgan, J.; Charamisinau, I.; Nabi, H. A.; Oseroff, A.; Pandey, R. K. Multimodality Agents for Tumor Imaging (Pet, Fluorescence) and Photodynamic Therapy. A Possible "See and Treat" Approach. *J. Med. Chem.* **2005**, *48*, 6286−6295.

(200) Edrei, R.; Gottfried, V.; van Lier, J. E.; Kimel, S. Sulfonated Phthalocyanines: Photophysical Properties, in Vitro Cell Uptake and Structure-Activity Relationships. *J. Porphyrins Phthalocyanines* **1998**, *2*, 191−199.

(201) Chan, W. M.; Lim, T. H.; Pece, A.; Silva, R.; Yoshimura, N. Verteporfin PDT for Non-Standard Indications-A Review of Current Literature. *Graefe's Arch. Clin. Exp. Ophthalmol.* **2010**, *248*, 613−626.

(202) Skupin-Mrugalska, P.; Piskorz, J.; Goslinski, T.; Mielcarek, J.; Konopka, K.; Düzgüneş, N. Current Status of Liposomal Porphyrinoid Photosensitizers. *Drug Discovery Today* **2013**, *18*, 776−784.

(203) Yuzhakova, D. V.; Lermontova, S. A.; Grigoryev, I. S.; Muravieva, M. S.; Gavrina, A. I.; Shirmanova, M. V.; Balalaeva, I. V.; Klapshina, L. G.; Zagaynova, E. V. In Vivo Multimodal Tumor Imaging and Photodynamic Therapy With Novel Theranostic Agents Based on the Porphyrazine Framework-Chelated Gadolinium (III) Cation. *Biochim. Biophys. Acta, Gen. Subj.* **2017**, *1861*, 3120−3130.

(204) Lim, E. K.; Kim, T.; Paik, S.; Haam, S.; Huh, Y. M.; Lee, K. Nanomaterials for Theranostics: Recent Advances and Future Challenges. *Chem. Rev.* **2015**, *115*, 327−394.

(205) Louie, A. Multimodality Imaging Probes: Design and Challenges. *Chem. Rev.* **2010**, *110*, 3146−3195.

(206) Edwards, W. B.; Xu, B.; Akers, W.; Cheney, P. P.; Liang, K.; Rogers, B. E.; Anderson, C. J.; Achilefu, S. Agonist - Antagonist Dilemma in Molecular Imaging: Evaluation of a Monomolecular Multimodal Imaging Agent for the Somatostatin Receptor. *Bioconjugate Chem.* **2008**, *19*, 192−200.

(207) Walia, S.; Acharya, A. Silica Micro/Nanospheres for Theranostics: From Bimodal MRI and Fluorescent Imaging Probes to Cancer Therapy. Beilstein. *Beilstein J. Nanotechnol.* **2015**, *6*, 546−558.

(208) Pandey, S. K.; Kaur, J.; Easwaramoorthy, B.; Shah, A.; Coleman, R.; Mukherjee, J. Multimodality Imaging Probe for Positron Emission Tomography and Fluorescence Imaging Studies. *Mol. Imaging* **2014**, *13*, 1−7.

(209) Wolfbeis, O. S. An Overview of Nanoparticles Commonly Used in Fluorescent Bioimaging. *Chem. Soc. Rev.* **2015**, *44*, 4743−4768.

(210) Thomas, R.; Park, I. K.; Jeong, Y. Y. Magnetic Iron Oxide Nanoparticles for Multimodal Imaging and Therapy of Cancer. *Int. J. Mol. Sci.* **2013**, *14*, 15910−15930.

(211) Vanderesse, D. B. Innovations of Photodynamic Therapy for Brain Tumors: Potential of Multifunctional Nanoparticles. *J. Carcinog. Mutagen.* **2014**, *8*, 8.

(212) Glasgow, M. D. K.; Chougule, M. B. Recent Developments in Active Tumor Targeted Multifunctional Nanoparticles for Combination Chemotherapy in Cancer Treatment and Imaging. *J. Biomed. Nanotechnol.* **2015**, *11*, 1859−1898.

(213) Nafiujjaman, M.; Revuri, V.; Nurunnabi, M.; Jae Cho, K.; Lee, Y. K. Photosensitizer Conjugated Iron Oxide Nanoparticles for Simultaneous in Vitro Magneto-Fluorescent Imaging Guided Photodynamic Therapy. *Chem. Commun.* **2015**, *51*, 5687−5690.

(214) Wang, D.; Fei, B.; Halig, L. V.; Qin, X.; Hu, Z.; Xu, H.; Wang, Y. A.; Chen, Z.; Kim, S.; Shin, D. M.; Chen, Z. Targeted Iron-Oxide Nanoparticle for Photodynamic Therapy and Imaging of Head and Neck Cancer. *ACS Nano* **2014**, *8*, 6620−6632.

(215) Luo, J.; Chen, L. F.; Hu, P.; Chen, Z. N. Tetranuclear Gadolinium(III) Porphyrin Complex as a Theranostic Agent for Multimodal Imaging and Photodynamic Therapy. *Inorg. Chem.* **2014**, *53*, 4184−4191.

(216) Spernyak, J. A.; White, W. H.; Ethirajan, M.; Patel, N. J.; Goswami, L.; Chen, Y.; Turowski, S.; Missert, J. R.; Batt, C.; Mazurchuk, R.; Pandey, R. K. Hexylether Derivative of Pyropheophorbide-a (HPPH) on Conjugating with 3 Gadolinium(III) Aminobenzyldiethylenetriaminepentaacetic Acid Shows Potential for In Vivo Tumor Imaging (MR, Fluorescence) and Photodynamic Therapy. *Bioconjugate Chem.* **2010**, *21*, 828−835.

(217) An, F. F.; Chan, M.; Kommidi, H.; Ting, R. Dual PET and Near-Infrared Fluorescence Imaging Probes as Tools for Imaging in Oncology. *AJR, Am. J. Roentgenol.* **2016**, *207*, 266−273.

(218) Seibold, U.; Wängler, B.; Schirrmacher, R.; Wängler, C. Bimodal Imaging Probes for Combined PET and OI: Recent Developments and Future Directions for Hybrid Agent Development. *BioMed Res. Int.* **2014**, *16*, 1.

(219) Nguyen, Q. T.; Tsien, R. Y. Fluorescence-Guided Surgery with Live Molecular Navigation-A New Cutting Edge. *Nat. Rev. Cancer* **2013**, *13*, 653−662.

(220) Ghosh, S. C.; Azhdarinia, A. Advances in the Development of Multimodal Imaging Agents for Nuclear/Near-Infrared Fluorescence Imaging. *Curr. Med. Chem.* **2015**, *22*, 3390−3404.

(221) Zeng, C.; Shang, W.; Wang, K.; Chi, C.; Jia, X.; Fang, C.; Yang, D.; Ye, J.; Fang, C.; Tian, J. Intraoperative Identification of Liver Cancer Microfoci Using a Targeted Near-Infrared Fluorescent Probe for Imaging-Guided Surgery. *Sci. Rep.* **2016**, *6*, 21959.

(222) Li, X.; Zhang, X.-N.; Li, X.-D.; Chang, J.; Li, X.; Zhang, X.-N.; Li, X.-D.; Chang, J. Multimodality Imaging in Nanomedicine and Nanotheranostics. *Cancer Biol. Med.* **2016**, *13*, 339−348.

(223) Durnev, A. D. Toxicology of Nanoparticles. Bull. *Bull. Exp. Biol. Med.* **2008**, *145*, 72−74.

(224) Liu, Z.; Kiessling, F.; Gätjens, J. Advanced Nanomaterials in Multimodal Imaging: Design, Functionalization, and Biomedical Applications. *J. Nanomater.* **2010**, *2010*, 1.

(225) Head, H. W.; Dodd, G. D.; Bao, A.; Soundararajan, A.; Garcia-Rojas, X.; Prihoda, T. J.; McManus, L. M.; Goins, B. A.; Santoyo, C. A.; Phillips, W. T. Combination Radiofrequency Ablation and Intravenous Radiolabeled Liposomal Doxorubicin: Imaging and Quantification of Increased Drug Delivery to Tumors. *Radiology* **2010**, *255*, 405−414.

(226) Ljungkvist, A. S. E.; Bussink, J.; Kaanders, J. H. A. M.; van der Kogel, A. J. Dynamics of Tumor Hypoxia Measured with Bioreductive Hypoxic Cell Markers. *Radiat. Res.* **2007**, *167*, 127−145.

(227) Vaupel, P.; Mayer, A. Hypoxia in Cancer: Significance and Impact on Clinical Outcome. *Cancer Metastasis Rev.* **2007**, *26*, 225−239.

(228) Brown, J. M. Tumor Hypoxia, Drug Resistance, and Metastases. *J. Natl. Cancer Inst.* **1990**, *82*, 338−339.

(229) Challapalli, A.; Carroll, L.; Aboagye, E. O. Molecular Mechanisms of Hypoxia in Cancer. *Clin. Transl. Imaging* **2017**, *5*, 225−253.

(230) Dewhirst, M. W.; Cao, Y.; Moeller, B. Cycling Hypoxia and Free Radicals Regulate Angiogenesis and Radiotherapy Response. *Nat. Rev. Cancer* **2008**, *8*, 425−437.

(231) Kushibiki, T.; Hirasawa, T.; Okawa, S.; Ishihara, M. Responses of Cancer Cells Induced by Photodynamic Therapy. *J. Healthc. Eng.* **2013**, *4*, 87−108.

(232) Li, S.; Meng, W.; Guan, Z.; Guo, Y.; Han, X. The Hypoxia-Related Signaling Pathways of Vasculogenic Mimicry in Tumor Treatment. *Biomed. Pharmacother.* **2016**, *80*, 127−135.

(233) Yao, J.; Feng, J.; Gao, X.; Wei, D.; Kang, T.; Zhu, Q.; Jiang, T.; Wei, X.; Chen, J. Neovasculature and Circulating Tumor Cells Dual-Targeting Nanoparticles for the Treatment of the Highly-Invasive Breast Cancer. *Biomaterials* **2017**, *113*, 1−17.

(234) Gray, L. H.; Conger, A. D.; Ebert, M.; Hornsey, S.; Scott, O. C. The Concentration of Oxygen Dissolved in Tissues at the Time of Irradiation as a Factor in Radiotherapy. *Br. J. Radiol.* **1953**, *26*, 638−648.

(235) Mottram, J. C. A. Factor of Importance in the Radio Sensitivity of Tumours. *Br. J. Radiol.* **1936**, *9*, 606−614.

(236) Arbeit, J. M.; Brown, J. M.; Chao, K. S. C.; Chapman, J. D.; Eckelman, W. C.; Fyles, A. W.; Giaccia, A. J.; Hill, R. P.; Koch, C. J.; Krishna, M. C.; Krohn, K. A.; Lewis, J. S.; Mason, R. P.; Melillo, G.; Padhani, A. R.; Powis, G.; Rajendran, J. G.; Reba, R.; Robinson, S. P.; Semenza, G. L.; Swartz, H. M.; Vaupel, P.; Yang, D.; Tatum, J. L. Hypoxia: Importance in Tumor Biology, Noninvasive Measurement by Imaging, and Value of Its Measurement in the Management of Cancer Therapy. *Int. J. Radiat. Biol.* **2006**, *82*, 699−757.

(237) Chapman, J. D.; Franko, A. J.; Sharplin, J. A Marker for Hypoxic Cells in Tumours with Potential Clinical Applicability. *Br. J. Cancer* **1981**, *43*, 546−550.

(238) Gallez, B.; Baudelet, C.; Jordan, B. F. Assessment of Tumor Oxygenation by Electron Paramagnetic Resonance: Principles and Applications. *NMR Biomed.* **2004**, *17*, 240−262.

(239) Kwock, L.; Gill, M.; McMurry, H. L.; Beckman, W.; Raleigh, J. A.; Joseph, A. P. Evaluation of a Fluorinated 2-Nitroimidazole Binding to Hypoxic Cells in Tumor-Bearing Rats by ^{19}F Magnetic Resonance Spectroscopy and Immunohistochemistry. *Radiat. Res.* **1992**, *129*, 71.

(240) Dunn, J. F.; O'Hara, J. A.; Zaim-Wadghiri, Y.; Lei, H.; Meyerand, M. E.; Grinberg, O. Y.; Hou, H.; Hoopes, P. J.; Demidenko, E.; Swartz, H. M. Changes in Oxygenation of Intracranial Tumors With Carbogen: A BOLD MRI and EPR Oximetry Study. *J. Magn. Reson. Imaging* **2002**, *16*, 511−521.

(241) Landuyt, W.; Hermans, R.; Bosmans, H.; Sunaert, S.; Beatse, E.; Farina, D.; Meijerink, M.; Zhang, H.; Bogaert, W.; Lambin, P.; Marchal, G. BOLD Contrast FMRI of Whole Rodent Tumour During Air or Carbogen Breathing Using Echo-Planar Imaging at 1.5 T. *Eur. Radiol.* **2001**, *11*, 2332−2340.

(242) Kelada, O. J.; Carlson, D. J. Molecular Imaging of Tumor Hypoxia with Positron Emission Tomography. *Radiat. Res.* **2014**, *181*, 335−349.

(243) Vaupel, P. Tumor Microenvironmental Physiology and Its Implications for Radiation Oncology. *Semin. Radiat. Oncol.* **2004**, *14*, 198−206.

(244) Mees, G.; Dierckx, R.; Vangestel, C.; Van De Wiele, C. Molecular Imaging of Hypoxia with Radiolabelled Agents. *Eur. J. Nucl. Med. Mol. Imaging* **2009**, *36*, 1674−1686.

(245) Lee, S. T.; Scott, A. M. Hypoxia Positron Emission Tomography Imaging With ^{18}F-Fluoromisonidazole. *Semin. Nucl. Med.* **2007**, *37*, 451−461.

(246) Koh, W. J.; Griffin, T. W.; Rasfy, J. S.; Laramore, G. E. Positron Emission Tomography: A New Tool for Characterization of Malignant Disease and Selection of Therapy. *Acta Oncol.* **1994**, *33*, 323−327.

(247) Cortezon-Tamarit, F.; Sarpaki, S.; Calatayud, D. G.; Mirabello, V.; Pascu, S. I. Applications of "Hot" and "Cold" Bis-(Thiosemicarbazonato) Metal Complexes in Multimodal Imaging. *Chem. Rec.* **2016**, *16*, 1380−1397.

(248) Hueting, R.; Kersemans, V.; Cornelissen, B.; Tredwell, M.; Hussien, K.; Christlieb, M.; Gee, A. D.; Passchier, J.; Smart, S. C.; Dilworth, J. R.; Gouverneur, V.; Muschel, R. J. A Comparison of the Behavior of ^{64}Cu-Acetate and ^{64}Cu-ATSM in Vitro and in Vivo. *J. Nucl. Med.* **2014**, *55*, 128−134.

(249) Holland, J. P.; Aigbirhio, F. I.; Betts, H. M.; Bonnitcha, P. D.; Burke, P.; Christlieb, M.; Churchill, G. C.; Cowley, A. R.; Dilworth, J. R.; Donnelly, P. S.; Green, J. C.; Peach, J. M.; Vasudevan, S. R.; Warren, J. E. Functionalized Bis(Thiosemicarbazonato) Complexes of Zinc and Copper: Synthetic Platforms Toward Site-Specific Radiopharmaceuticals. *Inorg. Chem.* **2007**, *46*, 465−485.

(250) Fujibayashi, Y.; Taniuchi, H.; Yonekura, Y.; Ohtani, H.; Konishi, J.; Yokoyama, A. Copper-62-ATSM: A New Hypoxia Imaging Agent with High Membrane Permeability and Low Redox Potential. *J. Nucl. Med.* **1997**, *38*, 1155−1160.

(251) Sarpaki, S.; Cortezon-Tamarit, F.; De Aguiar, S. R. M. M.; Exner, R. M.; Divall, D.; Arrowsmith, R. L.; Ge, H.; Palomares, F. J.; Carroll, L.; Calatayud, D. G.; Paisey, S. J.; Aboagye, E. O.; Pascu, S. I. Radio- and Nano-Chemistry of Aqueous Ga(III) Ions Anchored onto Graphene Oxide-Modified Complexes. *Nanoscale* **2020**, *12*, 6603−6608.

(252) Alam, I.; Arrowsmith, R.; Cortezon-Tamarit, F.; Tyman, F.; Kociok-Köhn, G.; Botchway, S.; Dilworth, J.; Carroll, L.; Aboagye, E.; Pascu, S. Microwave Gallium-68 Radiochemistry for Kinetically Stable Bis(Thiosemicarbazone) Complexes: Structural Investigations and Cellular Uptake Under Hypoxia. *Dalt. Trans.* **2016**, *45*, 144−155.

(253) Mirabello, V.; Cortezon-Tamarit, F.; Pascu, S. I. Oxygen Sensing, Hypoxia Tracing and in Vivo Imaging with Functional Metalloprobes for the Early Detection of Non-Communicable Diseases. *Front. Chem.* **2018**, *6*, 27.

(254) Schwartz, J.; Grkovski, M.; Rimner, A.; Schöder, H.; Zanzonico, P. B.; Carlin, S. D.; Staton, K. D.; Humm, J. L.; Nehmeh, S. A. Pharmacokinetic Analysis of Dynamic ^{18}F-Fluoromisonidazole Pet Data in Non-Small Cell Lung Cancer. *J. Nucl. Med.* **2017**, *58*, 911−919.

(255) Beck, R.; Röper, B.; Carlsen, J. M.; Huisman, M. C.; Lebschi, J. A.; Andratschke, N.; Picchio, M.; Souvatzoglou, M.; Machulla, M. J.; Piert, M. Pretreatment ^{18}F-Faza Pet Predicts Success of Hypoxia-Directed Radiochemotherapy Using Tirapazamine. *J. Nucl. Med.* **2007**, *48*, 973−980.

(256) Michalski, M. H.; Chen, X. Molecular Imaging in Cancer Treatment. *Eur. J. Nucl. Med. Mol. Imaging* **2011**, *38*, 358−377.

(257) Bonnitcha, P.; Grieve, S.; Figtree, G. Clinical Imaging of Hypoxia: Current Status and Future Directions. *Free Radical Biol. Med.* **2018**, *126*, 296−312.

(258) Carlin, S.; Zhang, H.; Reese, M.; Ramos, N. N.; Chen, Q.; Ricketts, S. A. A Comparison of the Imaging Characteristics and Microregional Distribution of 4 Hypoxia PET Tracers. *J. Nucl. Med.* **2014**, *55*, 515−521.

(259) Lewis, J.; McCarthy, D.; McCarthy, T.; Fujibayashi, Y.; Welch, M. Evaluation of ^{64}Cu-ATSM In Vitro and In Vivo in a Hypoxic Tumor Model. *J. Nucl. Med.* **1999**, *40*, 177−183.

(260) Pérès, E. A.; Toutain, J.; Paty, L. P.; Divoux, D.; Ibazizène, M.; Guillouet, S.; Barré, L.; Vidal, A.; Cherel, M.; Bourgeois, M.; Bernaudin, M.; Valable, S. ^{64}Cu-Atsm/^{64}Cu-Cl2 and Their Relationship to Hypoxia in Glioblastoma: A Preclinical Study. *EJNMMI Res.* **2019**, *9*, 114.

(261) Lewis, J. S.; Sharp, T. L.; Laforest, R.; Fujibayashi, Y.; Welch, M. J. Tumor Uptake of Copper-Diacetyl-Bis(N4-Methylthiosemicarbazone): Effect of Changes in Tissue Oxygenation. *J. Nucl. Med.* **2001**, *42*, 655−661.

(262) Colombié, M.; Gouard, S.; Frindel, M.; Vidal, A.; Chérel, M.; Kraeber-Bodéré, F.; Rousseau, C.; Bourgeois, M. Focus on the Controversial Aspects of ^{64}Cu-ATSM in Tumoral Hypoxia Mapping by Pet Imaging. *Front. Med.* **2015**, *2*, 58.

(263) Yuan, H.; Schroeder, T.; Bowsher, J. E.; Hedlund, L. W.; Wong, T.; Dewhirst, M. W. Intertumoral Differences in Hypoxia Selectivity of the PET Imaging Agent ^{64}Cu(II)-Diacetyl-Bis(N4-Methylthiosemicarbazone). *J. Nucl. Med.* **2006**, *47*, 989−998.

(264) Supuran, C. T. Carbonic Anhydrase Inhibition and the Management of Hypoxic Tumors. *Metabolites* **2017**, *7*, 48.

(265) Park, W.; Bae, B. Chan; Na, K. A Highly Tumor-Specific Light-Triggerable Drug Carrier Responds to Hypoxic Tumor Conditions for Effective Tumor Treatment. *Biomaterials* **2016**, *77*, 227−234.

(266) Wilson, W. R.; Hay, M. P. Targeting Hypoxia in Cancer Therapy. *Nat. Rev. Cancer* **2011**, *11*, 393−410.

(267) Lin, Q.; Bao, C.; Yang, Y.; Liang, Q.; Zhang, D.; Cheng, S.; Zhu, L. Highly Discriminating Photorelease of Anticancer Drugs Based on Hypoxia Activatable Phototrigger Conjugated Chitosan Nanoparticles. *Adv. Mater.* **2013**, *25*, 1981−1986.

(268) Qian, C.; Yu, J.; Chen, Y.; Hu, Q.; Xiao, X.; Sun, W.; Wang, C.; Feng, P.; Shen, Q. D.; Gu, Z. Light-Activated Hypoxia-Responsive Nanocarriers for Enhanced Anticancer Therapy. *Adv. Mater.* **2016**, *28*, 3313−3320.

(269) Mitton, D.; Ackroyd, R. A Brief Overview of Photodynamic Therapy in Europe. *Photodiagn. Photodyn. Ther.* **2008**, *5*, 103−111.

(270) Floeth, F. W.; Sabel, M.; Ewelt, C.; Stummer, W.; Felsberg, J.; Reifenberger, G.; Steiger, H. J.; Stoffels, G.; Coenen, H. H.; Langen, K. J. Comparison of ^{18}F-FET PET and 5-ALA Fluorescence in Cerebral Gliomas. *Eur. J. Nucl. Med. Mol. Imaging* **2011**, *38*, 731−741.

(271) Quirk, B. J.; Brandal, G.; Donlon, S.; Vera, J. C.; Mang, T. S.; Foy, A. B.; Lew, S. M.; Girotti, A. W.; Jogal, S.; LaViolette, P. S.; Connelly, J. M.; Whelan, H. T. Photodynamic Therapy (PDT) for Malignant Brain Tumors - Where Do We Stand? *Photodiagn. Photodyn. Ther.* **2015**, *12*, 530−544.

(272) Suzuki, H. I.; Katsura, A.; Matsuyama, H.; Miyazono, K. MicroRNA Regulons in Tumor Microenvironment. *Oncogene* **2015**, *34*, 3085−3094.

(273) Waghorn, P. A.; Jones, M. W.; Theobald, M. B. M.; Arrowsmith, R. L.; Pascu, S. I.; Botchway, S. W.; Faulkner, S.; Dilworth, J. R. Shining Light on the Stability of Metal Thiosemicarbazonate Complexes in Living Cells by FLIM. *Chem. Sci.* **2013**, *4*, 1430−1441.

(274) Nie, S.; Xing, Y.; Kim, G. J.; Simons, J. W. Nanotechnology Applications in Cancer. *Annu. Rev. Biomed. Eng.* **2007**, *9*, 257−288.

(275) McCarthy, J. R. Multifunctional Agents for Concurrent Imaging and Therapy in Cardiovascular Disease. *Adv. Drug Delivery Rev.* **2010**, *62*, 1023−1030.

(276) Warenius, H. M. Technological Challenges of Theranostics in Oncology. *Expert Opin. Med. Diagn.* **2009**, 3, 381−393.

(277) Habermeyer, B.; Guilard, R. Some Activities of Porphychem Illustrated by the Applications of Porphyrinoids in PDT, PIT and PDI. *Photochem. Photobiol. Sci.* **2018**, *17*, 1675−1690.

(278) Singh, S.; Aggarwal, A.; Bhupathiraju, N. V. S. D. K.; Arianna, G.; Tiwari, K.; Drain, C. M. Glycosylated Porphyrins, Phthalocyanines, and Other Porphyrinoids for Diagnostics and Therapeutics. *Chem. Rev.* **2015**, *115*, 10261−10306.

(279) Zhang, Y.; Lovell, J. F. Recent Applications of Phthalocyanines and Naphthalocyanines for Imaging and Therapy. *Wiley Interdiscip. Rev. Nanomed. Nanobiotechnol.* **2017**, *9*, e1420.

(280) Shao, S.; Rajendiran, V.; Lovell, J. F. Metalloporphyrin Nanoparticles: Coordinating Diverse Theranostic Functions. *Coord. Chem. Rev.* **2019**, *379*, 99−120.

(281) Tsolekile, N.; Nelana, S.; Oluwafemi, O. S. Porphyrin as Diagnostic and Therapeutic Agent. *Molecules* **2019**, *24*, 2669.

(282) Pucelik, B.; Paczyński, R.; Dubin, G.; Pereira, M. M.; Arnaut, L. G.; Dąbrowski, J. M. Properties of Halogenated and Sulfonated Porphyrins Relevant for the Selection of Photosensitizers in Anticancer and Antimicrobial Therapies. *PLoS One* **2017**, *12*, e0185984.

(283) Xie, J.; Lee, S.; Chen, X. Nanoparticle-Based Theranostic Agents. *Adv. Drug Delivery Rev.* **2010**, *62*, 1064−1079.

(284) Lammers, T.; Kiessling, F.; Hennink, W. E.; Storm, G. Nanotheranostics and Image-Guided Drug Delivery: Current Concepts and Future Directions. *Mol. Pharmaceutics* **2010**, *7*, 1899−1912.

(285) Darwent, J. R.; McCubbin, I.; Phillips, D. Excited Singlet and Triplet State Electron-Transfer Reactions of Aluminium(III) Sulphonated Phthalocyanine. *J. Chem. Soc., Faraday Trans. 2* **1982**, *78*, 347−357.

(286) Couleaud, P.; Morosini, V.; Frochot, C.; Richeter, S.; Raehm, L.; Durand, J. O. Silica-Based Nanoparticles for Photodynamic Therapy Applications. *Nanoscale* **2010**, *2*, 1083−1095.

(287) Oluwole, D. O.; Nyokong, T. Photophysicochemical Behaviour of Metallophthalocyanines When Doped onto Silica Nanoparticles. *Dyes Pigm.* **2017**, *136*, 262−272.

(288) Tang, L.; Cheng, J. Nonporous Silica Nanoparticles for Nanomedicine Application. *Nano Today* **2013**, *8*, 290−312.

(289) Huang, D.; Hung, Y.; Ko, B.; Hsu, S.; Chen, W.; Chien, C.; Tsai, C.; Kuo, C.; Kang, J.; Yang, C.; Mou, C.; Chen, Y. Highly Efficient Cellular Labeling of Mesoporous Nanoparticles in Human Mesenchymal Stem Cells: Implication for Stem Cell Tracking. *FASEB J.* **2005**, *19*, 2014−2016.

(290) Lin, Y. S.; Wu, S. H.; Hung, Y.; Chou, Y. H.; Chang, C.; Lin, M. L.; Tsai, C. P.; Mou, C. Y. Multifunctional Composite Nanoparticles: Magnetic, Luminescent, and Mesoporous. *Chem. Mater.* **2006**, *18*, 5170−5172.

(291) Slowing, I. I.; Vivero-Escoto, J. L.; Wu, C. W.; Lin, V. S. Y. Mesoporous Silica Nanoparticles as Controlled Release Drug Delivery and Gene Transfection Carriers. *Adv. Drug Delivery Rev.* **2008**, *60*, 1278−1288.

(292) Tsai, C. P.; Hung, Y.; Chou, Y. H.; Huang, D. M.; Hsiao, J. K.; Chang, C.; Chen, Y. C.; Mou, C. Y. High-Contrast Paramagnetic Fluorescent Mesoporous Silica Nanorods as a Multifunctional Cell-Imaging Probe. *Small* **2008**, *4*, 186−191.

(293) Popat, A.; Hartono, S. B.; Stahr, F.; Liu, J.; Qiao, S. Z.; Lu, G. Q. Mesoporous Silica Nanoparticles for Bioadsorption, Enzyme Immobilisation, and Delivery Carriers. *Nanoscale* **2011**, 3, 2801−2818.

(294) Chouikrat, R.; Seve, A.; Vanderesse, R.; Benachour, H.; Barberi-Heyob, M.; Richeter, S.; Raehm, L.; Durand, J.-O.; Verelst, M.; Frochot, C. Non Polymeric Nanoparticles for Photodynamic Therapy Applications: Recent Developments. *Curr. Med. Chem.* **2012**, *19*, 781−792.

(295) Lucky, S. S.; Soo, K. C.; Zhang, Y. Nanoparticles in Photodynamic Therapy. *Chem. Rev.* **2015**, *115*, 1990−2042.

(296) Piao, Y.; Burns, A.; Kim, J.; Wiesner, U.; Hyeon, T. Designed Fabrication of Silica-Based Nanostructured Particle Systems for Nanomedicine Applications. *Adv. Funct. Mater.* **2008**, *18*, 3745−3758.

(297) Ohulchanskyy, T. Y.; Roy, I.; Goswami, L. N.; Chen, Y.; Bergey, E. J.; Pandey, R. K.; Oseroff, A. R.; Prasad, P. N. Organically Modified Silica Nanoparticles With Covalently Incorporated Photo-

sensitizer for Photodynamic Therapy of Cancer. *Nano Lett.* **2007**, *7*, 2835−2842.

(298) Tang, W.; Xu, H.; Kopelman, R.; A. Philbert, M. Photodynamic Characterization and In Vitro Application of Methylene Blue-Containing Nanoparticle Platforms. *Photochem. Photobiol.* **2005**, *81*, 242.

(299) Biju, V. Chemical Modifications and Bioconjugate Reactions of Nanomaterials for Sensing, Imaging, Drug Delivery and Therapy. *Chem. Soc. Rev.* **2014**, *43*, 744−764.

(300) Castilho, M. L.; Vieira, L. S.; Campos, A. P. C.; Achete, C. A.; Cardoso, M. A. G.; Raniero, L. The Efficiency Analysis of Gold Nanoprobes by FT-IR Spectroscopy Applied to the Non-Cross-Linking Colorimetric Detection of Paracoccidioides Brasiliensis. *Sens. Actuators, B* **2015**, *215*, 258−265.

(301) Khaing Oo, M. K.; Yang, Y.; Hu, Y.; Gomez, M.; Du, H.; Wang, H. Gold Nanoparticle-Enhanced and Size-Dependent Generation of Reactive Oxygen Species from Protoporphyrin IX. *ACS Nano* **2012**, *6*, 1939−1947.

(302) Amini, S. M.; Kharrazi, S.; Hadizadeh, M.; Fateh, M.; Saber, R. Effect of Gold Nanoparticles on Photodynamic Efficiency of 5-Aminolevolenic Acid Photosensitiser in Epidermal Carcinoma Cell Line: An In Vitro Study. *IET Nanobiotechnol.* **2013**, *7*, 151−156.

(303) Pasparakis, G. Light-Induced Generation of Singlet Oxygen by Naked Gold Nanoparticles and Its Implications to Cancer Cell Phototherapy. *Small* **2013**, *9*, 4130−4134.

(304) Sherwani, M. A.; Tufail, S.; Khan, A. A.; Owais, M. Gold Nanoparticle-Photosensitizer Conjugate Based Photodynamic Inactivation of Biofilm Producing Cells: Potential for Treatment of C. Albicans Infection in BALB/c Mice. *PLoS One* **2015**, *10*, e0131684.

(305) Penon, O.; Marín, M. J.; Russell, D. A.; Pérez-García, L. Water Soluble, Multifunctional Antibody-Porphyrin Gold Nanoparticles for Targeted Photodynamic Therapy. *J. Colloid Interface Sci.* **2017**, *496*, 100−110.

(306) Basu, S.; Alavi, A. SPECT-CT and PET-CT in Oncology - An Overview. *Curr. Med. Imaging Rev.* **2011**, *7*, 202−209.

(307) Chopra, A.; Shan, L.; Eckelman, W. C.; Leung, K.; Menkens, A. E. Important Parameters to Consider for the Characterization of PET and SPECT Imaging Probes. *Nucl. Med. Biol.* **2011**, *38*, 1079−1084.

(308) Frangioni, J. V. In Vivo Near-Infrared Fluorescence Imaging. *Curr. Opin. Chem. Biol.* **2003**, *7*, 626−634.

(309) Ntziachristos, V.; Bremer, C.; Weissleder, R. Fluorescence Imaging With Near-Infrared Light: New Technological Advances That Enable in Vivo Molecular Imaging. *Eur. Radiol.* **2003**, *13*, 195−208.

(310) Peng, C.-L.; Shih, Y.-H.; Lee, P.-C.; Hsieh, T. M.-H.; Luo, T.-Y.; Shieh, M.-J. Multimodal Image-Guided Photothermal Therapy Mediated by ^{188}Re-Labeled Micelles Containing a Cyanine-Type Photosensitizer. *ACS Nano* **2011**, *5*, 5594−5607.

(311) Shen, X.; Li, L.; Wu, H.; Yao, S. Q.; Xu, Q. H. Photosensitizer-Doped Conjugated Polymer Nanoparticles for Simultaneous Two-Photon Imaging and Two-Photon Photodynamic Therapy in Living Cells. *Nanoscale* **2011**, *3*, 5140−5146.

(312) Tian, J.; Ding, L.; Xu, H. J.; Shen, Z.; Ju, H.; Jia, L.; Bao, L.; Yu, J. S. Cell-Specific and PH-Activatable Rubyrin-Loaded Nanoparticles for Highly Selective Near-Infrared Photodynamic Therapy Against Cancer. *J. Am. Chem. Soc.* **2013**, *135*, 18850−18858.

(313) Tsai, H. C.; Tsai, C. H.; Lin, S. Y.; Jhang, C. R.; Chiang, Y. S.; Hsiue, G. H. Stimulated Release of Photosensitizers from Graft and Diblock Micelles for Photodynamic Therapy. *Biomaterials* **2012**, *33*, 1827−1837.

(314) Kim, H.; Mun, S.; Choi, Y. Photosensitizer-Conjugated Polymeric Nanoparticles for Redox-Responsive Fluorescence Imaging and Photodynamic Therapy. *J. Mater. Chem. B* **2013**, *1*, 429−431.

(315) Wang, C.; Cheng, L.; Liu, Y.; Wang, X.; Ma, X.; Deng, Z.; Li, Y.; Liu, Z. Imaging-Guided PH-Sensitive Photodynamic Therapy Using Charge Reversible Upconversion Nanoparticles Under Near -Infrared Light. *Adv. Funct. Mater.* **2013**, *23*, 3077−3086.

(316) Yoon, H. Y.; Koo, H.; Choi, K. Y.; Lee, S. J.; Kim, K.; Kwon, I. C.; Leary, J. F.; Park, K.; Yuk, S. H.; Park, J. H.; Choi, K. Tumor-Targeting Hyaluronic Acid Nanoparticles for Photodynamic Imaging and Therapy. *Biomaterials* **2012**, *33*, 3980−3989.

(317) Lee, S. J.; Koo, H.; Jeong, H.; Huh, M. S.; Choi, Y.; Jeong, S. Y.; Byun, Y.; Choi, K.; Kim, K.; Kwon, I. C. Comparative Study of Photosensitizer Loaded and Conjugated Glycol Chitosan Nanoparticles for Cancer Therapy. *J. Controlled Release* **2011**, *152*, 21−29.

(318) Taratula, O.; Patel, M.; Schumann, C.; Naleway, M. A.; Pang, A. J.; He, H.; Taratula, O. Phthalocyanine-Loaded Graphene Nanoplatform for Imaging-Guided Combinatorial Phototherapy. *Int. J. Nanomed.* **2015**, *10*, 2347−2362.

(319) Choi, Y.; Kim, S.; Choi, M.-H.; Ryoo, S.-R.; Park, J.; Min, D.-H.; Kim, B.-S. Photodynamic Therapy: Highly Biocompatible Carbon Nanodots for Simultaneous Bioimaging and Targeted Photodynamic Therapy In Vitro and In Vivo. *Adv. Funct. Mater.* **2014**, *24*, 5774−5774A.

(320) Koo, H.; Lee, H.; Lee, S.; Min, K. H.; Kim, M. S.; Lee, D. S.; Choi, Y.; Kwon, I. C.; Kim, K.; Jeong, S. Y. In Vivo Tumor Diagnosis and Photodynamic Therapy via Tumoral PH-Responsive Polymeric Micelles. *Chem. Commun.* **2010**, *46*, 5668−5670.

(321) Lovell, J. F.; Jin, C. S.; Huynh, E.; MacDonald, T. D.; Cao, W.; Zheng, G. Enzymatic Regioselection for the Synthesis and Biodegradation of Porphysome Nanovesicles. *Angew. Chem., Int. Ed.* **2012**, *51*, 2429−2433.

(322) Yi, X. M.; Wang, F. L.; Qin, W. J.; Yang, X. J.; Yuan, J. L. Near-Infrared Fluorescent Probes in Cancer Imaging and Therapy: An Emerging Field. *Int. J. Nanomed.* **2014**, *9*, 1347−1365.

(323) Hu, J. J.; Liu, L. H.; Li, Z. Y.; Zhuo, R. X.; Zhang, X. Z. MMP-Responsive Theranostic Nanoplatform Based on Mesoporous Silica Nanoparticles for Tumor Imaging and Targeted Drug Delivery. *J. Mater. Chem. B* **2016**, *4*, 1932−1940.

(324) Kim, J.; Tung, C. H.; Choi, Y. Smart Dual-Functional Warhead for Folate Receptor-Specific Activatable Imaging and Photodynamic Therapy. *Chem. Commun.* **2014**, *50*, 10600−10603.

(325) Haedicke, K.; Kozlova, D.; Gräfe, S.; Teichgräber, U.; Epple, M.; Hilger, I. Multifunctional Calcium Phosphate Nanoparticles for Combining Near-Infrared Fluorescence Imaging and Photodynamic Therapy. *Acta Biomater.* **2015**, *14*, 197−207.

(326) Schneider, R.; Schmitt, F.; Frochot, C.; Fort, Y.; Lourette, N.; Guillemin, F.; Müller, J. F.; Barberi-Heyob, M. Design, Synthesis, and Biological Evaluation of Folic Acid Targeted Tetraphenylporphyrin as Novel Photosensitizers for Selective Photodynamic Therapy. *Bioorg. Med. Chem.* **2005**, *13*, 2799−2808.

(327) Wang, F.; Chen, X.; Zhao, Z.; Tang, S.; Huang, X.; Lin, C.; Cai, C.; Zheng, N. Synthesis of Magnetic, Fluorescent and Mesoporous Core-Shell-Structured Nanoparticles for Imaging, Targeting and Photodynamic Therapy. *J. Mater. Chem.* **2011**, *21*, 11244−11252.

(328) Kenanova, V.; Wu, A. M. Tailoring Antibodies for Radionuclide Delivery. *Expert Opin. Drug Delivery* **2006**, *3*, 53−70.

(329) Vieira, P.; Rajewsky, K. The Half-Lives of Serum Immunoglobulins in Adult Mice. *Eur. J. Immunol.* **1988**, *18*, 313−316.

(330) Decristoforo, C.; Pickett, R. D.; Verbruggen, A. Feasibility and Availability of 68Ga-Labelled Peptides. *Eur. J. Nucl. Med. Mol. Imaging* **2012**, *39*, 31−40.

(331) Liang, B.; Shao, W.; Zhu, C.; Wen, G.; Yue, X.; Wang, R.; Quan, J.; Du, J.; Bu, X. Mitochondria-Targeted Approach: Remarkably Enhanced Cellular Bioactivities of TPP2a as Selective Inhibitor and Probe toward TrxR. *ACS Chem. Biol.* **2016**, *11*, 425−434.

(332) Isabel, M.; Prata, M. Gallium-68: A New Trend in PET Radiopharmacy. *Curr. Radiopharm.* **2012**, *5*, 142−149.

(333) Roesch, F. Maturation of a Key Resource − The Germanium-68/Gallium-68 Generator: Development and New Insights. *Curr. Radiopharm.* **2012**, *5*, 202−211.

(334) Gaedicke, S.; Braun, F.; Prasad, S.; Machein, M.; Firat, E.; Hettich, M.; Gudihal, R.; Zhu, X.; Klingner, K.; Schüler, J.; Herold-Mende, C. C.; Grosu, A. L.; Behe, M.; Weber, W.; Mäcke, H.;

Niedermann, G. Noninvasive Positron Emission Tomography and Fluorescence Imaging of CD133+ Tumor Stem Cells. *Proc. Natl. Acad. Sci. U. S. A.* **2014**, *111*, E692−E701.

(335) Cho, Y. W.; Park, S. A.; Han, T. H.; Son, D. H.; Park, J. S.; Oh, S. J.; Moon, D. H.; Cho, K. J.; Ahn, C. H.; Byun, Y.; Kim, I. S.; Kwon, I. C.; Kim, S. Y. Vivo Tumor Targeting and Radionuclide Imaging with Self-Assembled Nanoparticles: Mechanisms, Key Factors, and Their Implications. *Biomaterials* **2007**, *28*, 1236−1247.

(336) Mitra, A.; Nan, A.; Line, B.; Ghandehari, H. Nanocarriers for Nuclear Imaging and Radiotherapy of Cancer. *Curr. Pharm. Des.* **2006**, *12*, 4729−4749.

(337) Yamamoto, F.; Yamahara, R.; Makino, A.; Kurihara, K.; Tsukada, H.; Hara, E.; Hara, I.; Kizaka-Kondoh, S.; Ohkubo, Y.; Ozeki, E.; Kimura, S. Radiosynthesis and Initial Evaluation of ^{18}F Labeled Nanocarrier Composed of Poly(L-Lactic Acid)-Block-Poly-(Sarcosine) Amphiphilic Polydepsipeptide. *Nucl. Med. Biol.* **2013**, *40*, 387−394.

(338) Jerabek, P. A.; Patrick, T. B.; Kilbourn, M. R.; Dischino, D. D.; Welch, M. J. Synthesis and Biodistribution of 18F-Labeled Fluoronitroimidazoles: Potential in Vivo Markers of Hypoxic Tissue. *Int. J. Radiat. Appl. Instrumentation.* **1986**, *37*, 599−605.

(339) Grierson, J. R.; Link, J. M.; Mathis, C. A.; Rasey, J. S.; Krohn, K. A. A Radiosynthesis of Fluorine-18 Fluoromisonidazole. *J. Labelled Compd. Radiopharm.* **1989**, *30*, 343−350.

(340) Lopci, E.; Grassi, I.; Chiti, A.; Nanni, C.; Cicoria, G.; Toschi, L.; Fonti, C.; Lodi, F.; Mattioli, S.; Fanti, S. Pet Radiopharmaceuticals for Imaging of Tumor Hypoxia: A Review of the Evidence. *Am. J. Nucl. Med. Mol. Imaging* **2014**, *4*, 365−384.

(341) Bourgeois, M.; Rajerison, H.; Guerard, F.; Mougin-Degraef, M.; Barbet, J.; Michel, N.; Cherel, M.; Faivre-Chauvet, A. Contribution of [64Cu]-ATSM PET in Molecular Imaging of Tumour Hypoxia Compared to Classical [18F] - MISO - A Selected Review. *Nucl. Med. Rev.* **2011**, *14*, 90−95.

(342) Hoigebazar, L.; Jeong, J. M. Hypoxia Imaging Agents Labeled with Positron Emitters. *Recent Results Cancer Res.* **2013**, *194*, 285−299.

(343) Takasawa, M.; Moustafa, R. R.; Baron, J. C. Applications of Nitroimidazole in Vivo Hypoxia Imaging in Ischemic Stroke. *Stroke* **2008**, *39*, 1629−1637.

(344) Lee, N. Y.; Mechalakos, J. G.; Nehmeh, S.; Lin, Z.; Squire, O. D.; Cai, S.; Chan, K.; Zanzonico, P. B.; Greco, C.; Ling, C. C.; Humm, J. L.; Schöder, H. Fluorine-18-Labeled Fluoromisonidazole Positron Emission and Computed Tomography-Guided Intensity-Modulated Radiotherapy for Head and Neck Cancer: A Feasibility Study. Int. *Int. J. Radiat. Oncol., Biol., Phys.* **2008**, *70*, 2−13.

(345) Padhani, A. R. Where Are We With Imaging Oxygenation in Human Tumours? *Cancer Imaging* **2005**, *5*, 128−130.

(346) Lapi, S. E.; Voller, T. F.; Welch, M. J. PET Imaging of Hypoxia. *PET Clin* **2009**, *4*, 39−47.

(347) Hustinx, R.; Eck, S. L.; Alavi, A. Potential Applications of PET Imaging in Developing Novel Cancer Therapies. *J. Nucl. Med.* **2000**, *11*, 433−441.

(348) Chen, K.; Chen, X. Positron Emission Tomography Imaging of Cancer Biology: Current Status and Future Prospects. *Semin. Oncol.* **2011**, *38*, 70−86.

(349) Zhang, P.; Sadler, P. J. Redox-Active Metal Complexes for Anticancer Therapy. *Eur. J. Inorg. Chem.* **2017**, *2017*, 1541−1548.

(350) Agdeppa, E. D.; Spilker, M. E. A Review of Imaging Agent Development. *AAPS J.* **2009**, *11*, 286−299.

(351) Miller, A.; Hoogstraten, B.; Staquet, M.; Winkler, A. Reporting Results of Cancer Treatment. *Cancer* **1981**, *47*, 207.

(352) O'Connell, M. PET−CT Modification of RECIST Guidelines. *J. Natl. Cancer Inst.* **2004**, *96*, 801.

(353) Frank, R. A.; Långström, B.; Antoni, G.; Montalto, M. C.; Agdeppa, E. D.; Mendizabal, M.; Wilson, I. A.; Vanderheyden, J. L. The Imaging Continuum: Bench to Biomarkers to Diagnostics. *J. Labelled Compd. Radiopharm.* **2007**, *50*, 746−769.

(354) Robertson, C. A.; Evans, D. H.; Abrahamse, H. Photodynamic Therapy (PDT): A Short Review on Cellular Mechanisms and Cancer Research Applications for PDT. *J. Photochem. Photobiol., B* **2009**, *96*, 1−8.

(355) Chauhan, P.; Hadad, C.; Sartorelli, A.; Zarattini, M.; Herreros-Lopez, A.; Mba, M.; Maggini, M.; Prato, M.; Carofiglio, T. Nanocrystalline Cellulose−Porphyrin Hybrids: Synthesis, Supramolecular Properties, and Singlet-Oxygen Production. *Chem. Commun.* **2013**, *49*, 8525−8527.

(356) Adler, A. D.; Longo, F. R.; Finarelli, J. D.; Goldmacher, J.; Assour, J.; Korsakoff, L. A Simplified Synthesis for Meso-Tetraphenylporphine. *J. Org. Chem.* **1967**, *32*, 476.

(357) Mannancherril, V.; Therrien, B. Strategies Toward the Enhanced Permeability and Retention Effect by Increasing the Molecular Weight of Arene Ruthenium Metallaassemblies. *Inorg. Chem.* **2018**, *57*, 3626−3633.

(358) Yoo, J. O.; Ha, K. S. New Insights into the Mechanisms for Photodynamic Therapy-Induced Cancer Cell Death. *Int. Rev. Cell Mol. Biol.* **2012**, *295*, 139−174.

(359) Li, S. Y.; Xie, B. R.; Cheng, H.; Li, C. X.; Zhang, M. K.; Qiu, W. X.; Liu, W. L.; Wang, X. S.; Zhang, X. Z. A Biomimetic Theranostic O$_2$-Meter for Cancer Targeted Photodynamic Therapy and Phosphorescence Imaging. *Biomaterials* **2018**, *151*, 1−12.

Chapter 2 – Results and Discussion

2.1. Chemistry Results

2.1.1. The photosensitizers

For the reasons mentioned in the first chapter, the starting molecule for the construction of PDT theranostic agents should be either a porphyrin or a phthalocyanine. In this work, some were bought and used directly for the preparation of the theranostic agents (**Figure 12, P1-P3**), while others were synthesized through an Adler-Longo Method[1] (**Figure 12, P4-P5**), with **P4** being obtained *via* a two-step synthesis that includes reduction of the nitro group.

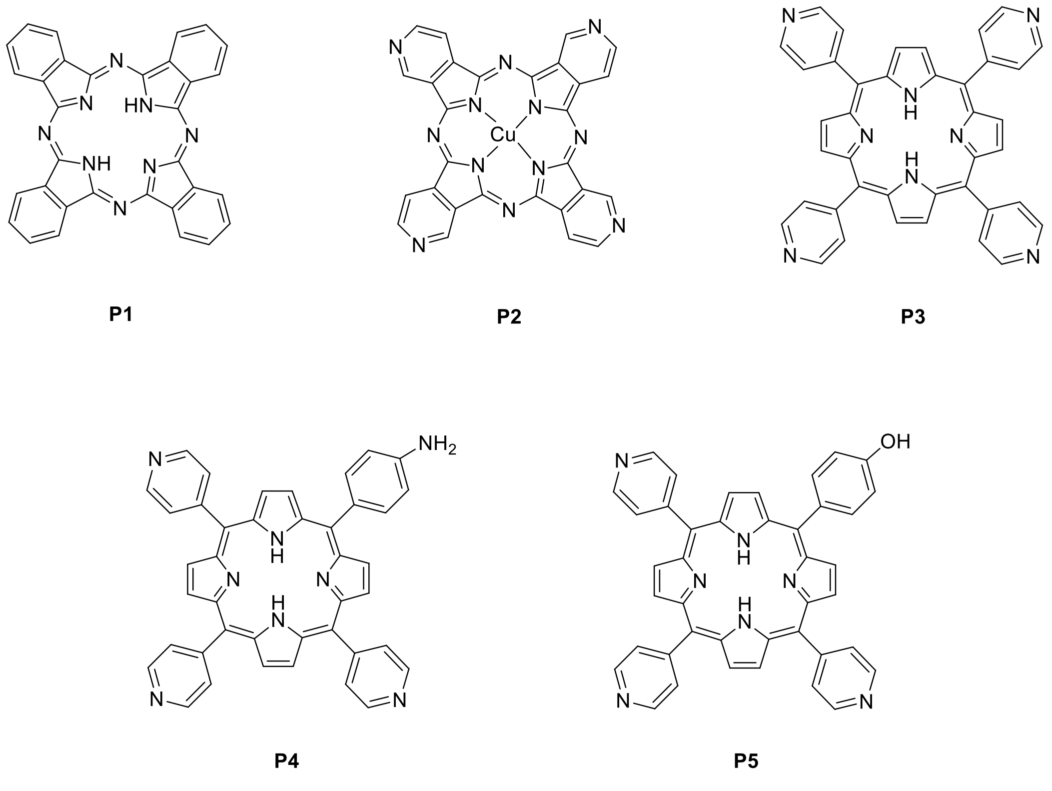

P1 P2 P3

P4 P5

Figure 12 – Structural representation of the photosensitizers used in this work.

Given that the photosensitizer is one of the three essential components for successful photodynamic therapy, modulating its characteristics can influence the overall PDT efficacy. The amine (**P4**) and phenol (**P5**) derivatives of 5,10,15,20-tetra(4-pyridyl)-21H,23H-porphine (**P3**) were added to the commercially available photo-responsive molecules to create a library of compounds. These pyridyl-derivatives can be coordinated to ruthenium metalla-clips, allowing the formation of metalla-assemblies. Then, the phenol or amine function can be exploited to link the metalla-assemblies to cellulose nanocrystals. Synthesis and coordination were carried out efficiently. UV-Vis absorption and fluorescence spectra were measured for both porphyrins, and their absorption spectra in dichloromethane showed the typical Soret and Q-bands. Certain features, such as relative hydrophobicity, must be present in order to obtain the most efficient PS. Lipophilic molecules diffuse quickly and passively into cancer cells, settling in internal membrane structures such as mitochondria and endoplasmic reticulum (ER), whereas more polar molecules are taken up by the active process of endocytosis, necessitating a longer DLI. However, one of the most known drawbacks of porphyrins and phthalocyanines is their low solubility and their tendency to aggregate in aqueous media.

2.1.2. Constructing Metalla-clips and metalla-assemblies

Gathering all this information, it was decided to take the photosensitizers, both bought and synthesized, and construct metalla-assemblies with the aim of ameliorating their solubility and stability for their posterior use *in vitro* and *in vivo*. This requires several steps starting with the synthesis of organic ligands/spacers to obtain to ruthenium metalla-clips. From those, the most promising were used to build tetrapyrrolic metalla-assemblies. All these steps are further described in the **Experimental Section** (**Chapter 4**).

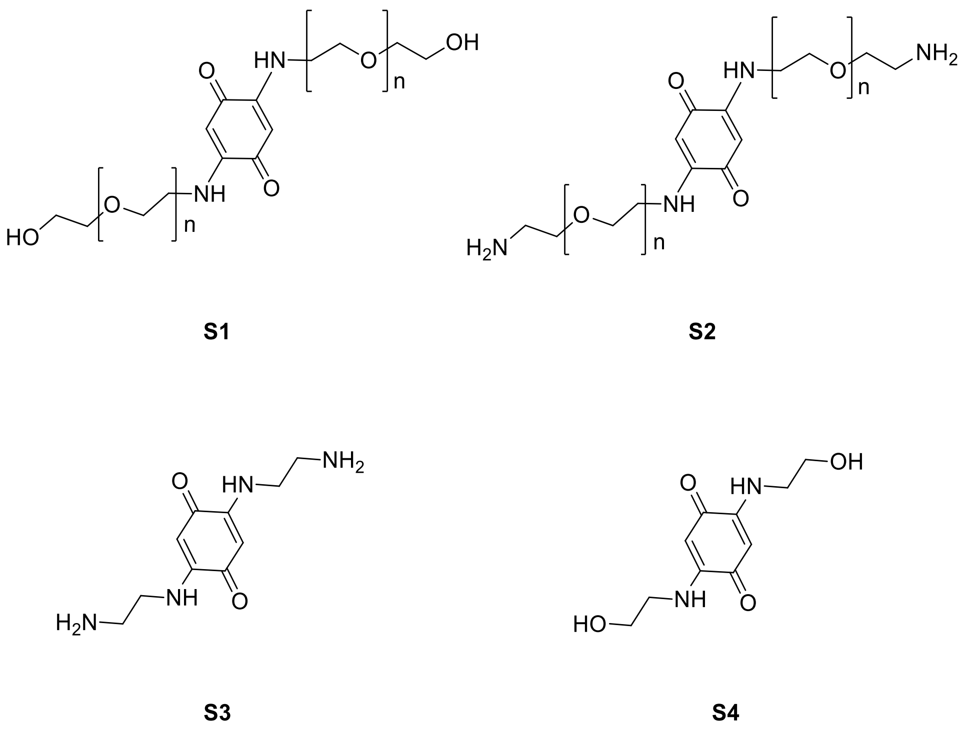

Figure 13 – Structural representation of **S1**-**S4**.

Firstly, the different **S1**-**S4** spacers / organic ligands (**Figure 13**) were synthesized following a protocol found in the literature,[134] and characterized before being used to construct metalla-clips **C1**-**C4** (**Figure 14**). The ^{1}H NMR spectra of **S1** and **S2**, more specifically the number of protons attributed to the CH_2 groups, allowed to determine the n value for the PEG moieties covalently bound to the benzoquinone backbone. For **S1**, it was concluded that n=1, while for **S2** n=3. For **S3** and **S4**, the protocol used was the same,[134] resulting in the combination of 1,4-benzoquinone with either ethylenediamine or ethanolamine, respectively.

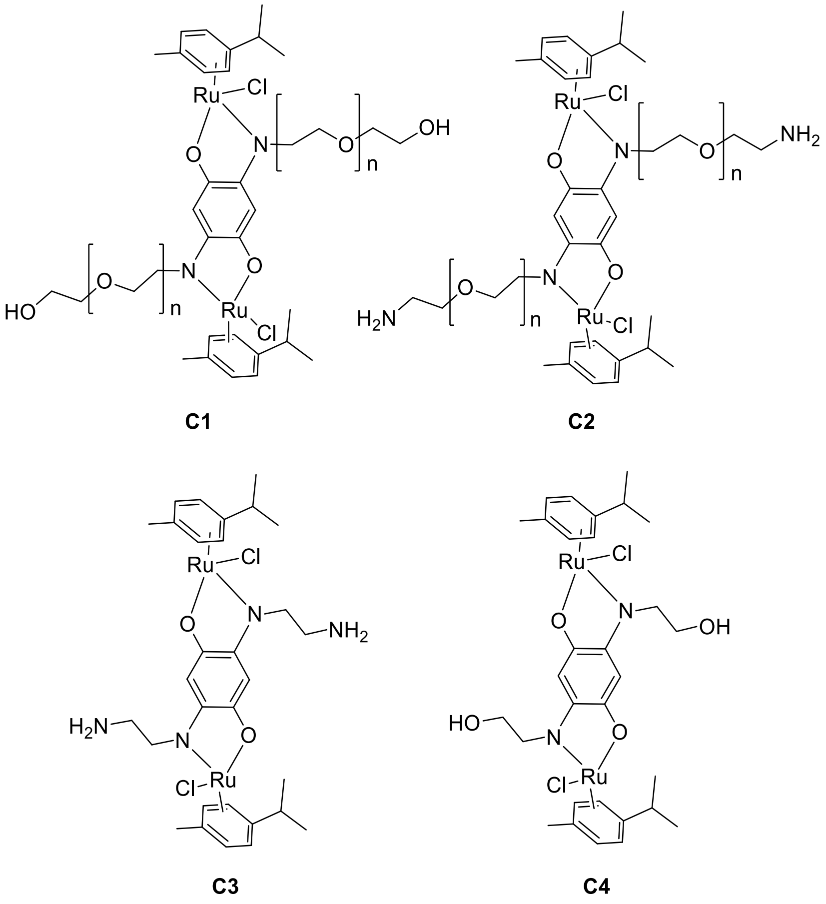

Figure 14 - Structural representation of metalla-clips **C1**-**C4** resulted from the reaction of spacers **S1**-**S4** with dichloro(*p*-cymene)ruthenium(II) dimer

The ^{1}H NMR spectra of **C1** and **C2**, compared to the non-coordinated **S1** and **S2**, not only presented new signals, at for example ~8.40 and 8.80 ppm (aryl protons), but also a downfield chemical shift of the benzoquinone protons. In the case of **S1** to **C1**, the signal for the aromatic protons in the benzoquinone moiety shifts from 7.78 to 7.95 ppm, and for **S2** to **C2** it goes from 7.28 to 7.42 ppm. The peaks corresponding to the -NH protons disappear when the spacer is coordinated to ruthenium, and the signals for the -NH_2 and -OH PEG moieties are also shifted upfield, more specifically the protons from the two OH groups in **S1** shift from 2.51 to 1.19, while the NH_2 protons in **S2** change from 2.89 to 2.25 ppm. The downfield and upfield shifts were not observed to such extent when **S3** was turned into **C3**. For example, the signal for the benzoquinone aromatic protons has only a slight shift from 7.29 to 7.31 ppm, and for the protons in the side chain -NH_2 groups from 3.68 to 3.72 ppm, suggesting that these changes might be due to the length of the side chains linked to the benzoquinone backbone. From these three spacers, **C3** was chosen to proceed for the construction of metalla-assemblies **M1**-**M3**, using **P1**-**P3;** and **C4** for **M4** and **M5,** respectively (**Schemes 1** and **2**). The main reason for the choice of **C3** and **C4** was that they have a similar structure, only changing the functional group in the side chain, and therefore would be easier to compare between each other *in vitro* and *in vivo*, reducing the variables for any differences that might be observed.

Regarding the formation of the metalla-assemblies **M1**, **M2** and **M3,** this was first confirmed by ^{1}H NMR, and later through electrospray ionization mass spectrometry (ESI-MS), as well as elemental analysis. Typical peak multiplicities and chemical shifts of the arene ruthenium units are observed in their ^{1}H NMR spectra (**Figure 15**). The ^{1}H NMR spectra of **M1, M2,** and **M3** show typical peak multiplicities and chemical shifts of the arene ruthenium units. While the metalla-clip signals are slightly displaced downfield, signals connected with the aromaticity of the porphyrin or phthalocyanine panels between 9.00 and 8.00 ppm are consistent with the creation of the metalla-assemblies. The signal patterns of the related phthalocyanines and *p*-cymene protons are comparable in the ^{1}H-NMR spectra of **M1** and **M2** in DMSO-d6, but **M3** shows signals associated with the porphyrin and *p*-cymene precursors. Between 9.00 and 7.00 ppm, aryl protons are detected, with signals between 8.99-8.36 and 8.87-8.35 ppm assigned to the aromatic protons of the phthalocyanine moieties of **M1** and **M2**, respectively, and from 8.66 to 8.15 ppm attributed to the pyridyl and -pyrrolic protons of **M3**. The peak for the aromatic protons of spacer **S3** in all compounds was observed at 7.2-7-0 ppm. While for the aromatic protons of the *p*-cymene, the signals can be found between 6 and 5 ppm, as expected. Furthermore, the –CH isopropyl groups have a peak at approximately 2.60 ppm. The methyl groups and isopropyl protons from *p*-cymene can be found from 2.10 to 1.20 ppm. Alkyl protons associated with the side chains of the spacer, as well as the -NH_2 protons, appeared from 3.75 to 2.75 ppm. Finally, internal NH protons were detected at -2.9 ppm for **M1** and **M3**, but not for **M2**, since'**M2**'s core is coordinated with copper (II).

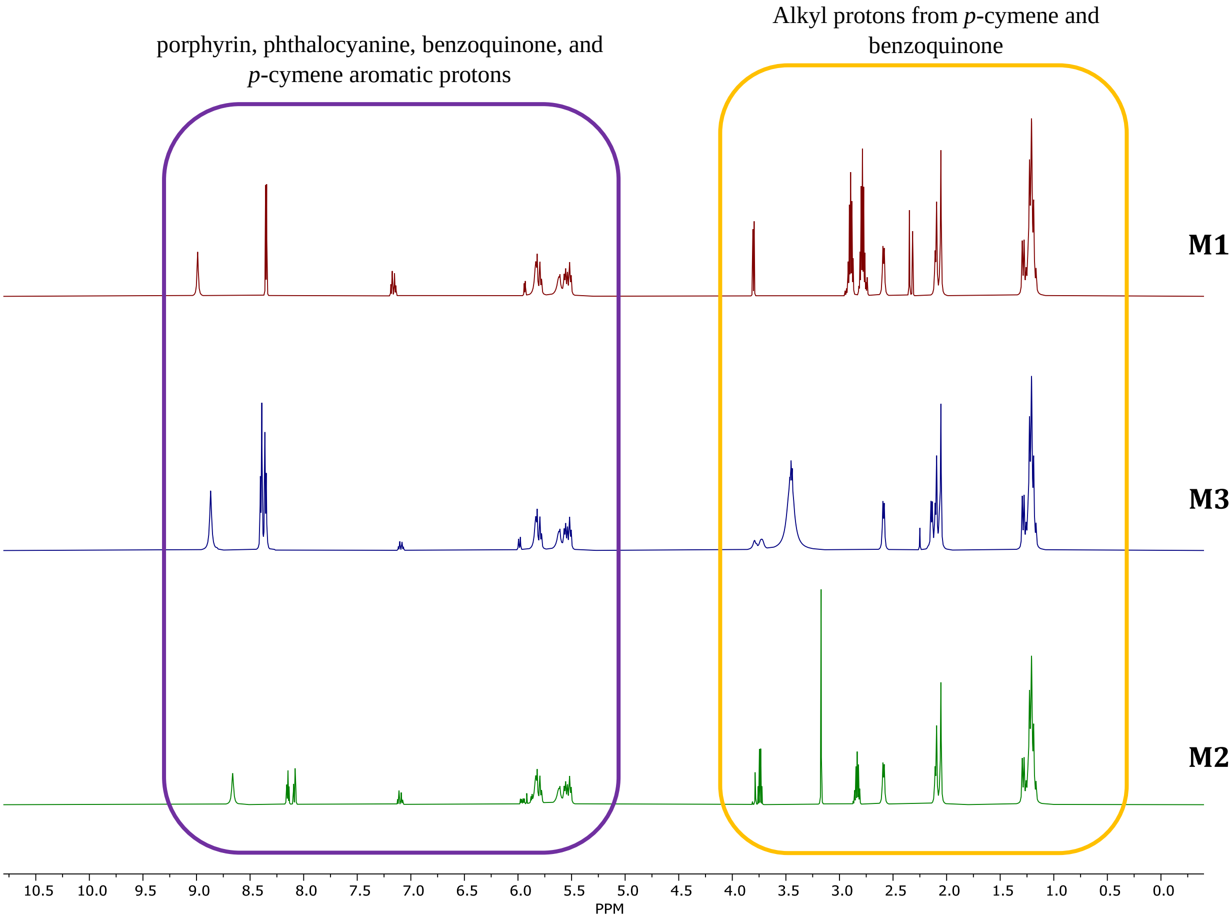

Figure 15 - ^{1}H NMR spectra (between 0 and 10 ppm) of **M1**, **M2**, and **M3,** respectively**,** in DMSO-d6.

2

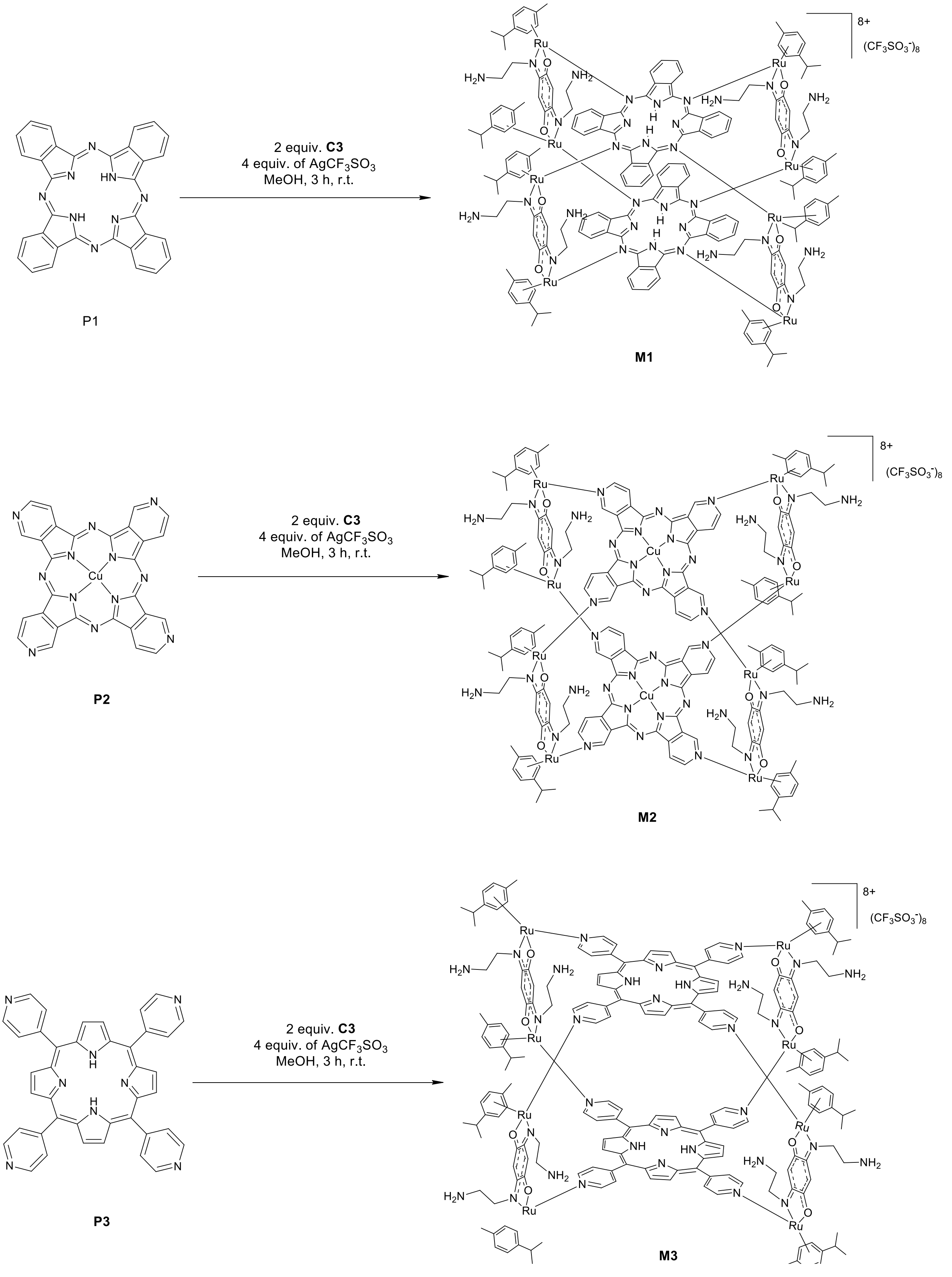
P1
2 equiv. **C3**
4 equiv. of $AgCF_3SO_3$
MeOH, 3 h, r.t.
M1
8+
$(CF_3SO_3^-)_8$
P2
2 equiv. **C3**
4 equiv. of $AgCF_3SO_3$
MeOH, 3 h, r.t.
M2
8+
$(CF_3SO_3^-)_8$
P3
2 equiv. **C3**
4 equiv. of $AgCF_3SO_3$
MeOH, 3 h, r.t.
M3
8+
$(CF_3SO_3^-)_8$

Scheme 1 - Overview of the synthetic route for the metalla-macrocyclic assemblies **M1-M3**.

Mass spectrometry was also used to confirm the formation of the metalla-assemblies (**Figures S1-S3**, supplementary information). Due to the loss of the triflate (OTf−) counterion, a series of peaks with different charge states from 4+ to 6+ was observed for **M1-M3**. It is interesting to observe that for both phthalocyanine-based metalla-assemblies **M1** and **M2**, and for the porphyrin-based metalla-assembly **M3,** the pattern and species found in mass spectrometry was very similar. The spectra for **M1** and **M2** showed the typical pattern of arene ruthenium metalla-assemblies with trifluoromethanesulfonate as counterions. Most noticeable were the tetra-, penta-, and hexacationic peaks, with the most prominent of these being the pentacationic peak corresponding to [**M1**–5($CF_3SO_3^-$)]$^{5+}$ and [**M2**–5($CF_3SO_3^-$)]$^{5+}$, respectively at m/z = 849.52 and m/z = 920.54. In comparison, for **M3**, the parent peak could be attributed to the tetracationic species [**M3**–4($CF_3SO_3^-$)]$^{4+}$ at m/z = 1151.22. Peaks for the penta-, and hexacationic species [**M3**–5($CF_3SO_3^-$)]$^{5+}$ and [**M3**–6($CF_3SO_3^-$)]$^{6+}$ could also be observed at m/z = 891.178 and m/z = 717.82, respectively.

After the formation of metalla-assemblies **M1-M3**, it was decided to also explore metalla-clip **C4** and construct metalla-assemblies **M4** and **M5** (**Scheme 2**).

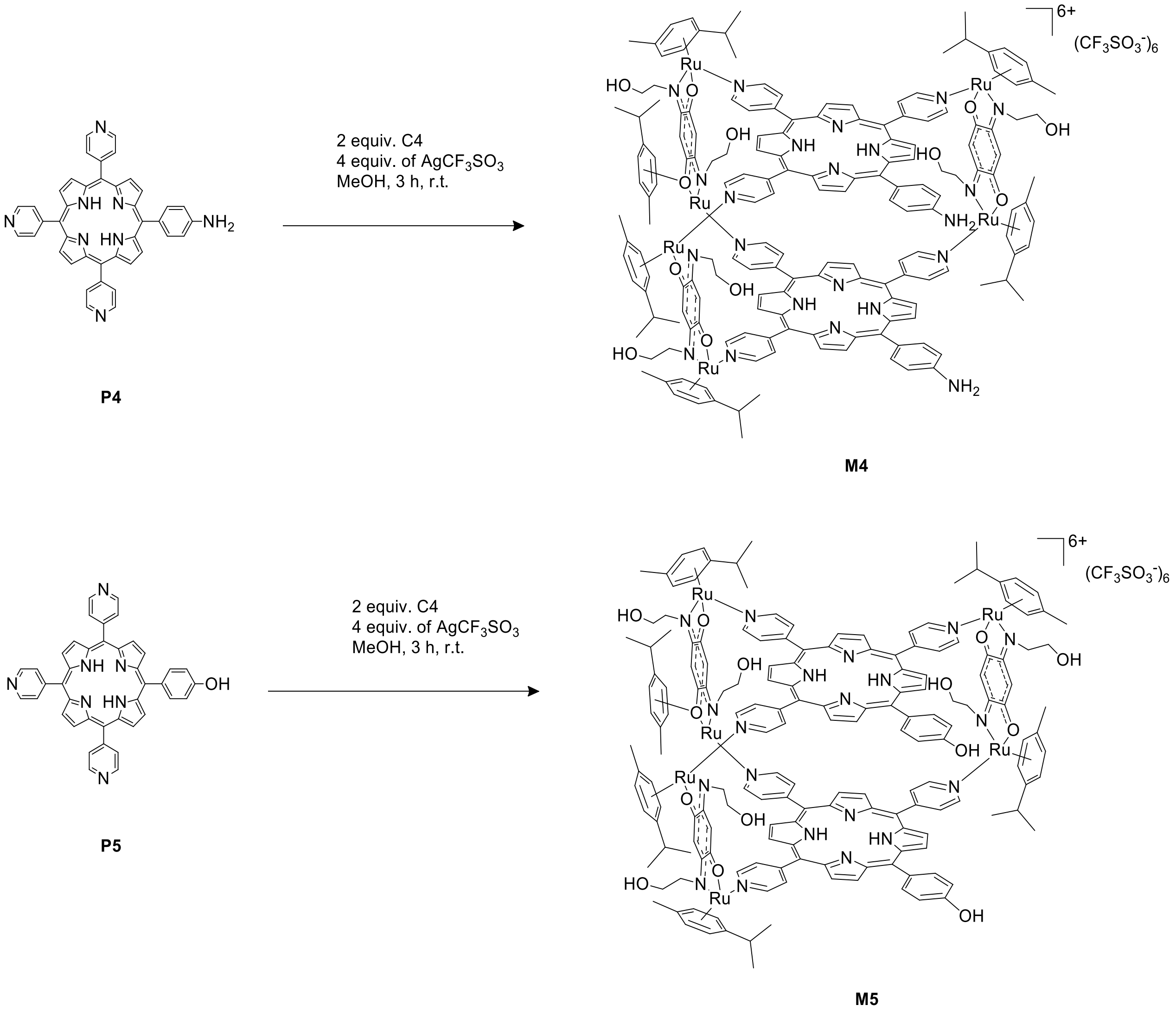

Scheme 2 - Overview of the synthetic route for the metalla-macrocycle assemblies **M4** and **M5**

The obtained supramolecular systems possess the arene ligands that protect and stabilize the ruthenium atom in a +2 oxidation state; multidentate anionic spacers that modulate the size of the cavity; and multidentate N-donor panels that dictate the shape and geometry of the assembly. The molecular structure of the metalla-assemblies was confirmed by a combination of NMR spectroscopy (**Figure 16**), mass spectrometry (**Figures S4-S5**, supplementary information), and elemental analysis. Upon formation of these metalla-prisms, the ^{1}H NMR signals assigned to the metalla-clips can still be observed, while new signals associated with the porphyrin panels appear (10.0-7.5 ppm, aromatic signals).

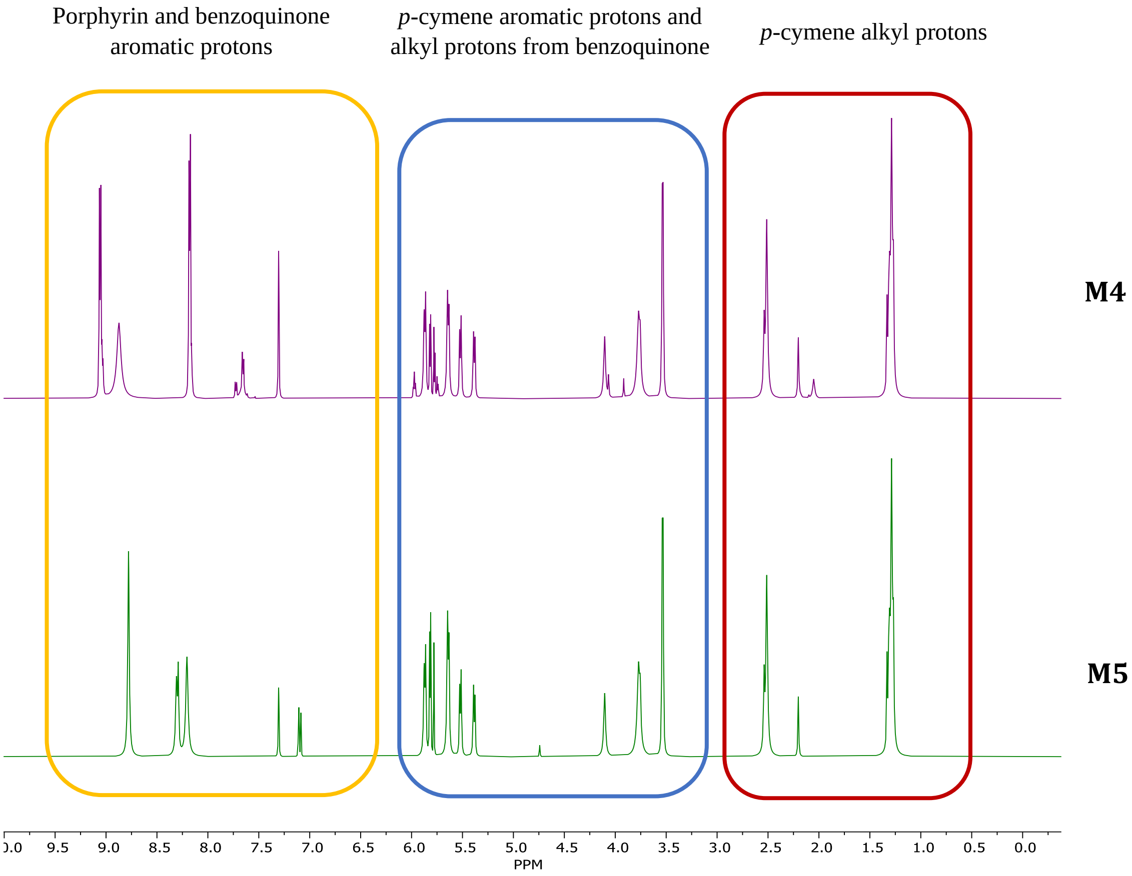

Figure 16 – ^{1}H NMR spectra (between 0 and 10 ppm) of **M4** (top) and **M5** (bottom) in DMSO-d$_6$

These observations are consistent with the formation of the metalla-assemblies. The well-defined signals in the ^{1}H NMR spectra support the formation of a discrete and highly symmetrical assembly as a sole thermodynamic product. The ^{1}H NMR spectra of **M4** and **M5** in DMSO-d$_6$ display a similar signal pattern of the corresponding porphyrin and *p*-cymene protons. The *p*-cymene moieties show peaks around δ ~1.3-1.2 ppm for the protons of the isopropyl groups (alkyl protons), singlets around ~2.5 ppm for the methyl groups (alkyl protons), and signals in the 6.0-5.0 ppm corresponding to aromatic protons. Around 9.1-7.1 ppm, more aromatic signals can be found corresponding to the pyridyl and *β*-pyrrolic protons of the porphyrin moieties as well as the corresponding aromatic protons of the aniline (**M4**) and phenol (**M5**) groups. In complexes **M4** and **M5**, additional signals at ~ 4.1 and ppm can be found for the protons of the hydroxyl groups of spacer **S4**. Finally, at δ ~ 7.3 ppm, a peak corresponding to the benzoquinone protons is observed. The signals of the porphyrinic NH protons were observed at -2.9 ppm.

From all the synthesized metalla-assemblies, **M4** and **M5** were chosen to proceed for the next modification which consists of grafting cellulose nanocrystals. The choice to use these two metalla-assemblies came down to the fact that they have extra functional groups (amine and phenol) that can be used to graft them to the CNC, while still leaving the hydroxyl groups in the metalla-clip strucure free if necessary for other posterior modifications. Due to this, and to the fact that these will be used for PDT treatment *in vitro*, UV-Vis absorption and fluorescence spectra were measured in DMSO for both metalla-assemblies. Their absorption spectra (**Figure 17**) showed the typical Soret band (415 and 412 nm for **M4** and **M5**, respectively) and Q-bands of porphyrin-based compounds in the region of 500-650 nm, which are attributed to the absorption transition between the ground state and the first excited singlet state (S0–S1).

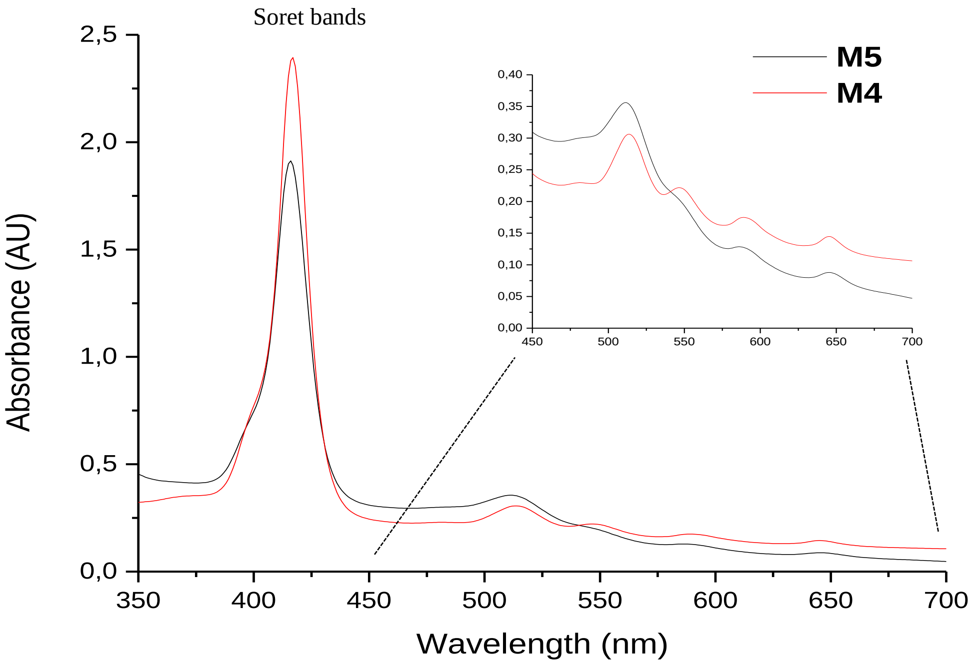

Figure 17 – UV-Vis spectra of **M4** (red) and **M5** (black) in DMSO. The peaks show the typical Soret band at 412 and 415 nm, respectively, as well as the Q-bands (500-650 nm).

2.1.3. Grafting to Cellulose Nanocrystals

After synthesis and characterization of the metalla-assemblies, two of them were selected to be grafted to oxidized cellulose nanocrystals, which are obtained by hydrolysis of cellulose with sulfuric acid solution (64% w/w) followed by several washings, centrifugation and dialysis against distilled water until neutrality.[135] This acid hydrolysis consists in breaking cellulose chains within the amorphous domain, thus getting free nanocrystals, which can then be selectively oxidized in their primary alcohols with TEMPO. The CNCs suspension can be easily linked to other moieties through the newly added carboxylic acid groups. The best results were achieved through a covalent bond between the functional groups in each of the photosensitizers; amine group in **M4**, or the phenol group in **M5**, and the oxidized CNCs (**Scheme 3**).

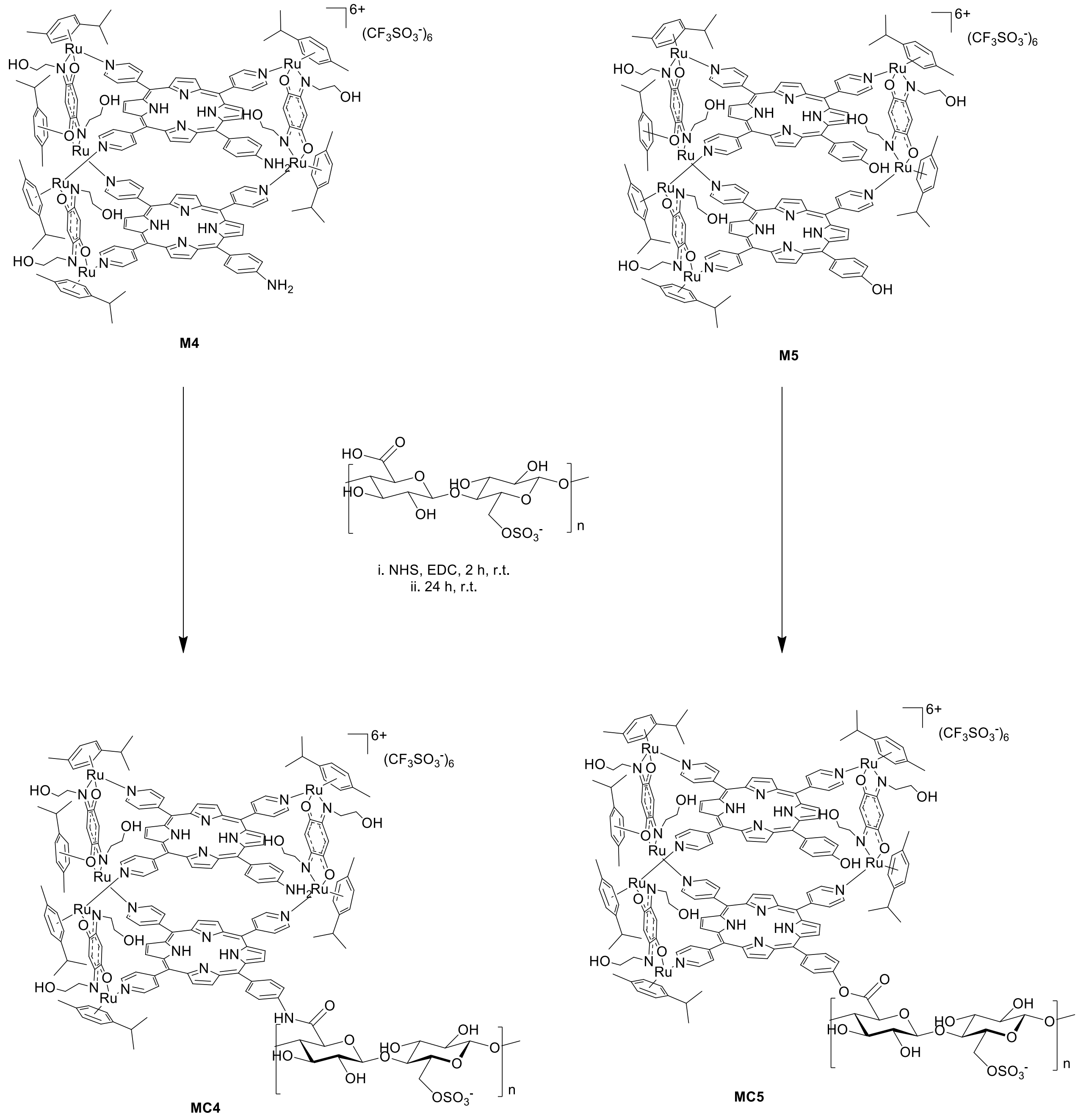

Scheme 3 - Synthetic route for the grafting of **M4** and **M5** to CNCs by reaction with N-hydroxysuccinimide (NHS) and 1-ethyl-3-(-3-dimethylaminopropyl) carbodiimide hydrochloride (EDC).

Regarding their IR spectra, the observed peaks (**Figure 18**) around 3700-2900 cm^{-1} are characteristic to the stretching vibration of O-H and C-H bonds in polysaccharides.[136,137] This broad peak includes also the inter- and intra-molecular hydrogen bond vibrations of cellulose.[138] The band at 2890 cm^{-1} is attributed to CH stretching vibration of the hydrocarbon constituents of polysaccharides.[136,139] Typical bands assigned to cellulose were also observed in the region of 1700-800 cm^{-1}. These peaks correspond to vibrations of water molecules absorbed in cellulose,[136,139] or belong to stretching and bending vibrations of $-CH_2$, -CH, -OH and C-O bonds in cellulose.[140,141] The band at around ~1100 cm^{-1} is associated with the amount of the crystalline structure of the cellulose, while the band at ~750 cm^{-1} is assigned to the amorphous region in cellulose.[142] Compared to the initial CNCs, the appearance of a strong peak at 1739 cm^{-1} suggests the presence of an ester bond presumably between the hydroxyl group of the porphyrin in metalla-assembly **M5** or the hydroxyl groups in the alkyl chain of the metalla-assembly with the cellulose nanocrystals. On the other hand, the strong peak around 1644 cm^{-1} suggests the presence of an amide bond between the carboxylic function of CNCs and the amine group of the porphyrin in metalla-assembly **M4**. Simultaneously, the ATR FT-IR spectrum of both CNCs-linked metalla-assemblies showed that the intensities of the C–H vibration band of methyl groups (2820-2976 cm^{-1}) were strengthened. The N–H bending vibration peak of porphyrin units appeared at 1658 cm^{-1}. All this supports the successful combination of CNCs with porphyrin derivatives. The molar grafting ratio (%) was calculated from the difference between the reacted porphyrin amount and the unreacted porphyrin present at the end of the grafting reaction. [143,144]

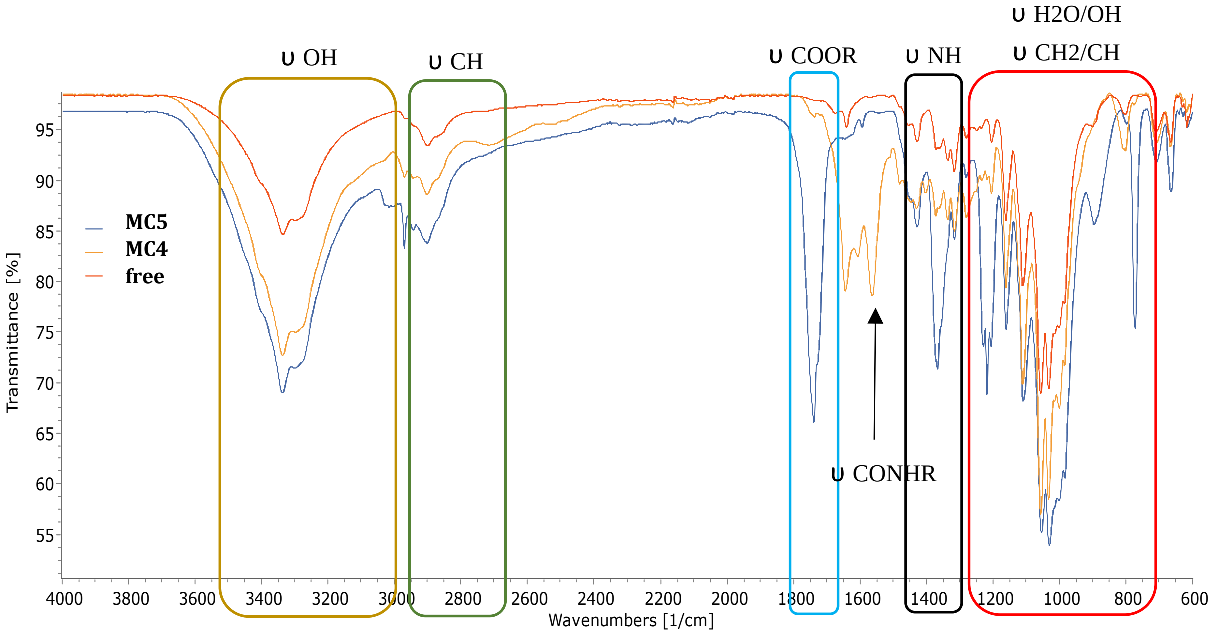

Figure 18 – IR spectra **MC4** (orange) and **MC5** (blue), and free CNC (red).

2.2. Radiolabelling & Kinetic Studies

Porphyrin **P5**, its respective metalla-assembly **M5**, as well as the CNC-grafted derivative **MC5** (**Scheme 4**), were chosen to be radiolabelled because **M5** and **MC5** showed the most promising results *in vitro*, making them the most interesting molecules to be used as theranostic agents. For such, all three compounds were radiolabelled with two different radionuclides, technetium-99m and indium-111, giving us two separate lines of action for the posterior cellular uptake and *in vivo* imaging, and allowing them to be compared structurally. In addition, having the same compounds radiolabelled with either one of the radionuclides allows comparison between each radionuclide and determine which one is the best choice for the creation of theranostic agents.

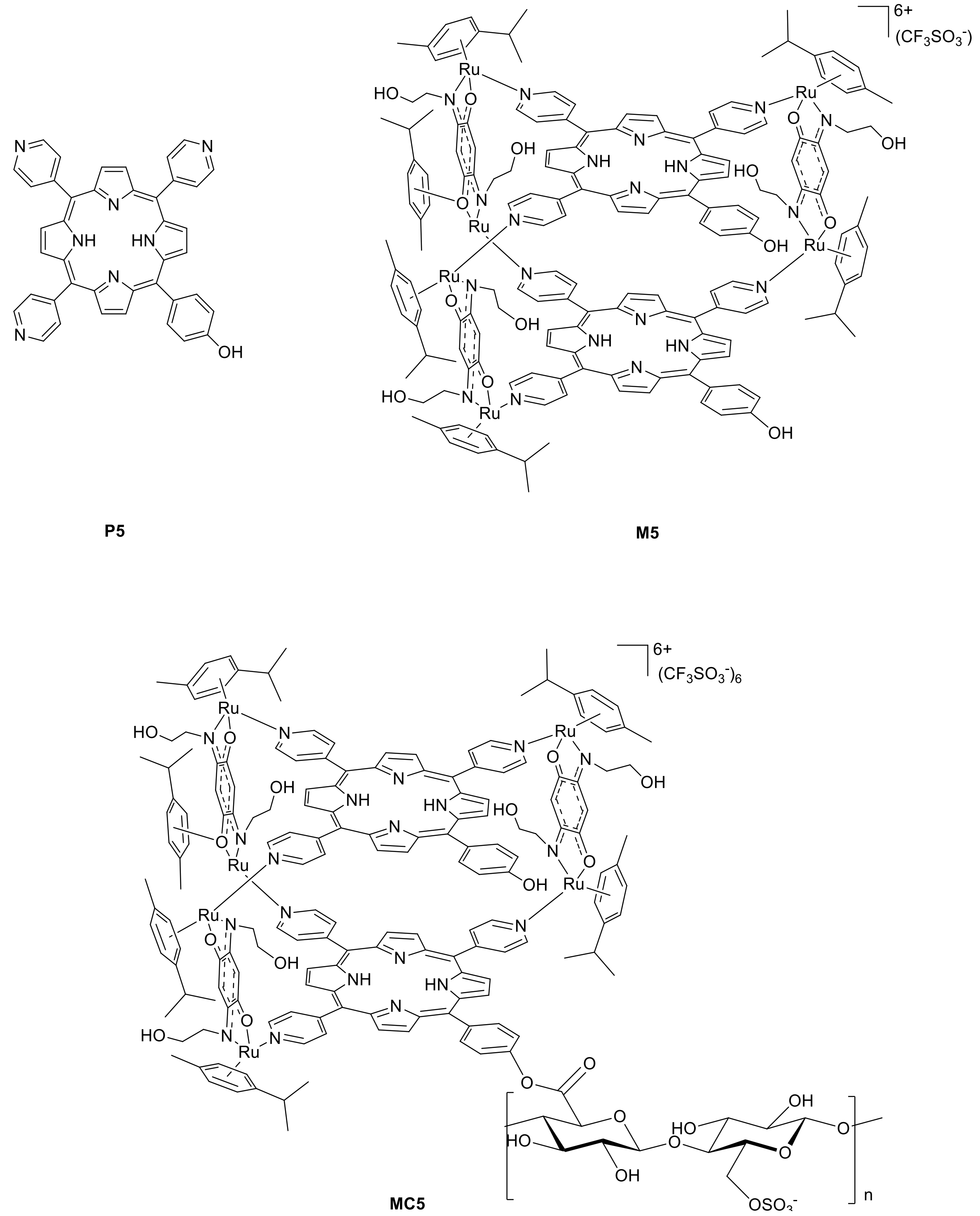

P5

M5

MC5

Scheme 4 – Structural representation of **P5**, **M5**, and **MC5.**

Regarding the radiolabeling of **P5-MC5**, a simple method of direct labelling was performed for both radionuclides used:

2.2.1. Radiolabelling with technetium-99m

After the synthesis, direct radiolabelling was performed and showed promising potential of these molecules to be used as multimodal imaging agents, which is the main goal of this Thesis. Radiolabelling with technetium-99m was completed with a radiochemical incorporation of over 90% for all three compounds. It is possible to conclude that the reaction for **P5** is complete (93%) and that little to no traces of free-$[^{99m}Tc]TcO_4^-$ are observed. The same results were achieved for **M5** (98%) and **MC5** (95%). **Figures 19** and **20** shows the successful radiolabelling of the compounds.

It should be noted that the basic chemical principle of technetium-99m labelling involves the reduction of technetium-99m to a lower oxidation state that will bind to a chelating molecule of interest, in this case **P5**-**MC5**. In the pertechnetate ion from the eluted $[^{99m}Tc]TcO_4^-$, technetium has the oxidation state +7, and after the addition of the stannous ions (Sn^{2+}) in HCl reduction to technetium +4 occurs. It is only in this low oxidation state that technetium-99m can form a complex with molecules through the formation of bonds between Tc and the amine groups of the porphyrin core (the bond of the nitrogen atom with hydrogen is replaced by a bond of the nitrogen atom with technetium). It is therefore important that the pH of the reaction is neutralized after the reduction of Tc and before the addition of **P5**-**MC5**, because otherwise the labelling will not occur.

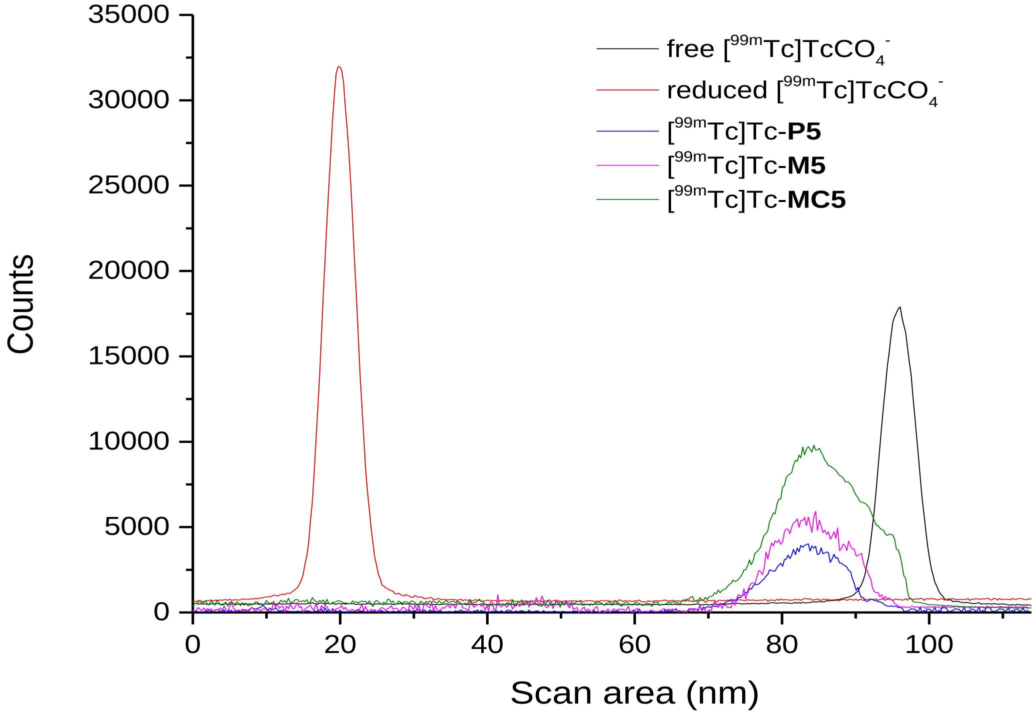

Figure 19 - Radiochemical data of free, reduced $[^{99m}Tc]TcO_4^-$, and radiolabelled compounds. The radio-iTLCs were developed on Whatman 1 MM with saline as the mobile phase, RCC 99.0%.

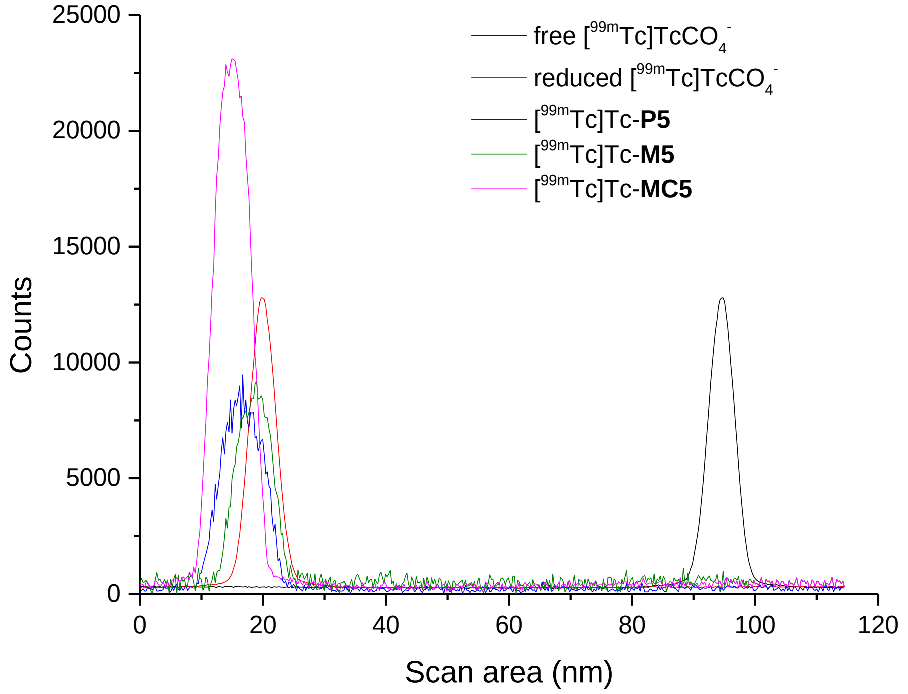

Figure 20 - Radiochemical data of free, reduced [^{99m}Tc]TcO$_4^-$, and radiolabeled compounds·. The radio-iTLCs were developed on Whatman 1 MM with acetone as the mobile phase, RCC 99.0%.

Figure 21 shows the stability of [^{99m}Tc]Tc-**MC5** at 37 °C on different mediums for different timepoints to better replicate physiological conditions, beginning after 15 minutes and going as long as 24 h.

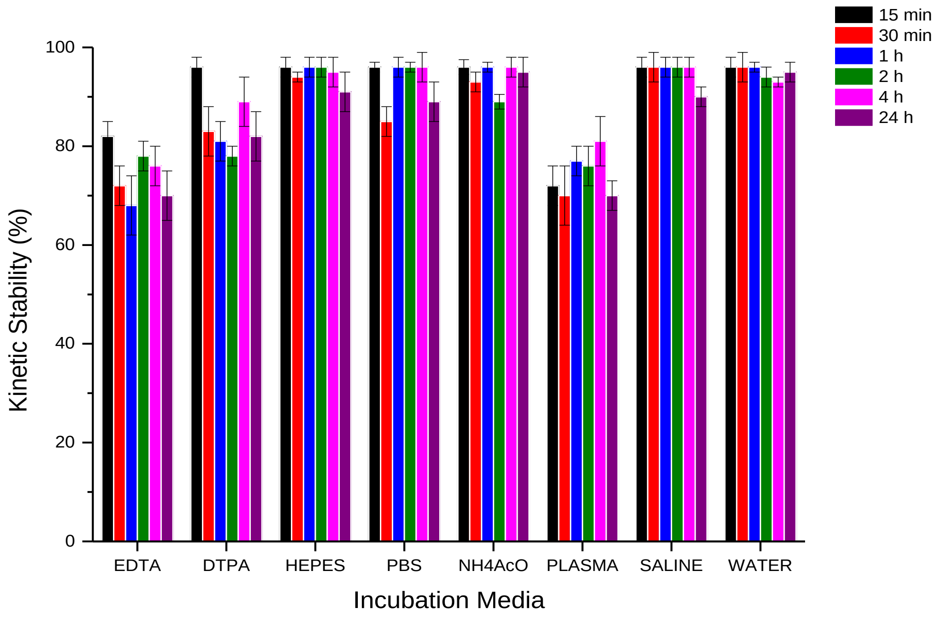

Figure 21 - Graph presenting the results obtained from kinetic stability tests of [^{99m}Tc]Tc-**MC5**. The radioactive molecule was incubated at 37 ˚C with different media (1:10) for up to 24 h. Error bar stands for standard error (±SE), calculated from three repeated measurements.

The different media chosen for the kinetic studies have a reason: plasma, water and saline mimic the main components of the bloodstream where the compound will be injected for *in vivo* experiments, and so it is believed to be a good idea to test the stability of these compounds in them before proceeding to these experiments to have an idea of how the compound behaves. Besides this, the behaviour of these compounds in DTPA and EDTA solutions is also important to be studied because EDTA and DTPA form stable complexes with most transition metals such as Cu, Tc, and Zn meaning they can be used as antagonistic chelators, thus pulling out the radionuclide from [^{99m}Tc]Tc-**P5,** [^{99m}Tc]Tc-**M5**, and [^{99m}Tc]Tc-**MC5** into the DTPA or EDTA structure. Finally, HEPES and NH_4AcO buffer solutions are the main buffers used for radiolabelling, so it is also important to verify the stability of these compounds in these media.

It is possible to determine that there is no significant difference as late as 24 h when it comes to kinetic stability for most of the media tested, with some differences occurring mainly in the cases of EDTA and plasma, right after 15 min, but after this timepoint they seem to stay stable for the rest of the study. This could be due to the fact that, as said before, EDTA is a strong chelator of technetium-99m, and that plasma also has components such as magnesium ions that can compete with the technetium for the coordination with the centre of the porphyrins. Similar results were observed for [^{99m}Tc]Tc-**P5** and [^{99m}Tc]Tc-**M5.**

2.2.2. Radiolabelling with indium-111

Direct radiolabelling was also achieved with [^{111}In]$InCl_3$ under mild reaction conditions (60 min at 60˚C) with radiochemical incorporation of over 95% for all compounds (**Figure 22**). Apart from the different radionuclide used, the main difference between the two protocols is the pH, while for technetium-99m labelling, the compound is added to a previously neutralized solution of reduced technetium-99m, for indium-111, the reaction did not seem to be successful at pH 7, resulting in a much lower radiochemical incorporation (< 50%). This demonstrated the importance of the pH depending on the radionuclide used, with the reaction needing an acidic media (pH 5.5) to occur if indium-111 is being used instead of technetium-99m.

A kinetic study was once again carried out in order to follow the stability. An example for compound [^{111}In]In**-MC5** can be found in **Figure 23**. When analysing the kinetic stability results, it is possible to observe that, contrary to its analogue [^{99m}Tc]Tc**-MC5**, there is a significant difference over time for some of the media used, more specifically in the cases of saline, water, DTPA and EDTA solutions. In these media, it can be detected that [^{111}In]In**-MC5** is degraded as early as 30 min after being incubated, and that after 24 h, the kinetic stability drops as low as 10% in the cases of saline and water. However, in ammonium acetate, PBS, and plasma, the stability seems to be constant for all timepoints, and since the radiolabelling is performed in NH_4AcO, and is then expected to be injected into the mouse's bloodstream, it is believed that the stability of the compound will be sufficient, and therefore the experiments *in vivo* can be performed. Similar results were observed for [^{111}In]In**-P5** and [^{111}In]In**-M5**.

Lastly, the necessity to determine the ideal stoichiometry for the radiolabelling process was obvious, due to the presence of two product peaks, meaning that, since it is expected that the radionuclide attaches to the porphyrin centre and that for [^{111}In]In**-M5** and [^{111}In]In **-MC5** there are two porphyrin moieties per molecule, it can label either one or both of them, which makes the results not reliable. The ideal conditions were found to be 1:1. Thus, suggesting the radiolabelling of only one porphyrin per system, which allows for a more reliable comparison between the radiolabelled-**P5** and radiolablled-**M5** and **MC5**, because **P5** consists of the porphyrin by itself, and therefore when reading the activity for each system, linear correlation can be traced between all of them.

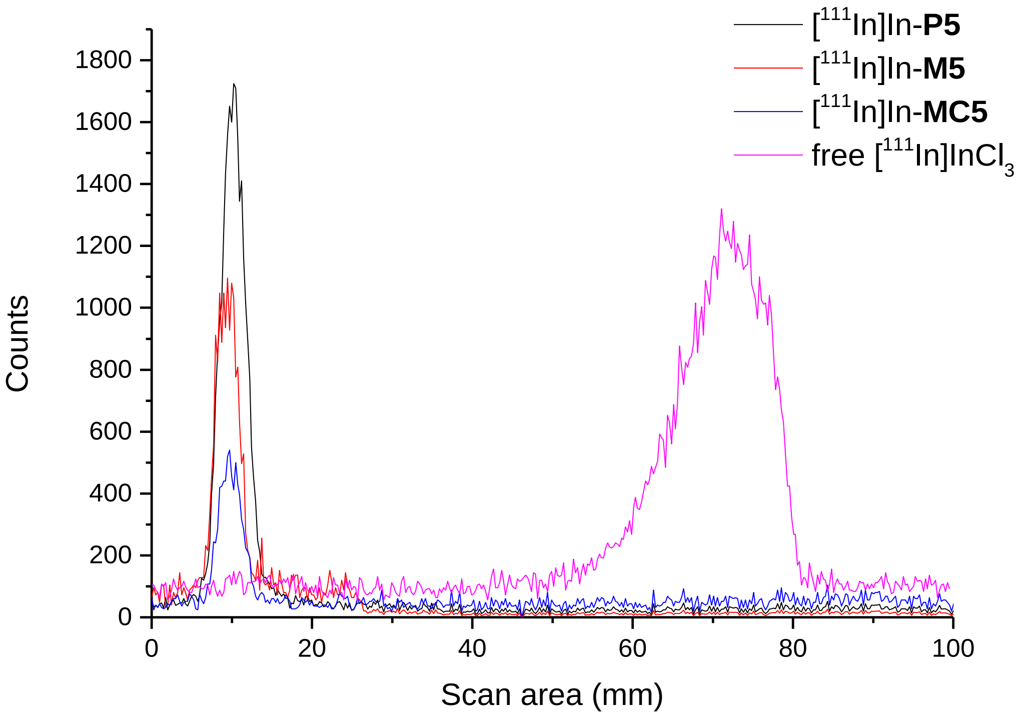

Figure 22 - Radiochemical data of free [^{111}In]InCl$_3$, and radiolabelled compounds. The radio-iTLCs were developed on Whatman paper 3 MM with EDTA 1M as the mobile phase showing RCC 95.0%.

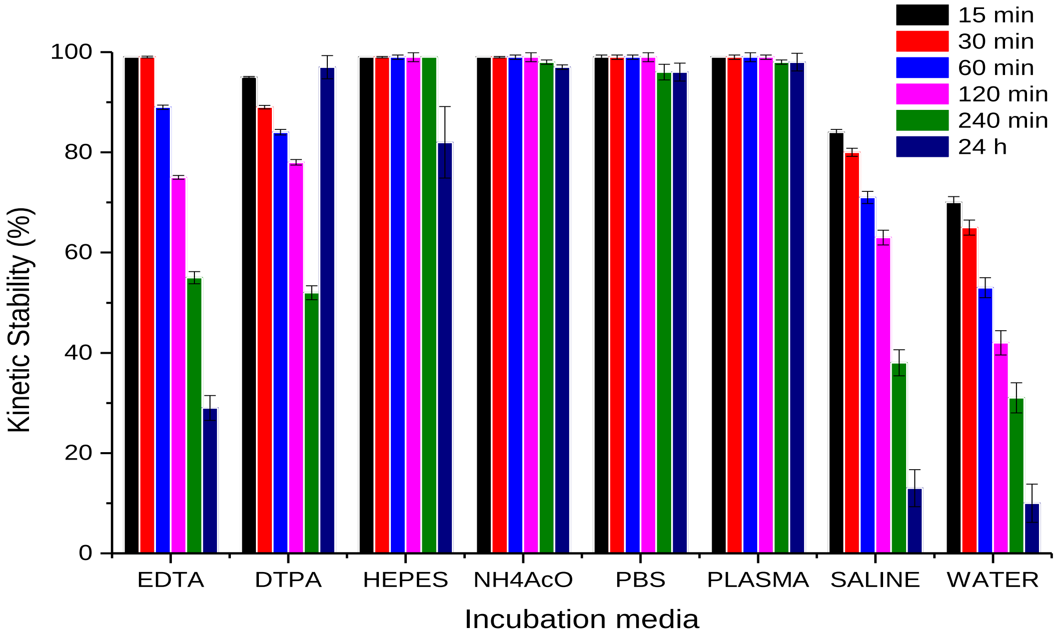

Figure 23 - Graph presenting the results obtained from kinetic stability tests of [^{111}In]In-**MC5**. The radioactive molecule was incubated at 37 ˚C with different media (1:10) for up to 24 h. Error bar stands for standard error (±SE), calculated from three repeated measurements.

In summary, in this section we discussed the synthesis and characterization of different organic ligands, metalla-clips, tetrapyrrolic macrocycles and cellulose nanocrystals. After having all these components, different combinations were made that culminated in a library of compounds that can be tested *in vitro* and *in vivo*, regarding their PDT action, inhibition of metabolic activity, as well as their ability to be used as imaging probes. Compounds **M4** and **M5**, built from **C4**, were further functionalized and linked to CNCs forming **MC4** and **MC5**, in order to understand the influence of adding these to their structure at the *in vitro* and *in vivo* level. Since **P4, P5, M4, M5, MC4**, and **MC5** are all novel compounds, they were tested *in vitro* and comparison was performed.

2.3. The *in vitro* Results

Having several components in our systems (**M1**-**M5**), photosensitizers (**P1**-**P5**), organometallic spacers (**C1**-**C4**), and cellulose nanocrystals (**MC4**-**MC5**), our first goal was to evaluate the impact of each component on the *in vitro* activity. Therefore, various experiments were designed to answer this basic question.

2.3.1. Metabolic Inhibition Assays

To identify the best photosensitizers, the **C3** series was tested. In short (**Figure 24**), we first start by growing and seeding the desired cell lines into plates at a specific density of cells per well. After giving the cells time to attach to the bottom of the wells, a series of dilutions for each compound was prepared and administered. After an incubation period, tests were performed; one involving irradiation of the cells and one that is exactly the same, except there is no irradiation in order to check basic cytotoxicity of the compounds in the dark. The next step implies the performance of MTT assays, a spectrophotometric method that, based on the functional state of the cells, allows for simple, rapid, and accurate evaluation of proliferation rate and cell viability. In parallel, cytotoxicity studies after irradiation of metalla-assemblies **M4** and **M5**, with their corresponding porphyrins and cellulose grafted compounds (**MC4**-**MC5**), were carried out in order to evaluate their potential as photosensitizer candidates for PDT.

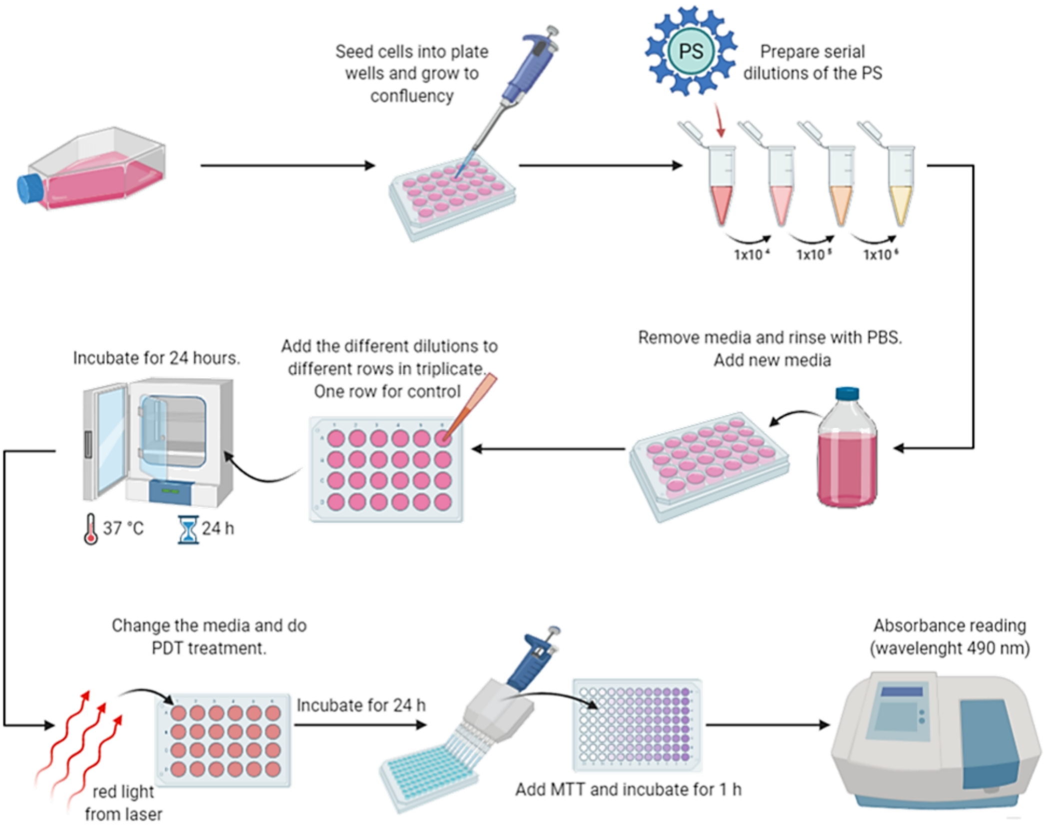

Figure 24 – Schematic representation of an *in vitro* study from cell culture to PDT treatment and metabolic inhibition assays.

The first step was to find the ideal conditions for these tests. In order to determine how a longer DLI can affect PDT, two tests were made, one at 4 h after drug administration and one after 48 h. It was concluded that longer incubation periods lead to IC_{50} twice as high. Cytotoxicity studies and PDT treatment of all compounds were therefore carried out 48-hour post-administration in human ovarian carcinoma cancer cell lines (A2780 and A2780cis), and on the healthy human liver cell line (HEK293T).

	Cell lines					
	A2780cis		**A2780**		**HEK293T**	
	Without irradiation	**Irradiated**	**Without irradiation**	**Irradiated**	**Without irradiation**	**Irradiated**
M1	2.40 ± 0.39	1.07 ± 0.28	1.23 ± 0.21	0.67 ± 0.05	9.96 ± 1.79	0.35 ± 0.03
M2	5.07 ± 0.91	0.70 ± 0.06	2.45 ± 0.31	0.37 ± 0.03	8.57 ± 1.58	2.99 ± 0.43
M3	6.36 ± 1.19	1.86 ± 0.16	3.14 ± 0.45	0.42 ± 0.3	14.31 ± 2.14	1.18 ± 0.14
M4	7.11 ± 0.58	0.61 ± 0.09	2.43 ± 0.21	0.9 ± 0.03	4.35 ± 0.32	1.84 ± 0.13
M5	6.79 ± 0.70	0.33 ± 0.05	4.52 ± 0.28	0.1 ± 0.02	27.1 ± 1.50	0.50 ± 0.11

Table 2 – IC_{50} values **±** standard deviation (in μM) of **M1-M5** against three cell lines (A2780cis, A2780, and HEK293T)

Table 2 summarizes the findings of the metabolic activity inhibition (IC_{50}) against all cell lines. When it comes to metalla-assemblies **M1** and **M2**, the phthalocyanine derivatives, they showed IC_{50} values between 1.2 and 10 μM in the dark, and from 0.35 to 3 μM under light, which demonstrates that after the PDT treatment the compounds show a stronger cytotoxicity of up to 10x higher, with IC_{50} values as low as 0.35 μM. It should also be noted that both compounds show relative selectivity for cancer cells, with lower IC_{50} in cancer cell lines when compared to the healthy one (HEK293T), which is a positive result. A significant difference between **M1** and **M2** is the fact that **M2** is metalated with copper (II), and copper coordinated to the centre of these structures is known for improving their ability to decrease the viability and proliferation of human tumor cells.[145] When comparing the non-metalated **M1** with the metalated **M2**, it is possible to observe that the metalated one appears to have lower IC_{50} when irradiated and higher when not, for cancer cell lines; on the other hand, for the healthy cell line, the metalated metalla-assembly **M2** shows less selectivity (**Table 2**, first and second lines).

Furthermore, it appears that **M3**, the porphyrin conjugate, is more selective towards cancer cell lines without irradiation than the previous two, which might be important when we are considering systemic side effects when using these compounds for cancer treatments (**Table 2,** third line). Also for **M3**, the same results can be seen after irradiation, with lower IC_{50} in comparison to the same compound when non-irradiated. In all cell lines, this metalla-assembly appears to be less cytotoxic in the dark than its phthalocyanine analogue **M1**. When we compare **M1-M3** after irradiation, an intriguing result emerges - depending on the cell line, **M3** does not differ significantly regarding its PDT activity. This can be attributed possibly to the fact that phthalocyanines present stronger Q bands in their absorbance spectra, meaning they possible absorb more radiation at the wavelength used, consequently generating more singlet oxygen, the molecule responsible for oxidative stress inside the cells and their subsequent death.

Additionally, it is worth mentioning that these compounds were tested not only on the A2780 ovarian cancer cell line, but also in the A2780cis cell line, which is resistant to Cisplatin®, a chemotherapeutic medication that is commonly used to treat a variety of malignancies, including ovarian cancer. After this evaluation, it was possible to conclude that the activity of compounds **M2** and **M3** against the A2780 and A2780cis cell lines is different: just like in the case of Cisplatin, these molecules appear to have lower IC_{50} for the non-resistant cell line, meaning that these compounds also suffer some sort of resistance towards the cisplatin-resistant cancer cell line A2780cis. However, when **M1** and the standard deviations associated with its IC_{50} are taken into account (**Table 2,** third line), it shows a similar activity between the two cell lines, meaning that it does not suffer resistance at such an extensive level as the other two.

As previously discussed, arene ruthenium complexes by themselves inherently possess some cytotoxicity, and given that in **M4** and **M5** there are less of these units per molecule, (**M1-M3** uses four **C3** metalla-clip to construct their metalla-assemblies, while **M4-M5** uses only three **C4**), they could influence the cytotoxicity in the dark. This means that a fair comparison across **M1-M5** is not possible.

In any case, focusing solely on the IC_{50} values of these compounds before and after irradiation, **M1** could seem, at first sight, the best compound. However, it also presents the highest cytotoxicity in the dark of all the tested compounds, which is undesirable. It then becomes clear that **M5** is the overall best compound, presenting the lowest IC_{50} when irradiated and the biggest difference before and after irradiation, while also showing the best selectivity towards cancer cell lines (**Table 2,** fifth line)**.** Furthermore, **M5**, when compared to **M4**, has IC_{50} values similar for both A2780cis and A2780, meaning that it operates differently from cisplatin in cells. It is also possible to observe that comparing **M3**, **M4**, and **M5**, the three metalla-assemblies with porphyrinic panels, that the results do not differ significantly across the three, except on the matter of selectivity, with **M4** showing the worst selectivity (**Table 2,** fourth line)**.**

Observing **Table 3,** which summarizes the selectivity (SI) and photodynamic efficiency (PE) indexes, it is possible to better visualize the statements made previously. While SI gives us a value of selectivity towards cancer cell lines (either A2780cis or A2780) of these compounds in comparison with the healthy cell line HEK293T before irradiation (time of accumulation), PE compares the performance of the compounds as photosensitizers in all cell lines tested. The higher the SI ratio (between IC50 in healthy cells and cancer cells) and the PE values, the theoretically safer and more effective, respectively, a drug would be during *in vivo* treatment.

	SI		**PE**		
	A2780cis	**A2780**	**A2780cis**	**A2780**	**HEK293T**
M1	4.15 ± 1.09	8.09 ± 1.24	2.24 ± 0.26	1.84 ± 0.31	28.46 ± 1.89
M2	1.69 ± 1.25	3.50 ± 0.67	7.24 ± 0.72	6.62 ± 0.68	2.87 ± 0.67
M3	2.25 ± 1.67	4.56 ± 1.05	3.42 ± 0.35	7.48 ± 1.2	12.13 ± 1.76
M4	0.61 ± 0.45	1.79 ± 0.81	11.66 ± 0.96	2.7 ± 0.41	2.36 ± 0.25
M5	3.99 ± 1.1	5.99 ± 0.89	20.57 ± 1.31	45.2 ± 1.2	54.2 ± 2.53

Table 3 –Selectivity index (SI) and Photodynamic Efficiency (PE) index values of **M1-M5**.

As previously mentioned, **M1** and **M5** show the highest selectivity, being up to 4 times more selective towards A2780cis, and between 6 to 8 times more selective towards A2780 than HEK293T. At the same time, **M5** shows the highest efficiency as a photosensitizer of all compounds tested, with values of 20 to 45 times more efficient after irradiation in cancer cell lines, than before irradiation.

Understanding that these results felt incomplete, further tests were conducted to analyse the effect of further functionalizing two of the initial photosensitizers. For that, **P4** and **P5** were selected, since these were the ones synthesized and not bought. Focusing now on **P4**, **P5**, **M4**, **M5**, **MC4**, and **MC5,** their metabolic activity inhibition against all cell lines were determined in the form of dose-response curves (**Figures S8-S10,** supplementary information) and can be found summarized in **Table 4.** In addition, **Table 5** summarizes the SI and PE indexes of these compounds.

	Cell lines					
	A2780cis		**A2780**		**HEK293T**	
	Without irradiation	**Irradiated**	**Without irradiation**	**Irradiated**	**Without irradiation**	**Irradiated**
P4	32 ± 2.41	0.41 ± 0.01	28.81 ± 3.92	0.4 ± 0.04	25.14 ± 1.73	0.41 ± 0.01
M4	7.11 ± 0.58	0.61 ± 0.09	2.43 ± 0.21	0.9 ± 0.03	4.35 ± 0.32	1.84 ± 0.13
MC4	0.89 ± 0.02	0.17 ± 0.02	0.82 ± 0.03	0.12 ± 0.01	0.86 ± 0.44	0.24 ± 0.01
P5	61 ± 2.67	1.41 ± 0.08	52.30 ± 4.50	1.3 ± 0.09	43.61 ± 4.01	3.57 ± 0.42
M5	6.79 ± 0.70	0.33 ± 0.05	4.52 ± 0.28	0.1 ± 0.02	27.1 ± 1.50	0.50 ± 0.11
MC5	0.96 ± 0.03	0.12 ± 0.01	1.65 ± 0.27	0.10 ± 0.01	1.88 ± 0.72	0.19 ± 0.01
Cisplatin	26	-	2	-	48	-
RAPTA-C	>200	-	>200	-	>200	-

Table 4 – IC_{50} values **±** standard deviation (in µM) of different compounds against three cell lines (A2780cis, A2780, and HEK293T), and corresponding selectivity indexes (SI)

Starting with the comparison between **P4** and **P5**, these seem to not be selective towards cancer cell lines, however they showed good results regarding resistance, with no significant difference in IC_{50} values (**Table 4,** first and fourth line) or SI values (**Table 5,** first and fourth line) between both cancer cell lines**.** Interestingly, **P4** also appears to have lower $IC_{50,}$ half to that of **P5** under all conditions tested.

When it comes to **P4'**s corresponding metalla-assembly **M4**, lower IC_{50} values can be observed for both when irradiation is applied. The metalla-assembly in all cell lines presents itself as a stronger anticancer agent than the porphyrin, but only when irradiation is not performed, as can be seen by the lower PE values. Upon irradiation, however, an interesting result is observed: the porphyrin by itself seems to be a better PDT agent than the metalla-assembly (**Table 5**, first and second line).

Regarding **P5** and its corresponding metalla-assembly **M5**, although the porphyrin alone showed IC_{50} values after irradiation between 1 µM and 3 µM, when it is further functionalized, it shows higher cytotoxicity with IC_{50} values down to only 0.5 µM. It must be noted that the IC_{50} values for all the compounds are at least 10x lower when irradiated.

This comparison is not completely true because given the molecular weight of the assemblies, for the same dose in µM, despite the assemblies having 2 porphyrinic moieties per molecule, is will still be less PS/µM, meaning that it's not really comparable. For example, if the calculations are done for **M4** and **M5** we have, respectively, 3 and 4% the porphyrin amount necessary to have the same PDT effect compared to **P4** and **P5.** This is interesting because it appears less PS can have better results if less aggregated.

In addition, it is possible to notice that while **P4** has better IC_{50} values than **P5**, the opposite happens in the cases of **M4** and **M5**. Given that they are structurally almost identical, this could be an indication that part of their difference in activity can be traced to the hydroxyl/amine group. This change theorizes that the function of these groups can be affected when the porphyrins are assembled into these organometallic structures, therefore changing their influence. Otherwise, **M4** would continue to have a better IC_{50} than **M5**. What is left to determine is what is the influence that the assembly of the PS has on these groups. A possible explanation is that there is less aggregation in these arrangements and therefore the hydroxyl group, being more accessible, can exert his full activity, which could have been diminished before. Like this, we could hypothesize that this group is better for PDT treatment than the amine, but only if it is reachable.

The next step was to evaluate the effect on the PDT activity that linking these structures to CNCs might bring. **Figure 25**, for example, shows the comparison between **P5, M5** and **MC5**.

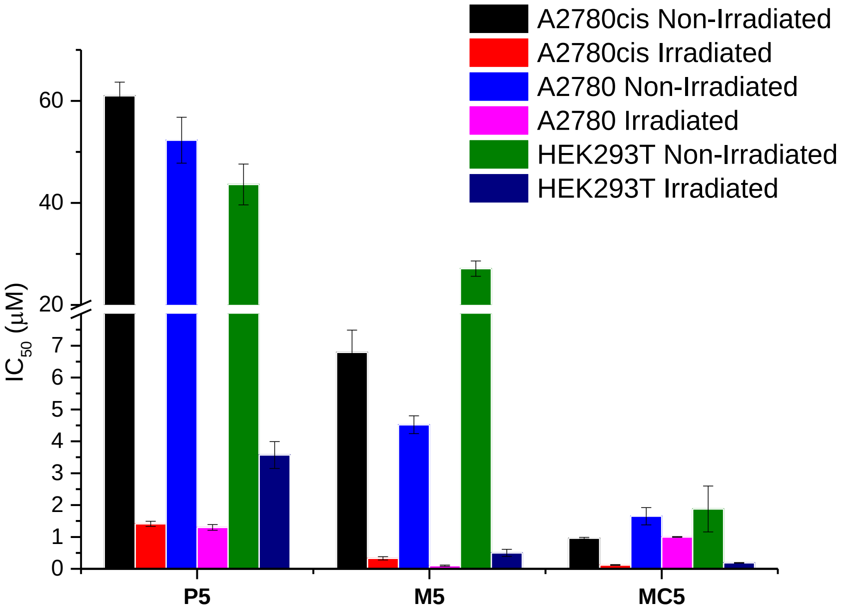

Figure 25 – Comparison of the IC_{50} values of P5, **M5** and **MC5** against the ovarian cancer cell lines A2780 and A2780cis, as well as the normal hepatic cell line HEK293T, in the dark and after irradiation.

Table 5 summarizes even further the results obtained from the metabolic activity assays of these compounds to their SI and PE values. From the analysis of both **Tables 4** and **5,** it was possible to determine that with the introduction of the nanocrystals into their structure, **MC4** and **MC5** show a significant decrease regarding their IC_{50} values. It is important to note that these does not necessarily mean they have a better photodynamic efficiency as observed by the results on **Table 5**. In fact, although **MC4** and **MC5** show the lowest IC_{50}, meaning that these compounds need the lowest doses to kill cells after irradiation; this accompanied by a decrease of their IC_{50} in the dark as well, meaning that, when compared to the metalla-assemblies before CNC-grafting, they end up presenting lower efficiency.

	SI		PE		
	A2780cis	**A2780**	**A2780cis**	**A2780**	**HEK293T**
P4	0.78 ± 0.06	0.87 ± 0.06	78.05 ± 2.17	72.03 ± 3.25	61.31 ± 2.63
M4	0.61 ± 0.45	1.79 ± 0.81	11.66 ± 0.96	2.7 ± 0.41	2.36 ± 0.25
MC4	0.97 ± 0.12	1.05 ± 0.06	5.24± 0.29	6.83 ± 0.11	3.58 ± 0.08
P5	0.71 ± 0.09	0.83 ± 0.07	43.26 ± 2.11	40.23 ± 1.87	12.22 ± 0.48
M5	3.99 ± 1.1	5.99 ± 0.89	20.57 ± 1.31	45.2 ± 1.2	54.2 ± 2.53
MC5	1.80 ± 0.04	1.13 ± 0.04	8 ± 0.34	16.5 ± 0.41	9.89 ± 0.29

Table 5 –Selectivity (SI) and Photodynamic efficiency (PE) index values of **P4**, **P5**, **M4**, **M5**, **MC4**, and **MC5**.

The decrease in their IC_{50} might be related to the fact that the CNCs improve solubility and target the surface of cells through their glucose moieties since it has been previously reported that one of the factors contributing to the greater efficiency of PDT is the accumulation of PS in tumor cells.[10] Therefore, this increase in the cytotoxicity of the more amphiphilic derivatives will, theoretically, be related to their increased uptake by cells. On the other hand, the selectivity towards cancer cell lines is completely lost, showing the same IC_{50} values between the cancerous and healthy cell lines tested. This is also confirmed by their SI values of approximately 1, which mean that their preference for healthy cell lines is the same as for cancer cell lines.

In addition, when the activity of **MC4** and **MC5** against the A2780 and A2780cis cell lines is compared, it can be observed that there is no significant difference between the two, contrary to the case of cisplatin (**Table 4**, seventh line). These compounds seem to not discriminate between the two cell lines, which is a very important and interesting result because they could potentially be used to treat cancers resistant to common oncogenic drugs such as cisplatin. Not only that, before or after irradiation, **MC4** and **MC5** show better IC_{50} values than cisplatin for all cell lines tested, proving that they are better anticancer agents. Even more interesting is the fact that all tested compounds (**P4-P4**, **M1-M5** and **MC4-MC5**) appear to behave equally for both cell lines after irradiation, which is the objective given that these are to be used as PDT agents. So even if some differences can be observed in the dark, it is possible to conclude that they are good candidates in the battle to tackle resistance mechanisms and to be used as PDT agent.

On the other hand, given that these compounds have arene ruthenium units, it is necessary to also compare them with a standard arene ruthenium complex, such as [Ru(η^6-*p*-cymene)Cl_2(pta)] (RAPTA-C, pta = 1,3,5-triaza-7-phosphaadamantane), RAPTA stands for ruthenium arene PTA. As previously discussed, arene ruthenium is a class of experimental cancer drugs that consist of a central ruthenium (II) atom coordinated to an arene group, chlorides, and an additional ligand, thus forming an organo-ruthenium half-sandwich compound. Several derivatives of RAPTA have been synthesized, and the most notable is RATPA-C. When analysed, the IC_{50} of RAPTA-C and of these metalla-assemblies show a significant difference: RAPTA-C has IC_{50} values always higher than 200 µM, independently of the cell line, and no effect when irradiated, because it doesn't have a photosensitive agent in its structure.

In conclusion, all the studied compounds revealed dose-dependent anti-proliferative effects. The relationship that can be established through the analysis of these results is that: Further functionalization of the initial photosensitizers increases their PDT activity (lower IC_{50}) but decreases selectivity. In fact, derivatives with increased amphiphilicity, obtained by cellulose linkage or by coordination with ruthenium metalla-clips, showed a much higher activity against all cell lines when compared with the porphyrin itself, especially in the dark. Regarding their selectivity, this is expected since most of the selectivity aimed at this project relies on the EPR effect, which cannot be tested *in vitro*, and on the local use of the light source. Therefore, if any questions regarding the necessity or relevance of functionalizing these structures is raised, they are settled by the great improvement of their PDT activity, as well as the lower resistance from A2780cis towards these compounds. In any case, in order to further understand and clarify the effect of the grafting of CNCs to the metalla-assemblies at the cellular level, internalization assays were performed using the radiolabelled analogues.

2.3.2. Cellular Uptake of Radiolabelled Compounds

It was decided to take **P5**, **M5**, and **MC5** (the best PDT agents from the previous *in vitro* study) and take advantage of the fact they can be radiolabelled, and their radioactivity measured and tracked to assess their cellular uptake in the same cell lines as their metabolic inhibition assays. It is important to note that a direct correlation between the *in vitro* studies and the cellular uptake can be established.

2.3.2.1. Technetium-99m

For the internalization assays, a simple protocol was followed that consisted of radiolabelling these compounds with reduced technetium-99m and then incubating cells over different timepoints and assessing the percentage of compound attached or internalized in the cells by measuring the radioactivity of the cells after being washed to make sure any non-attached compound was removed. When comparing the cellular uptake from radiolabelled **P5**-**MC5** with technetium-99m (**Figures 26-29**), it was possible to observe that [^{99m}Tc]Tc-**P5** has a lower cellular uptake, never surpassing 8% even after 4 h of incubation, and for [^{99m}Tc]Tc-**M5** and [^{99m}Tc]Tc-**MC5** the uptake increases up to 10%, which is not considered statistically significant. This is an important information because it implies that the uptake is not influenced by the functionalization, and so the differences in PDT activity cannot be linked to these results. This also suggests that for each porphyrin that enters or is attached to cells when [^{99m}Tc]Tc-**P5** is administered, one metalla-assembly or one CNC-grafted metalla-assembly does the same. It is possible to know this because when the radiolabelling is performed, the conditions used guaranteed that only one of the porphyrins is radiolabelled, and not both, so there is a 1:1 stoichiometry that is preserved in all compounds. This can explain the lower IC_{50} of [^{99m}Tc]Tc-**M5** and [^{99m}Tc]Tc-**MC5** when compared to **P5**, because while for n molecules of [^{99m}Tc]Tc-**P5** there is n [^{99m}Tc]Tc-**M5** or [^{99m}Tc]Tc-**MC5** molecules, there are the double of porphyrin/photosensitizer moieties (2n) for [^{99m}Tc]Tc-**M5** and [^{99m}Tc]Tc-**MC5**, meaning that when they are irradiated, there can be a synergetic PDT action, which can be caused by both porphyrins being irradiated and their activity influencing one another.

Another interesting result is that the normal liver cell line HEK293T presents the lowest cellular uptake for all compounds tested, which can also explain the higher IC_{50} observed for this cell line and corroborates a certain selectivity of these compounds towards the cancer cell lines A2780 and A2780cis, with the best results being found for A2780. In addition, it is observed that there is first a faster uptake until the 1 or 2 h timepoint and that after that, the uptake seems to reach a plateau for most of the compounds on all cell lines. Overall, it can be concluded that the cell uptake appears to vary from 5 to 10%, at the 4 h post-administration mark, depending on the cell line, with higher uptake for the cancer cells (A2780 and A2780cis) than the liver cells (HEK293T) over time, as expected by our previous metabolic activity assays.

Lastly, it should also be noted that these comparisons between cellular uptake and metabolic activity inhibition is only up to 4 h and given that PDT is performed 48 h after PS administration, we still cannot have a fair line of cause and effect between the two.

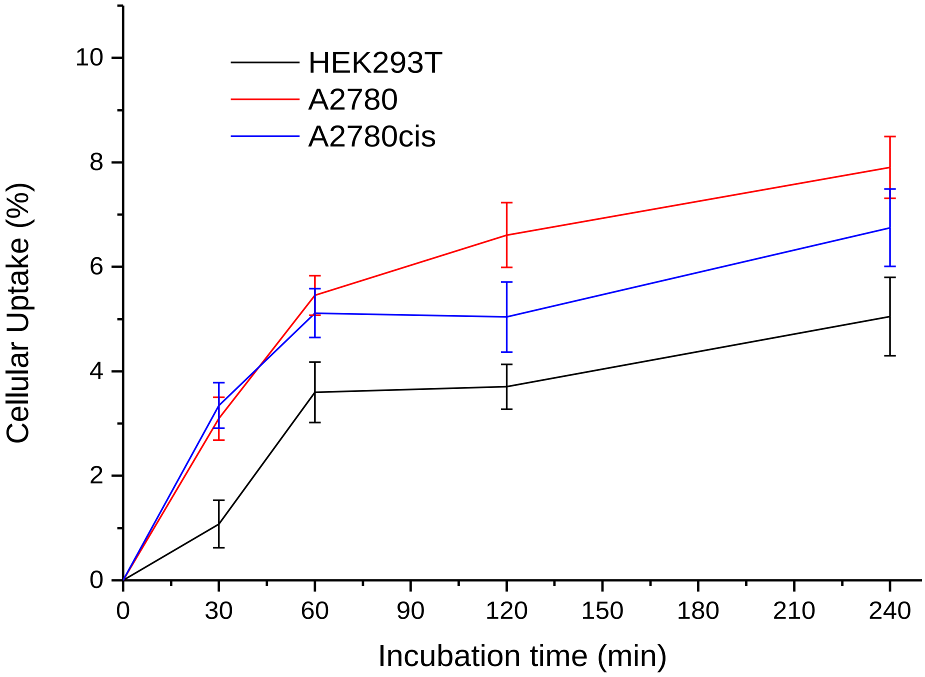

Figure 26 - Cellular uptake for **[^{99m}Tc]Tc-P5** in the HEK293T, A2780, and A2780cis cell lines up to 4 h. Standard errors (±SE) calculated from 3 repeated measurements.

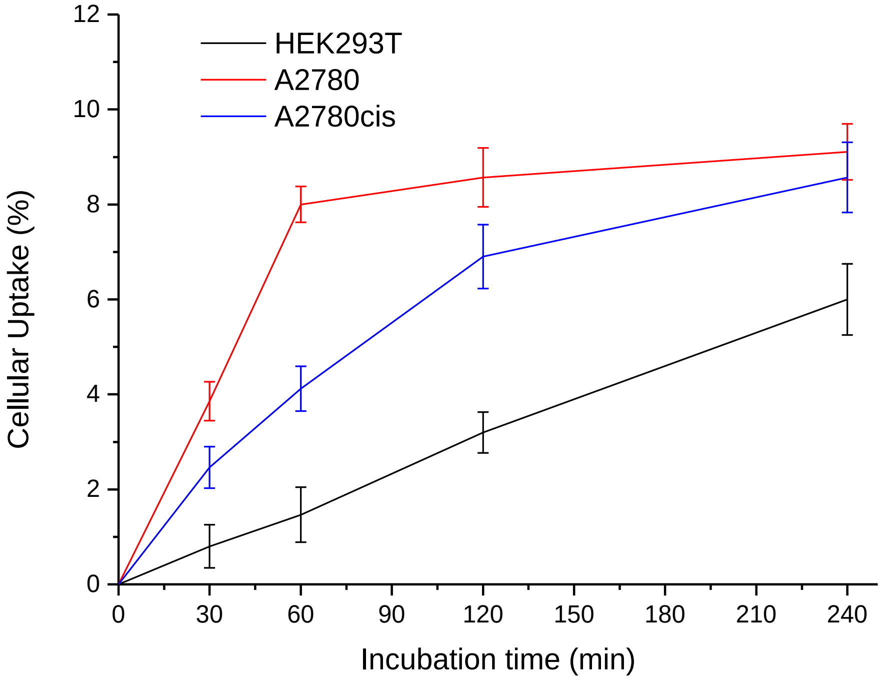

Figure 27 - Cell uptake for **[^{99m}Tc]Tc-M5** in the HEK293T, A2780, and A2780cis cell lines up until 4 h. Error bar stands for standard error (±SE), calculated from 3 repeated measurements.

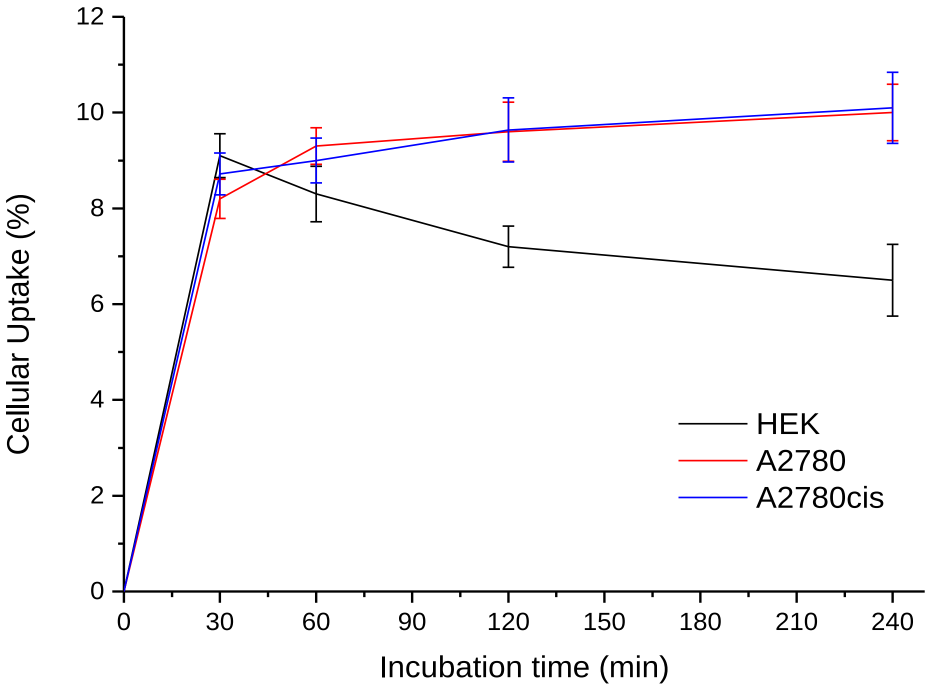

Figure 28 - Cell uptake for **[^{99m}Tc]Tc-MC5** in the HEK293T, A2780, and A2780cis cell lines up until 4 h. Error bar stands for standard error (±SE), calculated from 3 repeated measurements.

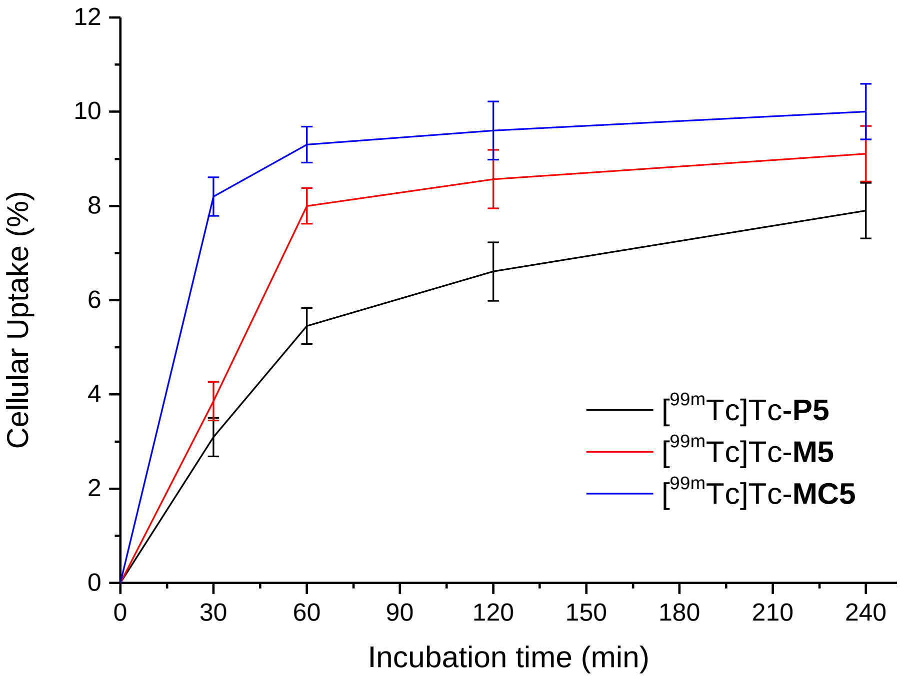

Figure 29 - Cell uptake for **[^{99m}Tc]Tc-P5**, **[^{99m}Tc]Tc-M5**, and **[^{99m}Tc]Tc-MC5** in the A2780 cancer cell line up until 4 h. Error bar stands for standard error (±SE), calculated from 3 repeated measurements.

2.3.2.2. Indium-111

On the other hand, when it comes to the cellular uptake from radiolabelled **P5**-**MC5** with indium-111 (**Figures 30-32**), for the three cell lines used, it was also possible to observe that [^{111}In]In-**P5** has a lower cellular uptake, from 8 to 10% at 4 h post-incubation, while for [^{111}In]In-**MC5** and [^{111}In]In-**MC5** the uptake goes up to 18%. In comparison to the technetium-99m radiolabelled compounds, this difference between **P5** and **M5** or **MC5** is more obvious, and the cellular uptake appears to be higher. The same result is found when it comes to normal liver cell line versus the other two cancer cell lines, with HEK293T having the lowest cellular uptake for all tested compounds. The different uptake can only be traced to the radionuclide used. Through the previous kinetic stability studies, this can be due to the fact that technetium-99m labelled compounds are less stable in plasma (the closest medium to blood) than when indium-111 is used. Interestingly, [^{111}In]In-**M5** appears to present a higher uptake in A2780 than [^{111}In]In-**MC5** when indium-111 is used instead of technetium-99m for the radiolabelling (**Figure 33**). In addition, [^{111}In]In-**M5** and [^{111}In]In-**MC5** do not reach a plateau at 4 h for some of the cell lines, which also differs from the technetium-99m labelled **M5** and **MC5**. Lastly, it is important to note that the knowledge acquired from the *in vitro* assays can be used to establish a better *in vivo* study, determining the safest dose to be injected in the animal model.

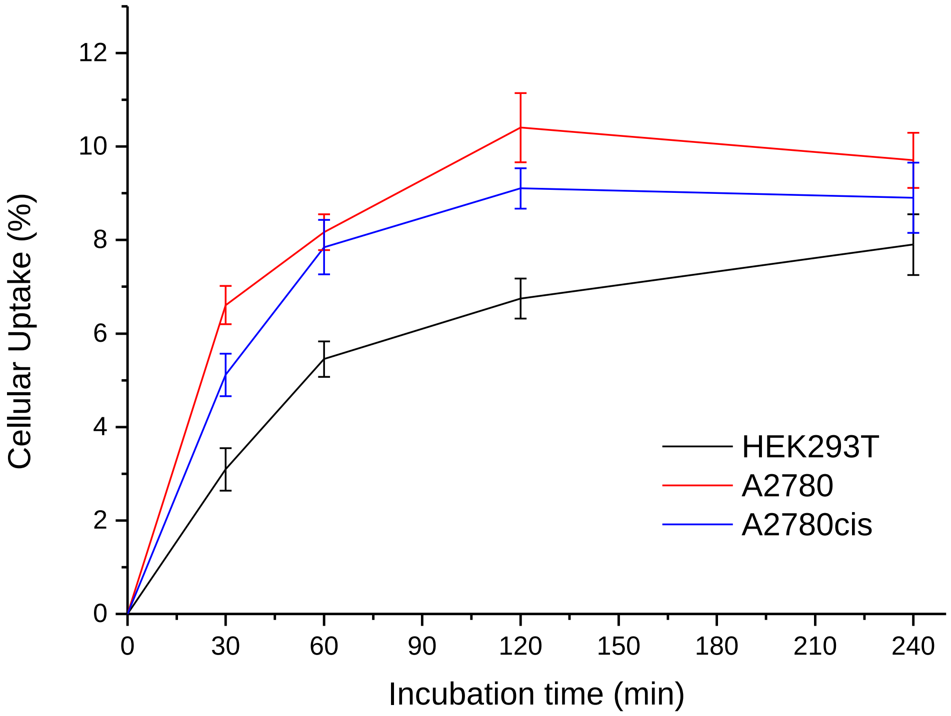

Figure 30 – Cellular uptake for **[^{111}In]In-P5** in the HEK293T, A2780, and A2780cis cell lines up to 4 h. Standard errors (±SE) calculated from 3 repeated measurements.

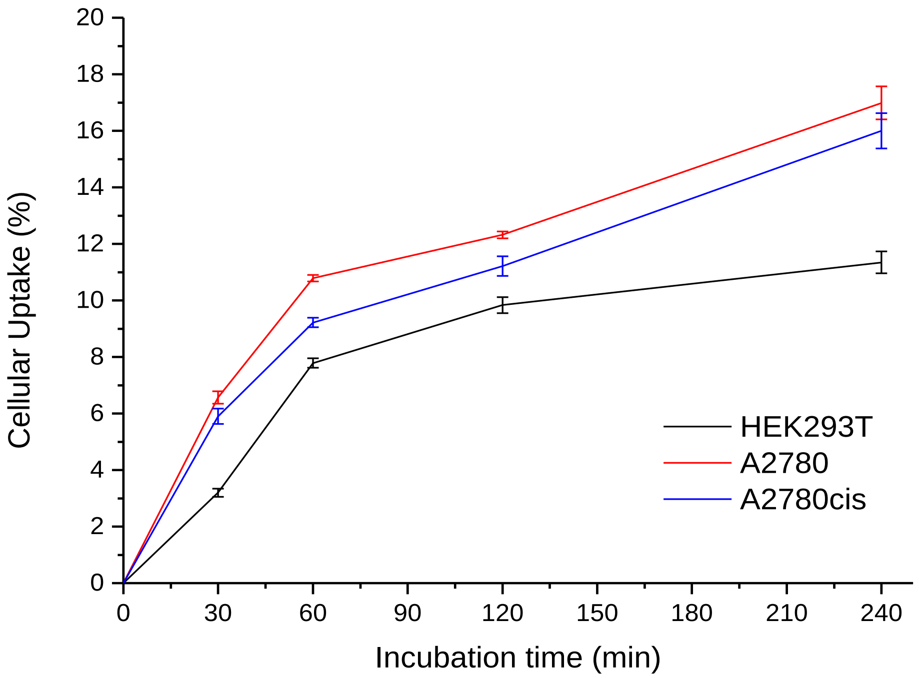

Figure 31 – Cell uptake for **[^{111}In]In-M5** in the HEK293T, A2780, and A2780cis cell lines up until 4 h. Error bar stands for standard error (±SE), calculated from 3 repeated measurements.

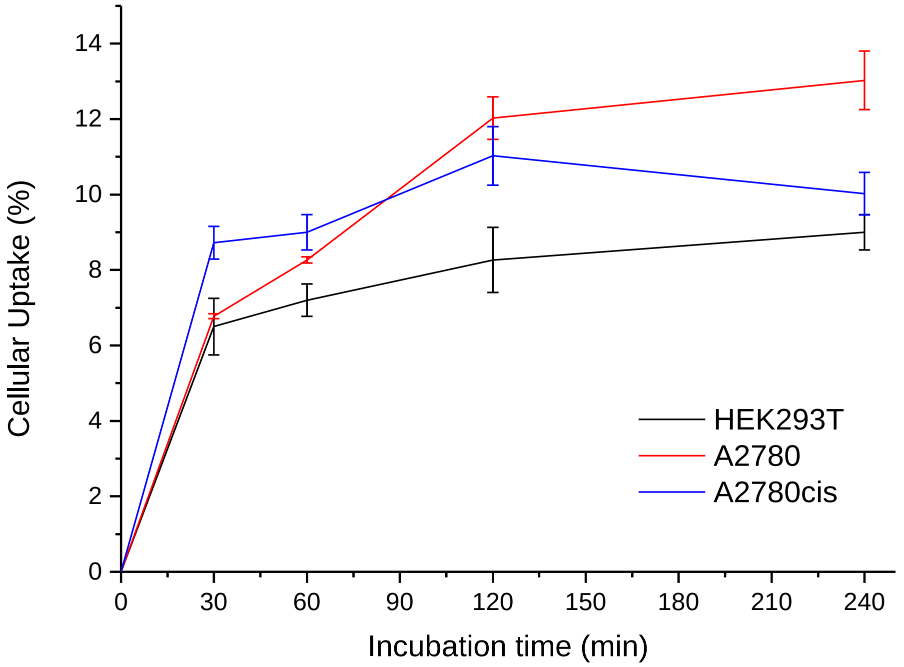

Figure 32 – Cell uptake for **[^{111}In]In-MC5** in the HEK293T, A2780, and A2780cis cell lines up until 4 h. Error bar stands for standard error (±SE), calculated from 3 repeated measurements.

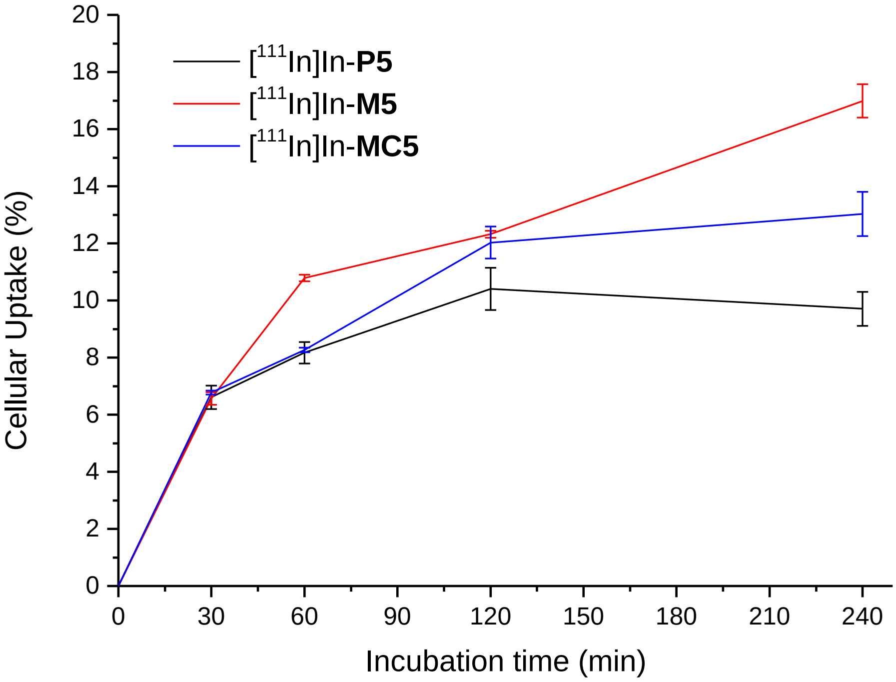

Figure 33 – Cell uptake for **[^{111}In]In -P5**, **[^{111}In]In -M5**, and **[^{111}In]In -MC5** in the A2780 cancer cell line up until 4 h. Error bar stands for standard error (±SE), calculated from 3 repeated measurements.

2.4. The *In vivo* Results

Animal models are critical in the development of new imaging agents, biodistribution research, and pathophysiologic studies, because they can be used to improve target selection efficiency and accuracy, as well as therapeutic safety and efficacy.[146–148] *Ex vivo* tissue analysis or autoradiography, for example, are employed in biodistribution studies to investigate various radiopharmaceuticals, biomolecules, and disease models. They do, however, need a large number of animals, which limits the design of experimental methods and presents economic and ethical concerns. Nuclear medicine techniques and other imaging modalities (ultrasound, optical imaging, X-ray computed tomography (CT), and magnetic resonance imaging (MRI)) enable *in vivo* analysis of complex biochemical phenomena,[149–151] by supplying repeated recordings for the same animal spanning days or even weeks.[146] The use of mixed multimodal imaging (PET/CT, SPECT/CT, PET/MRI) has improved over the last two decades the data integrity by introducing accurate anatomical localisation to traditional PET and SPECT imaging and boosting quantification.[152] While these integrated systems have exceptional performance, if they are not handled by specialists, they have limitations and drawbacks.[152,153] Furthermore, their high purchase and maintenance costs, as well as their requirement for highly-trained technicians to properly exploit their capabilities, make them only affordable to a small percentage of field workers. As a result, most small and medium-sized groups, which make up the majority of researchers who create new radiopharmaceuticals, biomolecules, and nanoparticles and study molecular mechanisms, still rely on biodistribution studies rather than imaging.[154] Another big role that imaging can provide is an early cancer detection. Understanding the tumor conditions is critical for an effective treatment, making it is self-evident that diagnostic agents play a crucial role in determining which cancer therapy technique to choose.[155] Imaging is an intriguing tool since it presupposes a follow-up to therapies to assess the treatment's success and identify any potential recurrence damage. It also allows for the monitoring of any changes that occur on the tumor and the evaluation of therapy efficacy.[155] Imaging techniques paired with PDT open up new possibilities for treating various malignancies, including cancer. This notion introduces the so-called theranostic agent, a single substance with both imaging and therapy capabilities, allowing for both visualization and treatment in a dual fashion.[156,157]

Simple scintigraphic imaging can provide not only an efficient assessment of the *in vivo* behaviour of a new probe, but also an estimate on its biodistribution over time. The main researchers' needs are then focused on simple and fast screening of laboratory mice in a cost-effective way, avoiding large, lengthy, and costly biodistribution studies, and using less animals, therefore agreeing with good laboratory practices, ethical handling of animals and the use of the R's: Reduction, Reuse and Refinement. Accordingly, it was decided that the *in vivo* imaging part of this work would be performed using BioEmTech®'s scintigraphic system "γ-eye",[154] which detects the γ radiation from the radioactive decay of radionuclides such as technenitum-99m and indium-111.[156,158] In this section, we are presenting the imaging *in vivo* results of PDT agents administered retro-orbitally in SCID (severe combined immunodeficiency) mice through BIOEMTECH's benchtop scintigraphic system,[154] suitable for whole-body mouse static and dynamic imaging. The biodistribution of the radiolabelled compounds at different timepoints, up to 24 h, was determined.

For the *in vivo* imaging studies, only the radiolabelled compounds **M5** and **MC5** were used, since they showed the best results *in vitro*, possessing the best characteristics for PDT and *in vivo* administration.

The protocol consisted of a 100 µL retro-orbital injection of the radiolabelled compounds [^{99m}Tc]Tc-**M5,** [^{99m}Tc]Tc-**MC5,** [^{111}In]In-**M5,** or [^{111}In]In-**MC5** with a radioactivity of approximately 100 µCi in female SCID mice, and performing imaging at different timepoints. Although **MC5** is expected to better target tumors due to the EPR effect, both compounds, with and without CNC were studied, as a proof-of-concept.

2.4.1. Imaging of ^{99m}Tc-labelled compounds

Through the analysis of the images acquired with [^{99m}Tc]Tc-**M5** (**Figure 34**) and [^{99m}Tc]Tc-**M5** (**Figure 35**), it is clear that the biodistribution from 1 to 24 h post-injection for both compounds is very similar. In the first hour, they seem to accumulate preferentially in the liver and some portion of the intestines. The dominant accumulation organ is the liver, extending over 24 h, thus suggesting that these compounds if administered in a dose that has an effect without irradiation could have some inherent hepatotoxicity. In the dynamic study conducted during the first hour for both compounds, it could be observed the flux of [^{99m}Tc]Tc-**M5** and [^{99m}Tc]Tc-**MC5** from the injection point (retro-orbital) through the blood stream and the slow accumulation in the liver. The biodistribution seems to stay constant during the whole study, focusing on the injection point and the liver, with some small accumulation in the intestines at earlier timepoints

It should be noted that preliminary results using different concentrations of [^{99m}Tc]Tc-**MC5**, more specifically 1500 nM and 750 nM, were tested before determining the ideal concentration/injection dose of 375 nM. For the highest concentration (1500 nM), some mortality was observed (33%), and both compounds seemed to allocate at the lungs instead of the liver and intestines (**Figure 36**). At half concentration 750 nM, the biodistribution was similar to the one found for 375 nM with some extra accumulation at the injection site (**Figure 37**). At this concentration a toxic effect at the injection site was noticed, possibly due to a local photoreaction, since the eye is constantly exposed to light. Therefore, it was decided to lower further the concentration, trying to achieve the same results with the lowest concentration possible. This concentration was considered safe because no fatality occurred, and when the images for [^{99m}Tc]Tc-**MC5** are analysed, it was possible to observe that some accumulation still happens at the injection site for this compound, but no damage to the eyes of the mice was observed. The accumulation of [^{99m}Tc]Tc-**MC5** in the injection site at 375 nM but not of [^{99m}Tc]Tc-**M5** at the same concentration might be due to its larger size**.**

Furthermore, when looking at the clearance yields for both compounds at 375 nM (**Figure 38**), it is possible to conclude that they have similar behaviours, not depending much on whether or not the compound is bound to the cellulose nanocrystals, but rather the concentration of the injected solution. This is more evidently seen when we compare 3 different concentrations of [^{99m}Tc]Tc-**MC5** (375, 750 and 1500 nM) and notice that the higher the concentration administered, the longer it takes for the compound to be cleared from the mouse's body. At 375 nM, for example, we have a clearance at 24 h of around 50%, while for 1500 nM, at the same timepoint, the clearance is less than half, rounding 20%. Lastly, it seems that the grafting or not grafting of CNC to these compounds impacts more directly the clearance at earlier timepoints and is less relevant in later timepoints.

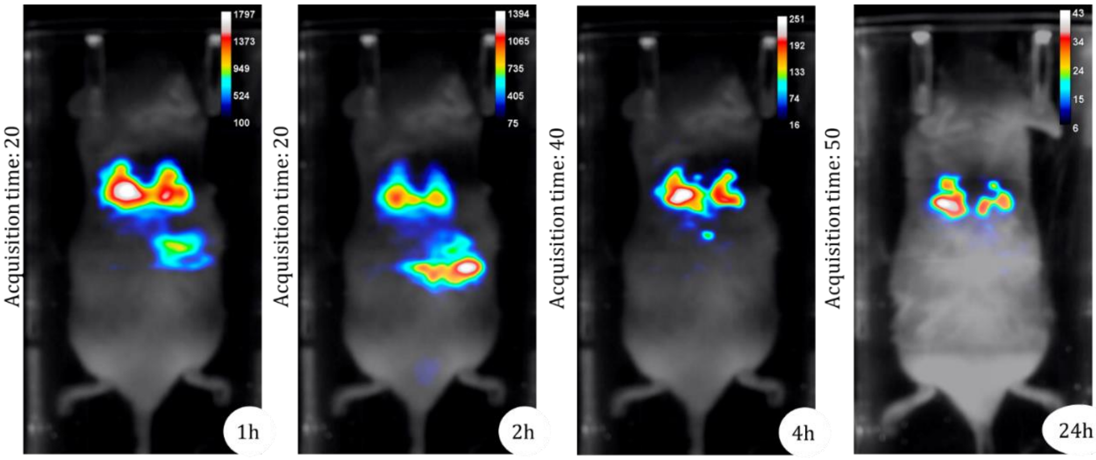

Figure 34 - Indicative static 20 – 50 min scintigraphy/optical images of a normal Swiss Albino mouse intratracheal administered with [^{99m}Tc]Tc-**M5** (375 nM) at 1, 2, 4 and 24 hours p.i. The gradual alteration in colour indicates a lower to a higher number of recorded counts.

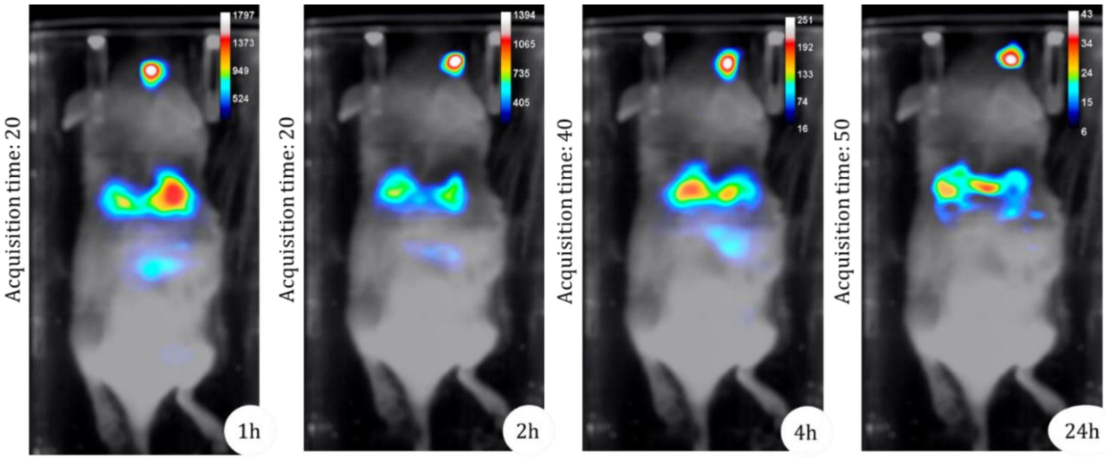

Figure 35 - Indicative static 20 – 50 min scintigraphy/optical images of a normal Swiss Albino mouse intratracheal administered with [^{99m}Tc]Tc-**MC5** (375 nM) at 1, 2, 4 and 24 hours p.i The gradual alteration in colour indicates a lower to a higher number of recorded counts.

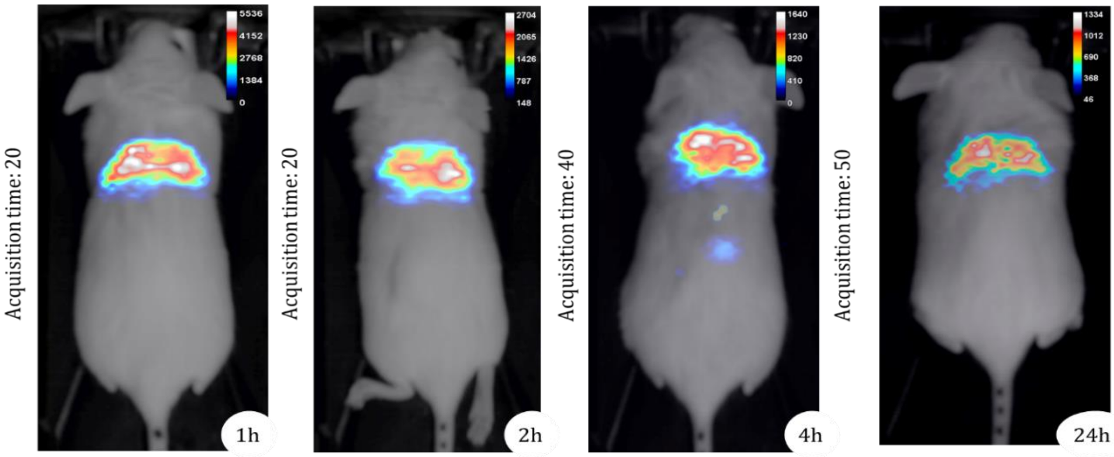

Figure 36 - Indicative static 20 – 50 min scintigraphy/optical images of a normal Swiss Albino mouse intratracheal administered with [^{99m}Tc]Tc-**MC5** (1500 nM) at 1, 2, 4 and 24 hours p.i. The gradual alteration in colour indicates a lower to a higher number of recorded counts.

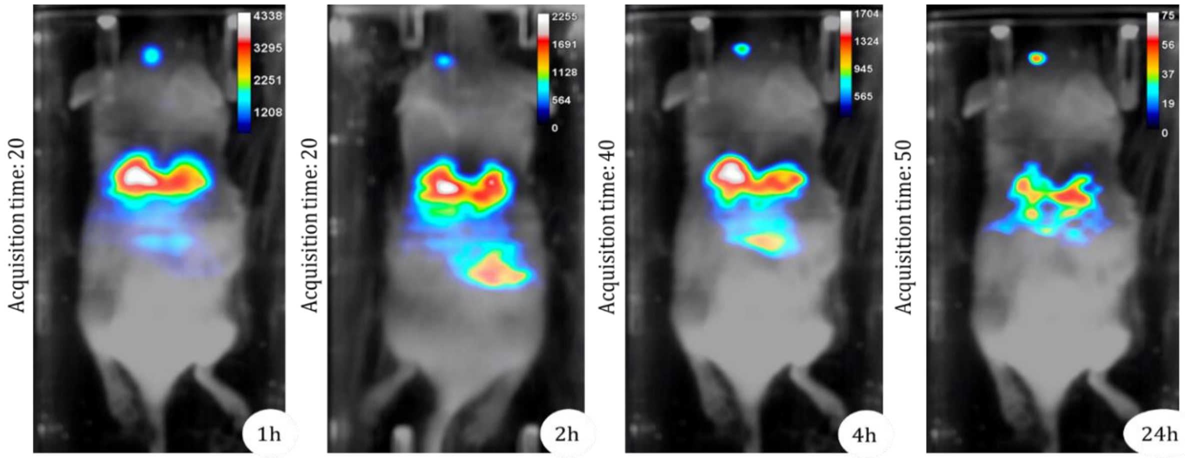

Figure 37 - Indicative static 20 – 50 min scintigraphy/optical images of a normal Swiss Albino mouse intratracheal administered with [^{99m}Tc]Tc-**MC5** (750 nM) at 1, 2, 4 and 24 hours p.i. The gradual alteration in colour indicates a lower to a higher number of recorded counts.

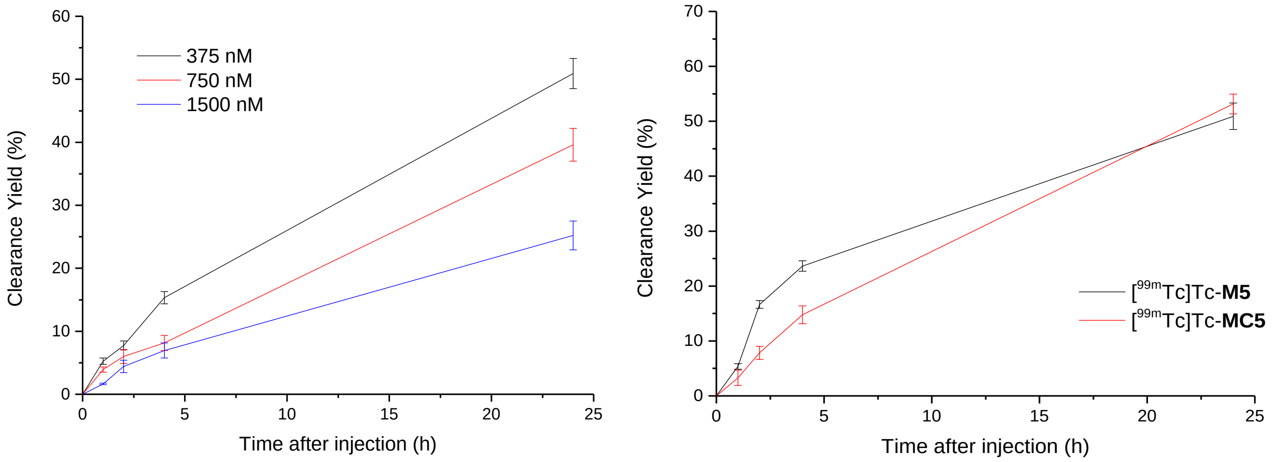

Figure 38 - Clearance Yield for [^{99m}Tc]Tc-**MC5** at different concentration: 375, 750 and 1500 nM (**right**); and for [^{99m}Tc]Tc-**M5** and [^{99m}Tc]Tc-**MC5** at 375 nM (**left**). Error bar stands for standard error (±SE), calculated from three repeated measurements Error bar stands for standard error (±SE), calculated from three repeated measurements.

2.4.2. Imaging of ^{111}In-labellled compounds

Radiolabelling with indium-111 was also completed with a radiochemical incorporation of over 90% for compounds **M5** and **MC5**. As in the case of technetium-99m, after the radiolabelling the final solution was diluted with water for injection to a final concentration of 375 nM. It was then administered into a SCID mouse via retro-orbital injection, with a radioactive activity of around 90-110 μCi, with the injected activity being measured in a dose-calibrator. The scintigraphic images acquired for [^{111}In]In-**M5** (**Figure 39**) and [^{111}In]In-**MC5** (**Figure 40**) showed some differences regarding their biodistribution from 1 to 24 h post-injection for both compounds compared to their analogous technetium-99m radiolabelled compounds. In the first hour, [^{111}In]In-**M5** seems to accumulate preferentially in the kidneys instead of the liver, which indicates a better clearance and biodistribution right from the start. In the case of [^{111}In]In-**MC5**, while still showing some accumulation at the kidney level, already at 1 h it shows preferential accumulation at the liver level. For [^{111}In]In-**MC5**, in addition can also be seen some accumulation in the bladder as well and residual traces at the intestines, which could indicate a faster clearance from the mouse's body. Both compounds, however, at the 2 h timepoint start to show the same pattern of accumulation in the liver of [^{99m}Tc]Tc-**M5** and [^{99m}Tc]Tc-**MC5**, which is expected because the difference in radionuclide shouldn't affect biodistribution very much given the whole structure of these compounds.

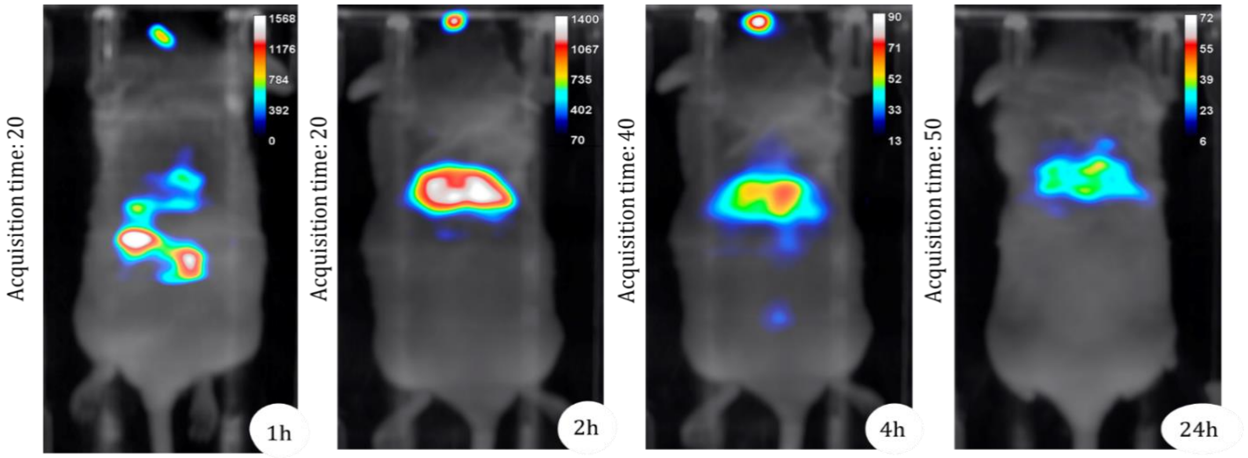

Figure 39 - Indicative static 20 – 50 min scintigraphy/optical images of a normal Swiss Albino mouse intratracheal administered with [^{111}In]In-**M5** (375 nM at 1, 2, 4 and 24 hours p.i, The gradual alteration in colour indicates a lower to a higher number of recorded counts.

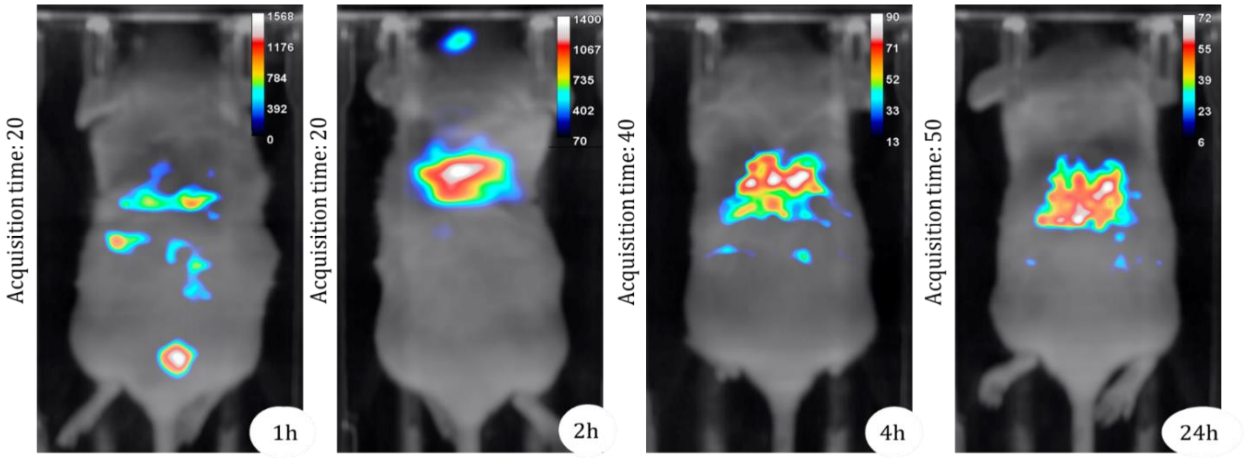

Figure 40 - Indicative static 20 – 50 min scintigraphy/optical images of a normal Swiss Albino mouse intratracheal administered with [^{111}In]In-**MC5** (375 nM) at 1, 2, 4 and 24 hours p.i. The gradual alteration in colour indicates a lower to a higher number of recorded counts.

Even though some accumulation in the liver is observed for both at earlier timepoints (2 and 4 h), it is possible that this might be in a much lower extent since the clearance yields between [^{111}In]In-**M5** and [^{111}In]In-**MC5** at 375 nM are higher than for [^{99m}Tc]Tc-**M5** and [^{9m}Tc]Tc-**MC5** (**Figure 41**) reaching the 40% as soon as 4 h post-injection while for the technetium-99m analogues the clearance at the same timepoint is around half. Since the only difference between them is the radionuclide used, it is interesting to assume that the use of indium-111 instead of techenteium-99m in some way affects the clearance of the compounds. On the other hand, it does not seem to make much of a difference much at the 24 h timepoint, with all compounds showing the same clearance here. It should be noted that the clearance is corrected according to the natural decay of the isotopes in order to avoid any artifacts regarding false clearance signals.

It is also interesting that, until this point, it seems that the **M5** (non-grafted) appears to always have a better clearance compared to **MC5** (CNC-grafted), regardless of the radionuclide used. It can also be concluded, that the accumulation in the liver seems to be linked to the presence of CNC moieties as well. This might be due to the fact that **MC5** being linked to the cellulose nanocrystals can influence its retention by the liver with sequent passages of the compound over the mouse's systemic circulation. The liver being the main organ of accumulation, if a compound has specific affinity to the liver, then it is understandable that it will have a worse clearance. This helps us understand that the main factor of influence to a faster or slower clearance, besides concentration is linked to an accumulation in the liver. This is corroborated by the fact that the indium-111 labeled compounds present a faster clearance in the first hour, and it can be seen through the scintigraphic imaging that for the first hour these compounds don't accumulate as much in the liver, but rather the kidneys.

In conclusion, this work intended to use cellulose nanocrystals to transport and deliver photo-responsive molecules to biological targets. The main objectives consisted of preparing and characterizing cellulose nanocrystals as well as photo-responsive molecules; to load the nanocrystals with the photo-responsive compounds; and to evaluate the biological potential of the newly developed nano-carriers *in vitro* and *in vivo*.

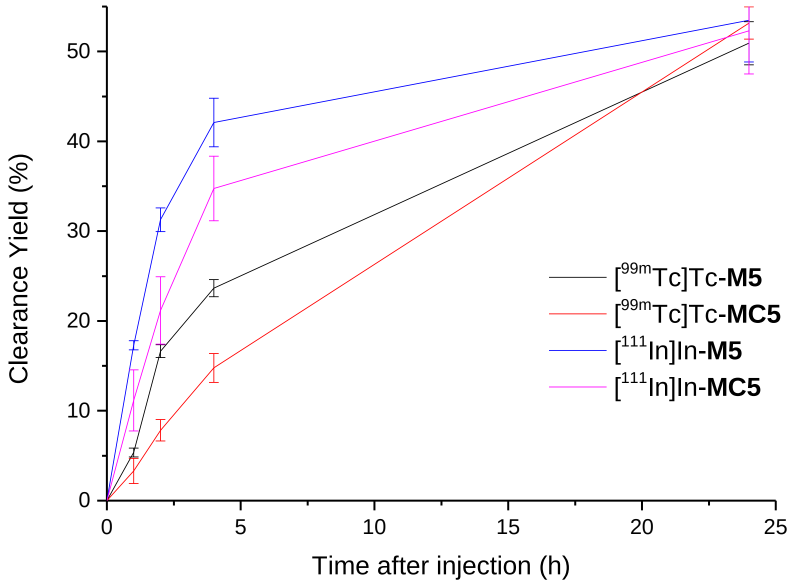

Figure 41 – Clearance Yield for [^{111}In]In-**M5**, [^{111}In]In-**MC5**, [^{99m}Tc]Tc-**M5,** and [^{99m}Tc]Tc-**MC5** at 375 nM. Error bar stands for standard error (±SE), calculated from three repeated measurements.

Chapter 3 – Conclusions and Future Perspectives

With the idea of enhancing the innate characteristics of the most commonly used group of photosensitizers (porphyrins and phthalocyanines), it was thought of changing their chemical structure therefore hoping to reduce their disadvantages. This was achieved by combining the individual characteristics of different molecules such as ruthenium organometallic clips and cellulose nanocrystals, which help with targeting, delivery, and solubility. At the same time, besides the therapeutic advantages of these compounds, these structures are also fitting for radiolabeling, which would allow them to be used in some imaging techniques. This means that, if successful, as was in our case, we would obtain a new class of compounds that gather both therapeutic and diagnostic (follow up through imaging) in one single compound, the so-called theranostic agents. Having achieved this goal, some conclusions were taken, starting with the understanding that the further the photosensitizers were functionalized, the better results they showed *in vitro* and *in vivo*. This is reason enough to say that the initial premise was correct and shows the importance of rational design when developing new molecules. Furthermore, the results obtained demonstrate that these compounds meet some of the main requirements of an ideal PS and are, thereby, potential photosensitizers for PDT. These requirements come down to low activity in the dark, but high PDT activity upon irradiation, selectivity towards cancer cells and not healthy cells, controllable and adjustable properties through simple modifications, and the ability to be radiolabelled through direct procedures.

In addition, the efficient radiolabelling of these compounds showed that they can be used not only as therapeutic agents in the treatment of cancer, but also that they can be applied to imaging, and, therefore, may be useful imaging probes for follow-up after treatment and even diagnosis. It is also interesting that the dose needed to be administered to achieve successful imaging *in vivo* is lower than the dose needed to have a cytotoxic effect in the dark. This means that when no irradiation is exerted, the molecules are considered safe. Or in other words, since the dose needed for imaging is lower than the one needed for PDT, upon irradiation these molecules can be administered at this concentration and used for imaging and still should not affect healthy tissue. The possibility that of using the same molecule for both treatment and diagnosis makes these compounds interesting theranostic agents.

In conclusion, we were able to prepare and characterize photo-responsive coordinated with ruthenium dimers to form metalla-assemblies, which were subsequently linked to CNCs. These modifications enhanced the solubility, selectivity, targeting, and transport to biological targets. After synthesis, *in vitro* assays were performed to determine the IC_{50} and it was concluded that these moelcules were active PDT agents and also selective towards cancer cell lines. The resulting photo-responsive compounds were also radiolabelled, allowing them to also be used as imaging probes. The administration of these compounds in SCID mice allowed to follow their biodistribution for 24h through SPECT imaging, showing preferential accumulation in the liver for non-tumor bearing mice.

Lastly, when designing the *in vivo* experiments for this project, it was also intended to conduct experiments with *in vivo* models of cancer in order to assess both the PDT action of these compounds as well as to confirm their ability to image tumors selectively, proving, like this, their theranostic nature. Although it was not possible to proceed with these, due to the results in vitro, it is expected that these molecules would show selectivity for the tumor area *in vivo* as well. It is hoped that these experiments can be done in the future, so that we can further confirm that the construction of novel multimodal agents for PDT treatment and imaging has been achieved.

Chapter 4 – Experimental Section

4.1. Chemistry

4.1.1. MATHERIALS AND METHODS

All reagents not synthesized were commercially available (Sigma-Aldrich, Brunschwig, Basel, Switzerland) and used as received. All reactions were performed under an inert atmosphere when indicated, and all solvents were dried before use according to standard procedures. NMR spectra were recorded with a Bruker Advance Neo Ascend 600MHz spectrometer (600.13 MHz for ^1H NMR spectra; Massachusetts, United States). UV–vis absorption spectra were recorded with a PerkinElmer UV–vis spectrophotometer (Waltham, MA, USA). IR spectra were recorded with a Thermoscientific Nicolet iS5 spectrometer. Electrospray ionization mass spectrometry (ESI-MS) spectra were obtained in positive or negative mode with a LCQ Finnigan mass spectrometer. Microanalyses were carried out by the Mikroelementaranalytisches Laboratorium, ETH Zürich (Zürich, Switzerland). Technetium-99m in the form of $[^{99m}Tc]NaTcO_4$ was collected by elution of a $[^{99}Mo]Mo/[^{99m}Tc]Tc$ TEKCIS generator (Auckland, New Zealand) calibrated at 6 GBq. Indium-111 as an $[^{111}In]InCl_3$ solution was purchased from Curium Pharma (Petten, The Netherlands). Dynamic light scattering (DLS) was used for the measurement of average hydrodynamic diameters (Malvern Zetasizer Nano-ZS, Malvern Instruments, UK). Each suspension (0.025 wt%) in pure water was analysed in triplicate at 20 °C with a scattering angle of 173°. Pure water was used as a reference-dispersing medium. The ζ-potential data were collected through electrophoretic light scattering at 20 °C, 150 V, in triplicate for each suspension (0.25 wt%) using the same instrument and at neutral pH. The instrument was calibrated with a Malvern -68 mV standard before each analysis cycle.

4.1.2. SYNTHESIS & CHARACTERIZATION

4.1.2.1. Synthesis of porphyrins and phthalocyanines

The first synthesized porphyrin (5-(4-aminophenyl)-10,15,20-tri(4-pyridyl)porphyrin) was obtained via two-step synthesis, according to the protocol described by Ringot *et al.*[144] First, 4 equivalents of pyrrole (1mL, 15mmol), 1 equivalent (eq.) of 4-nitrobenzaldehyde (0.5 mg, 3.6 mmol) and 3 eq. of 4-pyridine-carboxaldehyde (2 mL, 11.4 mmol) were refluxed (140 °C) for 2 hours in a 25 mL mixture of propionic acid and propionic anhydride. The solution was cooled to room temperature and the propionic acid was removed by distillation to give a dark residue. The residue was then purified by column chromatography on silica gel (MeOH / $–HCl_3$ - 95/5). This reaction gave the desired mono-nitroporphyrin in an acceptable yield (11%). The subsequent reduction of the nitro group into the amino group was carried out in a mixture of hydrochloric acid in the presence of an excess (12 eq.) of $SnCl_2.2H_2O$, while protecting the reaction mixture from the light. The final 5-(4-aminophenyl)-10,15,20-tris(4-pyridyl)-porphyrin was obtained in 71% yield. The reaction was confirmed using ^1H-NMR [δH(500 MHz, $CDCl_3$) ppm = 9.09 (d, 8H, Hpyrr); 8.87 (s, 8H, Hb); 8.19 (d, 8H, Hpyrr); 5.30 (s, 2H, NH_2); - 2.90 (s, 2H, NH)]. Due to the fact that this is not a novel porphyrin, its full characterization was not performed.

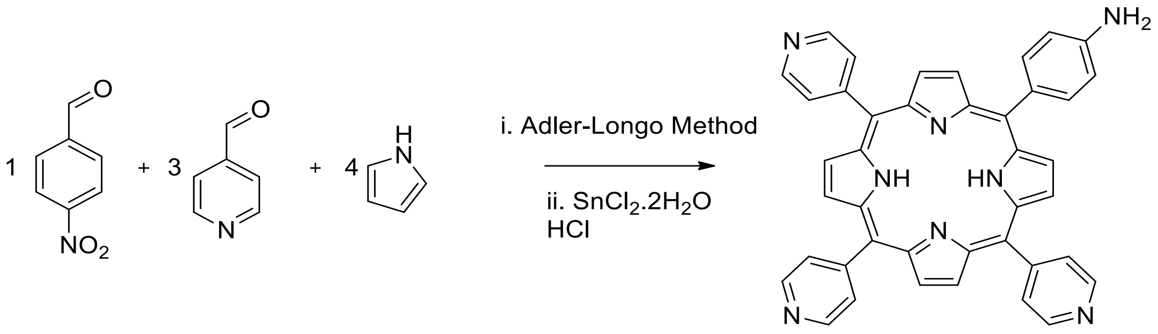

Scheme 5 –Synthetic route for the synthesis of 5-(4-aminophenyl)-10,15,20-tri(4-pyridyl)porphyrin (**P4**).

For (5-(4-hydroxyphenyl)-10,15,20-tri(4-pyridyl)porphyrin), stoichiometric quantities of the corresponding aldehydes: 4-pyridinecarboxaldehyde (0.34 mL, 2 mmol) and 4-hydroxybenzaldehyde (0.244 g, 2 mmol), and pyrrole (0.27 mL, 4 mmol), in propionic acid (15 mL) were left to react under reflux for 1h, as previously described by Adler-Longo.[1] The solution was cooled down to room temperature and the propionic acid was removed by distillation to give a dark residue. The residue was then purified by column chromatography on silica gel (MeOH / $CHCl_3$ – 95/5). The product was collected as a purple solid (15% yield). The reaction was confirmed using ^{1}H-NMR [δH(500 MHz, $CDCl_3$) ppm = 9.04 (d, 8H, Hpyrr); 8.80 (s, 8H, Hb); 8.17 (d, 8H, Hpyrr); 4.73 (s, 1H, OH); - 2.90 (s, 2H, NH) ppm.]. Due to the fact that this is not a novel porphyrin, its full characterization was not performed.

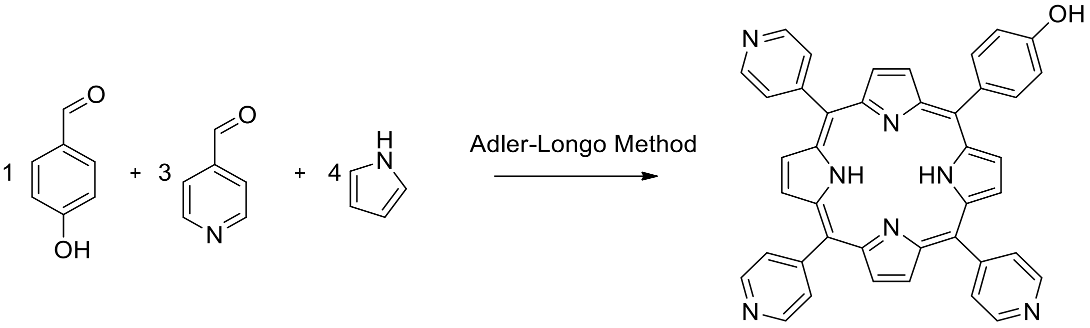

Scheme 6 –Synthetic route for the synthesis of 5-(4-hydroxyphenyl)-10,15,20-tri(4-pyridyl)porphyrin (**P5**).

4.1.2.2. Synthesis of dichloro(*p*-cymene)ruthenium(II) dimer

A solution of 2 g of hydrated ruthenium trichloride (~$RuCl_3.3H_2O$, containing 38-39% Ru) in 100 mL ethanol is treated with an excess of a-phellandrene (10 mL) and heated under reflux in a 250-mL, round-bottomed flask for 4 hours. A nitrogen atmosphere can be used but is not strictly necessary. The solution is cooled to room temperature, and the red, micro-crystalline product is filtered off. Additional product is obtained by evaporating the orange-yellow filtrate under reduced pressure to approximately half-volume, refrigerating it overnight and then proceed with a further filtration.

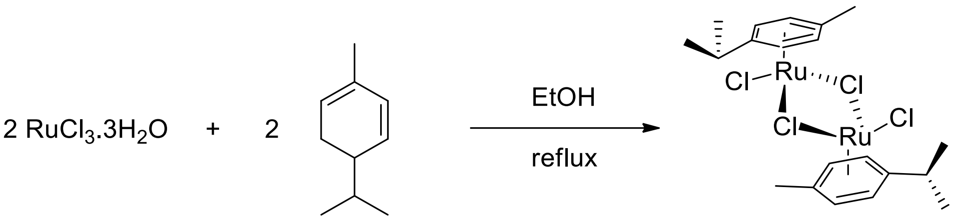

Scheme 7 – Synthesis of $[(\eta 6\text{-}p\text{-cymene})2Ru_2(\mu 2\text{-}Cl)_2Cl_2]$.

4.1.2.3. Synthesis of organic ligands/spacers

For the synthesis of spacers **S1-S4 (Figure 42)**, the protocol was replicated as found on the literature.[134] The mixture was heated under reflux for 60 min., and then cooled to 0°C for at least two hours. The crude 2,5-dimethoxy-1,4-benzoquinone was collected as a brown solid, washed with cold methanol, and airdried (58% yield). This material was used in the next step without further purification.

For spacer **S1**, 100 mg of 2,5-dimethoxy-1,4-benzoquinone were dispersed in 50 ml of ethanol and 1 g O-(2-aminoethyl)polyethylene glycol (PEG-NH_2) was used to construct the side chains of the benzoquinone skeleton; while for **S2**, it was used 1g of O,O′-bis(2-aminoethyl)polyethylene glycol (PEG-diamine) instead. In the case of spacer **S3**, 16 g of EDA (ethylenediamine) were added to 4 g of of 2,5-dimethoxy-1,4-benzoquinone were dispersed in 200 ml of ethanol, while for **S4** 16 g of EtA (ethanolamine) was used instead. None of these spacers was novel, being replicated as found on the literature, as previously mentioned, so their characterization is not presented.

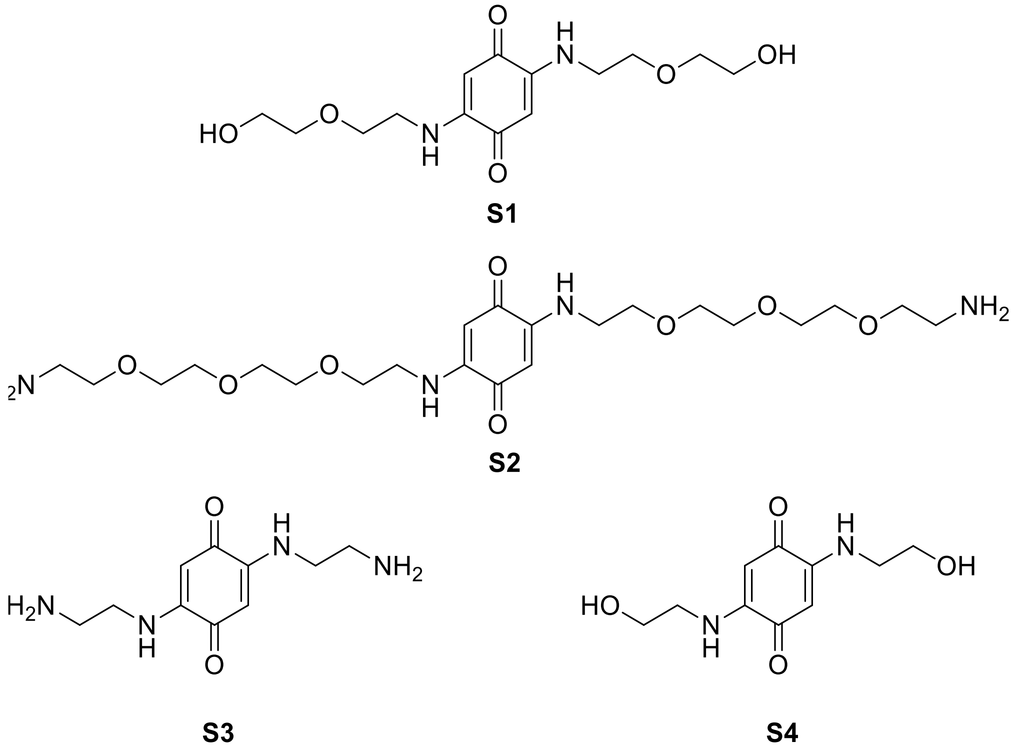

S1

S2

S3

S4

Figure 42 – Structural representation of the different spacers synthesized (**S1-S4**).

4.1.2.4. Synthesis of metalla-clips: conjugation of spacer and dimer

The metalla-clips were synthesized by reacting dichloro(*p*-cymene)ruthenium(II) dimer with the quinones previously synthesized and 2 eq. of sodium acetate, in EtOH at reflux for 48 hours (**Figure 43**), following an analogous method to one found in literature.[159]

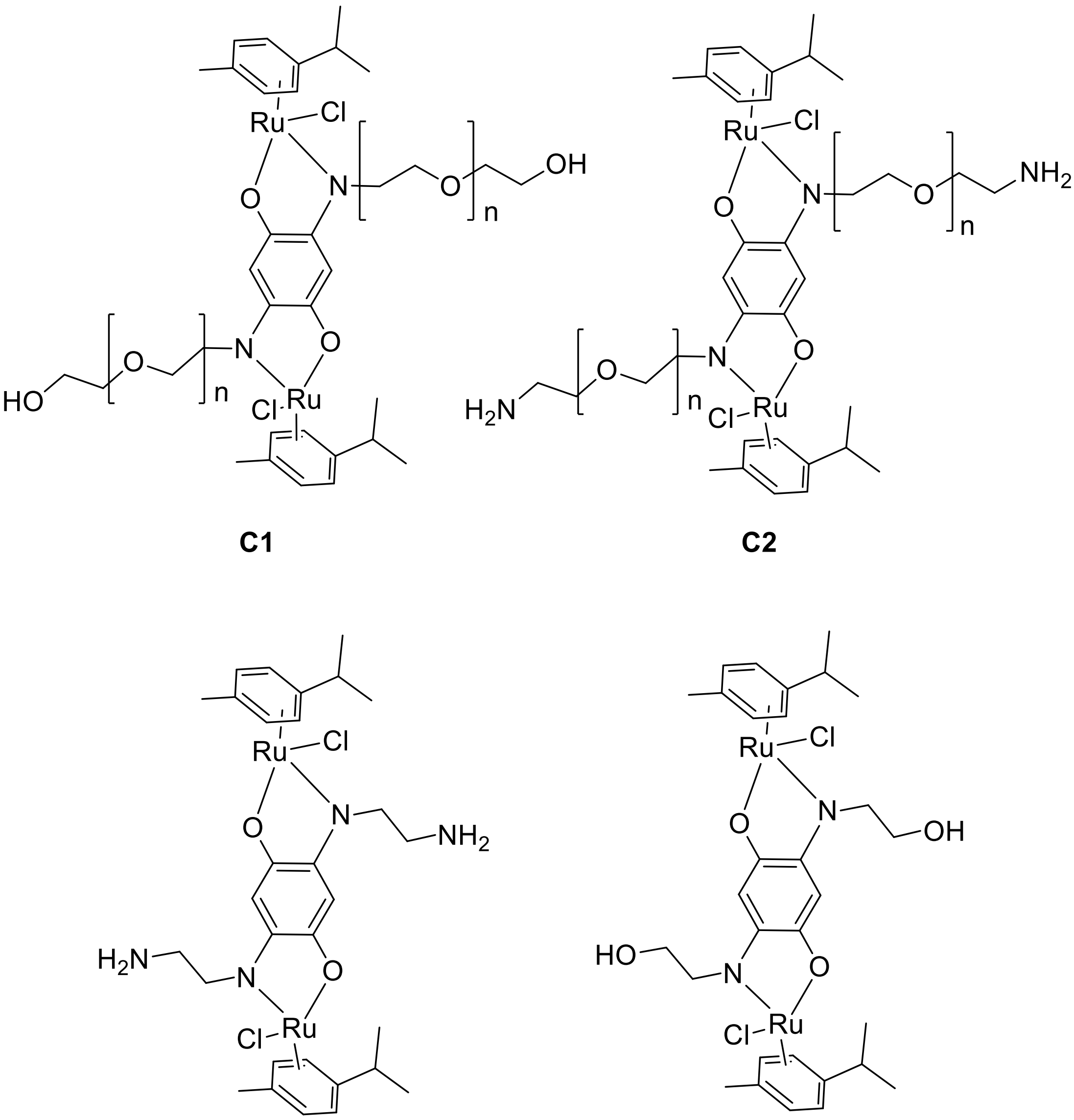

C1

C2

C3

C4

Figure 43 – Structural representation of the different metalla-clips synthesized (**C1-C4**).

For metalla-clips **C1-C4**, a mixture of [Ru(p-cymene)Cl_2]$_2$ (145.0 mg, 0.23 mmol), CH_3COONa (38.4 mg, 0.46 mmol) and either **S1** (72.3 mg, 0.23 mmol), **S2** (112.4 mg, 0.23 mmol), **S3** (51.5 mg, 0.23 mmol), or **S4** (52.0 mg, 0.23 mmol) were added in ethanol (25 mL) and stirred at reflux for 24 h. The reaction was allowed to cool to room temperature, the volume was reduced to half, and the mixture was stored in the refrigerator overnight. The violet precipitate was fialtered and washed with cold H_2O to obtain the desired product as a violet solid. The desired products were all obtained in yields superior to 70%. Their full conversion was followed by ^{1}H-NMR (ESI, **Figures S11-S12**). Since **C3** and **C4** were the novel metalla-clips decided to be used to construct the following metalla-assemblies, they were fully characterized through mass spectrometry and elemental analysis besides ^{1}H-NMR.

C3: ^{1}H-NMR: δH(600 MHz, CD_3OD) ppm = 7.31 (s, 2H, Har benzo), 5.62-5.54 (m, 8H, Har *p*-cym), 3.86 (t, *J* = 5.3 Hz, 8H, CH_2 benzo), 3.72 (t, *J* = 5.3 Hz, 4H, NH_2 benzo), 2.63 (m, *J* = 6.1 Hz, 8H, $(CH_3)_2C\underline{H}$ *p*-cym), 2.12 (s, 6H, CH_3 *p*-cym), 1.26 (d, *J* = 6.1 Hz, 12H, $(C\underline{H}_3)_2CH$ *p*-cym). **Elem anal.** Calcd for $C_{30}H_{42}Cl_2N_4O_2Ru_2$ (764.08): C, 47.18; H, 5.54; N, 7.34. Found: C, 47.21; H, 5.61; N, 7.37. **MS** (ESI$^+$). Calcd for $[C_{30}H_{42}Cl_2N_4O_2 - Cl^-]^+$: m/z 730.08. Found: m/z 730.02.

C4: **^{1}H-NMR**: δH(600 MHz, CD_3OD) ppm = 7.30 (s, 2H, Har benzo), 5.87-5.34 (m, 8H, Har *p*-cym), 3.76 (t, *J* = 5.14 Hz, 2H, OH benzo), 3.54 (t, *J* = 5.14 Hz, 8H, CH_2 benzo), 2.51 (s, 6H, CH_3 *p*-cym), 2.05 (m, *J* = 6.3 Hz, 2H, $(CH_3)_2C\underline{H}$ *p*-cym), 1.29 (d, *J* = 6.3 Hz, 12H, $(C\underline{H}_3)_2CH$ *p*-cym). **Elem anal**. Calcd for $C_{30}H_{40}Cl_2N_2O_4Ru_2$ (766.05): C,47.06; H, 5.27; N, 3.66. Found: C, 47.1; H, 5.22; N, 3.68. **MS** (ESI$^+$). Calcd for $[C_{30}H_{40}Cl_2N_2O_4 - Cl^-]^+$: m/z 732.05 Found: m/z 732.04.

4.1.2.5. Synthesis of metalla-assemblies

For the construction of **M1-M5**, a protocol found in the literature was followed.[2] In the cases of metalla-assemblies **M1-M3**, 4 eq. of the metalla-clip **C3** (50 mg) were suspended in MeOH (20 mL), to which 8 eq. of $AgCF_3SO_3$ (32 mg) were added. The mixture was stirred at RT for 3 h. At this point, one of three photosensitizers **P1** (29H,31H-phthalocyanine; 16 mg), **P2** (copper (II) 4,4',4'',4'''-tetraaza-29H,31H-phthalocyanine; 18 mg), or **P3** (5,10,15,20-tetra(4-pyridyl)-21H,23H-poprhine; 20 mg) was added (2 eq.) to obtain **M1**, **M2**, or **M3**, respectively. The mixture was heated to 60 °C under stirring for 24 h. The solution was then filtered to remove silver chloride and allowed to cool to room temperature. After evaporation under vacuum, the crude product was dissolved in 1mL of CH_2Cl_2. The product was precipitated by addition of 50mL of diethylether/pentane. After filtration and washing with ethyl acetate then dried, compounds were obtained with 68%, 74%, and 72% yield respectively with 29H,31H-phthalocyanine, 5,10,15,20-tetra(4-pyridyl)-21H,23H-porphine, or copper (II) 4,4',4'',4'''-tetraaza-29H,31H-phthalocyanine. ^{1}H NMR spectrum showed full conversion of the starting material (ESI, **Figures S13-S15**).

M1: **^{1}H-NMR:** δH(600 MHz, DMSO-d6) ppm = 8.99 (s, 16H, Har phthalo), 8.35 (s, 16H, Har phthalo), 7.17-7.12 (m, 8H, H_{ar} benzo), 5.95-5.75 (m, 16H, Har *p*-cym), 5.65-5.50 (m, 16H, Har *p*-cym), 2.95-2.74 (m, 32H, CH_2 benzo; 16H, NH_2 benzo), 2.59 (m, *J* = 6.3 Hz, 8H, $(CH_3)_2C\underline{H}$ *p*-cym), 2.09 (s, 24H, CH_3 *p*-cym), 1.21 (d, *J* = 6.3 Hz, 48H, $(C\underline{H}_3)_2CH$ *p*-cym), -2.94 (s, 4H, NH). **MS** (ESI$^+$). Calcd for: $[\mathbf{M1}\text{-}4(CF_3SO_3^-)]^{4+}$: m/z 1099.53. Found: m/z 1099.52; $[\mathbf{M1}\text{-}5(CF_3SO_3^-)]^{5+}$: m/z 849.52. Found: m/z 849.52; $[\mathbf{M1}\text{-}6(CF_3SO_3^-)]^{6+}$: m/z 683.10. Found: m/z 683.10; **Elem anal.** Calcd for $[C_{184}H_{204}N_{32}O_8Ru_8][CF_3SO_3]_8$ (4992.61): C, 46.19; H, 4.12; N, 8.98. Found: C, 45.48; H, 4.25; N, 8.74. **UV-vis** ($(CH_2)_4$º): λ_{max}, nm (log ε) 343(5.09), 627(5.18), 691(5.96)

M2: **^{1}H-NMR:** δH(600 MHz, DMSO-d6) ppm = 8.87 (s, 8H, Har phthalo), 8.35 (dd, 16H, Har phthalo), 7.08 (s, 8H, Har benzo), 5.98-5.77 (m, 16H, Har *p*-cym), 5.69-5.52 (m, 16H, Har *p*-cym), 3.72-3.45 (m, 32H, CH_2 benzo; 16H, NH_2 benzo), 2.61 (m, *J* = 6.4 Hz, 8H, $(CH_3)_2C\underline{H}$ *p*-cym), 2.11 (m, 24H, CH_3 *p*-cym), 1.22 (d, *J* = 6.4 Hz, 48H, $(C\underline{H}_3)_2CH$ *p*-cym). **MS** (ESI$^+$). Calcd for: $[\mathbf{M2}\text{-}4(CF_3SO_3^-)]^{4+}$: m/z 1187.92. Found: m/z 1187.92; $[\mathbf{M2}\text{-}5(CF_3SO_3^-)]^{5+}$: m/z 920.53. Found: m/z 920.54; $[\mathbf{M2}\text{-}6(CF_3SO_3^-)]^{6+}$: m/z 742.28. Found: m/z 742.28; **Elem anal**. Calcd for $[C_{176}H_{192}Cu_2N_{56}O_8Ru_8][CF_3SO_3]_8$ (5347.68): C, 41.32; H, 3.62; N, 14.67. Found: C, 41.92; H, 3.68; N, 14.81. **UV-vis** ($(CH_2)_4$º): λ_{max}, nm (log ε) 341(5.14), 623(5.39), 682(5.91).

M3: **^{1}H-NMR:** δH(600 MHz, DMSO-d6) ppm = 8.66 (s, 16H, Hb porph), 8.15 (m, 32H, Har porphyrin), 7.12-7.09 (m, 8H, Har benzo), 5.91-5.73 (m, 16H, Har *p*-cym), 5.66-5.50 (m, 16H, Har *p*-cym), 3.75 (m, 16H, NH_2 benzo), 2.83 (m, 32H, CH_2 benzo), 2.58 (m, *J* = 6.1 Hz, 8H, $(CH_3)_2C\underline{H}$ *p*-cym), 2.05 (s, 24H, CH_3 *p*-cym), 1.27 (d, *J* = 6.1 Hz, 48H, $(C\underline{H}_3)_2CH$ *p*-cym), -2.91 (s, 4H, NH). **MS** (ESI+) Calcd for: [**M3**-$4(CF_3SO_3^-)]^{4+}$: m/z 1151.22. Found: m/z 1152.22; [**M3**- $5(CF_3SO_3^-)]^{5+}$: m/z 891.18. Found: m/z 891.18; and [**M3**-$6(CF_3SO_3^-)]^{6+}$: m/z 717.81. Found: m/z 717.82; **Elem anal.** Calcd for $[C_{200}H_{220}N_{32}O_8Ru_8][CF_3SO_3]_8$ (5200.89): C, 48.03; H, 4.26; N, 8.62. Found: C, 47.30; H, 4.35; N, 8.69. **UV-vis** ($(CH_2)_4O$): λ_{max}, nm (log ε) 414(5.59), 512(4.19), 545(3.96), 587(3.78), 644(3.52).

Finally, for the construction of **M4-M5**, 3 eq. of **C4** (37.5 mg) were suspended in MeOH (20 mL), and $AgCF_3SO_3$ (6 eq., 24 mg) was added. The mixture was stirred at RT for 3 h. At this point, **P4** (20 mg) or **P5** (20 mg) were added (2 eq.), and the mixture heated to 60 °C. The reaction was stirred for 24-30 h. ^{1}H NMR spectrum showed full conversion of the starting material. Then, the solution was filtered to remove silver chloride and allowed to cool to room temperature. The solvent was removed under reduced pressure, and the crude product was dried overnight. CH_2Cl_2 (1 mL) was added to dissolve the solid, and diethylether was added to induce precipitation. The obtained solid (71% and 66% yield, respectively for **M4** and **M5**) was filtered and dried under vacuum. ^{1}H NMR spectrum showed full conversion of the starting material (ESI, **Figures S15-S17**). Further characterization for these both can be found below:

M4: ^{1}H-NMR: δH(600 MHz, DMSO-d6) δ/ppm = 9.05 (m, 16H, H-3,5 pyridyl (12H) and H-β pyrrolic (4H)), 8.87 (m, 12H, H-β pyrrolic), 8.18 (m, H-2,6 aminophenyl (4H) and H-2,6 pyridyl (12H)), 7.29 (s, 6H, Har benzo), 5.98 (s 4H, H-3,5 aminophenyl), 5.87-5.38 (m, 24H, Har *p*-cym), 4.09 (t, *J* = 6.7 Hz, 6H, OH benzo), 3.76 (d, *J* = 6.7 Hz, 24H, CH_2 benzo), 2.55 (s, 18H, CH_3 *p*-cym), 2.20 (s, 6H, $(CH_3)_2C\underline{H}$ *p*-cym), 1.30 (m, 36H, $(C\underline{H}_3)_2CH$ *p*-cym), - 2.90 (s, 4H, NH). **MS** (ESI^+). Calcd for: [**M4**-$3(CF_3SO_3^-)]^{3+}$: m/z 1266.5. Found: m/z 1266.5; [**M4**-$4(CF_3SO_3^-)]^{4+}$: m/z 912.6. Found: m/z 912.6; **M4**-$5(CF_3SO_3^-)]^{5+}$: m/z 700.3. Found: m/z 700.3. **Elem anal.** Calcd for $C_{178}H_{176}F_{18}N_{22}O_{30}Ru_6S_6$ (4246.52): C, 50.37 H, 4.18; N, 7.26. Found: C, 50.41; H, 4.41; N, 7.60. **UV-vis** (C_2H_6OS): λ_{max}, nm (log ε) 415(5.72), 513(4.23), 549(3.86), 587(3.78), 648(3.57).

M5: ^{1}H-NMR: δH(600 MHz, DMSO-d6) ppm = 8.78 (s, 16H, Har porphyrin), 8.27 (dd, 32H, Har porphyrin), 7.31 (s, 6H, Har benzo), 5.92-5.37 (m, 32H, Har *p*-cym), 4.73 (s, 2H, H-3,5 hydroxyphenyl); 4.10 (t, *J* =6.8 Hz, 6H, OH benzo), 3.53 (d, *J* =6.8 Hz, 24H, CH_2 benzo), 2.53 (s, 18H, CH_3 *p*-cym), 2.20 (s, 6H, $(CH_3)_2C\underline{H}$ *p*-cym), 1.29 (m, 36H, $(CH_3)_2$ *p*-cym), - 2.90 (s, 4H, NH). **MS** (ESI^+). Calcd for: [**M5**-$3(CF_3SO_3^-)]^{3+}$: m/z 1267.2. Found: m/z 1267.2; [**M5**-$4(CF_3SO_3^-)]^{4+}$: m/z 913.1. Found: m/z 913.1; [**M5**-$5(CF_3SO_3^-)]^{5+}$: m/z 700.7. Found: m/z 700.7. **Elem anal.** Calcd for $C_{178}H_{174}F_{18}N_{20}O_{32}Ru_6S_6$ (4248.49): C, 50.35; H, 4.13; N, 6.60. Found: C, 51.01; H, 4.19; N, 6.67. **UV-vis** (C_2H_6OS): λ_{max}, nm (log ε) 412(5.59), 514(4.18), 550(3.74), 588(3.68), 649(3.52).

4.1.2.6. Grafting of Metalla-Assembllies to CNC

First, CNCs were prepared and characterized (**Scheme 8**).[135] This started by pre-heating a paraffin bath at 50-55 °C. Then, a 100 mL of a 64% (v/v) H_2SO_4 solution was prepared. 1 g of cotton (1.1171 g) was weighted, cut it into small pieces and put on an Erlenmeyer. 20 mL of the H_2SO_4 solution was added to the Erlenmeyer with cotton along with a magnet and then left to stir in the paraffin bath until the cotton was dissolved. Once dissolved, it was left under stirring from 60 to 90 min, until the solution turned into a beige color. The solution was left to cool down. The content of the Erlenmeyer was distributed into 4 different centrifugation cups, all equal in weight, (fill with distilled water if needed to achieve this). The

4 cups underwent centrifugation for 10 min at 3700 rpm as many times as necessary until the supernatant was slightly blue in color. All previous supernatants were discarded until this point. When the supernatant was pale blue in color, one more centrifugation was done, and both two supernatants were kept. The pale blue color is an indicator that some of the acid excess has been washed off.

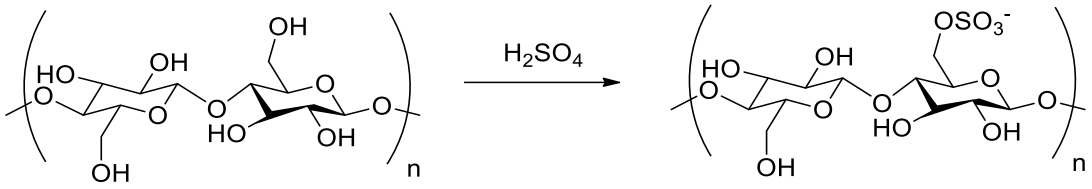

Scheme 8 – Overview of the H_2SO_4 hydrolysis of cellulose nanocrystals.

A 5L container was filled with distilled water, and dialysis membranes of 6000-8000 Da were washed and prepared as needed. The supernatant was put inside the membrane and all air removed before sealing it with a clip. The solution was left for 4 days in water dialysis, changing the water at least two times a day and then collecting the final solution. From this solution, 10 ml were collected for lyophilization and 1 ml for z-average size determination using a Nano Series (Malvern) zetasizer. The weight of the lyophilized nanocrystals in the 10 ml aliquot was measured and the yield subsequently calculated (~ 30%).

The next step was the oxidation of cellulose nanocrystals (**Scheme 9**). To an Erlenmeyer with the cellulose nanocrystals solution that has just been dialyzed, 16 mg (0.1 mmol) of TEMPO were added along with 100 mg (1 mmol) of NaBr. The mixture was left to stir at room temperature for about 1 hour. Sonication may be needed for better dissolution of the cotton in this mixture. After 1 hour of stirring, 2.5 mL (5 mmol) of NaOCl were added and the pH adjusted to 10. This was left to further stir for another 3 hours. The pH was then adjusted to 7 with an HCl solution of 0.1 M. The cellulose solution was decanted and then a further dialysis was performed following the method previously described using a dialysis membrane of 6000-8000 Da).

The final solution was collected and from this solution, 10 ml once again collected for lyophilization and 1 ml for z-average size determination and also for zeta potential. The weight of the lyophilized nanocrystals in the 10 ml aliquot was measured and the yield subsequently calculated (~ 27%). The z-average size was determined by DLS (d.: 101 nm) and the zeta potential calculated as well (-46.4 ± 5.2 mV).

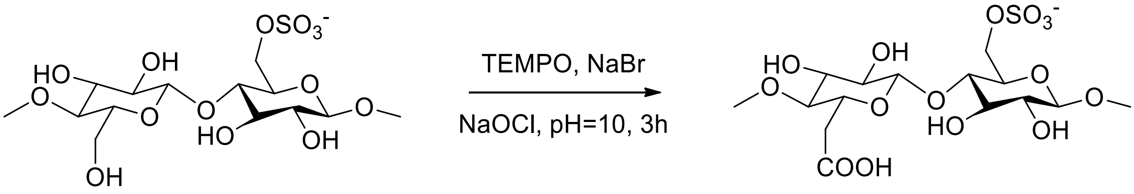

Scheme 9 – Overview of the TEMPO oxidation of cellulose nanocrystals.

After the preparation and characterization of CNCs following the procedure by Chauhan et. al,[160] and their oxidation according to a well-known procedure described in the literature.[5] For the grafting of **M4** and **M5** to CNCs, two 50 ml solutions of oxidized CNCs (1 eq.) in deionized water were activated with NHS (2 eq.) and EDC (2 eq.) each for 2 h at room temperature. Each metalla-assembly (**M4** or **M5**; 1 eq.) was then dissolved in 20 mL of methanol and added dropwise to the respective oxidized CNCs solution. The mixture was left to react for 24 h. After stirring for 1 day at room temperature, the CNC-metalla-assemblies (CNC-MA) were recovered by ultracentrifugation at 13000 rpm, after several washes with deionized water. The final solutions were collected and both z-average size and also zeta potential determined.

For compound **MC5**, for example, these values were 184.2 nm (**Figure S6,** supplementary information), and -38.3 ± 4.5 mV (**Figure S7,** supplementary information), respectively. Once **MC4** and **MC5** were obtained, it was possible to continue with them for either radiolabelling with technetium-99m or indium-111*, in vitro* and or *in vivo* studies.

4.1.3. Radiolabelling & Kinetic Studies

The compound that showed the best PDT results and IC_{50} values (**MC5**) was chosen to be radiolabelled and used to assess its cellular uptake. In addition, so that it was possible to draw more conclusion, its predecessors **P5** and **M5** were radiolabelled and tested as well, to better understand how these modifications affect the uptake. In short, the protocols for the radiolabelling of compounds **P5, M5,** and **MC5** with either technetium-99m or indium-111 are as follow:

4.1.3.1. Compound labelling with technetium-99m

[^{99m}Tc]TcPertechnetate was first eluted from a generator. After elution, a 2 mCi aliquot was then reduced with 0.5 ml of a solution of 0.1 mg $SnCI_2$ in 0.05 N HCI. After shaking vigorously for 1 min and allowing to stand at room temperature for 15 min, the pH of the reduced technetium-99m solution was adjusted to 7.4 with a NaOH 1M solution. A 1 mL aliquot of **P5**, **M5** or **MC5**, previously dissolved in DMSO and diluted to a concentration of 10 mg/ml, is then added to the neutralized [^{99m}Tc]Tc$SnCl_2$ mixture and incubated at 45°C for 30-60 min depending on the porphyrin/metalla-cage, and consequently labelled with ~1.5 mCi of technetium-99m by the chemical method described above. The binding efficiency is assessed by ascending paper radiochromatography with Whatman 3MM paper and iTLC-SG plates developed in acetone or saline as the mobile phase. The radiolabeling was successful with all compounds achieving a radiochemical incorporation higher than 93% . It is possible to conclude that the reaction is complete and little to no traces of free-[^{99m}Tc]TcO_4 are seen. The same results were achieved for the porphyrin-metalla-cage complex (**M5**) and the complex linked to the cellulose nanocrystals (**MC5**). The Rfs in acetone and saline, respectively, were 0.17 and 0.81, for [^{99m}Tc]Tc-**P5**, 0.19 and 0.82 for [^{99m}Tc]Tc-**M5,** and 0.18 and 0.83 for [^{99m}Tc]Tc-**MC5.**

4.1.1.1. Compound labelling with indium-111

A 100 µl aliquot of a 10 mg/mL solution of **P5**, **M5** or **MC5**, previously dissolved in DMSO and diluted to a concentration of 10 mg/ml was added to 100 µl of ammonium acetate (NH_4OAc) buffer (pH 5.5) with

$[^{111}In]InCl_3$ (~300 µCi) in 0,005 M HCl. The reaction mixture was allowed to stand at 60 °C for 45-60 min. It must be noticed that the variation of reaction time influences the presence of isomers for some of the compounds, and that longer time reaction give one single product while shorter time reactions appear to give us a mixture of isomers. The binding efficiency is assessed by ascending paper radiochromatography with Whatman paper 3MM developed in EDTA 0.2 N solution. It is possible to conclude that when the reaction is complete the radio-TLC peak for the labelled compounds stays at the bottom, while if it is incomplete, traces of free $[^{111}In]In(III)$ can be seen at the front of the radio-TLC.

4.1.1.2. Kinetic Studies

For all radiolabelled compounds, kinetic studier was carried out in order to follow their stability in various media, including saline, phosphate-buffered saline (PBS), deionized water, HEPES ((4-(2-hydroxyethyl)-1-piperazineethanesulfonic acid)) buffer solution (0.5 M, pH 5-6), ammonium acetate (0.5 M, pH 5.5), Plasma-Lyte 148 (pH 7.4), and saturated EDTA and DTPA solutions, at different time points (15, 30, 60, 120, 240 min, and 24 hrs). The stability was investigated by incubating the radiolabelled compound in the media (1:10) and was then evaluated through ascending paper radiochromatography with Whatman 3MM paper developed in saline for all $[^{99m}Tc]$Tc-labelled compounds, and in EDTA 0.2 N solution for all $[^{111}In]$In-labelled compounds. The lack or persistence of stability was attributed to the appearance of new peaks or the maintenance of the same, respectively.

4.2. *In vitro*

A2780 and A2780cis cell lines were obtained from the European Collection of Authenticated Cell Cultures (ECACC); and HEk293 was obtained from the American Type Culture Collection (ATCC, CRL-1619). For each experiment, cells were plated and kept in the incubator overnight, to allow the attachment of the cells. All cell lines were maintained according to the suppliers' recommendations at 37 °C in a humidified atmosphere with 95% air and 5% CO2 in a HeraCell 150 incubator and a Thermo Scientific Forma Steri-Cycle i160 CO2 incubator. Dulbecco's Modified Eagle's culture Medium (DMEM, Sigma D-5648) supplemented with 10% fetal bovine serum (Sigma F7524), 250 µM sodium pyruvate (Gibco 11360), and 1% antibiotic (100 U/ml penicillin and 10 µg/ml streptomycin; Sigma A5955) was used for the HEK293 cell line; while for the A2780 and A2780cis cell lines, Roswell Park Memorial Institute 1640 Medium (RPMI, Sigma R6504) culture medium supplemented with 10% fetal bovine serum, 1mM sodium pyruvate and 1% antibiotic was used.

4.2.1. Metabolic activity

For the performance of this study, 96-well plates of the A2780, A2780 cis and HEK293 cell lines were prepared. 48 h after being submitted to the procedure described in the previous section, cell culture medium was aspirated, and the plates washed with PBS. Subsequently, 100 µL of a solution of MTT (3-(4,5-dimethylthiazol-2-yl)-2,5-diphenyltetrazolium bromide; 0.5 mg/ml; Sigma M2128) in PBS, pH 7.4, was placed in each well, and each plate was left to incubate in the dark at 37 °C for at least 3 hours. All formazan crystals formed are then solubilized with DMSO, the contents of each well homogenized. The absorbance was then quantified at 570 nm with a 620 nm reference filter using the Molecular Devices®

SpectraMax M5E multi-mode plate reader. The obtained results were analyzed and processed in the program OriginPro 9.0, expressed in percentage of metabolic treated cells in relation to non-treated. Dose response curves were plotted and IC_{50} (half-maximal inhibitory concentration) values for each compound were determined.

Dark cytotoxicity tests were carried out as described previously, but without the irradiation phase and with larger sensitizer concentrations (5 to 20 mM). Finally, because the quantity of formazan crystals obtained is directly related to the metabolic activity of the cell, this method offers an indirect way of evaluating mitochondrial cell function. The results were expressed as a percentage of the metabolic activity of the cultures that were subjected to photodynamic treatment compared to the cultures that were only given the sensitizer administration vehicle. This approach allowed for the creation of dose-response curves and the determination of the sensitizer concentration that suppresses the metabolic activity of the cultures by 50%.

4.2.2. Photodynamic Treatment

For each experiment, cells were plated and kept in the incubator overnight, to allow the attachment of the cells. The formulation of the sensitizers consisted of a 20 mM solution in DMSO (Fisher Chemical, 200-664-3) and the desired concentrations being achieved by successive dilutions (from 10 mM to 10 nM). Controls were included on every plate, including untreated cell cultures and cultures treated only with the vehicle of administration of the sensitizers, *i.e.,* DMSO. The cell cultures submitted to the photodynamic treatment were incubated always for 48 h at the desired photosensitizer concentrations. In all studies, the cultures were irradiated during 30 min with an irradiance of 10 mW/cm^2, resulting in a light dose of 18 J/cm^2. Irradiations for photodynamic treatment were performed at 652 nm with a diode laser (Ceralas® D-50, Biolitec®, Bonn, Germany). The light delivered by this light source was coupled in the SMA connector of a frontal light distributor (Model FD1, Medlight SA, Switzerland; 2-mm outer diameter) producing a circular homogenous spot with sharp edges.

The photosensitizing efficiency (PE), defined by the ratio between IC_{50} in the dark and IC_{50} after PDT for a given PS, was employed to compare the performance of the three photosensitizers in both cancer cell lines and in the healthy cell line.

$$PE = \frac{IC_{50} dark}{IC_{50}\ PDT}$$

The *in vitro* activity of the tested compounds on all cell line was used to estimate the selectivity index with the formula described below. It should be noted that the IC_{50} values used are the ones before irradiation, for it is believed that *in vivo* PDT treatment implies a previous period of time for PS accumulation, which happens without irradiation, and that the difference in cytotoxicity in healthy and cancer cell lines in these conditions is the one that should be considered for selectivity.

$$SI = \frac{IC_{50}\ healthy\ cell\ line}{IC_{50}\ cancer\ cell\ line}$$

In order to generate comparable data, each PS was tested using the exact same protocol parameters, including concentrations, times of incubation, intervals between administration and irradiation, light dose, fluence, and fluence rate.

4.2.3. Internalization assays

To determine the cellular uptake of P5-MC5, internalization assays were conducted. For that, cells were seeded in a 12 well plate (~10^5 cells/well) overnight at 37 °C in a humidified incubator containing 5% CO_2. To the vial with the radiolabeled compound, cell culture medium was added until the 2ml mark, giving a final concentration of 50 μg/ml of compound with 37 to 55.5 MBq. Then, it was added 5.5-7.5 MBq of this solution to each well (A2780, A2780cis or HEK cell line), which was previously washed with phosphate-buffered saline (PBS) in order to remove any non-attached or dead cells. The administered dose (3 μg/ml) that is lower than the IC_{50} without radiation (> 8 μg/ml), but higher than the IC_{50} with radiation (< 1 μg/ml) for the purpose of having the most imaging agent we can, without harming the cells since no radiation is used for this procedure.

The amount of activity added is measured in a dose-calibrator. This process is repeated for the different wells in the 12 well-plates, and after they are left to incubate for different time periods varying from 15 minutes to 4 h. At the end of the desired time point, the wells are washed for at least 3 times with PBS. This step assures that any radiolabeled compound that doesn't enter the cells or attaches to their membrane is removed, and so the results are accurate and truly represent the uptake process. These washes are collected and also measured for radioactivity. After washing, cold methanol is used 2 or 3 times to lyse the cells and collect any compound that was inside them. Finally, the resulting lysate in each well was collected and the radioactivity measured in a dose-calibrator. Each condition is currently being performed in triplicates and the experiments repeated three times as well in order to assure the results are reliable and reproduceable.

Meanwhile, it can be concluded that the cell uptake appears to vary from 5 to 15% depending on the cell line, with higher uptake for the cancer cells (A2780) than the liver cells (HEK293T) over time, as expected by our previous metabolic activity essays.

4.3. In vivo

In vivo studies were performed at the NCSR Demokritos (Aghia-Paraskevi, Attica Prefecture, Greece), using female SICD mice (15-25 g) purchased from the Breeding Facilities of the NCSR Demokritos (Permit Number: EL 25 BIO 019, EL 25 BIO 020). The protocol and all the animal procedures were approved by the General Directorate of Veterinary Services (Athens, Attica Prefecture, Greece) and by the Bioethical Committee of the Institution (Permit number: EL 25 BIO 022, EL 25 BIO 042) on the basis of the European Directive 2010/63/EU on the protection of animals used for experimental purposes.

The imaging studies were performed on a dedicated benchtop mouse-sized gamma camera (γ-eye™ by BioEmTech), in combination with the X-ray part of a custom-made tri-modal system. The system's field of view is 5x10 cm^2, its spatial resolution is 2 mm and its energy resolution ~25%. The x-ray system consists of an x-ray tube and a CMOS detector, separated by a distance of 30 cm. The minimum pixel size is equal to 0.1 mm and the active area is approximately 12 ×12 cm^2.

4.3.1. Imaging Protocol

Once the radiolabelling, is complete following the protocol previously described, the final solution is diluted with water for injection to a concentration of 375 nM to a final volume of 80-100 µL and a final activity of 3.33-3.7 MBq (90-110 µCi) with the injected activity being calculated by measuring the syringe before and after the administration in a dose calibrator. After being previously anesthetized with isoflurane (3.5% for induction), a SCID mouse is injected retro-orbitally, and a scintigraphic/x-ray fused imaging profile in normal SCID mice is acquired. For such, the mice were positioned on the animal bed at a <0.5 cm distance from the camera head to allow whole body imaging with maximum spatial resolution and successive 2 min frames were collected for up to 1 h post injection (p.i.). After the first hour, static images were also acquired at 1, 2, 4, and 24 h p.i. Upon completion of the scintigraphy imaging, x-ray images were also acquired at the exact same mouse positioning to act as an anatomical guide for the organs' exact location. The x-ray imaging parameters were set to 35 kVp, 500 µA and 0.1 s exposure time. Fusion between scintigraphy and x-ray images was performed semi-automatically through an in-house standard procedure.

The x-ray imaging provides an anatomical image of very high resolution, that can act as an anatomical map of the mouse. The combination of the two imaging methods provides a detailed and clear biodistribution and placement of the studied substance throughout time.

The activity in the animal is also measured for each timepoint to determine the clearance yield of the compound through the difference of the expected activity if none of it was cleared out of the body, with the activity being corrected foe the expected decay at each timepoint, and the actual activity measured in the mouse. The animal is left to regain consciousness between timepoints in order to let the natural biodistribution of the compound occur without any external factor added. At each time point, one mouse will be anesthetized with isoflurane (3.5% for induction), placed on the animal bed of the stepping apparatus and maintained under anaesthesia (2% for maintenance) and at 37 °C by the air flow heated bed throughout the imaging procedure.

For each condition a set of 3 SCID mice was used. Acquisition times varied from 20 to 60 min depending on the timepoint and radioactivity decay in the animal, meaning that for expected lower activities, a longer acquisition time is needed to acquire a better image. The data acquired is treated with the help of ImageJ® software to reconstruct the images

References

(1) Adler, A. D.; Longo, F. R.; Finarelli, J. D.; Goldmacher, J.; Assour, J.; Korsakoff, L. A Simplified Synthesis for Meso-Tetraphenylporphine. *J. Org. Chem.* **1967**, *32* (2), 476. https://doi.org/10.1021/jo01288a053.

(2) Mannancherril, V.; Therrien, B. Strategies Toward the Enhanced Permeability and Retention Effect by Increasing the Molecular Weight of Arene Ruthenium Metallaassemblies. *Inorg. Chem.* **2018**, *57* (7), 3626–3633. https://doi.org/10.1021/acs.inorgchem.7b02668.

(3) Coverdale, J.; Laroiya-McCarron, T.; Romero-Canelón, I. Designing Ruthenium Anticancer Drugs: What Have We Learnt from the Key Drug Candidates? *Inorganics.* **2019**, *7* (3), 31. https://doi.org/10.3390/inorganics7030031.

(4) Chauhan, P.; Hadad, C.; Sartorelli, A.; Zarattini, M.; Herreros-López, A.; Mba, M.; Prato, M.; Prato, M.; Carofiglio, T. Nanocrystalline Cellulose–Porphyrin Hybrids: Synthesis, Supramolecular Properties, and Singlet-Oxygen Production. *Chem. Commun.* **2013**, *49* (76), 8525–8527. https://doi.org/10.1039/c3cc44852e.

(5) Ma, X.; Yu, H. Global Burden of Cancer. *YALE J. Biol. Med.* **2006**, *79*, 85–94.

(6) Ferlay, J.; Steliarova.-Foucher, E.; Lortet-Tieulent, J.; Rosso, S.; Coebergh, J. W. W.; Comber, H.; Forman, D.; Bray, F. Cancer Incidence and Mortality Patterns in Europe: Estimates for 40 Countries in 2012. *Eur. J. Cancer* **2013**, *49* (6), 1374–1403. https://doi.org/10.1016/J.EJCA.2012.12.027.

(7) Agostinis, P.; Berg, K.; Cengel, K. A.; Foster, T. H.; Girotti, A. W.; Gollnick, S. O.; Hahn, S. M.; Hamblin, M. R.; Juzeniene, A.; Kessel, D.; Korbelik, M.; Moan, J.; Mroz, P.; Nowis, D.; Piette, J.; Wilson, B. C.; Golab, J. Photodynamic Therapy of Cancer: An Update. *CA. Cancer J. Clin.* **2011**, *61* (4), 250–281. https://doi.org/10.3322/caac.20114.

(8) Vonarbourg, A.; Passirani, C.; Saulnier, P.; Benoit, J. P. Parameters Influencing the Stealthiness of Colloidal Drug Delivery Systems. *Biomaterials.* **2006**, *27* (24), 4356–4373. https://doi.org/10.1016/j.biomaterials.2006.03.039.

(9) Serra, A. C.; Pineiro, M.; Rocha Gonsalves, A. M. d. A.; Abrantes, M.; Laranjo, M.; Santos, A. C.; Botelho, M. F. Halogen Atom Effect on Photophysical and Photodynamic Characteristics of Derivatives of 5,10,15,20-Tetrakis(3-Hydroxyphenyl)Porphyrin. *J. Photochem. Photobiol. B Biol.* **2008**, *92* (1), 59–65. https://doi.org/10.1016/j.jphotobiol.2008.04.006.

(10) Abrahamse, H.; Hamblin, M. R. New Photosensitizers for Photodynamic Therapy. *Biochem. J.* **2016**, *473* (4), 347–364. https://doi.org/10.1042/BJ20150942.

(11) Mitton, D.; Ackroyd, R. A Brief Overview of Photodynamic Therapy in Europe. *Photodiagnosis Photodyn. Ther.* **2008**, *5* (2), 103–111. https://doi.org/10.1016/j.pdpdt.2008.04.004.

(12) Triesscheijn, M.; Baas, P.; Schellen, J. H. M.; Stewart, F.A. Photodynamic Therapy in Oncology. *Oncologist* **2006**, *11* (9), 1173–1179. https://doi.org/10.1634/THEONCOLOGIST.11-9-1034.

(13) Robertson, C. A.; Evans, D. H.; Abrahamse, H. Photodynamic Therapy (PDT): A Short Review on Cellular Mechanisms and Cancer Research Applications for PDT. *J. Photochem. Photobiol. B Biol.* **2009**, *96* (1), 1–8. https://doi.org/10.1016/j.jphotobiol.2009.04.001.

(14) Alsaab, H. O.; Alghamdi, M. S.; Alotaibi, A. S.; Alzhrani, R.; Alwuthaynani, F.; Althobaiti, Y. S.; Almalki, A. H.; Sau, S.; Iyer, A. K. Progress in Clinical Trials of Photodynamic Therapy for Solid Tumors and the Role of Nanomedicine. *Cancers (Basel).* **2020**, *12* (10), 1–26. https://doi.org/10.3390/CANCERS12102793.

(15) Phua, S. Z. F.; Xue, C.; Lim, W. Q.; Yang, G.; Chen, H.; Zhang, Y.; Wijaya, C. F.; Luo, Z.; Zhao, Y. Light-Responsive Prodrug-Based Supramolecular Nanosystems for Site-Specific Combination Therapy of Cancer. *Chem. Mater.* **2019**, *31* (9), 3349–3358. https://doi.org/10.1021/ACS.CHEMMATER.9B00439.

(16) Nackiewicz, J.; Kiber-Jasik, M.; Skonieczna, M. A Novel Pro-Apoptotic Role of Zinc Octacarboxyphthalocyanine in Melanoma Me45 Cancer Cell's Photodynamic Therapy (PDT). *J. Photochem. Photobiol. B.* **2019**, *190*, 146–153. https://doi.org/10.1016/J.JPHOTOBIOL.2018.12.002.

(17) Wu, H.; Minamide, T.; Yano, T. Role of Photodynamic Therapy in the Treatment of Esophageal Cancer. *Dig. Endosc.* **2019**, *31* (5), 508–516. https://doi.org/10.1111/DEN.13353.

(18) Aniogo, E. C.; Plackal Adimuriyil George, B.; Abrahamse, H. The Role of Photodynamic Therapy on Multidrug Resistant Breast Cancer. *Cancer Cell Int.* **2019**, *19* (1), 1–14. https://doi.org/10.1186/S12935-019-0815-0.

(19) Oda, D. F.; Duarte, M. A. H.; Andrade, F. B.; Moriyama, L. T.; Bagnato, V. S.; de Moraes, I. G. Antimicrobial Action of

Photodynamic Therapy in Root Canals Using LED Curing Light, Curcumin and Carbopol Gel. *Int. Endod. J.* **2019**, *52* (7), 1010–1019. https://doi.org/10.1111/IEJ.13092.

(20) Spring, B. Q.; Rizvi, I.; Xu, N.; Hasan, T. The Role of Photodynamic Therapy in Overcoming Cancer Drug Resistance. *Photochem. Photobiol. Sci.* **2015**, *14* (8), 1476–1491. https://doi.org/10.1039/C4PP00495G.

(21) Hu, S.; Yang, Y.; Jiang, B.; Su, D.; Zhang, L.; Huang, Z.; Zhang, F. Treatment of Condyloma Acuminatum Using the Combination of Laser Ablation and ALA-PDT. *Photodiagnosis Photodyn. Ther.* **2019**, *25*, 193–196. https://doi.org/10.1016/J.PDPDT.2018.12.006.

(22) Simões, J. A New Generation Of Ring-Fused Fluorinated Chlorins as Promising PDT Agents: From Synthesis To *In Vitro* Studies, Universide de Coimbra, **2018**.

(23) Patrice, T.; Moor, A. C. E.; Ortel, B.; Hasan, T. Mechanisms of Photodynamic Therapy. *Gan To Kagaku Ryoho*. **2003**, *23* (1), 19-58. https://doi.org/10.1039/9781847551658-00019

(24) Anand, S.; Ortel, B. J.; Pereira, S. P.; Hasan, T.; Maytin, E. V. Biomodulatory Approaches to Photodynamic Therapy for Solid Tumors. *Cancer Lett.* **2012**, *326* (1), 8–16. https://doi.org/10.1016/j.canlet.2012.07.026.

(25) Juarranz, Á.; Jaén, P.; Sanz-Rodríguez, F.; Cuevas, J.; González, S. Photodynamic Therapy of Cancer. Basic Principles and Applications. *Clin. Transl. Oncol.* **2008**, *10* (3), 148–154. https://doi.org/10.1007/s12094-008-0172-2.

(26) Yoo, J. O.; Ha, K. S. New Insights into the Mechanisms for Photodynamic Therapy-Induced Cancer Cell Death. *Int. Rev. Cell Mol. Bio*. **2012**, *295*, 139–174. https://doi.org/10.1016/B978-0-12-394306-4.00010-1.

(27) Byrne, A. T.; O'Connor, A. E.; Hall, M.; Murtagh, J.; O'Neill, K.; Curran, K. M.; Mongrain, K.; Rousseau, J. A.; Lecomte, R.; McGee, S.; Callanan, J. J.; O'Shea, D. F.; Gallagher, W. M. Vascular-Targeted Photodynamic Therapy With BF2-Chelated Tetraaryl-Azadipyrromethene Agents: A Multi-Modality Molecular Imaging Approach to Therapeutic Assessment. *Br. J. Cancer.* **2009**, *101* (9), 1565–1573. https://doi.org/10.1038/sj.bjc.6605247.

(28) Plaetzer, K.; Krammer, B.; Berlanda, J.; Berr, F.; Kiesslich, T. Photophysics and Photochemistry of Photodynamic Therapy: Fundamental Aspects. *Lasers Med. Sci.* **2009**, *24* (2), 259–268. https://doi.org/10.1007/S10103-008-0539-1.

(29) Kushibiki, T.; Hirasawa, T.; Okawa, S.; Ishihara, M. Responses of Cancer Cells Induced by Photodynamic Therapy. *J. Healthc. Eng.* **2013**, *4* (1), 87–108. https://doi.org/10.1260/2040-2295.4.1.87.

(30) Jerjes, W.; Upile, T.; Hamdoon, Z.; Nhembe, F.; Bhandari, R.; Mackay, S.; Shah, P.; Mosse, C. A.; Brookes, J. A. S.; Morley, S.; Hopper, C. Ultrasound-Guided Photodynamic Therapy for Deep Seated Pathologies: Prospective Study. *Lasers Surg. Med.* **2009**, *41* (9), 612–621. https://doi.org/10.1002/lsm.20853.

(31) Huang, Z.; Xu, H.; Meyers, A. D.; Musani, A. I.; Wang, L.; Tagg, R.; Barqawi, A. B.; Chen, Y. K. Photodynamic Therapy for Treatment of Solid Tumors - Potential and Technical Challenges. *Technol. Cancer Res. Treat.* **2008**, *7* (4), 309–320. https://doi.org/10.1177/153303460800700405.

(32) Agostinis, P.; Berg, K.; Cengel, K. A.; Foster, T. H.; Girotti, A. W.; Gollnick, S. O.; Hahn, S. M.; Hamblien, M. R.; Juzenine, A.; Kessel. D. *CA: Cancer J. Clin*. **2011**, *61* (4), 250-281. https://doi.org/10.3322/caac.20114.

(33) Allison, R. R. Photodynamic Therapy: Oncologic Horizons. *Futur. Oncol.* **2014**, *10* (1), 123–142. https://doi.org/10.2217/fon.13.176.

(34) Allison, R. R.; Bagnato, V. S.; Sibata, C. H. Future of Oncologic Photodynamic Therapy. *Future Oncol.* **2010**, *6* (6), 929–940. https://doi.org/10.2217/fon.10.51.

(35) Pucelik, B.; Paczyński, R.; Dubin, G.; Pereira, M. M.; Arnaut, L. G.; Dąbrowski, J. M. Properties of Halogenated and Sulfonated Porphyrins Relevant for the Selection of Photosensitizers in Anticancer and Antimicrobial Therapies. *PLoS One.* **2017**, *12* (10), e0185984. https://doi.org/10.1371/journal.pone.0185984.

(36) Allison, R. R.; Moghissi, K. Photodynamic Therapy (PDT): PDT Mechanisms. *Clin. Endosc.* **2013**, *46* (1), 24–29. https://doi.org/10.5946/ce.2013.46.1.24.

(37) Senge, M. O. MTHPC - A Drug on Its Way From Second to Third Generation Photosensitizer? *Photodiagnosis Photodyn. Ther.* **2012**, *9* (2), 170–179. https://doi.org/10.1016/j.pdpdt.2011.10.001.

(38) Ormond, A. B.; Freeman, H. S. Dye Sensitizers for Photodynamic Therapy. *Materials (Basel).* **2013**, *6* (3), 817–840. https://doi.org/10.3390/ma6030817.

(39) Pereira, N. A. M.; Serra, A. C.; Pinho e Melo, T. M. V. D. Novel Approach to Chlorins and Bacteriochlorins: [8π+2π] Cycloaddition of Diazafulvenium Methides with Porphyrins. *European J. Org. Chem.* **2010**, *2010* (34), 6539–6543. https://doi.org/10.1002/ejoc.201001157.

(40) Brown, S. B.; Brown, E. A.; Walker, I. The Present and Future Role of Photodynamic Therapy in Cancer Treatment.

Lancet Oncology. **2004**, *5* (8), 497–508. https://doi.org/10.1016/S1470-2045(04)01529-3.

(41) Dellian, M.; Yuan, F.; Trubetskoy, V. S.; Torchilin, V. P.; Jain, R. K. Vascular Permeability in a Human Tumour Xenograft: Molecular Charge Dependence. *Br. J. Cancer.* **2000**, *82* (9), 1513–1518. https://doi.org/10.1054/BJOC.1999.1171.

(42) Greish, K. Enhanced Permeability and Retention (EPR) Effect for Anticancer Nanomedicine Drug Targeting. *Methods Mol. Biol.* **2010**, *624*, 25–37. https://doi.org/10.1007/978-1-60761-609-2_3.

(43) Wong, E.; Giandomenico, C. M. Current Status of Platinum-Based Antitumor Drugs. *Chem. Rev.* **1999**, *99* (9), 2451–2466. https://doi.org/10.1021/CR980420V.

(44) Jakupec, M. A.; Galanski, M.; Arion, V. B.; Hartinger, C. G.; Keppler, B. K. Antitumour Metal Compounds: More than Theme and Variations. *Dalt. Trans.* **2007**, *2*, 183–194. https://doi.org/10.1039/B712656P.

(45) Kostova, I. Ruthenium Complexes as Anticancer Agents. *Curr. Med. Chem.* **2006**, *13* (9), 1085–1107. https://doi.org/10.2174/092986706776360941.

(46) Ai, Z.; Lu, Y.; Qiu, S.; Fan, Z. Overcoming Cisplatin Resistance of Ovarian Cancer Cells by Targeting HIF-1-Regulated Cancer Metabolism. *Cancer Lett.* **2016**, *373* (1), 36–44. https://doi.org/10.1016/J.CANLET.2016.01.009.

(47) Shen, D. W.; Pouliot, L. M.; Hall, M. D.; Gottesman, M. M. Cisplatin Resistance: A Cellular Self-Defense Mechanism Resulting from Multiple Epigenetic and Genetic Changes. *Pharmacol. Rev.* **2012**, *64* (3), 706–721. https://doi.org/10.1124/PR.111.005637.

(48) Parker, R. J.; Eastman, A.; Bostick-Bruton, F.; Reed, E. Acquired Cisplatin Resistance in Human Ovarian Cancer Cells is Associated with Enhanced Repair of Cisplatin-DNA Lesions and Reduced Drug Accumulation. *J. Clin. Invest.* **1991**, *87* (3), 772–777. https://doi.org/10.1172/JCI115080.

(49) Morris, R. E.; Aird, R. E.; Murdoch, P. S.; Chen, H.; Cumming, J.; Hughes, N. D.; Parson, S.; Parkin, A.; Boyd, G.; Jodrell, D. I.; Sadler, P. J. Inhibition of Cancer Cell Growth by Ruthenium(II) Arene Complexes. *J. Med. Chem.* **2001**, *44* (22), 3616–3621. https://doi.org/10.1021/JM010051M.

(50) Kandioller, W.; Balsano, E.; Meier, S. M.; Jungwirth, U.; Goschl, S.; Roller, A.; Jakupec, M. A.; Berger, W.; Keppler, B. K.; Hartinger, C. G. Organometallic Anticancer Complexes of Lapachol: Metal Centre-Dependent Formation of Reactive Oxygen Species and Correlation with Cytotoxicity. *Chem. Commun. (Camb).* **2013**, *49* (32), 3348–3350. https://doi.org/10.1039/C3CC40432C.

(51) Dougan, S. J.; Habtemariam, A.; McHale S. E.; Parsons, S.; Sadler, P. J. Catalytic Organometallic Anticancer Complexes. *Proc. Natl. Acad. Sci. U. S. A.* **2008**, *105* (33), 11628–11633. https://doi.org/10.1073/PNAS.0800076105.

(52) Zhang, P.; Sadler, P. J. Advances in the Design of Organometallic Anticancer Complexes. *J. Organomet. Chem.* **2017**, *839*, 5–14. https://doi.org/10.1016/J.JORGANCHEM.2017.03.038.

(53) Bergamo, A.; Masi, A.; Peacock, A. F. A.; Habtemariam, A.; Sadler, P. J.; Sava, G. *In Vivo* Tumour and Metastasis Reduction and *In Vitro* Effects on Invasion Assays of the Ruthenium RM175 and Osmium AFAP51 Organometallics in the Mammary Cancer Model. *J. Inorg. Biochem.* **2010**, *104* (1), 79–86. https://doi.org/10.1016/J.JINORGBIO.2009.10.005.

(54) Hayward, R. L.; Schornagel, Q. C.; Tente, R.; Macpherson, J. S.; Aaird, R. E.; Guichard, S.; Habtemariam, A.; Sadler, P.; Jodrell, D. I. Investigation of the Role of Bax, P21/Waf1 and P53 as Determinants of Cellular Responses in HCT116 Colorectal Cancer Cells Exposed to the Novel Cytotoxic Ruthenium(II) Organometallic Agent, RM175. *Cancer Chemother. Pharmacol.* **2005**, *55* (6), 577–583. https://doi.org/10.1007/S00280-004-0932-9.

(55) Carter, R.; Westhorpe, A.; Romero, M. J.; Habtemariam, A.; Gallevo, C. R.; Bark, Y.; Menezes, N.; Sadler, P. J.; Sharma, R. A. Radiosensitisation of Human Colorectal Cancer Cells by Ruthenium(II) Arene Anticancer Complexes. *Sci. Rep.* **2016**, *6*. https://doi.org/10.1038/SREP20596.

(56) Chen, H.; Parkinson, J. A.; Parsons, S.; Coxall, R. A.; Gould, R.O.; Sadler, P. J. Organometallic Ruthenium(II) Diamine Anticancer Complexes: Arene-Nucleobase Stacking and Stereospecific Hydrogen-Bonding in Guanine Adducts. *J. Am. Chem. Soc.* **2002**, *124* (12), 3064–3082. https://doi.org/10.1021/JA017482E.

(57) Aird, R. E.; Cummings, J.; Ritchie A. A..; Muir, M.; Morris, R. E.; Chen, H.; Sadler, P J.; Jodrell, D. I. *In Vitro* and *In Vivo* Activity and Cross Resistance Profiles of Novel Ruthenium (II) Organometallic Arene Complexes in Human Ovarian Cancer. *Br. J. Cancer* **2002**, *86* (10), 1652–1657. https://doi.org/10.1038/SJ.BJC.6600290.

(58) Zelonka, R. A.; Baird, M. C. Benzene Complexes of Ruthenium(II). *Can. J. Chem.* **2011**, *50* (18), 3063–3072. https://doi.org/10.1139/V72-486.

(59) Allardyce, C. S.; Dyson, P. J.; Ellis, D. J.; Heath, S. L. [Ru(H6-p-Cymene)Cl2(Pta)] (Pta = 1,3,5-Triaza-7-Phosphatricyclo-[3.3.1.1]Decane): A Water Soluble Compound That Exhibits PH Dependent DNA Binding Providing Selectivity for Diseased Cells. *Chem. Commun.* **2001**, *15*, 1396–1397. https://doi.org/10.1039/B104021A.

(60) Murray, B. S.; Babak, M. V.; Hartinger, C. G.; Dyson, P. J. The Development of RAPTA Compounds for the Treatment of Tumors. *Coord. Chem. Rev.* **2016**, *306*, 86–114. https://doi.org/10.1016/J.CCR.2015.06.014.

(61) Phillips, A. D.; Gonsalvi, L.; Romerosa, A.; Vizza, F.; Peruzzini, M. Coordination Chemistry of 1,3,5-Triaza-7-Phosphaadamantane (PTA): Transition Metal Complexes and Related Catalytic, Medicinal and Photoluminescent Applications. *Coord. Chem. Rev.* **2004**, *248* (11–12), 955–993. https://doi.org/10.1016/J.CCR.2004.03.010.

(62) Scolaro, C.; Bergamo, A; Brescacin, L; Delfino, R; Cocchietto, M; Laurenczy, G; Geldbach, T. J.; Sava, G.; Dyson, P. J. *In Vitro* and *in Vivo* Evaluation of Ruthenium(II)–Arene PTA Complexes. *J. Med. Chem.* **2005**, *48* (12), 4161–4171. https://doi.org/10.1021/JM050015D.

(63) Holtkamp, H. U.; Movassaghi, S.; Morrow, S. J.; Kubanik, M.; Hartinger, C. G. Metallomic Study on the Metabolism of RAPTA-C and Cisplatin in Cell Culture Medium and Its Impact on Cell Accumulation. *Metallomics.* **2018**, *10* (3), 455–462. https://doi.org/10.1039/C8MT00024G.

(64) Dyson, P. J. Systematic Design of a Targeted Organometallic Antitumour Drug in Pre-Clinical Development. *Chimia (Aarau).* **2007**, *61* (11), 698–703. https://doi.org/10.2533/chimia.2007.698.

(65) Lee, S. Y.; Kim, C. Y.; Nam, T. G. Ruthenium Complexes as Anticancer Agents: A Brief History and Perspectives. *Drug Des. Devel. Ther.* **2020**, *2020* (14), 5375–5392. https://doi.org/10.2147/DDDT.S275007.

(66) Alessio, E. Thirty Years of the Drug Candidate NAMI-A and the Myths in the Field of Ruthenium Anticancer Compounds: A Personal Perspective. *Eur. J. Inorg. Chem.* **2017**, *2017* (12), 1549–1560. https://doi.org/10.1002/EJIC.201600986.

(67) Clarke, M. J. Ruthenium Metallopharmaceuticals. *Coord. Chem. Rev.* **2003**, *236* (1–2), 209–233. https://doi.org/10.1016/S0010-8545(02)00312-0.

(68) Trondl, R.; Heffeter, P.; Kowol, C. R.; Jakupec, M. A.; Berger, W.; Keppler, B. K. NKP-1339, the First Ruthenium-Based Anticancer Drug on the Edge to Clinical Application. *Chem. Sci.* **2014**, *5* (8), 2925–2932. https://doi.org/10.1039/C3SC53243G.

(69) Dyson, P. J.; Sava, G. Metal-Based Antitumour Drugs in the Post Genomic Era. *Dalt. Trans.* **2006**, *16*, 1929–1933. https://doi.org/10.1039/B601840H.

(70) Morbidelli, L.; Donnini, S.; Filippi, S.; Messori, L.; Piccoli, F.; Orioli, P.; Sava, G.; Ziche, M. Antiangiogenic Properties of Selected Ruthenium(III) Complexes That Are Nitric Oxide Scavengers. *Br. J. Cancer* **2003**, *88* (9), 1484–1491. https://doi.org/10.1038/SJ.BJC.6600906.

(71) Feliers, D.; Chen, X.; Akis, N.; Choudhury, G. G.; Madaio, M.; Kasinath, B. S.. VEGF Regulation of Endothelial Nitric Oxide Synthase in Glomerular Endothelial Cells. *Kidney Int.* **2005**, *68* (4), 1648–1659. https://doi.org/10.1111/J.1523-1755.2005.00575.X.

(72) Oszajca, M.; Kuliś, E.; Stochel, G.; Brindell, M. Interaction of the NAMI-A Complex with Nitric Oxide under Physiological Conditions. *New J. Chem.* **2014**, *38* (8), 3386–3394. https://doi.org/10.1039/C3NJ01631E.

(73) Bergamo, A.; Pelillo, C.; Chambery, A.; Sava, G. Influence of Components of Tumour Microenvironment on the Response of HCT-116 Colorectal Cancer to the Ruthenium-Based Drug NAMI-A. *J. Inorg. Biochem.* **2017**, *168*, 90–97. https://doi.org/10.1016/J.JINORGBIO.2016.11.031.

(74) Therrien, B. Arene Ruthenium Cages: Boxes Full of Surprises. *Eur. J. Inorg. Chem.* **2009**, *2009* (17), 2445–2453. https://doi.org/10.1002/EJIC.200900180.

(75) Therrien, B.; Furrer, J. The Biological Side of Water-Soluble Arene Ruthenium Assemblies. *Adv. Chem.* **2014**, *2014*, 1-20. https://doi.org/10.1155/2014/589686.

(76) Süss-Fink, G. Water-Soluble Arene Ruthenium Complexes: From Serendipity to Catalysis and Drug Design. *J. Organomet. Chem.* **2014**, *751*, 2–19. https://doi.org/10.1016/J.JORGANCHEM.2013.07.039.

(77) Schmitt, F.; Govindaswamy, P.; Süss-Fink, G.; Wee, H. A.; Dyson, P. J.; Juillerat-Jeanneret, L.; Therrien, B. Ruthenium Porphyrin Compounds for Photodynamic Therapy of Cancer. *J. Med. Chem.* **2008**, *51* (6), 1811–1816. https://doi.org/10.1021/jm701382p.

(78) Süss-Fink, G. Arene Ruthenium Complexes as Anticancer Agents. *Dalton Trans*. **2010**, *7*, 1673–1688. https://doi.org/10.1039/b916860p.

(79) Yu, G.; Yu, S.; Saha, M. L; Zhou, J.; Cook, T. R.; Yung, B. C.; Chen, J.; Mao, Z.; Zhang, F.; Zhou, Z.; Liu, Y.; Shao, L.; Wang, S.; Gao, C.; Huang, F.; Stang, P .J.; Chen, X. A Discrete Organoplatinum(II) Metallacage as a Multimodality Theranostic Platform for Cancer Photochemotherapy. *Nat. Commun.* **2018**, *9* (1). 1-18. https://doi.org/10.1038/S41467-018-06574-7.

(80) Lucky, S. S.; Soo, K. C.; Zhang, Y. Nanoparticles in Photodynamic Therapy. *Chem. Rev.* **2015**, *115* (4), 1990–2042. https://doi.org/10.1021/cr5004198.

(81) Ethirajan, M.; Chen, Y.; Joshi, P.; Pandey, R. K. The Role of Porphyrin Chemistry in Tumor Imaging and Photodynamic Therapy. *Chem. Soc. Rev.* **2010**, *40* (1), 340–362. https://doi.org/10.1039/B915149B.

(82) Jiang, X.; Zhou, Z.; Yang, H.; Shan, C.; Yu, H.; Wojtas, L.; Zhang, M.; Mao, Z.; Wang, M.; Stang, P. J. Self-Assembly of Porphyrin-Containing Metalla-Assemblies and Cancer Photodynamic Therapy. *Inorg. Chem,* **2020**, *59*, 58. https://doi.org/10.1021/acs.inorgchem.9b02775.

(83) Schmitt, F.; Barry, N. P. E.; Juillerat-Jeanneret, L.; Therrien, B. Efficient Photodynamic Therapy of Cancer Using Chemotherapeutic Porphyrin-Ruthenium Metalla-Cubes. *Bioorganic Med. Chem. Lett.* **2012**, *22* (1), 178–180. https://doi.org/10.1016/j.bmcl.2011.11.058.

(84) Gasser, G.; Ott, I.; Metzler-Nolte, N. Organometallic Anticancer Compounds. *J. Med. Chem*. **2011**, *54* (1), 3–25. https://doi.org/10.1021/jm100020w.

(85) Heinemann, F.; Karges, J.; Gasser, G. Critical Overview of the Use of Ru(II) Polypyridyl Complexes as Photosensitizers in One-Photon and Two-Photon Photodynamic Therapy. *Acc. Chem. Res.* **2017**, *50* (11), 2727–2736. https://doi.org/10.1021/acs.accounts.7b00180.

(86) Karges, J.; Kuang, S.; Ong, Y. C.; Chao, H.; Gasser, G. One- and Two-Photon Phototherapeutic Effects of RuII Polypyridine Complexes in the Hypoxic Centre of Large Multicellular Tumor Spheroids and Tumor-Bearing Mice**. *Chem.-A Eur. J.* **2021**, *27* (1), 362–370. https://doi.org/10.1002/chem.202003486.

(87) Mari, C.; Huang, H.; Rubbiani, R.; Schulze, M.; Würthner, F.; Chao, H.; Gasser, G. Evaluation of Perylene Bisimide-Based RuII and IrIII Complexes as Photosensitizers for Photodynamic Therapy. *Eur. J. Inorg. Chem.* **2017**, *2017* (12), 1745–1752. https://doi.org/10.1002/ejic.201600516.

(88) Swavey, S.; Morford, K.; Tsao, M.; Comfort, K.; Kilroy, M. K. Heteroleptic Monometallic and Trimetallic Ruthenium(II) Complexes Incorporating a π-Extended Dipyrrin Ligand: Light-Activated Reactions with the A549 Lung Cancer Cell Line. *J. Inorg. Biochem.* **2017**, *175*, 101–109. https://doi.org/10.1016/j.jinorgbio.2017.07.012.

(89) Sibani, S. A.; McCarron, P. A.; Woolfson, A. D.; Donnelly, R. F. Photosensitiser Delivery for Photodynamic Therapy. Part 2: Systemic Carrier Platforms. *Expert Opin. Drug Deliv.* **2008**, *5* (11), 1241–1254. https://doi.org/10.1517/17425240802444673.

(90) Brigger, I.; Dubernet, C.; Couvreur, P. Nanoparticles in Cancer Therapy and Diagnosis. *Adv. Drug Deliv. Rev.* **2012**, *64*, 24–36. https://doi.org/10.1016/j.addr.2012.09.006.

(91) Maeda, H.; Tsukigawa, K.; Fang, J. A Retrospective 30 Years After Discovery of the Enhanced Permeability and Retention Effect of Solid Tumors: Next-Generation Chemotherapeutics and Photodynamic Therapy-Problems, Solutions, and Prospects. *Microcirculation.* **2016**, *23* (3), 173–182. https://doi.org/10.1111/MICC.12228.

(92) Jain, R. K.; Stylianopoulos, T. Delivering Nanomedicine to Solid Tumors. *Nat. Rev. Clin. Oncol.* **2010**, *7* (11), 653–664. https://doi.org/10.1038/nrclinonc.2010.139.

(93) Immunotherapy for Cancer - National Cancer Institute https://www.cancer.gov/about-cancer/treatment/types/immunotherapy (accessed Jul 8, 2021).

(94) Duncan, R. Polymer Conjugates as Anticancer Nanomedicines. *Nat. Rev. Cancer.* **2006**, *6* (9), 688–701. https://doi.org/10.1038/NRC1958.

(95) Akhlaghi, S. P.; Peng, B.; Yao, Z.; Tam, K. C. Sustainable Nanomaterials Derived from Polysaccharides and Amphiphilic Compounds. *Soft Matter.* **2013**, *9* (33), 7905–7918. https://doi.org/10.1039/C3SM50358E.

(96) Lima, M. M. de S.; Borsali, R. Rodlike Cellulose Microcrystals: Structure, Properties, and Applications. *Macromol. Rapid Commun.* **2004**, *25* (7), 771–787. https://doi.org/10.1002/MARC.200300268.

(97) Samir, M. A. S. A.; Alloin, F.; Dufresne, A. Review of Recent Research into Cellulosic Whiskers, Their Properties and Their Application in Nanocomposite Field. *Biomacromolecules.* **2005**, *6* (2), 612–626. https://doi.org/10.1021/BM0493685.

(98) Zhu, L.; Kumar, V.; Banker, G. S. Examination of Oxidized Cellulose as a Macromolecular Prodrug Carrier: Preparation and Characterization of an Oxidized Cellulose-Phenylpropanolamine Conjugate. *Int. J. Pharm.* **2001**, *223* (1–2), 35–47. https://doi.org/10.1016/S0378-5173(01)00725-6.

(99) Emerich, D. F.; Thanos, C. G. Targeted Nanoparticle-Based Drug Delivery and Diagnosis. *J. Drug Target.* **2007**, *15* (3), 163–183. https://doi.org/10.1080/10611860701231810.

(100) Beck-Candanedo, S.; Roman, M.; Gray, D. G. Effect of Reaction Conditions on the Properties and Behavior of Wood Cellulose Nanocrystal Suspensions. *Biomacromolecules.* **2005**, *6* (2), 1048–1054. https://doi.org/10.1021/BM049300P.

(101) Jackson, J. K.; Letchford, K.; Wasserman, B. Z.; L, Ye.; Hamad, W. Y.; Burt, H. M. The Use of Nanocrystalline Cellulose for the Binding and Controlled Release of Drugs. *Int. J. Nanomed.* **2011**, *6*, 321–330. https://doi.org/10.2147/IJN.S16749.

(102) Granström, M. Cellulose Derivatives: Synthesis, Properties and Applications, University of Helsinki, 2009.

(103) Staudinger, H. Grundlegende Begriffe. *Die Hochmolekularen Org. Verbindungen.* **1960**, 1–16. https://doi.org/10.1007/978-3-642-64954-7_1.

(104) Klemm, D., Philipp, B., Heinze, T., Heinze, U., Wagenknecht, W. Comprehensive Cellulose Chemistry. Volume 1. Fundamentals and Analytical Methods By D. Klemm, B. Philipp, T. Heinze, U. Heinze, and W. Wagenknecht. Wiley: Weinheim, Germany. 1998. 260 Pp. $236.25. ISBN 3-527-29413-9. *J. Am. Chem. Soc.* **1999**, *121* (37), 8677–8677. https://doi.org/10.1021/JA9857514.

(105) Thompson, L.; Azadmanjiri, J.; Nikzad, M.; Sbarski, I.; Wang, J.; Yu, A. Cellulose Nanocrystals: Production, Functionalization and Advanced Applications. *Rev. Adv. Mater. Sci.* **2019**, *58* (1), 1–16. https://doi.org/10.1515/rams-2019-0001.

(106) Orue, A.; Santamaria-Echart, A.; Eceiza, A.; Peña-Rodriguez, C.; Arbelaiz, A. Office Waste Paper as Cellulose Nanocrystal Source. *J. Appl. Polym. Sci.* **2017**, *134* (35), 45257. https://doi.org/10.1002/APP.45257.

(107) Danial, W. H.; Majid,Z. A.; Muhid, M. N. M.; Triwahyono, S.; Bakar, M. B.; Ramli, Z. The Reuse of Wastepaper for the Extraction of Cellulose Nanocrystals. *Carbohydr. Polym.* **2014**, *118*, 165–169. https://doi.org/10.1016/J.CARBPOL.2014.10.072.

(108) Wang, Z.; Yao, Z.; Zhou, J.; Zhzng, Y. Reuse of Waste Cotton Cloth for the Extraction of Cellulose Nanocrystals. *Carbohydr. Polym.* **2017**, *157*, 945–952. https://doi.org/10.1016/J.CARBPOL.2016.10.044.

(109) Udoetok, I. A.; Wilson, L. D.; Headley, J. V. Ultra-Sonication Assisted Cross-Linking of Cellulose Polymers. *Ultrason. Sonochem.* **2018**, *42*, 567–576. https://doi.org/10.1016/J.ULTSONCH.2017.12.017.

(110) Yu, H.; Qin, Z.; Liang, B.; Liu, N.; Zhou, Z.; Chen, L. Facile Extraction of Thermally Stable Cellulose Nanocrystals with a High Yield of 93% through Hydrochloric Acid Hydrolysis under Hydrothermal Conditions. *J. Mater. Chem. A* **2013**, *1* (12), 3938–3944. https://doi.org/10.1039/C3TA01150J.

(111) Alves Henrique, M.; Pires, W.; Neto, F.; Alves Silvério, H.; Ferreira Martins, D.; Vinícius, L.; Gurgel, A.; Da, H.; Barud, S.; Carlos De Morais, L.; Pasquini, D. Kinetic Study of the Thermal Decomposition of Cellulose Nanocrystals with Different Polymorphs, Cellulose I and II, Extracted from Different Sources and Using Different Types of Acids. *Ind. Crop. Prod.* **2015**, *76*, 128–140. https://doi.org/10.1016/j.indcrop.2015.06.048.

(112) Paakko, M.; Ankerfors, M.; Kosonen, H.; Nykanen, A.; Ahola, S.; Osterberg, M.; Ruokolainen, J.; Laine, J.; Larsson, P. T.; Ikkala, O.; Lindstom, T. Enzymatic Hydrolysis Combined with Mechanical Shearing and High-Pressure Homogenization for Nanoscale Cellulose Fibrils and Strong Gels. *Biomacromolecules.* **2007**, *8* (6), 1934–1941. https://doi.org/10.1021/BM061215P.

(113) Guo, J.; Guo, X.; Wang, S.; Yin, Y. Effects of Ultrasonic Treatment during Acid Hydrolysis on the Yield, Particle Size and Structure of Cellulose Nanocrystals. *Carbohydr. Polym.* **2015**, *135*, 248–255. https://doi.org/10.1016/J.CARBPOL.2015.08.068.

(114) Kargarzadeh, H.; Ahmad, I.; Abdullah, I.; Thomas, R.; Dufresne, A.; Thomas, S.; Hassan, A. Functionalized Liquid Natural Rubber and Liquid Epoxidized Natural Rubber: A Promising Green Toughening Agent for Polyester. *J. Appl. Polym. Sci.* **2015**, *132* (3). https://doi.org/10.1002/APP.41292.

(115) Kargarzadeh, H.; Sheltami, R. M.; Ahmad, I.; Abdullah, I.; Dufresne, A. Cellulose Nanocrystal Reinforced Liquid Natural Rubber Toughened Unsaturated Polyester: Effects of Filler Content and Surface Treatment on Its Morphological, Thermal, Mechanical, and Viscoelastic Properties. *Polymer (Guildf).* **2015**, *71*, 51–59. https://doi.org/10.1016/J.POLYMER.2015.06.045.

(116) Siqueira, G.; Bras, J.; Dufresne, A. New Process of Chemical Grafting of Cellulose Nanoparticles with a Long Chain Isocyanate. *Langmuir.* **2009**, *26* (1), 402–411. https://doi.org/10.1021/LA9028595.

(117) Roman, M. Toxicity of Cellulose Nanocrystals: A Review. *Industrial Biotech*. **2015**, *11* (1), 25–33. https://doi.org/10.1089/IND.2014.0024.

(118) Mahmoud, K. A.; Mena, J. A.; MAle, K. B.; Hrapovic, S.; Kamen, A.; Luong, J. H. Effect of Surface Charge on the Cellular Uptake and Cytotoxicity of Fluorescent Labeled Cellulose Nanocrystals. *ACS Appl. Mater. Interfaces.* **2010**, *2* (10), 2924–2932. https://doi.org/10.1021/AM1006222.

(119) Jawaid, M.; Mohammad, F. Nanocellulose and Nanohydrogel Matrices: Biotechnological and Biomedical Applications. *Nanocellulose Nanohydrogel Matrices Biotechnol. Biomed. Appl.* **2017**, 1–362. https://doi.org/10.1002/9783527803835.

(120) Hebeish, A.; Guthrie, J. T. The Chemistry and Technology of Cellulosic Copolymers. *Chem. Technol. Cellul. Copolym.* **1981**, *4*. https://doi.org/10.1007/978-3-642-67707-6.

(121) Eyley, S.; Thielemans, W. Surface Modification of Cellulose Nanocrystals. *Nanoscale.* **2014**, *6* (14), 7764–7779. https://doi.org/10.1039/C4NR01756K.

(122) Moon, R. J.; Martini, A.; Nairn, J.; Simonsen, J.; Youngblood, J. Cellulose Nanomaterials Review: Structure, Properties and Nanocomposites. *Chem. Soc. Rev.* **2011**, *40* (7), 3941–3994. https://doi.org/10.1039/C0CS00108B.

(123) Girouard, N. M.; Xu, S.; Schueneman, G. T.; Shofner, M. L.; Meredith, J. C. Site-Selective Modification of Cellulose Nanocrystals with Isophorone Diisocyanate and Formation of Polyurethane-CNC Composites. *ACS Appl. Mater. Interfaces.* **2016**, *8* (2), 1458–1467. https://doi.org/10.1021/ACSAMI.5B10723.

(124) Espinosa, S. C.; Kihnt, T.; Foster, E. J.; Weder, C. Isolation of Thermally Stable Cellulose Nanocrystals by Phosphoric Acid Hydrolysis. *Biomacromolecules.* **2013**, *14* (4), 1223–1230. https://doi.org/10.1021/BM400219U.

(125) Sadeghifar, H.; Filpponen, I.; Clarke, S. P.; Brougham, D. F.; Argyropoulos, D. S. Production of Cellulose Nanocrystals Using Hydrobromic Acid and Click Reactions on Their Surface. *Int. J. Mater. Sci.* **2011**, *46* (22), 7344–7355. https://doi.org/10.1007/S10853-011-5696-0.

(126) Habibi, Y.; Lucia, L. A.; Rojas, O. J. Cellulose Nanocrystals: Chemistry, Self-Assembly, and Applications. *Chem. Rev.* **2010**, *110* (6), 3479–3500. https://doi.org/10.1021/CR900339W.

(127) Eichhorn, S. J.; Dufresne, A.; Aranguren, M.; Marcovich, N. E.; Capadona, J. R.; Rowan, S. J.; Weder, C.; Thielemans, W.; Roman, M.; Renneckar, S.; Gindl, W.; Veigel, S.; Keckes, J.; Yano, H.; Abe, K.; Nogi, M.; Nakagaito, A. N.; Mangalam, A.; Simonsen, J.; Benight, A. S.; Bismarck, A.; Berglund, L. A.; Peijs, T. Review: Current International Research into Cellulose Nanofibres and Nanocomposites. *J. Mater. Sci.* **2010**, *45* (1), 1–33. https://doi.org/10.1007/S10853-009-3874-0.

(128) Lizundia, E.; Villas, J. L.; Léon, L. M. Crystallization, Structural Relaxation and Thermal Degradation in Poly(L-Lactide)/Cellulose Nanocrystal Renewable Nanocomposites. *Carbohydr. Polym.* **2015**, *123*, 256–265. https://doi.org/10.1016/J.CARBPOL.2015.01.054.

(129) Nooy, A. E. J. de; Besemer, A. C.; Bekkum, H. van. Highly Selective Tempo Mediated Oxidation of Primary Alcohol Groups in Polysaccharides. *Recl. des Trav. Chim. des Pays-Bas,* **1994**, *113* (3), 165–166. https://doi.org/10.1002/RECL.19941130307.

(130) Saito, T.; Kimura, S.; Nishiyama, Y.; Isogai, A. Cellulose Nanofibers Prepared by TEMPO-Mediated Oxidation of Native Cellulose. *Biomacromolecules.* **2007**, *8* (8), 2485–2491. https://doi.org/10.1021/BM0703970.

(131) Saito, T.; Okita, Y.; Nge, T. T.; Sugiyama, J.; Isogai, A. TEMPO-Mediated Oxidation of Native Cellulose: Microscopic Analysis of Fibrous Fractions in the Oxidized Products. *Carbohydr. Polym.* **2006**, *65* (4), 435–440. https://doi.org/10.1016/J.CARBPOL.2006.01.034.

(132) Saito, T.; Nishiyama, Y.; Putaux, J. L.; Vignon, M.; Isogai, A. Homogeneous Suspensions of Individualized Microfibrils from TEMPO-Catalyzed Oxidation of Native Cellulose. *Biomacromolecules.* **2006**, *7* (6), 1687–1691. https://doi.org/10.1021/BM060154S.

(133) Montanari, S.; Roumani, M; Heux, L.; Vignon, M. R. Topochemistry of Carboxylated Cellulose Nanocrystals Resulting from TEMPO-Mediated Oxidation. *Macromolecules.* **2005**, *38* (5), 1665–1671. https://doi.org/10.1021/MA048396C.

(134) Asahara, T.; Seno, M.; Teshirogi, T. Reactions of *p*-Benzoquinone Derivatives with Ethylenediamine. *Bull. Chem. Soc. Jpn.* **1971**, *44* (6), 1687–1689. https://doi.org/10.1246/bcsj.44.1687.

(135) Drogat, N.; Granet, R.; Le Morvan, C.; Bégaud-Grimaud, G.; Krausz, P.; Sol, V. Chlorin-PEI-Labeled Cellulose Nanocrystals: Synthesis, Characterization and Potential Application in PDT. *Bioorganic Med. Chem. Lett.* **2012**, *22* (11), 3648–3652. https://doi.org/10.1016/j.bmcl.2012.04.044.

(136) Rosa, M. F.; Medeiros, E. S.; Malmonge, J. A.; Gregorski, K. S.; Wood, D. F.; Mattoso, L. H. C.; Glenn, G.; Orts, W. J.; Imam, S. H. Cellulose Nanowhiskers from Coconut Husk Fibers: Effect of Preparation Conditions on Their Thermal and Morphological Behavior. *Carbohydr. Polym.* **2010**, *81* (1), 83–92. https://doi.org/10.1016/j.carbpol.2010.01.059.

(137) Poletto, M.; Ornaghi, H.; Zattera, A. Native Cellulose: Structure, Characterization and Thermal Properties. *Materials (Basel).* **2014**, *7* (9), 6105–6119. https://doi.org/10.3390/ma7096105.

(138) Popescu, M. C.; Popescu, C. M.; Lisa, G.; Sakata, Y. Evaluation of Morphological and Chemical Aspects of Different Wood Species by Spectroscopy and Thermal Methods. *J. Mol. Struct.* **2011**, *988* (1–3), 65–72.

https://doi.org/10.1016/j.molstruc.2010.12.004.

(139) Poletto, M.; Pistor, V.; Zeni, M.; Zattera, A. J. Crystalline Properties and Decomposition Kinetics of Cellulose Fibers in Wood Pulp Obtained by Two Pulping Processes. *Polym. Degrad. Stab.* **2011**, *96* (4), 679–685. https://doi.org/10.1016/j.polymdegradstab.2010.12.007.

(140) Fackler, K.; Stevanic, J. S.; Ters, T.; Hinterstoisser, B.; Schwanninger, M.; Salmén, L. FT-IR Imaging Microscopy to Localise and Characterise Simultaneous and Selective White-Rot Decay within Spruce Wood Cells. *Holzforschung.* **2011**, *65* (3), 411–420. https://doi.org/10.1515/HF.2011.048.

(141) Xu, F.; Yu, J.; Tesso, T.; Dowell, F.; Wang, D. Qualitative and Quantitative Analysis of Lignocellulosic Biomass Using Infrared Techniques: A Mini-Review. *Applied Energy*. **2013**, *104,* 801–809. https://doi.org/10.1016/j.apenergy.2012.12.019.

(142) Hospodarova, V.; Singovszka, E.; Stevulova, N. Characterization of Cellulosic Fibers by FTIR Spectroscopy for Their Further Implementation to Building Materials. *Am. J. Anal. Chem.* **2018**, *9*, 303–310. https://doi.org/10.4236/ajac.2018.96023.

(143) Mbakidi, J. P.; Herke, K.; Alvès, S.; Chaleix, V.; Granet, R.; Krausz, P.; Leroy-Lhez, S.; Ouk, T. S.; Sol, V. Synthesis and Photobiocidal Properties of Cationic Porphyrin-Grafted Paper. *Carbohydr. Polym.* **2013**, *91* (1), 333–338. https://doi.org/10.1016/j.carbpol.2012.08.013.

(144) Ringot, C.; Sol, V.; Barrière, M.; Saad, N.; Bressollier, P.; Granet, R.; Couleaud, P.; Frochot, C.; Krausz, P. Triazinyl Porphyrin-Based Photoactive Cotton Fabrics: Preparation, Characterization, and Antibacterial Activity. *Biomacromolecules.* **2011**, *12* (5), 1716–1723. https://doi.org/10.1021/bm200082d.

(145) Alexandrova, R.; Kalfin, R.; Tudose, R.; Fagadar-Cosma, E. Comparative Cytotoxicity Assays Performed Using a Free Porphyrin and its Zn(Ii), Co(Ii) and Cu(Ii) Complexes. Influence of Optical and Aggregation Properties. *Studia UBB Chem.* **2018**, *4*, 65-77. https://doi.org/10.24193/subbchem.2018.4.05.

(146) Balaban, R. S.; Hampshire, V. A. Challenges in Small Animal Noninvasive Imaging. *ILAR J.* **2001**, *42* (3), 248-262 https://doi.org/10.1093/ilar.42.3.248

(147) Peterson, T. E.; Shokouhi, S. Advances in Preclinical SPECT Instrumentation. *J. Nucl. Med.* **2012**, *53*, 841–844. https://doi.org/10.2967/jnumed.111.099853.

(148) Gomes, C. M.; Abrunhosa, A. J.; Ramos, P.; Pauwels, E. K. J. Molecular Imaging with SPECT as a Tool for Drug Development. *Adv. Drug Deliv. Rev.* **2011**, *63* (7), 547–554. https://doi.org/10.1016/j.addr.2010.09.015.

(149) Kagadis, G. C.; Loudos, G.; Katsanos, K.; Langer, S. G.; Nikiforidis, G. C. In Vivo Small Animal Imaging: Current Status and Future Prospects. *Med. Phys.* **2010**, *37* (12), 6421–6442. https://doi.org/10.1118/1.3515456.

(150) Peremans, K.; Cornelissen, B.; Van Den Bossche, B.; Audenaert, K.; Van De Wiele, C. A Review of Small Animal Imaging Planar and Pinhole SPECT Γ Camera Imaging. *Vet. Radiol. Ultrasound.* **2005**, *46* (2), 162–170. https://doi.org/10.1111/j.1740-8261.2005.00031.x.

(151) Franc, B. L.; Acton, P. D.; Mari, C.; Hasegawa, B. H. Small-Animal SPECT and SPECT/CT: Important Tools for Preclinical Investigation*. *J. Nucl. Med.* **2008**, *49*, 1651–1663. https://doi.org/10.2967/jnumed.108.055442.

(152) Stout, D. B.; Zaidi, H. Preclinical Multimodality Imaging *in Vivo*. *PET Clinics*. **2008**, *3* (3), 251–273. https://doi.org/10.1016/j.cpet.2009.03.001.

(153) Zanzonico, P. Principles of Nuclear Medicine Imaging: Planar, SPECT, PET, Multi-Modality, and Autoradiography Systems. *Radiat. Res*. **2012**, *177* (4), 349–364. https://doi.org/10.1667/RR2577.1.

(154) Georgiou, M.; Fysikopoulos, E.; Mikropoulos, K.; Fragogeorgi, E.; Loudos, G. Characterization of Βγ-Eye^: A Low-Cost Benchtop Mouse-Sized Gamma Camera for Dynamic and Static Imaging Studies. *Mol. Imaging Biol.* **2017**, *19*, 398–407. https://doi.org/10.1007/s11307-016-1011-4.

(155) Simões, J. C. S.; Sarpaki, S.; Papadimitroulas, P.; Therrien, B.; Loudos, G. Conjugated Photosensitizers for Imaging and PDT in Cancer Research. *J. Med. Chem.* **2020,** *63* (23), 14119-14150. https://doi.org/10.1021/acs.jmedchem.0c00047.

(156) Srivatsan, A.; Missert, J. R.; Upadhyay, S. K.; Pandey, R. K. Porphyrin-Based Photosensitizers and the Corresponding Multifunctional Nanoplatforms for Cancer-Imaging and Phototherapy. *J. Porphyr. Phthalocyanines.* **2015**, *19* (1–3), 109–134. https://doi.org/10.1142/S1088424615300037.

(157) Kharroubi Lakouas, D.; Huglo, D.; Mordon, S.; Vermandel, M. Nuclear Medicine for Photodynamic Therapy in Cancer: Planning, Monitoring and Nuclear PDT. *Photodiagnosis Photodyn. Ther.* **2017**, *18*, 236–243. https://doi.org/10.1016/j.pdpdt.2017.03.002.

(158) Jokerst, J. V.; Lobovkina, T.; Zare, R. N.; Gambhir, S. S. Nanoparticle PEGylation for Imaging and Therapy. *Nanomedicine.* **2011**, *6* (4), 715–728. https://doi.org/10.2217/nnm.11.19.

(159) Therrien, B.; Süss-Fink, G.; Govindaswamy, P.; Renfrew, A. K.; Dyson, P. J. The "Complex-in-a-Complex" Cations $[(\mathrm{Acac})_2\mathrm{M}\subset \mathrm{Ru}_6\text{-}(p\text{-}\mathrm{IPrC}_6\mathrm{H}_4\mathrm{Me})_6(\mathrm{Tpt})_2(\mathrm{Dhbq})_3]^{6+}$: A Trojan Horse for Cancer Cells. *Angew. Chemie-Int. Ed.* **2008**, *47* (20), 3773–3776. https://doi.org/10.1002/anie.200800186.

(160) Chauhan, P.; Hadad, C.; Sartorelli, A.; Zarattini, M.; Herreros-López, A.; Mba, M.; Prato, M.; Prato, M.; Carofiglio, T. Nanocrystalline Cellulose–Porphyrin Hybrids: Synthesis, Supramolecular Properties, and Singlet-Oxygen Production. *Chem. Commun.* **2013**, *49* (76), 8525–8527. https://doi.org/10.1039/c3cc44852e.

(161) Isogai, A.; Saito, T.; Fukuzumi, H. TEMPO-Oxidized Cellulose Nanofibers. *Nanoscale*. **2011**, *3* (1), 71–85. https://doi.org/10.1039/c0nr00583e.

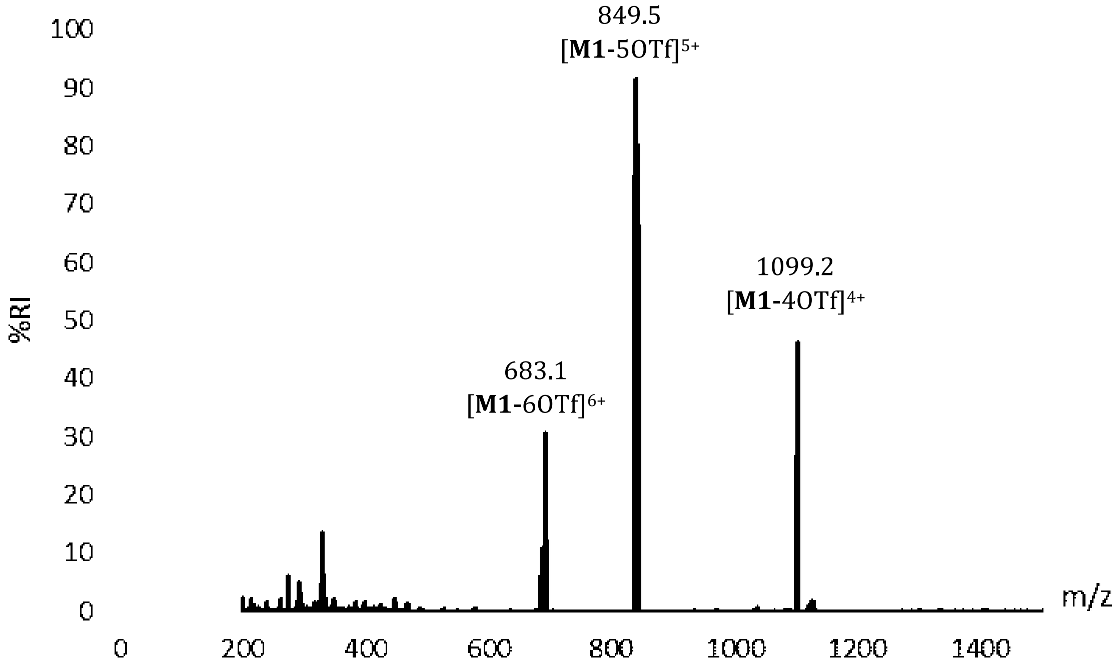

Figure S1. Mass spectrometry for **M1**– ESI (+)

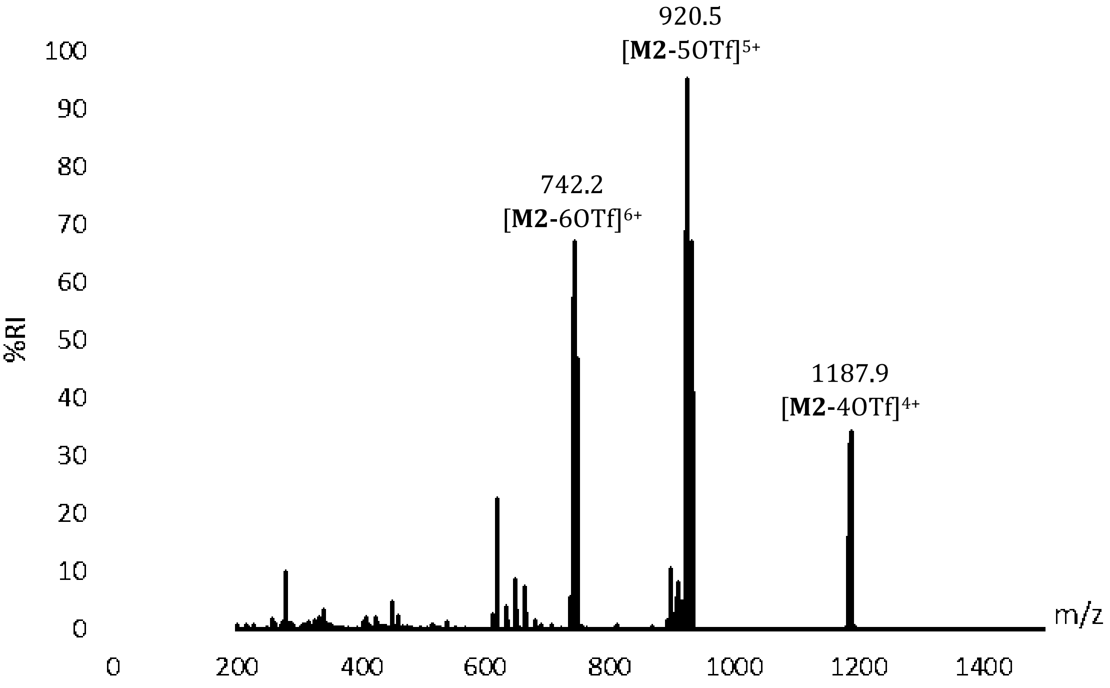

Figure S2. Mass spectrometry for **M2** – ESI (+)

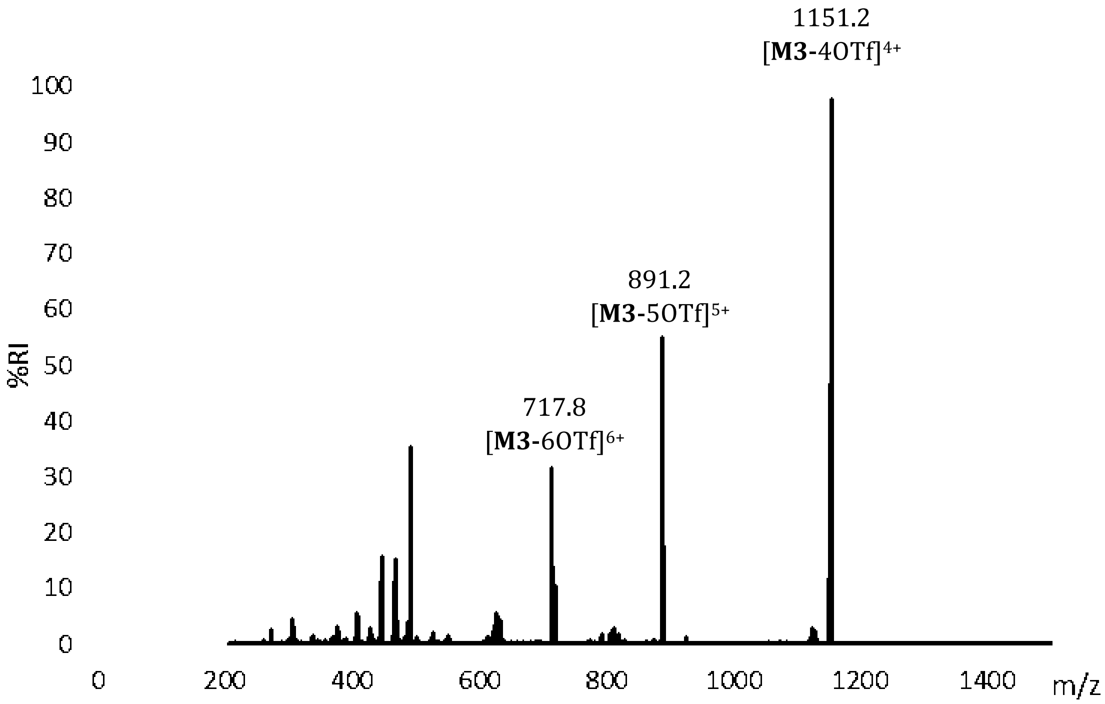

Figure S3. Mass spectrometry for **M3** – ESI (+)

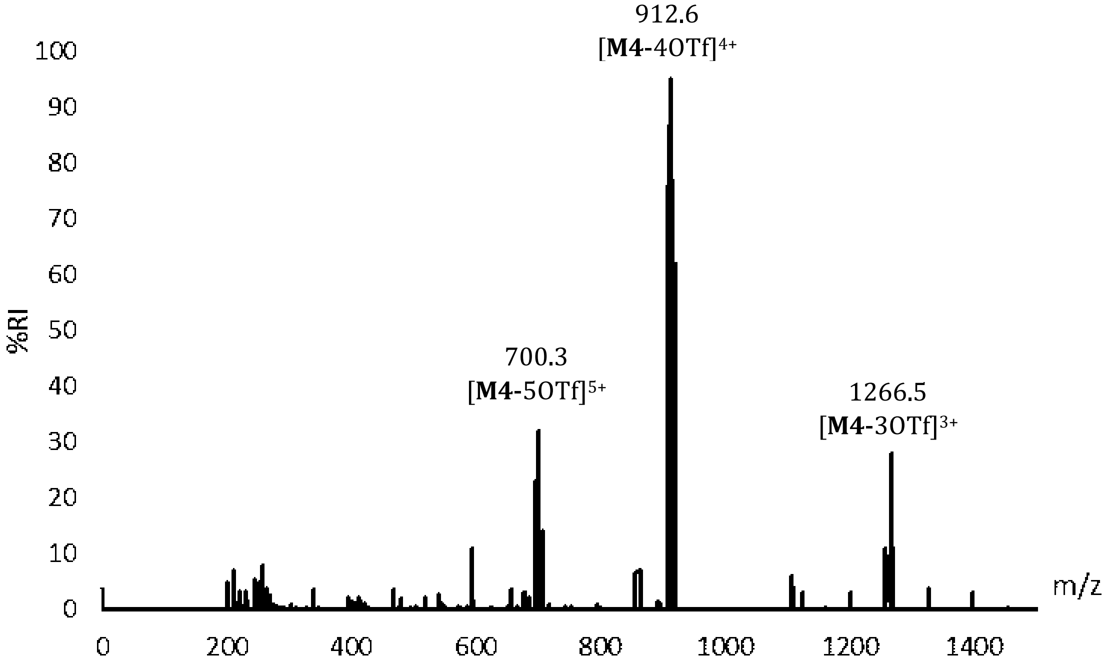

Figure S4. Mass spectrometry for **M4** – ESI (+)

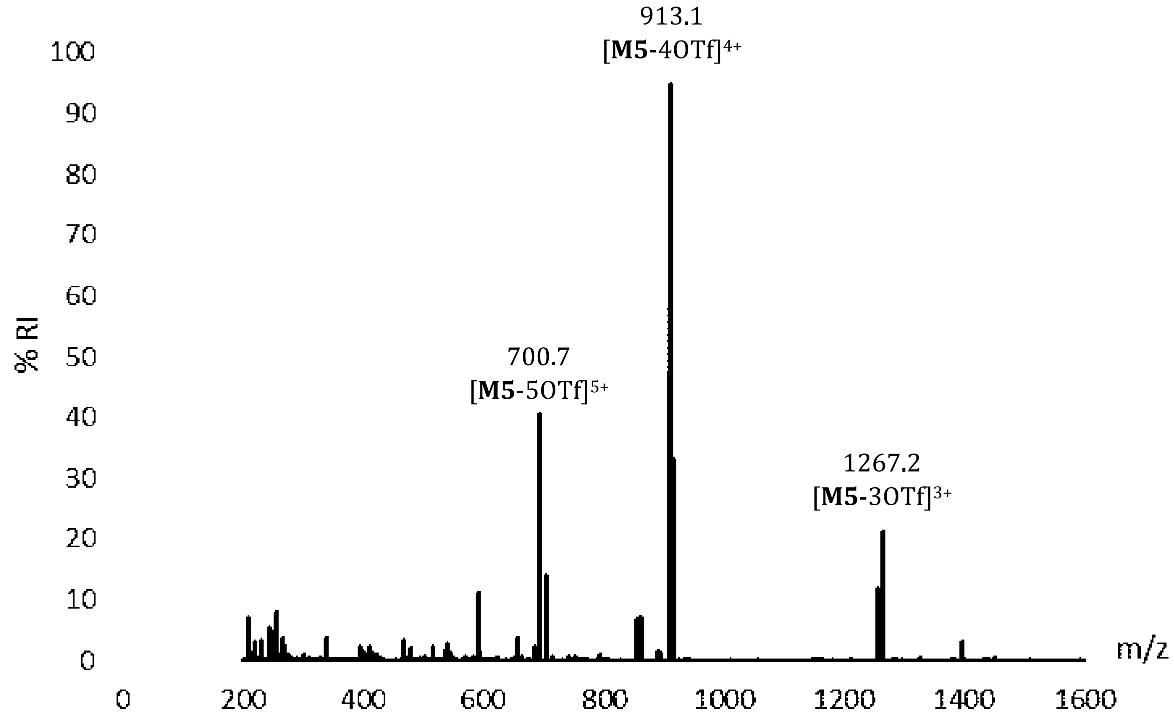

Figure S5. Mass spectrometry for **M5** – ESI (+)

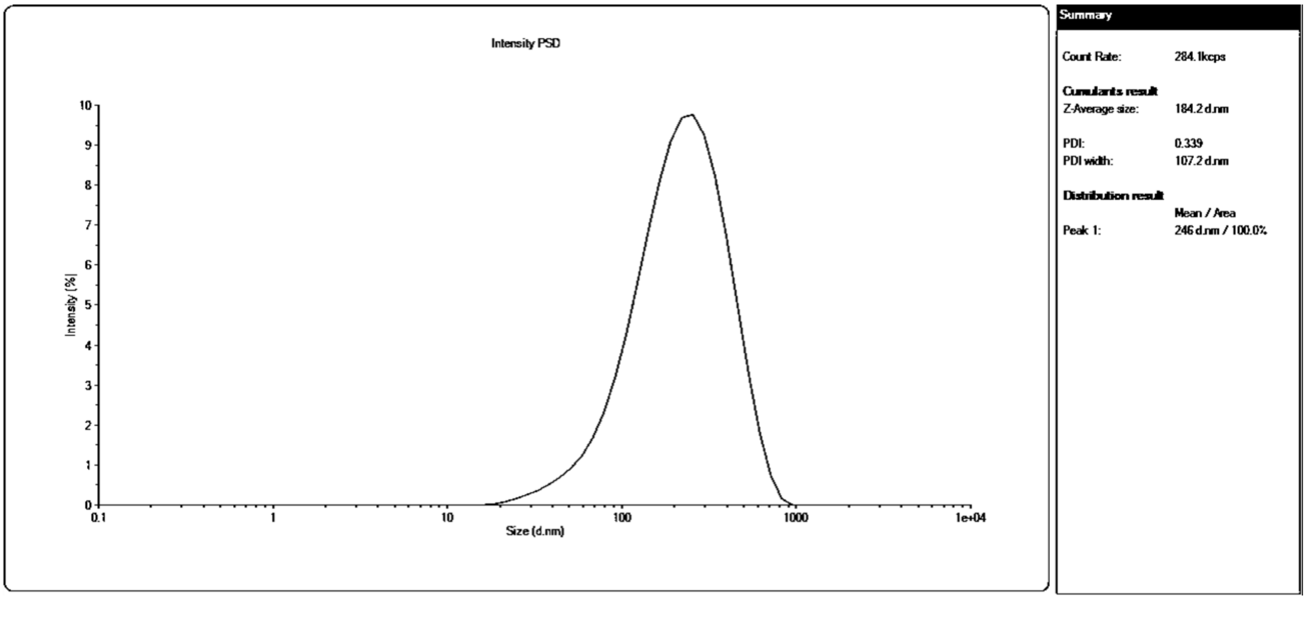

Count Rate:	284.1kcps
Cumulants result	
Z-Average size:	184.2 d.nm
PDI:	0.339
PDI width:	107.2 d.nm
Distribution result	
	Mean / Area
Peak 1:	246 d.nm / 100.0%

Figure S6 - Dynamic light scattering (DLS) data of **MC5** collected for the measurement of average hydrodynamic diameters.

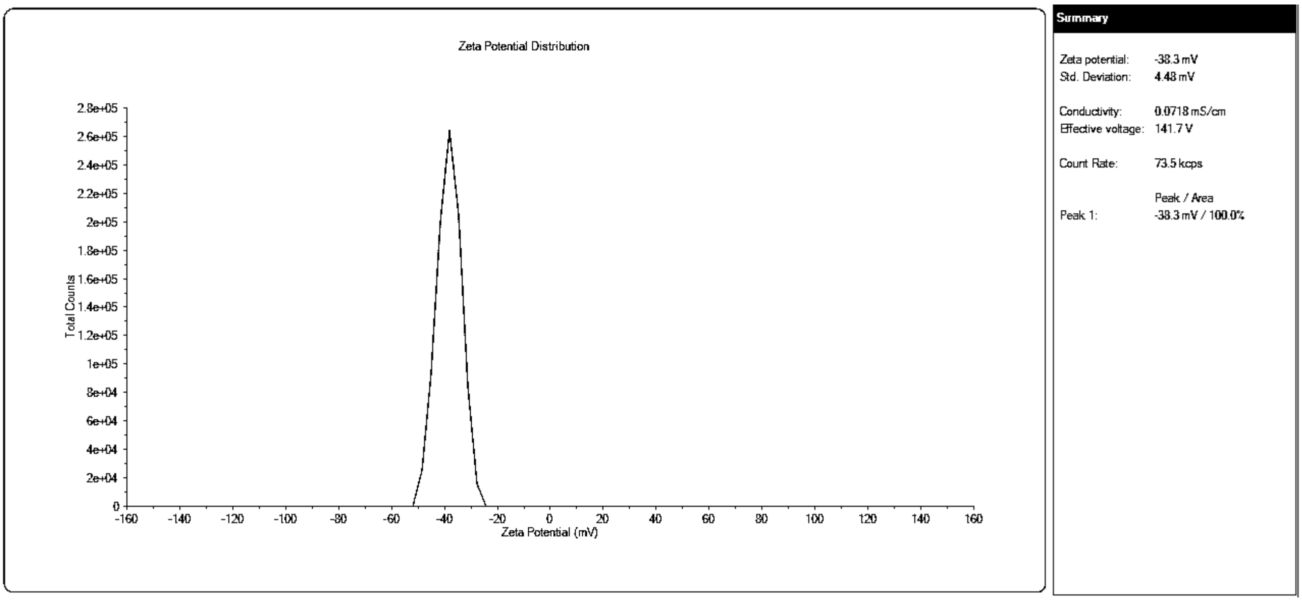

```
Summary

Zeta potential:       -38.3 mV
Std. Deviation:       4.48 mV

Conductivity:         0.0718 mS/cm
Effective voltage:    141.7 V

Count Rate:           73.5 kcps

                      Peak / Area
Peak 1:               -38.3 mV / 100.0%
```

Figure S7 - ζ-potential data of **MC5** collected through electrophoretic light scattering.

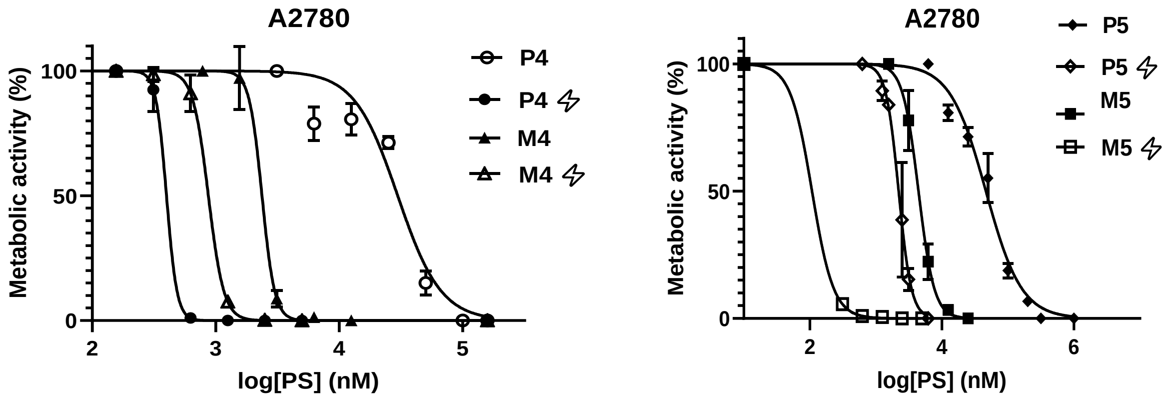

Figure S8 – Metabolic activity against ovarian cancer cell line A2780 in the dark and after irradiation (your lightning symbol). Standard error calculated from 3 repeated measurements.

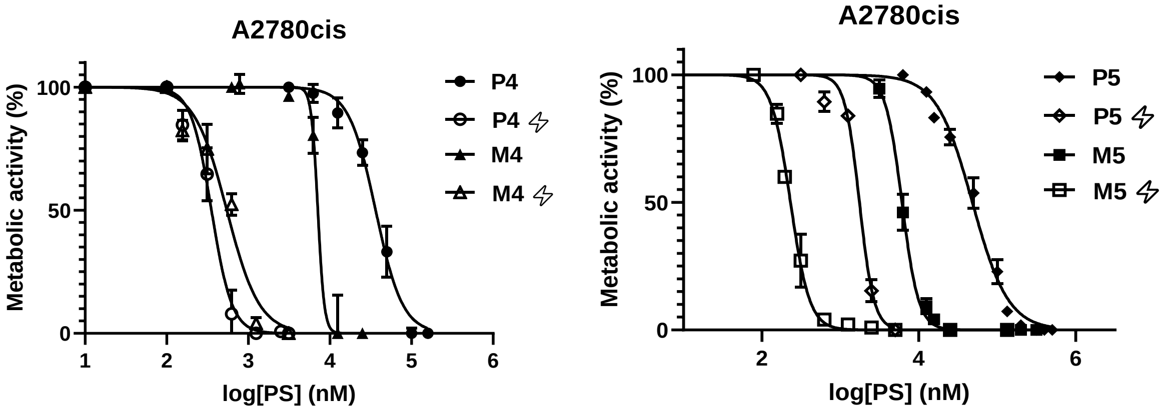

Figure S9 – Metabolic activity against ovarian cancer cell line A2780cis in both the dark and after irradiation. Error bar stands for standard error (±SE), calculated from 3 repeated measurements.

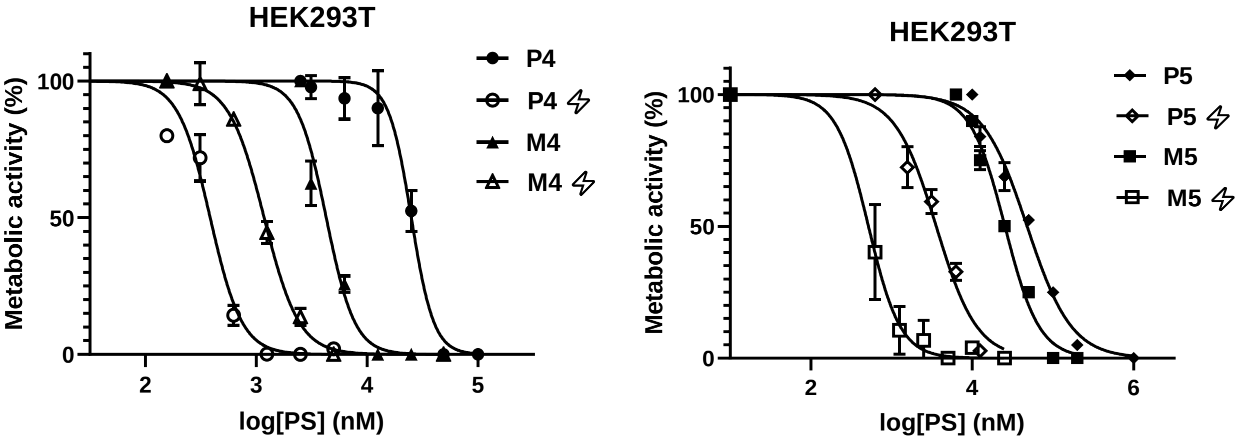

Figure S10 – Metabolic activity against normal liver cell line HEK293T in both the dark and after irradiation. Error bar stands for standard error (±SE), calculated from 3 repeated measurements.

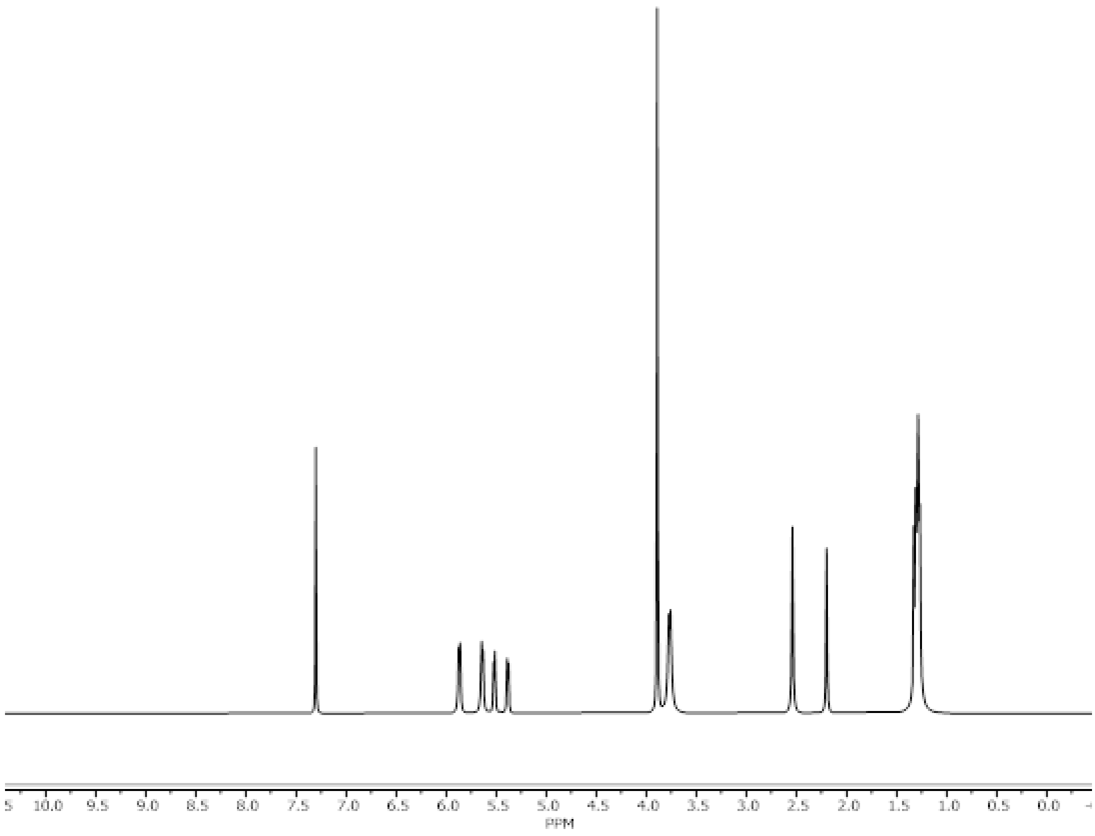

Figure S11: ^{1}H NMR spectra (between 0 and 10 ppm) of **C3** in DMSO-d$_6$

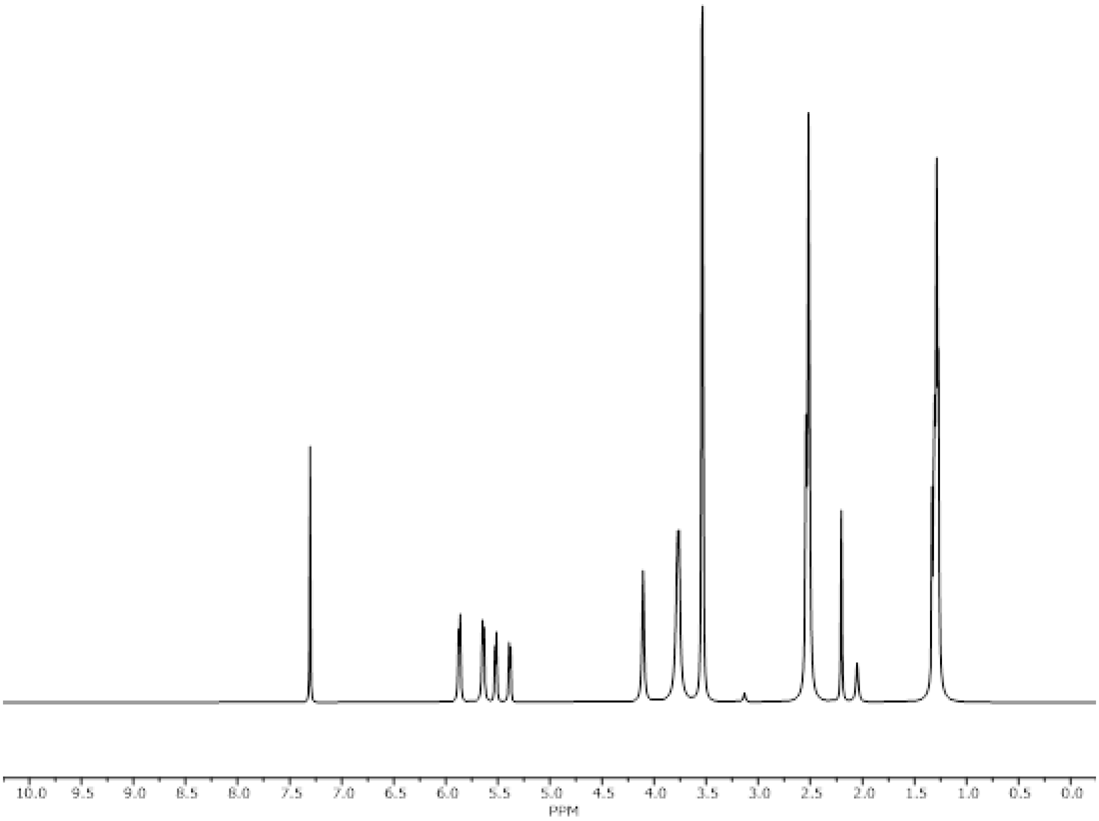

Figure S12: ^{1}H NMR spectra (between 0 and 10 ppm) of **C4** in DMSO-d_6

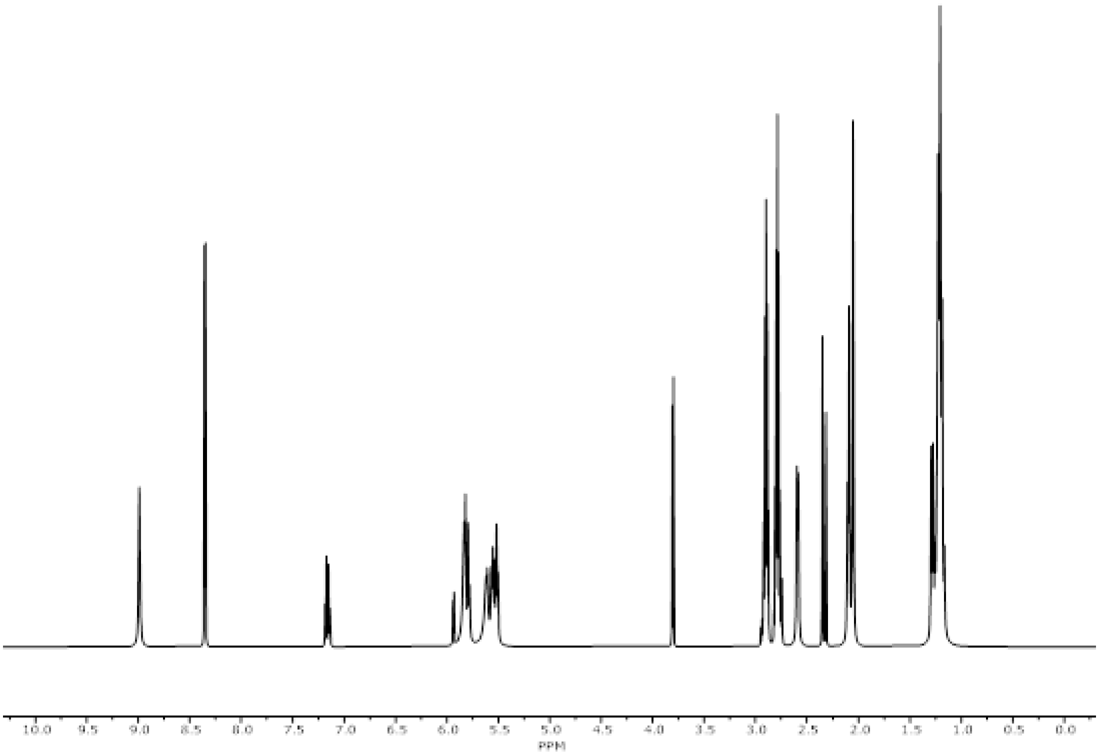

Figure S13: ^{1}H NMR spectra (between 0 and 10 ppm) of **M1** in DMSO-d_6

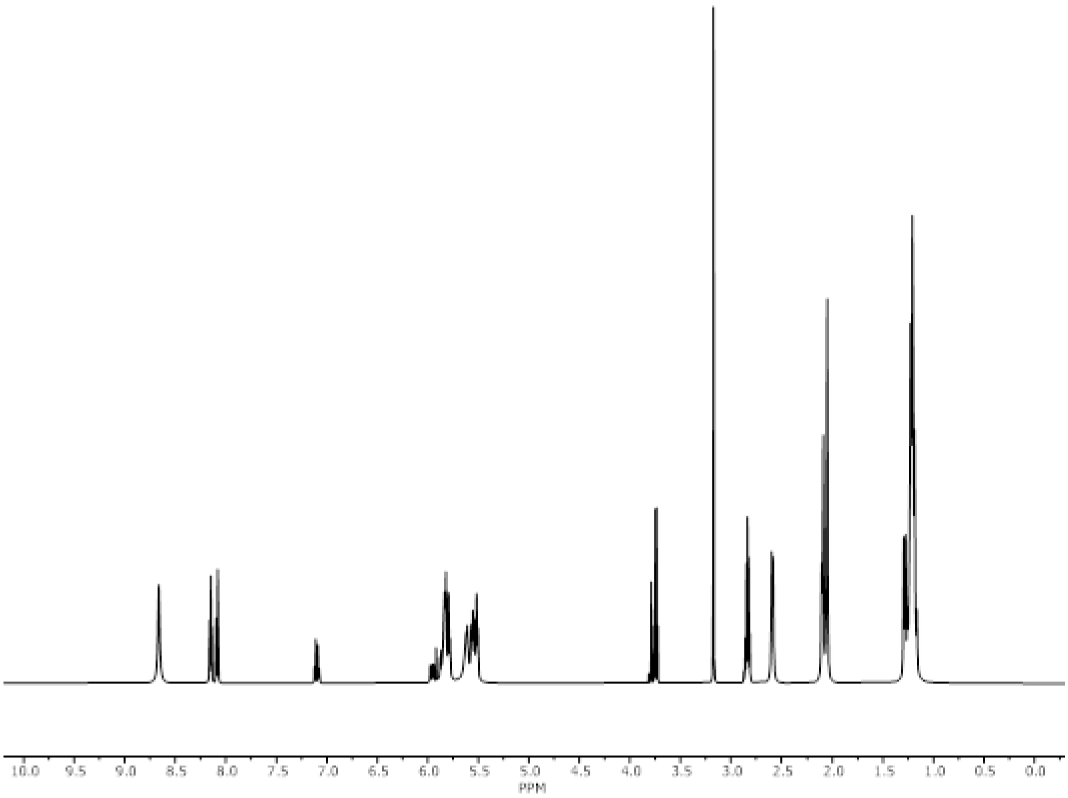

Figure S14: ^{1}H NMR spectra (between 0 and 10 ppm) of **M2** in DMSO-d_6

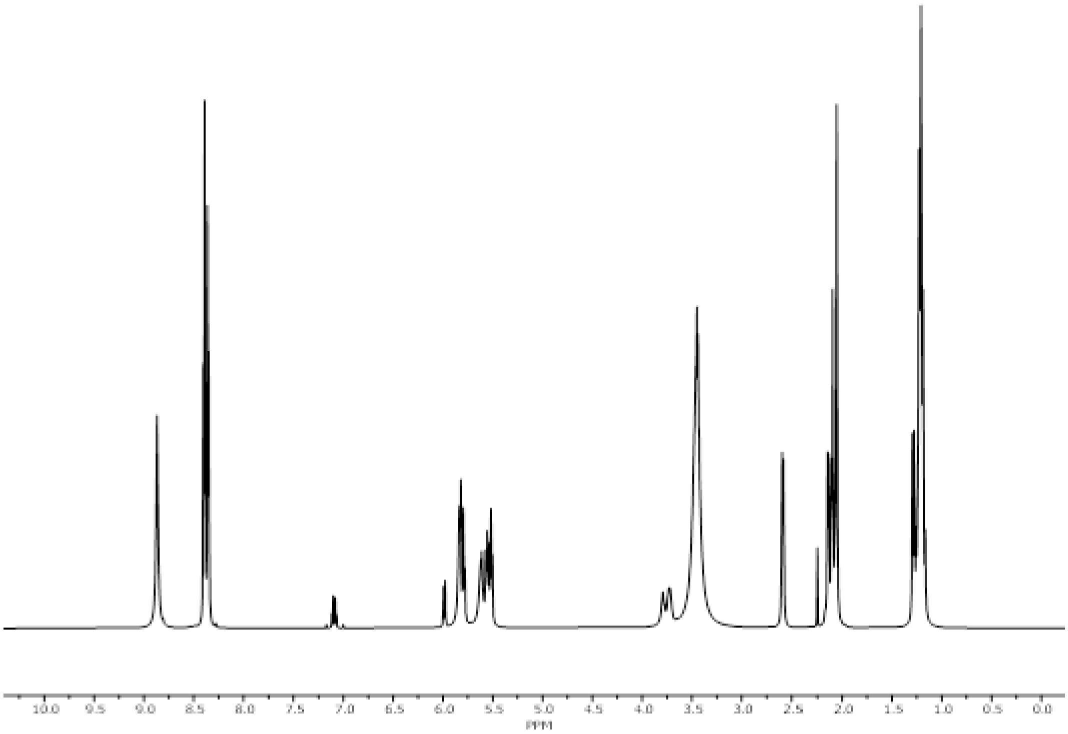

Figure S15: ^{1}H NMR spectra (between 0 and 10 ppm) of **M3** in DMSO-d_6

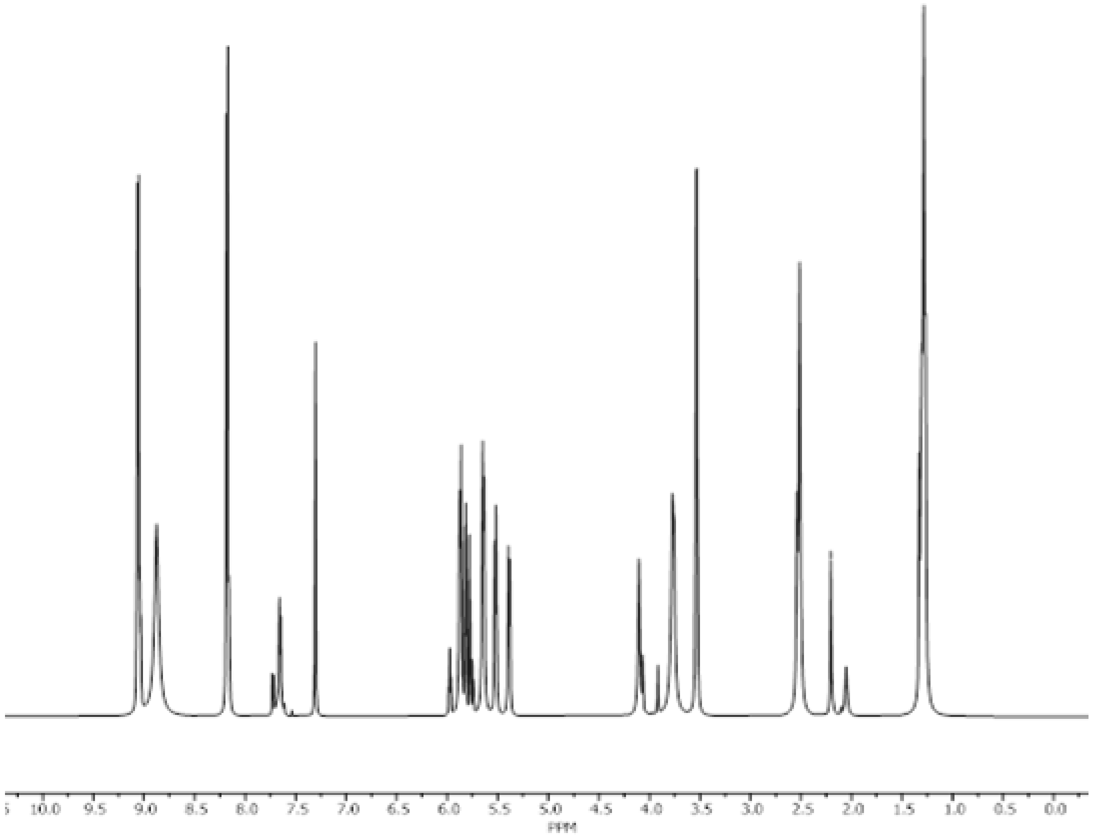

Figure S16: ^{1}H NMR spectra (between 0 and 10 ppm) of **M4** in DMSO-d_6

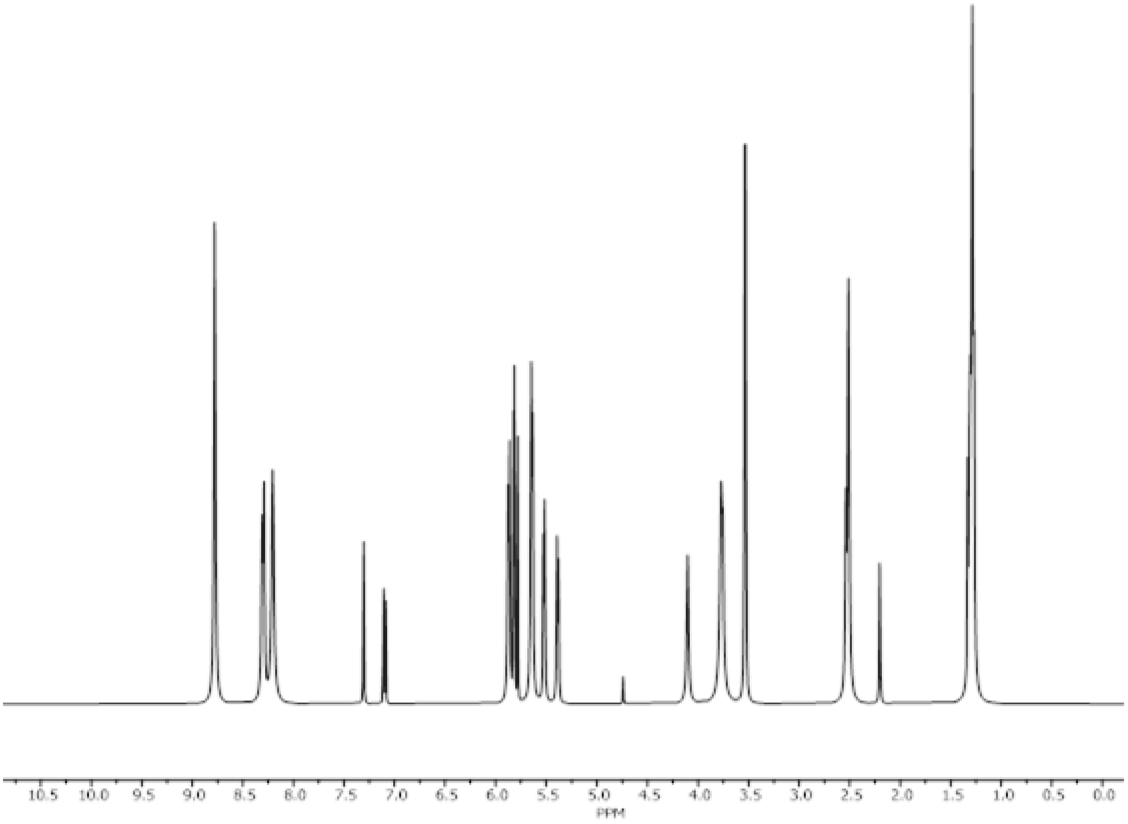

Figure S17: ^{1}H NMR spectra (between 0 and 10 ppm) of **M5** in DMSO-d_6